Sede Amministrativa: Università degli Studi di Padova
Dipartimento di Fisica e Astronomia “G. Galilei”

Corso di Dottorato di Ricerca in Astronomia
Ciclo XXX
Coordinatore: Ch.mo Prof. Giampaolo Piotto

Con menzione di cotutela / Avec mention de cotutelle:

Siège administratif: Université de Genève
Observatoire de Genève

Doctorat ès sciences Mention: Astronomie & Astrophysique
Coordinateur: Prof. Daniel Schaerer

Bridging the lower- and the upper-atmosphere of exoplanets through high-resolution transmission spectroscopy

Supervisori / Directeurs: Prof. Giampaolo Piotto; Prof. Francesco Pepe
Co-Supervisori / Co-Directeurs: Prof. Valerio Nascimbeni; Prof. David Ehrenreich

Dottorando / Doctorant: Lorenzo Pino

Contents

1 Introduction **6**
- 1.1 From discovery and statistics... 6
- 1.2 ... to in-depth characterization 8
- 1.3 The structure of atmospheres 10
- 1.4 The context of this thesis 11

2 Observations of transmission spectra **14**
- 2.1 Remote sensing of exoplanets through transmission spectroscopy 14
  - 2.1.1 Observable features in exoplanetary atmospheres 16
  - 2.1.2 Some key factors in exoplanet atmosphere observations 17
- 2.2 Main results from transmission spectroscopy of hot Jupiters 21
  - 2.2.1 Lower atmosphere 22
  - 2.2.2 Upper atmosphere 29
- 2.3 This thesis: towards a global view of exoplanet atmospheres 32

3 Towards a global interpretation of atmospheric structure **34**
- 3.1 Introduction 35
- 3.2 The $^{\pi}\eta$ code 37
  - 3.2.1 The η code 38
  - 3.2.2 Atmospheric structure 38
  - 3.2.3 Geometry 39
  - 3.2.4 Photoabsorption cross sections at high spectral resolution 39
- 3.3 Simulating observed transmission spectra 44
  - 3.3.1 Convolution with the instrumental LSF 44
  - 3.3.2 Binning 45
  - 3.3.3 Wavelength normalization 45
- 3.4 Transmission spectrum and planetary absorption 45
- 3.5 HD189733b case: methods 47
  - 3.5.1 HST data set 49
  - 3.5.2 HARPS data set 50
- 3.6 HD189733b case: results and discussion 50
  - 3.6.1 HST data set 50
  - 3.6.2 HARPS data set 52
- 3.7 Towards the atmosphere of HD189733b as a whole 57
- 3.8 Extending the project 59
  - 3.8.1 Extension based on HARPS and HARPS-N 59
  - 3.8.2 Extension based on HST 60
  - 3.8.3 The ESPRESSO and CARMENES opportunities 64
- 3.9 Conclusions 66

4 Observing the lower atmosphere at high-resolution **69**
4.1 Chromatic Rossiter–McLaughlin effect . . . 70
4.2 Stellar and planetary variability . . . 70
    4.2.1 Stellar activity . . . 72
    4.2.2 Planetary weather . . . 73
    4.2.3 Motivation of this work . . . 74
4.3 Diagnosing aerosols in extrasolar giant planets with water bands resolved at high-resolution . . . 74
4.4 Methods . . . 75
    4.4.1 High resolution template . . . 76
    4.4.2 Convolution with the LSF and binning . . . 79
    4.4.3 Cross-correlation . . . 79
4.5 Results and discussion . . . 81
    4.5.1 Ideal case . . . 81
    4.5.2 A metric to diagnose aerosols . . . 84
    4.5.3 Telluric contamination . . . 85
4.6 A search for water in the HARPS spectrum of HD189733b . . . 87
4.7 Conclusions and future prospects . . . 90

5 On the accuracy of $^{\pi}\eta$ (and more) **92**
5.1 Hydrostatic equilibrium . . . 93
5.2 Equilibrium and disequilibrium chemistry . . . 93
5.3 Aerosols . . . 96
5.4 Temperature profile . . . 102
5.5 Efficiently producing low- to medium-resolution spectra . . . 106

6 Conclusions **110**

Abstract

Only two decades have passed since the first exoplanets were discovered, yet we already know thousands of them. They show a huge range of masses, radii and orbits. Our planet formation and evolution theories, mostly based on the Solar System, are inadequate to explain such a variety, and need to be expanded. Sizes and masses (thus density) are now available for $\lesssim 1\,000$ exoplanets, but are insufficient to get the full picture. The bulk composition of a planet is a much better tracer of its formation and evolution history, but harder to access. Still, since about 15 years, a window on planetary interiors and chemistry is open: the study of their atmospheres.

The chemical composition of an atmosphere depends both on formation and evolution processes. The location where the planet formed (inside or outside the snow line) and the detailed formation process (core accretion or disk instability) determine the initial enrichment in heavy elements, best traced with the lower atmosphere composition. Subsequent processes, such as atmospheric evaporation in the upper atmosphere, cause a departure from the initial composition. Both the lower and the upper atmosphere need to be studied to disentangle these effects.

Transmission spectroscopy, in particular, offers the opportunity to probe atmospheres from ~ 10 bar, where composition more closely follows the bulk chemistry, to the outermost, non-collisional exosphere, where evaporation and other evolutionary processes take place. Two major challenges limit the effectiveness of transmission spectroscopy:

1. Observations of the lower and the upper atmosphere come from different instruments, in terms of wavelength coverage, resolving power, and sensitivity to the planetary continuum, hampered by the effects of Earth atmosphere for ground-based instruments. These differences make it challenging to combine them;

2. Scattering by aerosols can mask spectral features, preventing us from identifying key atmospheric components, but also bias our interpretation leading to wrong conclusions on the abundances of atmospheric constituents.

During my PhD, I developed the $^{\pi}\eta$ code to address these issues. $^{\pi}\eta$ is a flexible tool able to simulate transmission spectra observations from low- to high-resolution ($R \sim 10^2$–10^5), over a broad wavelength range (0.3 μm–2 μm), taken from ground or space, across the lower and the upper atmosphere.

First, I benchmarked $^{\pi}\eta$ by matching its predictions to optical, ground-based, high-resolution ($R \sim 10^5$) HARPS transmission spectra of hot gaseous giants. In WASP-49b, I determined that the strong cores of sodium lines are generated in the thermosphere, as their large intensity requires an atmospheric temperature in excess of $\sim 2\,000$ K compared to the equilibrium temperature of the planet. In HD189733b,

I showed that a non-detection of water with HARPS is consistent with the expectations, and determined that the new ESPRESSO spectrograph should be able to reveal water in a bright, aerosol-free hot Jupiter with just one transit.

Exploiting $^{\pi}\eta$, now validated, I combined for the first time low-resolution ($R \sim 10^2$), space-borne, optical to near-infrared (NIR), HST observations, and high-resolution ($R \sim 10^5$), ground-based, optical, HARPS observations of the sodium doublet. Combined, they probe from the lower to the upper atmosphere of HD189733b (Pino et al. 2017). Results on the separate HST and HARPS data sets are consistent with those reported in the literature (HST: e.g. Pont et al. 2013; Sing et al. 2016; HARPS: Wyttenbach et al. 2015). While the HST data set shows the prevalence of aerosols in the atmosphere of the planet, previous analyses of HARPS observations of the cores of the sodium doublet had assumed that these are too low to impact their intensity. Yet, by accounting for constraints from both data sets, I have shown that under this assumption they underestimated the thermospheric temperature, which may be as high as 10 000 K at 0.25 R_p (in accordance with models and far-UV observations; Koskinen et al. 2013a; Lecavelier Des Etangs et al. 2010). Alternatively, HD189733b may have up to 10^2 times solar abundance of sodium.

Besides impacting on the interpretation of atomic lines, aerosols constitute a limiting factor for transmission spectroscopy since they occult spectral features such as molecular bands. If not occulted, molecules can be revealed in high-resolution transmission spectra from their cross-correlation function (CCF). Water has several well separated absorption bands, with increasing intensity from the optical to the near-infrared. On the other hand, the intensity of scattering by aerosols is a decreasing, or constant, function of wavelength. Therefore, in the presence of aerosols, bluer molecular absorption bands are more muted than redder bands. The difference in the contrast of the CCF of different bands is thus a measure of how high in the atmosphere aerosols are. By simulating a grid of high-resolution transmission spectra of hot Jupiters with and without aerosols, I found that the contrast difference between the CCFs of two bands can reach ~ 100 ppm, which could be readily detectable with current or upcoming high-resolution stabilized spectrographs spanning a wide spectral range, such as ESPRESSO, CARMENES, HARPS-N+GIANO, HARPS+NIRPS, CRIRES+ or SPIRou.

Aerosols do not however impact our findings in WASP-43b, where a preliminary reduction of 3 HARPS/-N transmission spectra showed a deep sodium signature that could be matched only by putting sodium 200 scale heights up in the atmosphere, possibly in the exosphere. The host star is dim, and removal of telluric correction is thus not optimal. For this reason I asked for and obtained HST STIS G750M data at medium resolution ($R \sim 5\,000$) to confirm this unprecedented detection. Data reduction is ongoing, and the tools developed in this thesis will allow the combination of this data set with previous ground-based data.

Summarizing, this thesis benchmarked the possibility to characterize planetary atmospheres with a combination of different techniques, able to probe from the lower to the upper atmosphere. The issue of aerosols is also tackled, by providing an alternative and innovative method to diagnose them. Observations from JWST and the ELTs will provide key insights in planet formation and evolution theories, and may greatly benefit from a development of the ideas presented in this thesis.

Chapter 1

Introduction

1.1 From discovery and statistics...

When I told my grandfather that I wanted to be an astrophysicist, he told me all that he had learned by staring at the night-sky on the shore of the small village of Santo Saba (ME) 80 years ago. Considering that he was grown in a family of fishermen and later became a *carabiniere*, I was rather surprised that he already knew since when he was young that exoplanets – planets orbiting around other stars – existed. Indeed, until the second half of the 1900s, not everyone was as sure as my grandfather. The debate, that dates back to Epicurus, and possibly Anaximander and the atomists before him, who believed in infinite words, and Aristoteles, who instead postulated that there was only one, was however never supported by scientific evidence[1].

After an initial skepticism, mainly due to he predominance of the stellar encounter theory for the formation of planetary systems (a very unlikely event), the scientific community invested a lot of effort in the research of exoplanets. In part, this was due to detection claims based on astrometry on photographic plates (Strand 1943; Reuyl and Holmberg 1943) that were later disproved as due to systematic errors (Heintz 1978, 1988). In the early nineties, an exoplanet detection was within reach (Latham et al. 1989), and not unexpected. Nonetheless, the actual detection of the first exoplanets (Wolszczan and Frail 1992)[2], especially around the solar-type star 51–Peg (Mayor and Queloz 1995), was accompanied with great excitement. The newly found 51–Peg b is a so called "hot Jupiter", a gaseous giant orbiting its host star closer than Mercury to the Sun. It is immediate to ask oneself if this world is a peculiar case or the paradigm of planetary formation, as opposed to the very different Solar System, how it arrived or formed there, and what it is made of (my grandfather actually asked me all of these questions when I told him about 51–Peg b).

In 20 years, we made significant progress towards the answer to these and other questions. Thanks to technical realizations such as the sub-meter-per-second radial-velocity precision of the HARPS spectrograph (Mayor et al. 2003) and the tens of parts per million photometric precision of the *Kepler* space-telescope (Gilliland et al. 2011), the mass-radius (or density-radius) diagram of exoplanets was pop-

---

[1] Unless you truly believe that my grandfather spot an exoplanet by naked eye.

[2] There is no formal definition of an exoplanet from the IAU. According to the working definition by the Working Group of ExtraSolar Planets, the system of bodies orbiting the pulsar PSR B1257+12 is a planetary system.

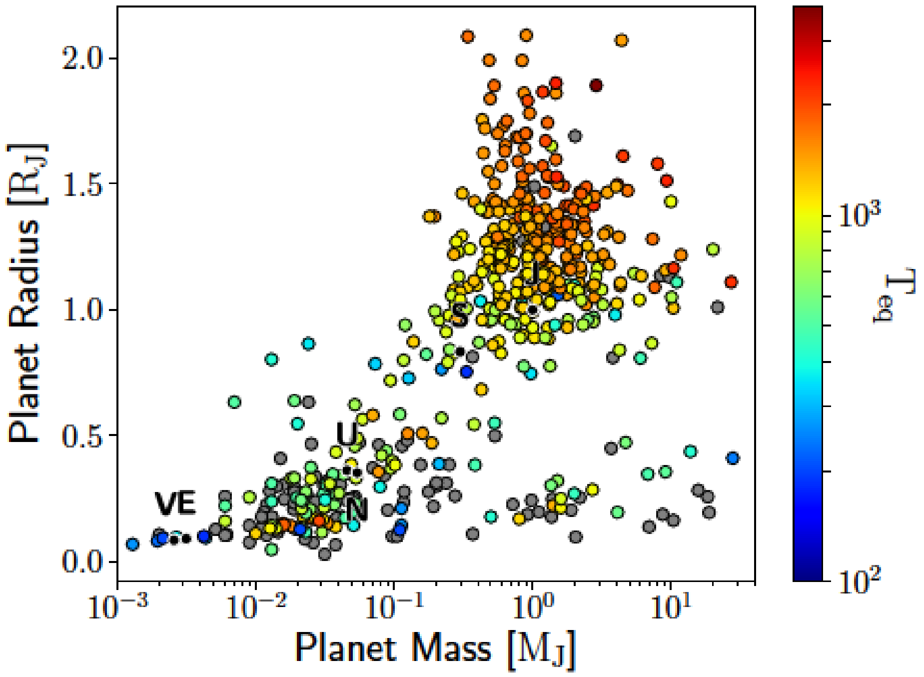

Figure 1.1: Mass-radius diagram for all planets of known mass and radius uncovered with the transit or radial velocity method, taken from the NASA exoplanets archive. The color indicates the equilibrium temperature (a measure of the irradiation of the planet; grey when unknown because of missing parameters). This diagram is fully affected by observational biases and many other uncertainties. Small planets occupy the whole region comprised between Earth and Neptune (hence the naming super-Earth or mini-Neptune). Hot Jupiters appear as planets of mass similar to Jupiter and Saturn. A clear correlation exists between radii and equilibrium temperature of hot Jupiters: part of the stellar energetic input is used to in inflate the radii of these extremely hot objects.

ulated covering extremely diverse regimes. Statistics of exoplanetary populations became a reality[3]. Currently, nearly 3000 transiting planets have been unveiled by vetting of Kepler lightcurves (Morton et al. 2016), of which approximately 500 have also a mass and thus a density determined (and are thus confirmed, see Fig 1.1).
Among exoplanets with a known radius, the vast majority (2297/2770)[4] has a radius smaller than 6 Earth radii ($R_\oplus$). These are the so called “small planets”, further divided a “super-Earth” regime ($R < 1.5R_\oplus$) and a “mini-Neptune” regime ($1.5R_\oplus < R < 6R_\oplus$), following the transit community nomenclature. These planets are common and found in all conditions of irradiation and metallicity of their host star (a widely accepted conclusion, but see e.g. Zhu et al. 2016; Wang and Fischer 2015; Adibekyan et al. 2012), and show very disparate densities (and thus compositions, see Fig. 1.2). The remaining Saturn- and Jupiter-sized planets are predominantly found around metal-rich stars, favouring core accretion theory. The

---

[3] Contributions from ground-based transit photometry are also important, while microlensing and direct imaging are complementary in terms of observational biases.

[4] `https://exoplanetarchive.ipac.caltech.edu/docs/counts_detail.html`

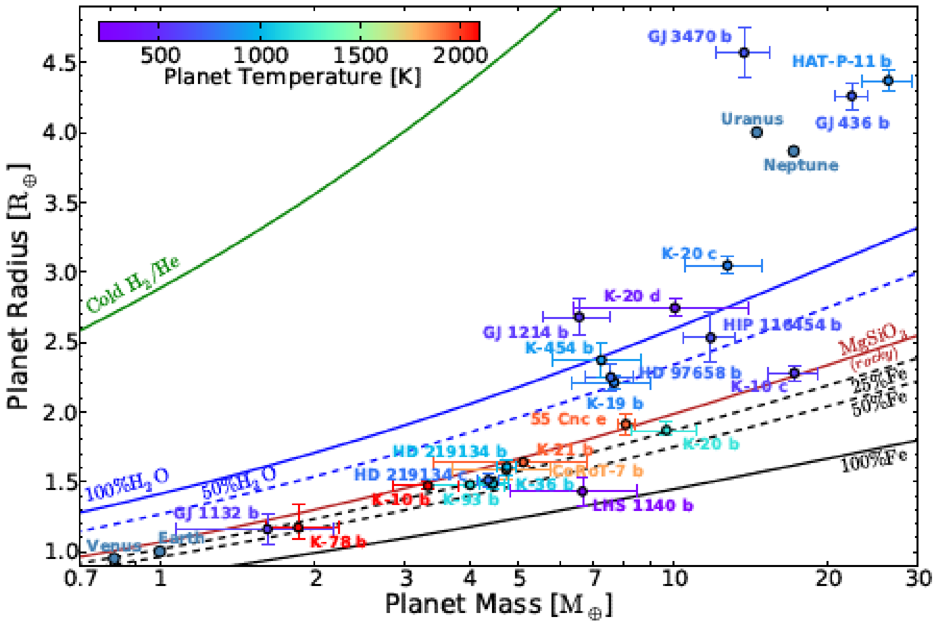

Figure 1.2: Figure courtesy of A. Wyttenbach, from his PhD thesis. Masses (measured through radial velocities) and radii (inferred from transit depth) of well characterized small planets. The comparison with models by Zeng et al. (2016) illustrate the wide variety in compostion that these planets show. Figure originally adapted from Motalebi et al. (2015); Dressing et al. (2015).

size of hot Jupiters, that orbit their hosts with periods of days or hours, is correlated with their level of irradiation (see Fig. 1.1).

The diversity of exoplanets found in the mass–radius diagram shows, at the least, that planetary formation takes place in disparate conditions of metallicity and irradiation. However, limited insight on formation pathways and evolution of planets can be extracted from just their average density and radius. A clear example is provided by studies of Jupiter, in the Solar System. Information on its average density and radius is not enough to infer the fraction of heavy elements in its interior (Guillot 1999; Wahl et al. 2017), a fundamental constraint for theories of formation and evolution of the planet (Helled and Lunine 2014), and important enough to partially justify the dedicated space mission *Juno* (Bolton and Juno Science Team 2006; Matousek 2007; see section 1.2).

Likewise, a more detailed characterization of exoplanets must accompany the discovery process. Despite the difficulties of the task, a window on the chemistry of exoplanets has already been opened: the study of their atmospheres.

1.2 ... to in-depth characterization

Experience gained in the Solar System has shown that characterization of planetary atmospheres is the path to follow to better understand formation and evolution processes of planetary systems. A primary aim of the aforementioned *Juno* mission is to measure for the first time the global water abundance in Jupiter, down to $P \sim 100$ bar in its atmosphere. The task is challenging, since water is condensed down at pressures greater than ~ 10 bar because of the low temperature ($T \lesssim 125$ K). Still, this is a key passage to constrain the composition of the planet, and thus formation theories (e.g. Madhusudhan et al. 2016). Indeed, the composition of the planet depends on the region of the disk where it formed (inside or outside the snow line? Lodders 2004) and by the detailed formation mechanism involved (core accretion or disk instability, and in which flavour?).

Albeit fundamental, determining water abundance in Jupiter's atmosphere is not sufficient to fully illuminate its formation history (and thus of the entire Solar System), as its interpretation is not straightforward (Leconte and Chabrier 2012; Helled and Lunine 2014). Additional constraints could come from similar observations on the other giant planets of the Solar System (e.g. from the comparison with Saturn, Lodders 2004; Helled and Lunine 2014). However, determining the composition of the outer giants is more difficult. Outer giants are indeed colder, which causes heavy elements to condense much deeper in the atmosphere, making them hardly observable.

Still, a comparison term for Jupiter is a necessary factor to pinpoint the key processes in planet formation. Luckily, we have thousands of them: exoplanets. It may seem rather pretentious to claim that exoplanets are a viable alternative to a deeper characterization of Solar System objects. The conundrum is solved by considering two main observational advantages of exoplanets. First, they are warmer (at least, the ones we can observe now). At higher temperature, removal processes of molecules from the atmosphere are less efficient (condensation and sinking, cold trap, ...). More chemicals are thus spectroscopically active in the atmosphere (thus observable; Madhusudhan 2012), and they are also more representative of their bulk composition. Second, in the next decades we will measure the atmospheric properties of hundreds – maybe thousands – of exoplanets (e.g. thanks to the TESS and PLATO surveys; Ricker et al. 2015; Rauer et al. 2014). These are found in different environments (metallicity, irradiation, ...), and thus form a statistical sample that will allow us to identify the parameters playing a prominent role in planetary formation.

The challenge is exciting, but tough. Evolutionary processes such as core erosion or evaporation of atmospheres are now nearly ascertained to play a role in shaping the density–radius–irradiation diagrams and the chemistry of exoplanets. Furthermore, the accuracy of exoplanet remote sensing techniques is hampered by the presence of exoatmospheric aerosols formed by refractory material (such as oxides of titanium/aluminum and calcium, iron, ...). Although clear evidence of their presence has been found (Sing et al. 2016), their composition, their particle size distribution and their formation pathways are poorly understood (Marley and Robinson 2015; Heng and Marley 2017). Currently, aerosols are one of the limiting factors in our studies on exoplanetary atmospheres: not only they mask spectral features, preventing their recognition (Kreidberg et al. 2014) or biasing their interpretation (Pino et al. 2017), but they introduce complexity and uncertainties in models (Marley and Robinson 2015).

Despite these difficulties, the challenge is worth taking. The study of exoplanets is the only way to understand how unique (or not) is the Solar System. By putting the Solar System in a broad context, we may eventually unveil the predominant planet formation mechanisms in our galaxy. The study of exoatmospheres is a necessary condition to reach this objective. However, before jumping a few parsecs away, it is worth summarizing our knowledge of how a planetary atmosphere is structured.

Necessarily, this comes from the study of the Solar System, and of the Earth in particular.

1.3 The structure of atmospheres

Atmospheric regions are defined according to vertical variations in some observable quantity, such as ionization rate, chemical composition or temperature profile. This information is not easy to get, and Solar System planetology often relies on in-situ observations. This is obviously impossible for exoplanets. Nowadays, through a combination of remote sensing techniques we are able to measure the vertical temperature profile over a good extent in the atmospheres of exoplanets (albeit not as precisely as we do in our Solar System), and it thus makes sense to focus on the definitions linked to it (most of what follows is based on Chamberlain and Hunten 1987; Irwin 2003).

I will refer to the *lower atmosphere* of a planet as that part of the atmosphere where pressure is higher than ~ 1 mbar. All the Solar System worlds that posses thick atmospheres show a decreasing temperature–pressure profile ($T-p$ profile) up to pressures of ~ 0.1 bar (Orton 1981; Robinson and Catling 2014). This behaviour defines the *troposphere*. Its name is derived by the Greek word $\tau\rho\acute{o}\pi o\zeta$, that used as a prefix indicates "changeability", "continuous change"[5]. The atmosphere here is optically thick, and radiative transport is too inefficient to dissipate heat. The temperature gradient becomes steep enough for convective instabilities to arise, hence the naming of the region. Equilibrium clouds form in this region of the atmosphere, when the partial pressure of a gas exceeds the saturated vapor pressure.

Higher up, the opacity of the atmosphere is reduced and radiative transport becomes the most efficient way to dissipate heat. The temperature tends to a "skin" value (a result of standard grey atmosphere calculations), reached in proximity of the *tropopause* (~ 0.1 bar). For lower pressures, the majority of Solar System objects shows a temperature inversion, which defines a *stratosphere*. Venus is the relevant exception (together with Mars, whose atmosphere is thin. See Fig. 1.3). The common factor is the transparency to thermal-radiation, that allows short-wave heating to dominate (Robinson and Catling 2014). The stratosphere is heated due to absorption of stellar light in the UV through photodissociation (e.g. of ozone on Earth) and optical and NIR absorption by aerosols and/or specific gaseous absorption bands (e.g. methane on giant planets in the Solar System). If it is close to radiative equilibrium, to allow the extra heat to be radiated away temperature needs to raise with height. Since it depends strongly on chemistry, a temperature inversion can be used as a tracer for specific compounds.

Upper atmosphere ($p < 1$ mbar) studies are concerned with photochemistry and atmospheric escape phenomena. The *thermosphere*, located at a pressures lower than 1 mbar, is heated up by absorption of far and extreme UV radiation (FUV, EUV), X-rays and cosmic rays. Photochemical reactions of hydrocarbons can lead to the production of high-altitude aerosols of small size (generally called "hazes"; likely observed in exoplanets as well, see chapter 2), that then can be mixed down to the lower part of the atmosphere. Heat is transported mainly by conduction. The result is a steep positive temperature gradient in the lower thermosphere, that tends to a constant value. This is usually called *exospheric temperature*, which is reached at the *thermopause* whose location depends on energy input and thermal

---

[5] https://en.wiktionary.org/wiki/tropo-

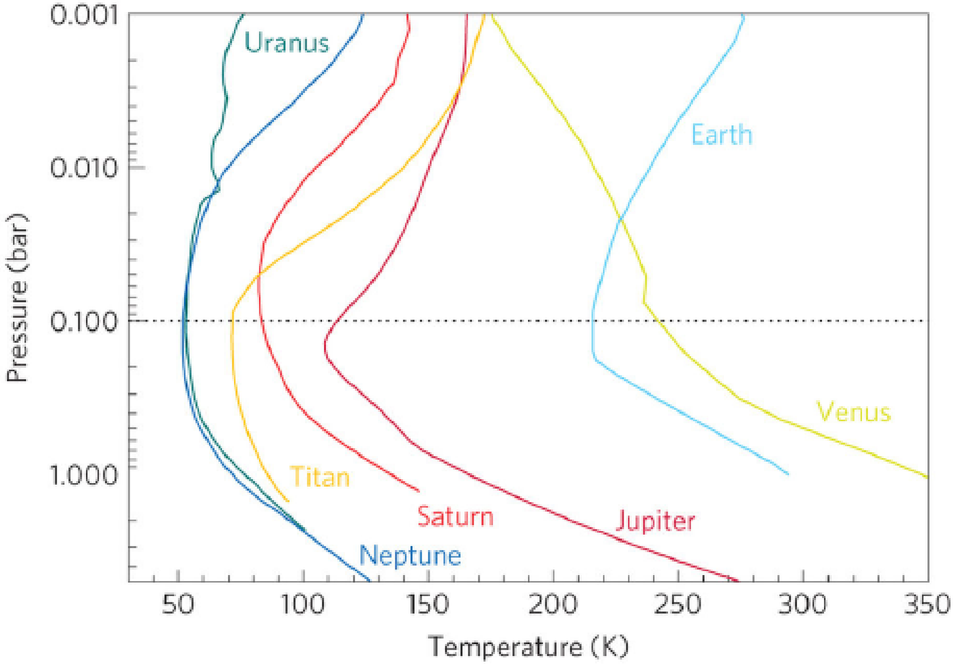

Figure 1.3: With the exception of Venus, that shows no stratosphere, all Solar System worlds that possess a thick atmosphere (Titan included) show a thermal inversion around 0.1 bar. This marks the onset of the stratosphere. Does this phenomenon occur on exoplanets as well? If so, does it present similar characteristics?

conduction. Above this level we find the *exosphere*, defined as the collisionless part of the atmosphere[6]. This is also the region where escape phenomena take place.

1.4 The context of this thesis

In the past two decades, several atomic (Na, K, Mg, ...) and molecular (H_2O, CO, CH_4, TiO, ...) species have been detected in the lower and upper atmospheres of giant planets (down to Neptune size). The temperature structure across the whole atmosphere is better and better understood, and provides a precious boundary condition for interior models. The importance of mass loss processes has been showcased thanks to the detection of evaporating atmospheres.

Clear questions and challenges have been posed by these observations. How do the conditions in planetary atmospheres depend on the formation and evolution history of the planet? How can we use atmospheres to quantitatively constrain planet formation theories? Which are the formation pathways of aerosols in extrasolar planets? How do we pierce through them?

The answer to these questions can only come from (1) studying the atmosphere of a large sample of planets and (2) interpreting all the evidence in a framework that connects the lower atmosphere (probe of the bulk chemistry, i.e. mainly of formation processes) and the upper atmosphere (where mass loss and other evolutionary processes take place). For example, the conditions for exospheric evaporation are determined by the thermospheric temperature, and convection phenomena may be

---

[6] The boundary between the upper thermosphere and the exosphere is not well defined: the decrease in importance in collision between molecules is gradual, and not sharp.

able to lift tropospheric species to the thermosphere.
Practically, until now, different instruments and observations have mainly been used to investigate the physical and chemical conditions in a single atmospheric region at a time. This was mainly due to limitations in the diagnostic power of these observations (set, in particular, by limited wavelength coverage and/or low resolving power, and by the difficulty of combining different observational techniques. See chapter 2). New instruments and observatories such as GIARPS, CARMENES, ESPRESSO, CRIRES+, JWST, the ELTs, etc., will be able to (1) access and characterize spectral features originated from the lower and the upper atmosphere simultaneously; (2) identify and characterize aerosol decks, and identify gaseous molecular species and possibly measure their abundance even in their presence.
These observatories will revolutionize our understanding of exoplanets, by finally providing a global view of their atmospheres, that goes from the lower to the upper atmosphere. However, current interpretative tools are mostly tuned on current observational capabilities, thus on specific atmospheric regions. Therefore, there is a need for a specific preparatory work.

Structure of this thesis: My thesis has its grounds in this context. Its main focus is transmission spectroscopy of the lower and the upper atmosphere of hot Jupiters, whose large gaseous envelope is more easily accessible to observations. I developed a tool (${}^{\pi}\eta$, Pino et al. 2017) to simulate observations over a large range of wavelengths at high-resolution, over tens of scale heights (the e-folding distance of pressure). As a result, with ${}^{\pi}\eta$ I could simulate the lower and the upper atmosphere as if observed with any kind of observatory (ground-based or space-borne, low- or high-resolution spectrographs or photometers, ...). Using this tool, I identified a few observational factors that determine which kind of science a given observation can access (**chapter 2**)[7].
Once these factors were identified and simulated, I could match models to observations. In **chapter 3**, I present the application of ${}^{\pi}\eta$ to high-resolution, ground-based optical spectra (published in Wyttenbach et al. 2017; Allart et al. 2017), and the observational context of which I am part of. This includes the preliminary results from an HST proposal to observe the sodium doublet in the hot Jupiter WASP-43b (GO14782; PI: Pino). Furthermore, with ${}^{\pi}\eta$ I was able to combine high-resolution, ground-based optical observations of the upper atmosphere and low-resolution, space-borne, optical to NIR observations of the lower atmosphere. Such a consistent interpretation from the lower to the upper atmosphere emphasized the crucial importance of accounting for aerosols, that impact observations of the whole atmosphere (Pino et al. 2017).
This prompted me to explore new possibilities to characterize aerosols. In **chapter 4**, I present an innovative technique to constrain the altitude of aerosols based on the relative contrast of the cross correlation function of different water bands. This technique, showcased on simulations (Pino et al. in prep), can be applied to ground-based, high-resolution transmission spectroscopy performed with current (or forthcoming) instruments with a broad wavelength coverage (GIANO+HARPS-N, NIRPS+HARPS, CARMENES, ESPRESSO, CRIRES+, ...).
The models of transmission spectra that I used in chapters 2-4 are computationally demanding. Thus, several simplifications were introduced in ${}^{\pi}\eta$, to make the code

---

[7] In chapter 2 I also present the detailed aims of this thesis in view of the current observational context.

more efficient. In **chapter 5**, I present a critical review of the hypotheses that I assumed and discuss which is their impact on my previous work (confirming the main conclusions that I drew). I also discuss which aspects of the code need to be ameliorated in view of future applications to data I already obtained (HST STIS observations of WASP-43b, Program 14782, PI: Pino), or data from future missions such as JWST.
Finally, in **chapter 6** I present the conclusions of this work and some future perspectives.

Chapter 2

Observations of transmission spectra

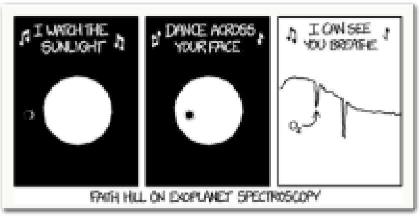

http://xkcd.com/1817/

The vast majority of known planets cannot be spatially resolved from their host stars. Thus, techniques have been developed to extract information in combined light (star + planet), by using the star itself as a constant reference point (Kreidberg 2017). They can be broadly divided in "Transit spectroscopy" (or "transmission spectroscopy") and "occultation spectroscopy" (or "emission spectroscopy"). These techniques are highly complementary: while the former is sensitive to trace species and allows to probe the region at $p < 10$ bar of the terminator of the planet up to the thermosphere, the latter is sensitive to the thermal profile between 100 bar and 10^{-5} bar (Seager 2010) in its day side. At the same time they are challenging to combine in a unique framework, as this needs to account for day-to-night circulation (e.g. Showman et al. 2009, 2013; Parmentier 2014).
Since occultation and emission spectra probe different latitudes and altitudes in the atmospheres of exoplanets, in first approximation they can be treated as independent (but see Line and Parmentier 2016). For this thesis work I decided to focus on transmission spectroscopy, as it probes a wider range of altitudes. Thus, it is the ideal tool to investigate a wide range of phenomena taking place from the lower to the upper atmosphere.

2.1 Remote sensing of exoplanets through transmission spectroscopy

Transmission spectroscopy is the most widely used combined light technique[1]. When the planet transits in front of its host star, the fraction of light that it blocks is proportional to the occulted surface, thus to the ratio of the areas of the planet

---

[1] The sections relative to transit and occultation spectroscopy of NASA exoplanet archive contain data for 88 and 47 planets, respectively.

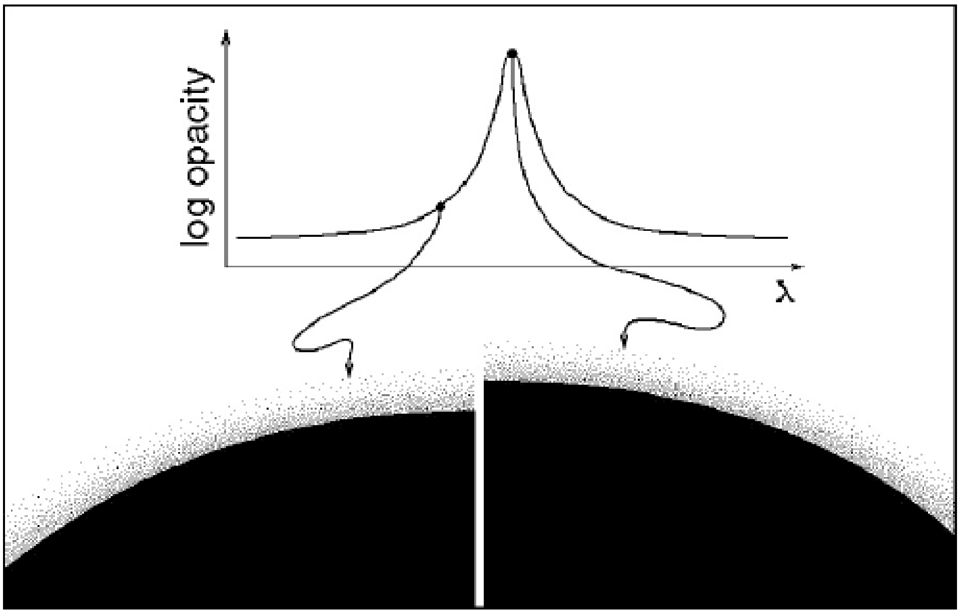

Figure 2.1: Figure from the seminal paper by Brown (2001). Transmission spectroscopy aims to measure the absorption of stellar flux due to the presence of an atmosphere around the planet. This can be done by observing variations with wavelength in the apparent radius of the planet. The technique relies on the comparison of in-transit spectra, taken while the planet is transiting in front of its host star, and out-of-transit spectra. The emission by the planet is usually neglected. This is especially justified in the case of short period planets, which are tidally locked and thus show to the observer the cold night side during the transit.

and the star (transit depth, δ). Transmission spectroscopy is time normalized: the stellar spectrum needs to be "removed" to isolate the planetary signal. This is done by comparing in-transit spectra, taken during the primary eclipse, and out-of-transit spectra. The result is a transit light curve, from which it is possible to record the area covered by the planet. In general, the atmosphere of the planet constitutes a tiny fraction of the total planetary area, however it has the unique feature that it absorbs *chromatically* (see Fig. 2.1). Specifically, features with a strong cross-section (such as the core of absorption lines) are able to absorb light even high up in the atmosphere, where the density is low (at the level of 1–0.1 mbar for molecular lines, up to the thermosphere for the sodium and potassium doublets).
At first approximation, the atmospheric signal in transmission spectroscopy is the area of the annulus occulted by the atmosphere:

$$\delta(\lambda) \sim \frac{2n_\lambda R_\mathrm{p} H}{R_\star^2} \propto n_\lambda T_\mathrm{eq} \rho_\mathrm{p}^{-1} R_\star^{-2}. \tag{2.1}$$

Here, $H = k_\mathrm{B}T/\mu g$ is the pressure scale height, i.e. the e-folding distance for pressure. At each wavelength, depending on the cross-section, the atmosphere is opaque over n_λ scale heights. Using Eq. 2.1, one obtains $\delta(\lambda) \sim n_\lambda \cdot 100$ ppm for the prototypical hot Jupiter HD189733b. In the most favourable cases, the signal from one scale height can reach up to 1000 $\sim$ ppm, while it drops to slightly less than 1 $\sim$ ppm for Earth. In Fig. 2.2 I show a typical transmission spectrum for a hot Jupiter, with the doublets of the alkali atoms and the water bands visible in the

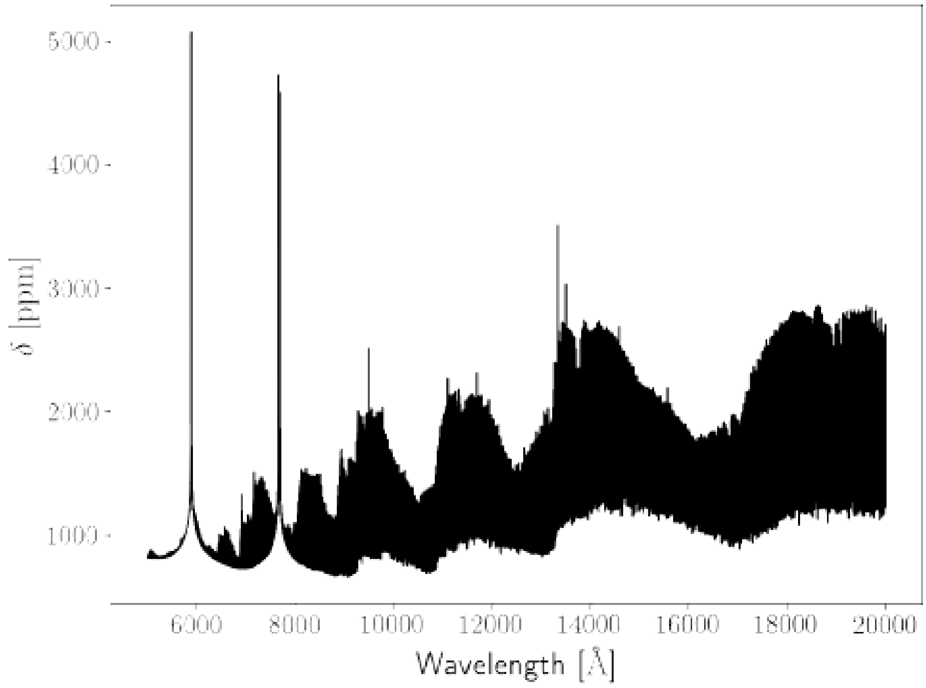

Figure 2.2: Transmission spectrum for a typical hot Jupiter, with $R_\mathrm{p} = 1.108\ R_\mathrm{J}$, $M_\mathrm{p} = 1.138\ M_\mathrm{J}$, $T = 1\,700$ K and solar abundances of sodium, potassium and water. R_p here is defined as the location where pressure equals 10 bar.

spectrum (calculated with $^\pi\eta$, Pino et al. 2017).

These order-of-magnitude estimates hold only for features originated in the region of the atmosphere where the barometric law applies. There are a few noticeable examples of features whose intensity cannot be explained without placing some material beyond the Roche-lobe of the planet, thus in the exosphere. In such cases, absorption amounts to up to 15% to 30% of the total stellar light. Until today, only UV observations accessed these extreme features (e.g. Vidal-Madjar et al. 2003; Ehrenreich et al. 2015).

Transmission spectra can be built using a variety of techniques and instruments. No technique has clearly outperformed the others. I first highlight some key aspects that determine which kind of science each technique can access. Later, I present the main results that were obtained with their combined efforts.

2.1.1 Observable features in exoplanetary atmospheres

Due to its geometry, transmission spectroscopy is sensitive to trace species high up in the atmosphere. Besides atoms and molecules in the gaseous state, that produce their characteristic absorption features, these species include aerosols that scatter light over a broad wavelength range.

Atoms can be studied through their narrow spectral lines (fractions of Angstrom wide). The optical sodium (Na I) and potassium (K I) doublets possess characteristic wings that absorb over hundreds of Angstrom. In the UV, broadening of lines by atoms is set by their movement within the collisionless atmosphere (e.g. Ly–α lines span ~ 1 Å; see section 2.2.2). Molecules have millions (up to billions) of absorption lines clustered in absorption bands. They can be studied by resolving the single lines or, at lower resolution, by resolving the bands that typically span hundreds of Angstroms. Finally, aerosols are particles of different sizes suspended in the atmosphere. They scatter light, producing much smoother optical and NIR features that span thousands of Angstroms.

2.1.2 Some key factors in exoplanet atmosphere observations

The core of my work of these three years consisted in producing models to be compared with observations of different kinds. This process has two steps: (1) Implementing a realistic model of an exoplanetary atmosphere, and (2) simulating observations of that model with the considered observational set-up. To accomplish this second step I focused on three main aspects that affect observations: resolving power, wavelength coverage and the effects of Earth atmosphere for ground-based observations. These factors determine the range of applicability of each technique, and if not taken into account lead to an improper interpretation of data.

Resolving power and resolution In this thesis, I define "resolving power" the Full Width Half Maximum (FWHM) of the Line Spread Function (LSF) of a spectrograph. By "resolution", I name the wavelength step between two consecutive points of the transmission spectrum. The resolving powers of the most commonly used spectrographs range between ~ 100 and $\sim 10^5$, while resolutions range between hundredths of Angstroms in the case of high-resolution transmission spectroscopy to thousands of Angstroms in the case of broadband photometry.

A high resolving power prevents spilled stellar light to smear out absorption features by the planet. There are two main consequences:

1. Since the shape of atmospheric features is better resolved, identification of the sources of the absorption is easier. Their shape is also a probe of the thermophysical conditions in the atmosphere of the exoplanets, which are thus better constrained. At the highest resolutions ($R \sim 10^5$, reached with Echelle spectrographs), molecular and atomic lines are singularly resolved[2], removing ambiguity and allowing for detailed characterization of the thermal structure.

2. Regions higher up in the atmosphere can be explored, as the value of n_λ in Eq. 2.1 is highest in the core of absorption lines. In table 2.1 I report the value of n_λ in the sodium lines and in the water band located around 1.4 μm, called (2ν), for a few typical values of the resolving power. I illustrate the effect for both cases in Fig. 2.3 and Fig. 2.4.

Wavelength coverage There are two main aspects connected with wavelength coverage. The first is that, generally speaking, the atmosphere of the planet appears larger when observed at the most energetic wavelengths. Indeed UV and X–rays are absorbed preferentially by ionized species and by hydrogen, which are found higher up in the atmosphere. Thus, the upper atmosphere can be studied preferentially at short wavelengths, starting from the near-UV ($\lambda < 3\,600$ Å), with the relevant exception of the sodium and potassium doublets. On the other hand, the lower atmosphere appears completely opaque at these wavelengths, and thus cannot be

---

[2] The lines in the alkali doublets are singularly resolved also at lower resolving powers (e.g. Huitson et al. 2012). However, at higher resolving power, their shape can better be reconstructed.

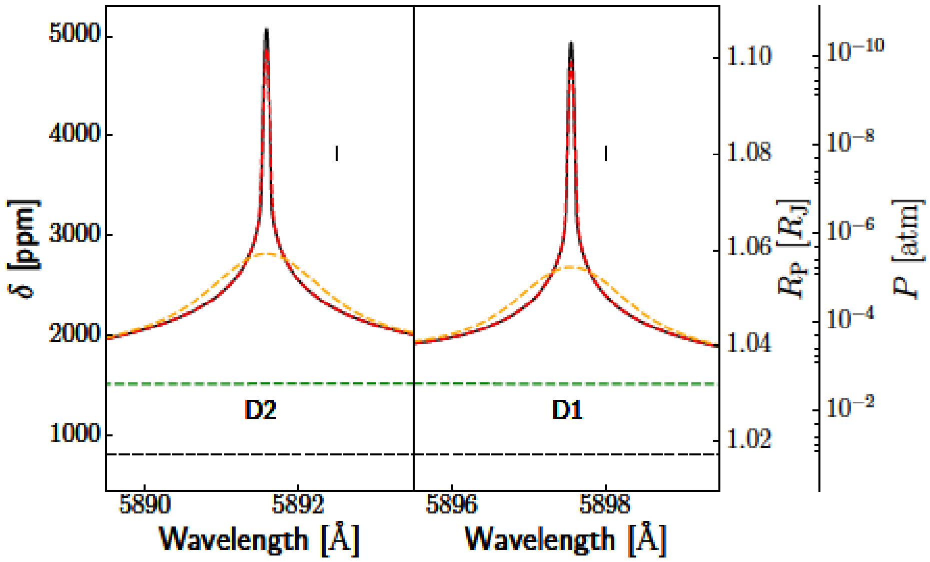

Figure 2.3: The same transmission spectrum as in Fig. 2.2, zoomed in the two lines of the sodium doublet and degraded at various resolving powers. Black solid line: full resolution. Red dashed line: HARPS/-N resolving power ($R \sim 115\,000$). Orange dashed line: STIS G750M resolving power ($R \sim 5\,000$). Green dashed line: ACS HRC G800L resolving power ($R \sim 140$). Black dashed line: level corresponding to the minimum radius, or zero atmospheric absorption. The black vertical dash is the signal corresponding to one scale height. Vertical axes represent the height in the atmosphere in various units, including pressure. Note that at the STIS G750M resolving power sodium probes the basis of the thermosphere, while at HARPS resolving power it reaches well inside the thermosphere.

Table 2.1: Typical values of n_λ when the transmission spectrum is observed with different resolving powers. The water band inspected is the 1.4 μm, observed multiple times with HST WFC3. The contrast of the water feature is computed as the peak to peak contrast in the 12 000–14 500 Å. For sodium, we consider the difference between the value in the peak of the absorption and the minimum in the region around 5 200 Å. $R = \infty$ indicates a model before any convolution is performed.

	$R = \infty$	$R = 115\,000$	$R = 5\,000$	$R = 140$
sodium	29	26	13.5	4.6

	$R = \infty$	$R = 75\,000$	$R = 50\,000$	$R = 130$
water (2ν)	13	11	10	4.4

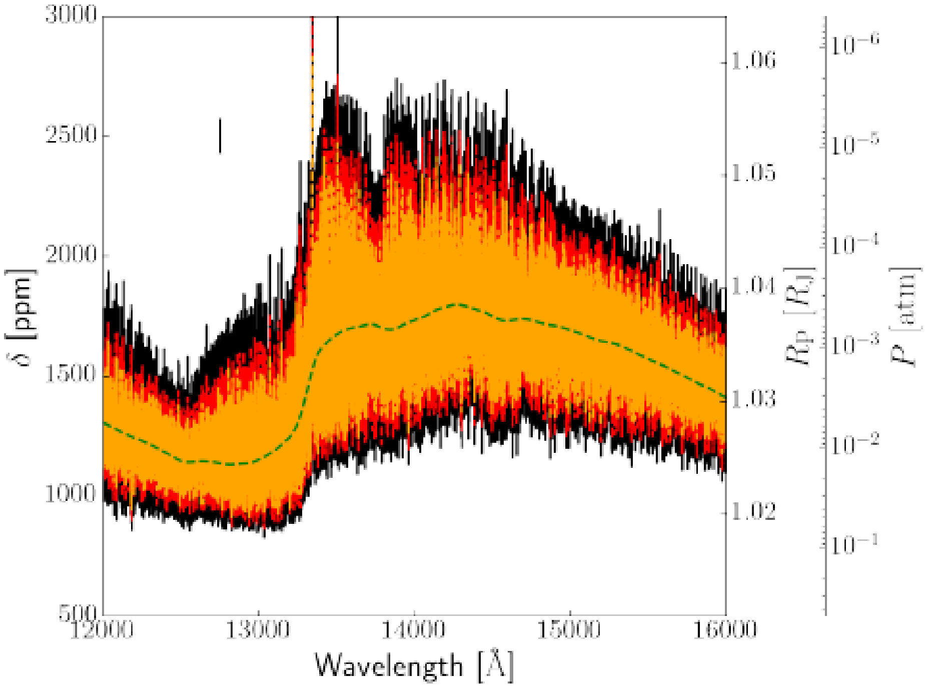

Figure 2.4: Same as 2.3, this time zoomed around the (2ν) water absorption band. Black solid line: full resolution. Red dashed line: CARMENES NIR resolving power ($R \sim 75\,000$). Orange dashed line: GIANO resolving power ($R \sim 50\,000$). Green dashed line: WFC3 resolving power ($R \sim 130$). The black vertical dash is the signal corresponding to one scale height. Vertical axes represent the height in the atmosphere in various units, including pressure. The water feature is intrinsically less intense than the single sodium lines, and it probes only the lower atmosphere.

accessed. Molecular species, found in the lower atmosphere, have a smaller cross-section and are best observed from the optical to the infrared. Thus, a wavelength coverage from the UV to the near-infrared is required to probe different layers in the atmosphere.
The second aspect is that wavelength coverage is fundamental to retrieve the atmospheric chemistry and physical conditions. Intuitively, the broader the wavelength coverage, the more molecular bands are covered, making detection of more species possible (e.g. de Kok et al. 2014). In addition, there is a subtler aspect. Transmission spectroscopy suffers for the presence of degeneracies. Given an observational data set, several different atmospheric models are usually able to explain the observations (see chapter 5 and e.g. Lecavelier Des Etangs et al. 2008a; Fraine et al. 2014). Thus, the atmospheric conditions cannot be uniquely inferred. However, several theoretical (e.g. Benneke and Seager 2013) and observational (e.g. Sing et al. 2016) works have shown how a broad wavelength coverage helps lifting these degeneracies (we will come back to this problem several times).

Effects of Earth atmosphere Observations gathered from the ground need to confront the fact that Earth atmosphere is between the telescope and the target[3]. The impact of the Earth atmosphere on transmission spectroscopy is twofold: (1) the spectral features of the gaseous species that it contains are imprinted on the stellar spectrum, and need to be removed; (2) it is not always possible to precisely trace variations of the continuum level of a star during the transit.

Telluric lines: Earth atmosphere contains a variety of gaseous species, such as H_2O, O_2, O_3, CH_4, CO, N_2O, Na and others (including some artificial compounds such as the CFC). These species imprint their absorption spectrum on top of the observations. The intensity of this spectrum depends on airmass and, at the second order, on meteorological variations (such as humidity).
Transmission spectroscopy requires a long observing baseline in order to acquire both the in-transit spectrum and the out-of-transit spectrum with enough signal-to-noise. Ground-based observations are thus usually performed by following one target for the whole night. During this lapse of time, the star spans a broad range of airmasses, and thus telluric contamination varies with time. Since the assumption underlying transmission spectroscopy is that any time-varying signal (on the timescale of the transit) is due to the planet, telluric lines need to be identified and removed.
For the telluric correction, it is necessary to obtain a reference telluric spectrum close to the one imprinted on the science spectrum. One possibility is to acquire the spectrum of a reference star that is angularly close to the observed star. This correction technique is particularly suitable when applied to multi-object spectrograph observations (Bean et al. 2010, 2011) or broadband photometry (Nascimbeni et al. 2013, 2015), as observations of the target and the reference stars are simultaneous. Echelle spectrographs can also benefit from this technique (Redfield et al. 2008; Jensen et al. 2011), but the time series needs to be interrupted, losing valuable signal-to-noise either in the in-transit or in the out-of-transit spectrum (Snellen et al. 2011).
These limitations prompted high-resolution observers to find alternative techniques to correct for telluric contamination. For example, an empirical telluric spectrum can

---

[3] Luckily, according to the author of the manuscript; maybe less so according to his colleagues on the observational side.

be obtained from the science observations themselves, by fitting the first order linear dependence of telluric absorption on airmass (Snellen et al. 2008, 2010; Astudillo-Defru and Rojo 2013; Wyttenbach et al. 2015, 2017). Other empirical methods rely on algorithms capable of finding common temporal modes among different wavelength channels in the detector (such as the Principal Component Analysis, PCA, e.g. Birkby et al. 2017). A further possibility is to use radiative models of the Earth's atmosphere (e.g. `MolecFit`, Smette et al. 2015; Kausch et al. 2015, applied by Allart et al. 2017 to transmission spectroscopy).

None of the aforementioned methods is clearly superior to the others. Their applicability varies on a target-to-target, and even night-by-night basis. However, it is still impossible to correct telluric lines within the strongest absorption bands. Indeed, if the density of telluric lines is too high, or if they become saturated, all the discussed correction methods fail. For this reason, ground-based observations can usually access a limited wavelength range compared to space-borne ones. These observational windows generally coincide with Earth transparency windows. Unfortunately, in some cases these regions overlap with the exoplanets transparency regions themselves, where the expected signal is lowest (e.g. water; chapter 4), and thus limit the science accessible with ground-based telescopes (see previous paragraph).

Photometry: If no reference star is available, or if the technique adopted does not allow to observe one simultaneously to the target star (e.g. Echelle spectroscopy), it is not possible to retrieve the absolute level of the continuum of the spectra. Then, a normalization in wavelength is required to combine all the spectra acquired during the night. This can be done by choosing a band where no planetary features are expected (e.g. Wyttenbach et al. 2015) or by using a polynomial interpolation (e.g. Snellen et al. 2010; Allart et al. 2017).

Unfortunately, this process removes large scale variations in the transmission spectrum over hundreds of Angstroms. Thus, broad features of the planetary continuum such as those due to aerosols cannot be studied with this widely used method. Measuring scattering by aerosols from the ground is still possible, but requires different techniques (such as spectrophotometry, or the chromatic Rossiter-McLaughlin effect method proposed by Snellen 2004; Di Gloria et al. 2015). Furthermore, since the absolute reference photometry of the star is missing, only variations in the planetary radius are measurable, but not its absolute value.

2.2 Main results from transmission spectroscopy of hot Jupiters

The key observational aspects discussed in section 2.1.2 determine which features can be studied, and where they lie in the atmosphere. We can define three "science domains": molecular and atomic spectral features in the lower and upper atmosphere, and continuum in the lower atmosphere (e.g. aerosols, Collisional Induced Absorption by H_2). A given combination of resolving power/resolution, wavelength coverage and photometry can only access some of these domains. Table 2.5 summarizes how current data reduction and analysis techniques are able to exploit the possible combinations of these three factors. A vast effort combining several observational set-ups is required to fully sound the atmosphere of an exoplanet.

Notwithstanding this challenge, in the last decade all of the domains were explored (separately) with dedicated observations. In the following I review current results on

Figure 2.5: This table summarizes how different instrumental set-ups have been exploited to study different features in different parts of the atmospheres of exoplanets. I emphasize that new techniques may extend the range of applicability of a given instrumental set-up beyond its current employment (Actually, already starting from this thesis. See chapter 4). By "low-resolution" I mean that the resolving power is $R \sim 10^2$, by "medium-resolution" $R \sim 10^3$ and by "high-resolution" $R \sim 10^4$–10^5. Note that no features of the continuum are present in the upper part of the atmosphere.

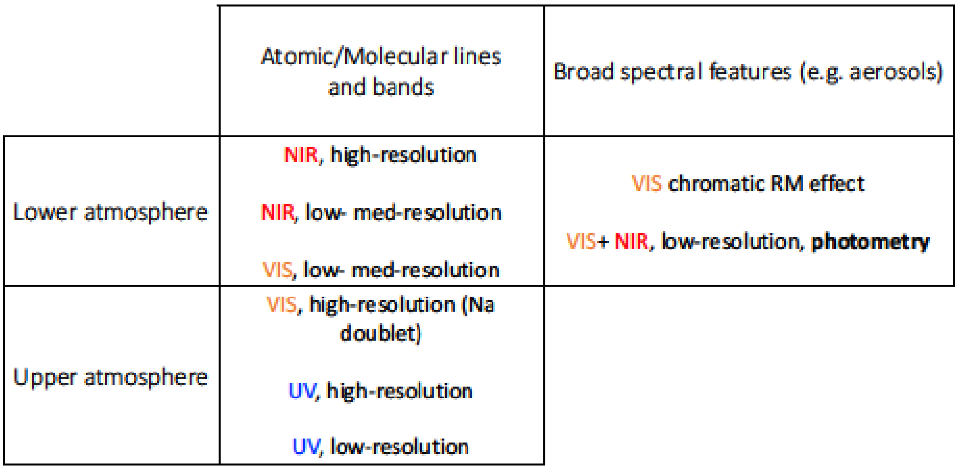

	Atomic/Molecular lines and bands	Broad spectral features (e.g. aerosols)
Lower atmosphere	NIR, high-resolution NIR, low- med-resolution VIS, low- med-resolution	VIS chromatic RM effect VIS+ NIR, low-resolution, **photometry**
Upper atmosphere	VIS, high-resolution (Na doublet) UV, high-resolution UV, low-resolution	

hot Jupiter atmospheres through transmission spectroscopy. Without claiming to be exhaustive, I will mainly focus on a few aspects that are further explored within this thesis.

2.2.1 Lower atmosphere

The most abundant species in the atmosphere of gaseous giants is expected to be molecular hydrogen (H_2; Fortney et al. 2007; Seager et al. 2007). While evident from their low bulk densities, H_2 in hot giant planets can in principle be detected through its Rayleigh scattering signature in the optical and through its Collisional-Induced Absorption (CIA) in the NIR. Indeed, an optical slope was detected in multiple targets, and can be explained with Rayleigh scattering (Lecavelier Des Etangs et al. 2008a; Pont et al. 2013; stellar activity can also produce a similar slope in the transmission spectrum, Oshagh et al. 2014; McCullough et al. 2014). A growing body of ground-based, low- to medium resolution ($R \sim 10^2$–10^3), spectrophotometric observations successfully measured or constrained the Rayleigh feature in several hot Jupiters (e.g. Stevenson et al. 2014; Angerhausen et al. 2015; Mallonn and Strassmeier 2016; Mallonn et al. 2016; Gibson et al. 2017; Lendl et al. 2017). Multicolor photometry can also be used (e.g. Nascimbeni et al. 2013, 2015; Dragomir et al. 2015; Chen et al. 2017; Mallonn and Wakeford 2017). However, as shown e.g. by Kirk et al. (2016), stellar activity is a particularly severe source of systematic error in this kind of measurements. Furthermore, a few results from this technique are controversial, indicating it still needs refinement. For example, Southworth et al. 2015 and Southworth and Evans 2016 detect a surprisingly large Rayleigh slope in

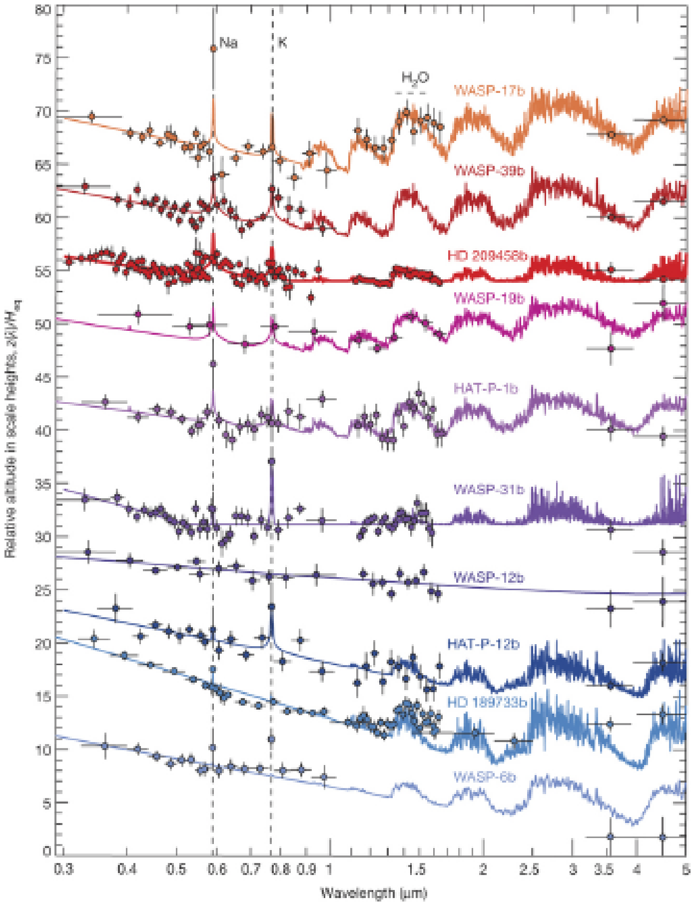

Figure 2.6: Figure from Sing et al. (2016). A combined analysis of HST and Spitzer spectra covering from the optical to the near infrared showed the predominance of aerosol-rich atmospheres in hot Jupiters. Aerosols of small size produce the slope in the spectrum visible in the optical (Rayleigh scattering), while aerosols of larger size produce acromatic scattering that mutes molecular features in the infrared.

WASP-103b, at strain with spectrophotometric measurements by Lendl et al. 2017; a similarly large slope was observed in TrES-3b by Parviainen et al. 2016 and is not reproducible by any model. Indeed, it was space-borne optical low-resolution observations that put the spotlight on this feature (Pont et al. 2008; Sing et al. 2008, 2011; Pont et al. 2013; Sing et al. 2015; Fischer et al. 2016; Sing et al. 2016), inspiring pioneering work on the interpretation of the slope. In particular, Lecavelier Des Etangs et al. (2008a,b) showed that: (1) from the steepness of the slope it is possible to measure the atmospheric temperature (assuming, among other things, that the scattering is pure Rayleigh from a single species); (2) the absolute reference pressure can also be measured in the assumption that the scattering is due to molecular hydrogen (see chapter 5).

In some cases, the optical slope is too steep to be interpreted as only due to hydrogen, and extra scattering from a population of small particle aerosols has been advocated (Pont et al. 2013; Sing et al. 2016). This is, for example, the case of HD189733b or HD209458b, where the wings of the sodium and potassium doublets are suppressed (Huitson et al. 2012; Charbonneau et al. 2002) and the water feature

also appears muted (McCullough et al. 2014; Deming et al. 2013). In some other cases, such as WASP-39b, a strong aerosol component is excluded because the whole wings of the alkali doublets are visible in the spectrum (Fischer et al. 2016). However, it was only by combining space-borne, low-resolution, optical observations of the spectral slope with space-borne, low-resolution, near infrared observations of the water feature that Pont et al. (2013) and Sing et al. (2016) demonstrated that the vast majority of hot Jupiters contain a population of small (< 1 μm) and/or large ($\gtrsim 2$ μm) aerosols (see also Fig. 2.6; Barstow et al. 2017).
Indeed, previous interpretations attributed the muting preferentially to sub-solar abundance of atmospheric constituents (Madhusudhan et al. 2014a). This debate brings us to the large sample of NIR observations of molecular bands in hot Jupiters. This kind of observations are of prime importance, as the C/O ratio of the envelope of hot Jupiters may carry the imprint of their formation history (Madhusudhan et al. 2014a; Madhusudhan et al. 2016; Madhusudhan et al. 2017). In particular, it depends on the location in the protoplanetary disk where the planet formed, on the formation mechanism, on the type of migration it underwent (if it did) and on other secondary processes (such as photoevaporation and core erosion).
Early inferences were based on broad band *Spitzer* photometry from space. H_2O was reported by Barman (2007), and Tinetti et al. (2007) and Beaulieu et al. (2008) in the two prototypical gas giants HD209458b and HD189733b. However, identification based on such broad bands is difficult and controversial, and successive analyses cast serious doubts on these detections, which sometimes did not account fully for systematic effects (Ehrenreich et al. 2007; Désert et al. 2009).
Progress has been made with multi-wavelength observations, that constrain the shape of the absorbent bands, and can be interpreted in the frame of an inverse modelling or retrieval scheme (Madhusudhan and Seager 2009; Madhusudhan et al. 2014b). HST WFC3 ($R = 140$, 1.1 μm–1.7 μm) is the instrument with the biggest record of homogeneous transmission spectra collected ($\sim$ 30 targets; see Tsiaras et al. 2017 for a recent overview of this data set). Analysis of this sample led to a detection of water in approximately half of the targets. Furthermore, these observations excluded methane dominated carbon-chemistry in most of the observed planets (confirming expectations based on their high temperature). Even a flat transmission spectrum can be precise enough to place constrains on abundance of water and cloud coverage (e.g. Kreidberg et al. 2014). Thus, several authors attempted retrieval including (and sometimes based solely) on this data (see Madhusudhan et al. 2014a; Benneke 2015; Sing et al. 2016; Barstow et al. 2017; Tsiaras et al. 2017 chapter 5). The emergent picture is still incomplete, but a few points are in common among the different analyses:

- Layers of aerosols of different sizes (from sub-micron to $\gtrsim 2\,\mu$m) are present in the atmosphere of more than half of the studied hot Jupiters. Trends with atmospheric parameters are still debated: at lower temperatures condensates are easier to form, which should show up as a correlation between equilibrium temperature and aerosol coverage. However, evidence for such a correlation is debated, and a complex interplay with facilitated sedimentation in cooler planets may be taking place (Stevenson 2016; Barstow et al. 2017).

- Water is the most abundant oxygen bearing species in the sampled population of exoplanets. Its retrieved abundance correlates with cloud coverage and is degenerated with the absolute reference pressure (see chapter 5), which causes order of magnitude uncertainties. Models (Benneke and Seager 2012; Benneke 2015) indicated that a larger wavelength coverage such as that provided by JWST could help breaking this degeneracy. A recent detection of both water bands in the WFC3 passband for HAT-P-26b (Wakeford et al. 2017b), that led to a precise determination of its metallicity ($4.8^{+21.5}_{-4.0}$ times the solar value, using water abundance as a proxy for all heavy elements), seems to confirm the simulations.

- The strong water features detected require enough oxygen to be formed. As a result, there is increasing consensus that hot Jupiters show a carbon-to-oxygen ratio (C/O) smaller than 1, indicating oxygen-dominated chemistry (Benneke 2015). However, the value of C/O remains largely unconstrained because of the difficulty of detecting at low resolution one of the major carbon-carriers at the temperatures of hot Jupiters, CO.

High-resolution, ground-based transmission spectra offer the opportunity to complement current space-borne observations. Indeed, Snellen et al. (2010) and Brogi et al. (2016) report a high-confidence detection of CO in the transmission spectra of two hot Jupiters with CRIRES ($R \sim 100\,000$, 2.287 μm–2.345 μm) at VLT (see Fig. 2.8). Their success can be attributed to the ability of high-resolution spectroscopy to resolve molecular lines, which leaves no ambiguity in the identification of the species responsible for the absorption, and better correction of telluric contamination.

At such high resolution, retrieval alogrithms are challenging to apply (see chapter 5). Nevertheless, Brogi et al. (2017) demonstrated that such an analysis is possible and leads to enhanced diagnostic power, with more precise abundances for atmospheric constituents (in some cases by orders of magnitude, e.g. H_2O and CO)[4]. They also report a precise determination of $C/O = 0.97^{+0.01}_{-0.03}$ (but the implementation of a full retrieval method is warranted to have more reliable error bars). At such precision, comparative planetology between Solar System giants and exoplanets is possible (see Fig. 2.7). Finally, resolving the individual molecular lines allows to probe dynamics of the atmosphere through their wavelength shift and their broadening, which constrain winds and rotation of the atmospheres respectively (Snellen et al. 2010; Brogi et al. 2016).

A further step will be done with JWST. Its broad spectral coverage (0.6 μm–28.3 μm), combined with resolving powers of $\sim 10^3$ from space, will remove much of the ambiguity that currently affects interpretation of low-resolution transmission spectra (e.g. Barstow et al. 2015). Its extended infrared spectral coverage (up to ~ 30 μm) covers a region of the transmission spectrum where most of the condensates are transparent. The mid-infrared MIRI instrument, in particular, will be able to access absorption features due to condensates, and thus identify them (silicates; Mollière et al. 2015, 2017).

Still, complementary optical and NIR space-borne and ground-based transmission spectra will play a key role to constrain global circulation, chemical composition and temperature profiles in hot Jupiters (and smaller planets). This is apparent from the recent result by Sedaghati et al. (2017), who report a FORS2 TiO detection in the $T_{\rm eq} > 2\,000$ K hot Jupiter WASP-19b, and can probably be regarded as the biggest success of ground-based spectrophotometry to date (see Fig. 2.9). This long-sought molecule (Désert et al. 2008; Hoeijmakers et al. 2015) is a strong optical absorber. As such, it absorbs the optical stellar light, which is then re-irradiated

---

[4] This result was obtained in emission, but a similar framework could be applied in transmission.

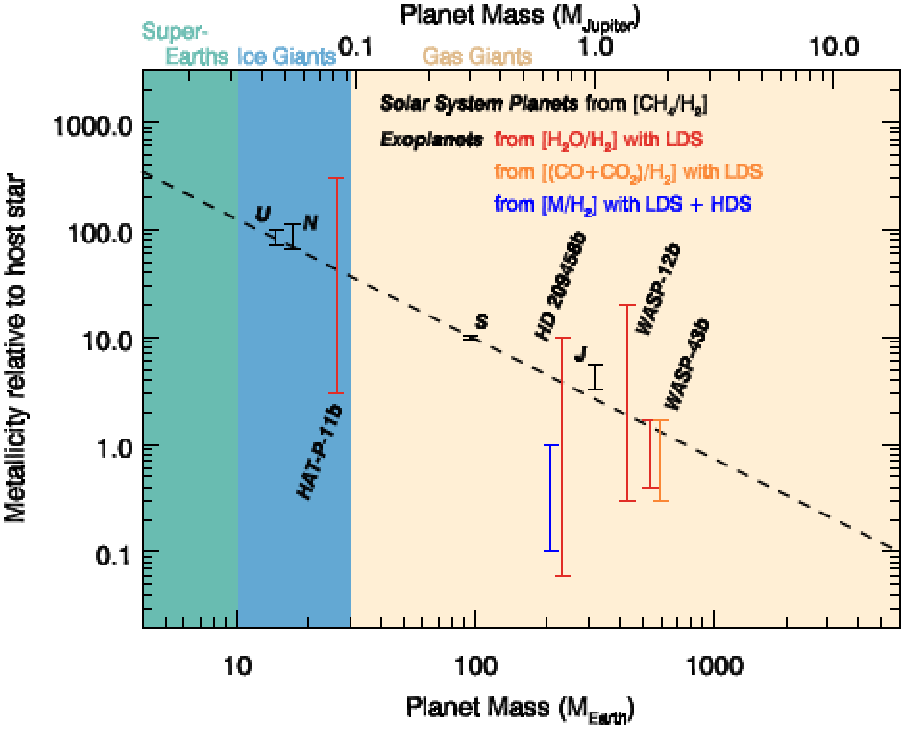

Figure 2.7: From Brogi et al. (2017). Metallicity-mass relation for Solar System planets and exoplanets. Metallicity is a proxy for composition, as detected molecules are different between Solar System objects and exoplanets (calculated as specified in the legend). The determination with low- and high-resolution observations of HD209458b (blue error bar) is ∼ 2 times more precise than from low-resolution only (adjacent red error bar).

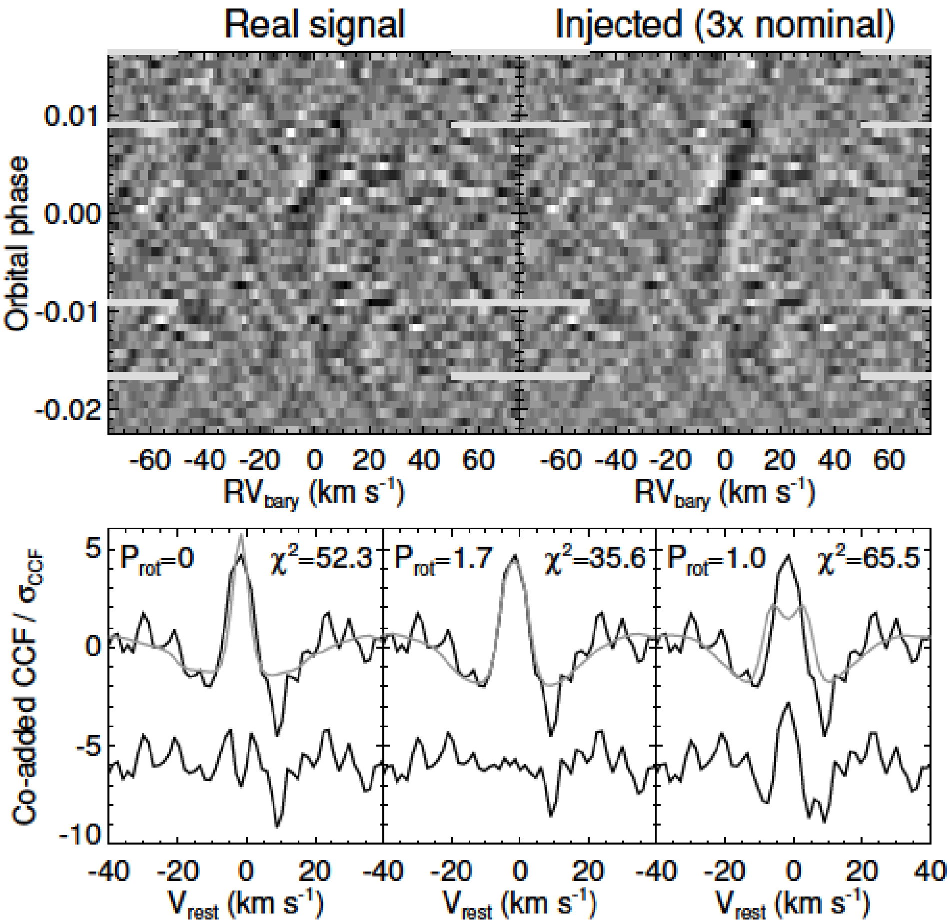

Figure 2.8: Figure from Brogi et al. (2016). The *top panel* shows the signal that is obtained by cross-correlating a high-resolution template for the atmosphere of HD189733b with data. The dark trace in the left panel corresponds to a peak in the cross-correlation, indicating a good match between model and data, that drifts in radial velocity during the phase of the orbit. This drift is due to the orbital motion of the planet around the star (simulated in the right panel). The *bottom panel* shows the peak in the cross-correlation function (black line), and best fits obtained for various rotational velocities of the planet (gray line). The authors conclude that they detect water and carbon monoxide in the atmosphere of the planet at 7.6 σ.

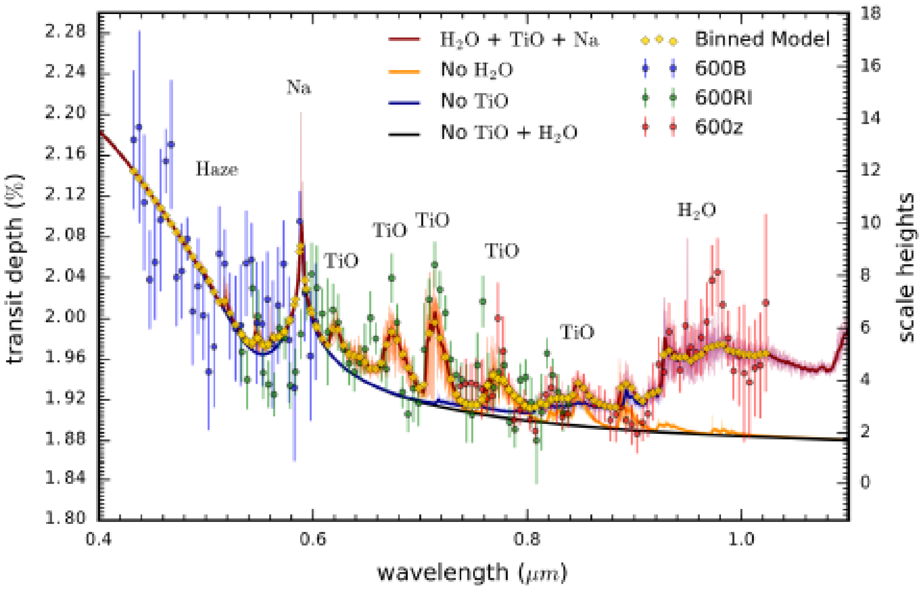

Figure 2.9: Figure from Sedaghati et al. (2017). The authors used three transits observed with three different grisms of the FORS2 spectrograph to study the atmosphere of WASP-17b at $R \sim 3\,000$. They identified an optical slope (likely due to aerosols of small size), molecular absorption by TiO and H_2O and, marginally, the sodium doublet.

in the infrared. If the optical-to-infrared opacity ratio is high, cooling is slow and the atmosphere heats up. The result is that such an absorber produces a temperature inversion in the dayside of the exoplanet (observed by e.g. Evans et al. 2017, predicted by Hubeny et al. 2003; Fortney et al. 2008). While TiO is expected in hot planets ($T_{\rm eq} > 2\,000$ K), condensation and successive sedimentation of aerosols such as CaTiO may remove it from the atmosphere ("cold-trap", Spiegel et al. 2009; Showman et al. 2009).

The near future of ground-based, high-resolution spectroscopy is bright. New high-resolution, stabilized spectrographs covering from the optical to the near infrared (GIARPS, CARMENES, ESPRESSO, ...) will increase the precision of CCF techniques thanks to increased collecting area and/or spectral coverage. Among the other results, they will lead to a final and unambiguous detection (or disproval) of TiO on several hot Jupiters, shedding light on a part of the complex interplay between their day- and night-sides. Indeed, (Allart et al. 2017) have demonstrated the exquisite precision that can be reached with these facilities (~ 20 ppm on the CCF, see chapter 4; see also Esteves et al. 2017). However, successful detections require accurate models as well. Indeed, Hoeijmakers et al. (2015) demonstrated that the TiO line list by Freedman et al. (2008), based on Schwenke (1998), was inadequate for searches at high resolution. Brogi et al. 2017 discussed the impact of the choice of the line list when computing the CCF. The advent of new line lists including billions of lines (e.g. ExoMol by Tennyson and Yurchenko 2012; see Lavie et al. 2017 for a discussion on the increased accuracy on methane) constitutes a formidable challenge for the computation of models (see chapter 5) but will likely enable us to reach the required accuracy.

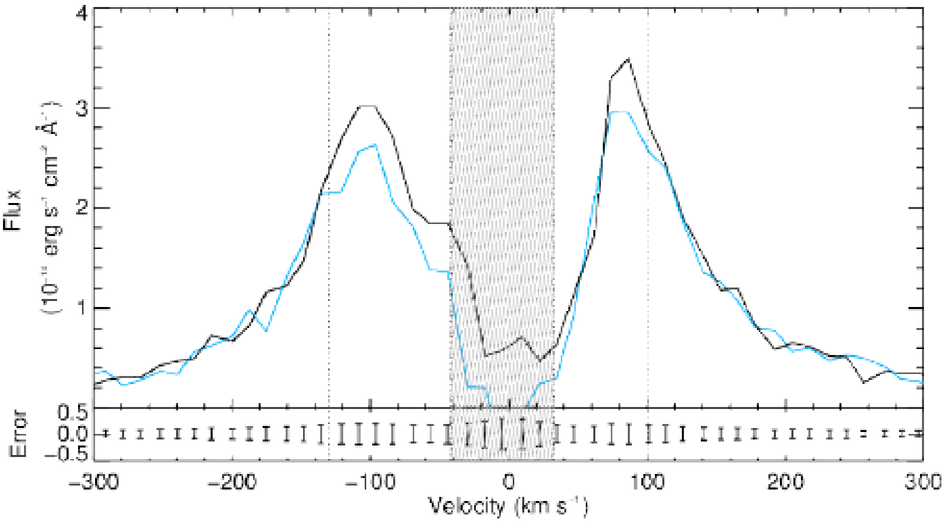

Figure 2.10: Figure from Bourrier et al. (2013a), data set from Vidal-Madjar et al. (2003). The figure shows the Lyman–α before (black line) and during (blue line) the transit of HD209458b. The absorption by the planet is large enough that it is visible by eye between the vertical dotted lines both in the blue and the red wing of the stellar Lyman–α line.

2.2.2 Upper atmosphere

The irradiated, upper atmosphere ($P < 0.1$ mbar) of an exoplanet was first detected by Vidal-Madjar et al. (2003) in HD209458b, with STIS G140M observations in the Far-UV (FUV; Fig. 2.10). The 15% absorption exceeds by far its optical counterpart in the sodium ($\sim 0.01\%$ in a similar wavelength bandpass of ~ 1 Å), and is *a priori* unexpected for a planet occulting 1.5% of its host star light. This measurement placed absorption well beyond the Roche lobe, indicating that the upper atmosphere of the planet is evaporating. Even if this interpretation was challenged by Ben-Jaffel (2007, 2008), multiple independent analyses on independent data sets confirmed the existence of a cloud of neutral hydrogen surrounding the planet (Vidal-Madjar et al. 2004; Ehrenreich et al. 2008; Ben-Jaffel and Sona Hosseini 2010). This “blow-off” scenario is further strengthened by detections of heavy elements at high altitudes such as O I, C II, Si III (Vidal-Madjar et al. 2004; Ben-Jaffel and Sona Hosseini 2010; Linsky et al. 2010), that are dragged upwards from the lower thermosphere by the evaporating hydrogen. Bourrier et al. (2013a) showed that the high velocities of escaping gas are supported by the stellar wind, which likely shapes them in a cometary tail behind the planet. Perhaps, HD189733b is an even more interesting case, with escaping hydrogen detected with unresolved Lyman–α HST/ACS observations (Lecavelier Des Etangs et al. 2010) and later with HST/STIS observations (Lecavelier des Etangs et al. 2012; Bourrier et al. 2013b. Si III and N V are also detected). Indeed, the escape of the planet is subject to significant temporal variation, and the high velocities in the gas (up to 300 km s^{-1} compared to 180 km s^{-1} for HD209458b) likely need an additional charge exchange mechanism with the protons in the stellar wind (Bourrier et al. 2013a).

Similar studies can be performed in the near-UV (NUV; 1 700–3 600 Å). Fossati et al. (2010) observed an HST COS transit of the hot Jupiter WASP-12b (obtaining spectra in three non-contiguous NUV wavelength ranges: 2539 Å–2580 Å, 2655 Å–2696 Å, 2770 Å–2811 Å), finding that the planet has an extended exosphere similar to HD189733b and HD209458b. In this wavelength range, Vidal-Madjar et al. (2013) detected escaping neutral magnesium in the upper thermosphere of HD209458b, at a distance of several planetary radii (between $2\,R_{\rm p}$, close to the exobase of the planet, and $7.5\,R_{\rm p}$) from the surface. This is the transition region between the thermosphere and the exosphere of the planet. The absence of ionized magnesium needs an efficient recombination mechanism, which takes indeed place at high temperatures ($>$ 6 000 K) if the electronic density is high enough (10^8–10^9 cm^{-3}). Interestingly, this is in agreement with models by Koskinen et al. (2013a), produced before the observations were published.

The optical doublets of neutral sodium and neutral potassium probe the lower part of the thermosphere, where the photons that are source for the expansion of the upper atmosphere, that higher up leads to escape, are deposited (Yelle 2004; Vidal-Madjar et al. 2011a; Koskinen et al. 2013a). Indeed, HST STIS G750M observations of the sodium doublet in HD209458b and HD189733b are consistent with a temperature inversion at the 0.1 mbar–0.01 mbar (Sing et al. 2008, complemented by Vidal-Madjar et al. 2011a adding data points by Snellen et al. 2008; Huitson et al. 2012), caused by heating from the stellar light (see chapter 5).

When seen at higher resolution (e.g. with HARPS, $R \sim 115\,000$; Fig. 2.11), the sodium doublet allows to probes pressures as low as 10^{-10} bar in the atmosphere (see Fig. 2.3), and can be used to probe high-altitude atmospheric winds through its Doppler shift. Wyttenbach et al. (2015) used this kind of observations to confirm the thermospheric origin of sodium in HD189733b, building the temperature-pressure profile up to 1.2 $R_{\rm P}$. In my work, Pino et al. (2017), I demonstrated that, when properly accounting for the presence of aerosols in the lower atmosphere, the data by Wyttenbach et al. (2015) is consistent with thermospheric temperatures of up to 10 000 K at 10^{-10} bar (see chapter 3), in qualitative agreement with models (Koskinen et al. 2013a) and observations of neutral magnesium (Vidal-Madjar et al. 2013; see chapter 3).

Several groups successfully detected the sodium doublet at high-resolution in the atmosphere of four hot Jupiters (HD189733b: e.g. Redfield et al. 2008; Jensen et al. 2011; Wyttenbach et al. 2015; HD209458b: Snellen et al. 2008; Langland-Shula et al. 2009; Jensen et al. 2011; WASP-17b: Wood et al. 2011; Zhou and Bayliss 2012; WASP-49b: Wyttenbach et al. 2017)[5]. Still, observations are challenging. The pioneering works by Snellen et al. (2008), Redfield et al. (2008), Jensen et al. (2011) and Wyttenbach et al. (2015) explored various techniques (e.g. telluric correction with a telluric standard, or directly on the science spectra with an empirical approach; stabilized vs. not stabilized spectrograph), and obtained the first successful detections. In particular, different groups studied the effect of systematics in the HARPS data set explored by Wyttenbach et al. (2015) (confirming the detection, albeit with differences). A non-comprehensive list follows:

- Louden and Wheatley (2015) explored the impact of the RM effect on the transmission spectrum, showing that it influences the retrieval of atmospheric winds;

---

[5] There are also detections of other elements, such as the Balmer H_α line (Cauley et al. 2016) or calcium and possibly scandium (Astudillo-Defru and Rojo 2013), but we do not discuss them here

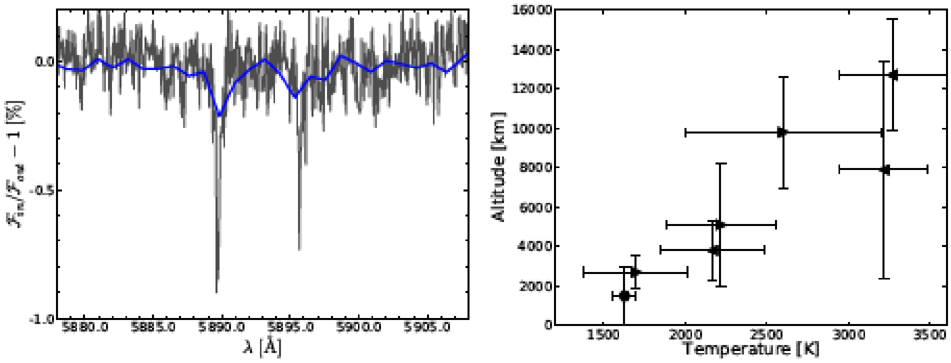

Figure 2.11: Figures from Wyttenbach et al. (2015). The *left panel* shows a comparison between the sodium doublet observations with HST G750M (blue line, $R \sim 5\,000$; Huitson et al. 2012) and HARPS (black line, $R \sim 115\,000$). The increased resolving power allows to probe the core of the lines, and to reconstruct the temperature profile up to $\sim 16\,000$ km sec^{-1} $= 1.2\ R_{\mathrm{P}}$ (*right panel*). The temperature increases with height, indicating that the sodium feature is originated in the thermosphere of the exoplanet atmosphere.

- Barnes et al. (2016) explored the impact of stellar activity, showing that a chromospheric component of the sodium lines can contaminate the signal;
- Yan et al. (2017) explored the effect of Center-to-Limb Variation (CLV) in the stellar spectra, which could introduce a time-dependent signal in the transmission spectrum mimicking the planetary signal.

These effects are sometimes hard to account for (especially in dim targets), and may cast doubts on the feasibility of this kind of observations. However, it can be hoped that the growing interest of the community in optical, high-resolution, ground-based transmission spectroscopy will lead to a solid method to disentangle stellar effects from the planet. Indeed, the first steps have already been taken. Khalafinejad et al. (2017) confirmed the detection of sodium in HD189733b with an independentent VLT UVES data set, accounting for stellar differential limb-darkening and for stellar activity (Czesla et al. 2015; the star flared close to mid-transit) Wyttenbach et al. (2017) detected the thermosphere of the inflated warm Saturn WASP-49b. Compared to Wyttenbach et al. (2015), the analysis is improved by applying the "Reloaded Rossiter-McLaughlin effect" (Cegla et al. 2016), which allows to measure the local CCF of the stellar surface occulted by the planet. The local CCFs can be used to construct a "transmission CCF", that would significantly deviate from a flat line if the RM effect was large enough (which is not the case in WASP-49b). The detection is also strengthened by a control experiment that led to a null detection of the sodium doublet of WASP-8b (see also Bourrier et al. 2017). The low scale height of WASP-8b suggests that the sodium signature should not be visible in the data; any recovered signal could thus be attributed to its host star, which is very similar to WASP-49 (they are both G6V stars) but more active. Since no sodium is visible in the spectrum of WASP-8b, the origin of the sodium excess in the WASP-49 system is likely planetary.

2.3 This thesis: towards a global view of exoplanet atmospheres

Summarizing, by probing both the lower atmosphere and the upper atmosphere of a planet, transmission spectroscopy gives the unique opportunity to constrain the chemical composition and the physical processes that take place in its atmosphere, such as photoevaporation. These are key ingredients to constrain theories of planet formation and evolution.

However, scattering by aerosols blurs our insights from these observations by muting spectral features by molecules and atoms. Observations in the last decade have shown that (1) high-resolution observations are able to probe features above the aerosol deck (e.g. Knutson et al. 2014; Wyttenbach et al. 2015), thus mostly unaffected by them, and (2) broad spectral coverage allows us to characterize the distribution of the sizes of the particles that produce scattering (e.g. Sing et al. 2016; Mollière et al. 2017).

Forthcoming optical-to-near infrared, ground-based high-resolution spectrographs (HARPS-N + GIANO, HARPS + NIRPS, CARMENES, ESPRESSO, CRIRES+, SPIRou, ...), and JWST with its infrared coverage up to $\sim 30\ \mu$m, will thus provide the necessary means to address the issue of aerosols. However, it is challenging to combine transmission spectra from these facilities in a unique framework, as they come from very different instruments (see chapter 2).

For a few benchmark cases, observations are already available over a broad spectral range, both from ground and space, at different resolving powers. A wealth of information is thus available both for the lower and the upper atmosphere of these planets, but was never combined. The main goal of my PhD was to assess the possibility to combine this information, and thus link the lower and the upper atmosphere. Thus:

1. I developed a line-by-line, 1D radiative transfer code (${}^{\pi}\eta$; Pino et al. 2017) able to simultaneously model the lower and upper atmosphere of a hot Jupiter (up to the core of the sodium lines). The code produces a high-resolution template that can be used to predict how the spectrum would appear if observed with different instruments. I simulated a wide set of cases, ranging from space-borne HST observations to high-resolution, ground-based observations. Therefore, I was able to predict observability of several atmospheric features. In particular, with specific simulations, I demonstrated that high-resolution, ground-based observations of water from the optical to the near infrared can be used to characterize aerosols in the atmosphere of a typical hot Jupiter (Pino et al., in prep; chapter 4). This approach is an original one, and extends the range of applicability of this kind of observations (compare with table 2.5).

2. ${}^{\pi}\eta$ was validated by comparing simulations of observations to real data sets. The cases I considered during my thesis range from optical, high-resolution spectroscopy in search of water in HD189733b (Allart et al. 2017), to simulations of the sodium doublet in WASP-49b as seen through the HARPS spectrograph (Wyttenbach et al. 2017). In Pino et al. (2017), I combined low- and high-resolution spectroscopy of the benchmark hot Jupiter HD189733b. The result is a model that for the first time simultaneously reproduces observations over tens of scale heights, from the lower to the upper atmosphere (Pino et al. 2017; chapter 3).

3. These applications showed that the model is able to reproduce real data sets. As a result, I am now involved in several projects were I am in charge of producing grids of models, with the aim of retrieving the chemical and physical conditions in the atmospheres of several exoplanets (see chapter 3). These include optical to near infrared, ground-based, high-resolution observations (e.g. the surveys HEARTS and SPADES, PI: D. Ehrenreich; see chapter 3), but also lower resolution space-borne HST STIS G750M observations that I obtained to study a possible hint of exospheric sodium in the hot Jupiter WASP-43b (see chapter 3).

Chapter 3

Towards a global interpretation of atmospheric structure

In this chapter I present ${}^{\pi}\eta$ (a Python code for Extra-solar Transiting Atmospheres), a code that I developed during this thesis. ${}^{\pi}\eta$ is an extension of ETA, previously developed by D. Ehrenreich and presented in Ehrenreich et al. (2006, 2012), and aims at simulating transmission spectra of atmospheres at high-resolution ($R \sim 10^6$), over a broad wavelength range (currently 0.3 μm–2 μm) and across the lower and upper atmosphere (10 bar $< P < 10^{-12}$ bar).

${}^{\pi}\eta$ is designed to simulate observations with different instruments and techniques (see also chapter 2). Here, I present its application to optical, high-resolution ($R \sim 10^5$), ground-based transmission spectra and optical to NIR, low- to medium-resolution ($R \sim 10^2$–10^3), space-borne transmission spectra. These applications demonstrate the capability of ${}^{\pi}\eta$ to reproduce data sets of different kinds, and validate the code. First, I present a novel interpretation of a combined data set of low- to high-resolution transmission spectra of the well studied hot Jupiter HD189733b, published in Pino et al. (2017). The atmosphere of this planet has been observed from the ultraviolet to the infrared, from space and from the ground, thus constituting one of the most complete data sets to date. In Pino et al. (2017), we combined for the first time optical, ground-based, high-resolution transmission spectroscopy and optical to NIR low-resolution, space-borne transmission spectroscopy of this planet. The resulting model is consistent with observations over tens of scale heights, from the lower to the upper atmosphere.

I focused the low- to medium-resolution analysis on four HST data sets covering the optical and infrared bands between 3 000 Å and 17 000 Å (STIS G430L, Sing et al. 2011; STIS G750M, Huitson et al. 2012; ACS HRC G800L, Pont et al. 2008; WFC3, McCullough et al. 2014). These data sets have been combined in Sing et al. (2016), with an analysis aimed at reducing the impact of stellar activity (that can offset observations taken at different times, see also Pont et al. 2013). Furthermore, the analyses performed by Sing et al. (2016) and Barstow et al. (2017), both indicating a prevalence of aerosols made of particles of different sizes, allowed me to validate ${}^{\pi}\eta$ by comparison. The high-resolution data set was taken by Wyttenbach et al. (2015), who combined three HARPS transits.

The low-resolution data set indicated a lower atmosphere with a clearly detected water feature (McCullough et al. 2014), but rich in aerosols (Pont et al. 2008; Lecavelier Des Etangs et al. 2008a; Pont et al. 2013; Sing et al. 2016; Barstow et al. 2017). At medium resolution, Huitson et al. (2012) was able to detect sodium and the presence of a thermospheric temperature inversion above the 0.025 R_p level. Wyttenbach et al. (2015) used the high-resolution data set to confirm and extend the temperature inversion to higher heights, with temperatures that reach up to 3 500 K at $\sim 0.15\ R_\mathrm{p}$. These works were based on observational techniques that are intrinsically different, and that probe different regions of the atmosphere. Therefore, their combination was never attempted.

The paper by Pino et al. (2017) has a technical imprint, as many aspects need to be under control when combining observations of such different kind. I thus add a discussion on how this paper contributed to the understanding of the atmosphere of HD189733b as a whole (section 3.7). Subsequently, I describe the context of the HEARTS and SPADES surveys (and additional programs led by the University of Padova) within which the technique was developed (section 3.8.1). This includes the application of $^{\pi}\eta$ to HARPS observations of WASP-49b (Wyttenbach et al. 2017), and the extension of these data sets with dedicated HST observations. Finally, I describe future developments that are the natural outcome of the work performed by Pino et al. (2017) and by the whole team in Geneva and collaborators in Padova.

The work presented in this chapter greatly benefited by collaborations and discussions with a number of people. They know the difficulties that I encountered to obtain these results, and that could have been showstoppers without their help. I thus take this chance to thank (in alphabetical order): V. Bourrier, D. Ehrenreich, S. Grimm, K. Heng, C. Lovis, M. Malik, V. Nascimbeni, F. Pepe, G. Piotto, A. Wyttenbach.

3.1 Introduction

By studying the variation in the apparent radius of a planet as a function of wavelength, i.e. by building its transmission spectrum, it is possible to retrieve the physical conditions and composition of its atmosphere. Despite efforts to use low-resolution spectroscopy and accurate photometry to obtain transmission spectra from the ground (e.g. Sedaghati et al. 2015; Nascimbeni et al. 2013), space-borne low- to medium-resolution spectroscopy ($\mathcal{R} \sim 10^2 - 10^3$) and ground-based high-resolution spectroscopy ($\mathcal{R} \sim 10^5$) remain the most solid techniques to date.

In the near-infrared (NIR), HST/WFC3 transmission spectra are available for tens of planets, comprising several hot Jupiters, some hot and warm Neptunes, and even some super-Earths (e.g. Kreidberg et al. 2015; Ehrenreich et al. 2014; Knutson et al. 2014). Observations of this kind are sensitive to water absorption bands at 1.1 μm and 1.4 μm, whose strength is often lower than predicted by theoretical models. Both aerosols (Seager and Sasselov 2000; Ehrenreich et al. 2012; Howe and Burrows 2012) and subsolar abundance of water (Seager et al. 2005; Madhusudhan et al. 2014a) could be responsible for weakening or even concealing these spectral features. Combining optical and infrared HST observations, Sing et al. (2016) were able to break this degeneracy; their analysis favoured the aerosol explanation (see also Barstow et al. 2017).

On the other side of the transmission spectrum, optical observations with HST/ACS and HST/STIS led to the detection of an enhanced optical slope in the transmission spectra of several exoplanets (Lecavelier Des Etangs et al. 2008a; Pont et al. 2008; Sing et al. 2016), which can be explained by scattering from small aerosols (see section 3.2.4 and e.g. Ehrenreich et al. 2014; Sing et al. 2015). The strongest spectral features, such as the sodium and potassium doublets, are generated above the aerosol deck and are thus visible in transmission spectra (e.g. Charbonneau et al. 2002, Sing et al. 2015). The broad spectral coverage and the accuracy of the optical and NIR HST observations allowed us to firmly detect many species and spectral features in exoplanet atmospheres (Na, K, H_2O, aerosols, etc.), but it is limited by relatively low resolving powers ($\mathcal{R} \sim 10^2 - 10^3$, see Eq. 3.11 and Table 3.1).

Ground-based observatories are able to achieve higher resolving powers of $\mathcal{R} \sim 10^5$. At such high spectral resolution, single absorption lines are spectrally resolved and molecular fingerprints are uniquely identified (Snellen et al. 2010; de Kok et al. 2014; Brogi et al. 2016; Allart et al. 2017). Even the single lines of the sodium and potassium doublets are resolved, and it is possible to probe lower pressures at high altitude in the atmosphere through their sharp cores (Vidal-Madjar et al. 2011a,b; Wyttenbach et al. 2015).

Space-born low-resolution and ground-based high-resolution transit spectroscopy are complementary. However, they are difficult to combine because the data-reduction process for the two techniques is different. Both techniques are time-differential, meaning that they compare stellar spectra taken at different times to record the transit radius. Ground-based, high-resolution transmission spectroscopy is 'double-differential', i.e. it also requires a wavelength differentiation. The wavelength differentiation is necessary to eliminate variations in the measured flux only due to instrumental effects and the atmosphere of the Earth (Snellen et al. 2008; Wyttenbach et al. 2015; Heng et al. 2015; Wyttenbach et al. 2017). During wavelength differentiation the absolute level of the absorption of the planet is lost. Thus, assembling transmission spectra obtained by the two techniques requires a common normalization framework.

Another challenge is the interpretation of the transit radius in terms of models. In particular, several authors have noted that the reference radius/pressure level and the abundance of atmospheric constituents are degenerate (Lecavelier Des Etangs et al. 2008a; Griffith 2014; Heng and Kitzmann 2017). However, in this paper we do not infer absolute abundances for the atmospheric constituents of the atmosphere, and the presence of this degeneracy does not affect our conclusions.

Brogi et al. (2017) presented a first attempt to combine high- and low-resolution transmission spectra. They combined high-resolution, ground-based, infrared ($\lambda \sim 2.287 - 2.345$ μm) CRIRES eclipse observations with HST WFC3 observations ($\lambda \sim 1.125 - 1.655$ μm) of lower resolution but more extended spectral coverage, which were used by Line et al. (2016) to retrieve the atmospheric conditions in HD209458b. The results show that high-resolution spectra on a narrow band are sufficient to increase the precision on the retrieved abundances of the molecular constituents of the atmosphere by at least one order of magnitude (several for CO).

Here, we combine for the first time optical high-resolution, ground-based transmission spectroscopy and optical and NIR space-borne transmission spectroscopy of one of the most well-studied hot Jupiters, HD189733b (Bouchy et al. 2005). Low- to medium-resolution data probe atmospheric layers from the troposphere ($P \sim 10$ bar $- 10^{-4}$ bar), where clouds, molecular bands and the wings of the alkali doublets are generated, to the base of the thermosphere (down to $P \gtrsim 10^{-6}$ bar). On the other hand, high-resolution optical data are sensitive to the fine cores of the alkali atoms (Wyttenbach et al. 2015, 2017) generated at higher altitudes in the lower thermosphere ($P \sim 10^{-4}$ bar $- 10^{-11}$ bar). These observations are complementary to near-UV transit spectroscopy, which probes the transition between the upper thermosphere and the exosphere (Vidal-Madjar et al. 2013), and to far-UV transit spectroscopy, which probes the exosphere. This is the outermost region of the atmosphere of the planet. Thermospheric heating by stellar X/EUV photons into the lower thermosphere is the source of the expansion of the HD189733b upper atmosphere (Vidal-Madjar et al. 2003; Lammer et al. 2003; Yelle 2004; Vidal-Madjar et al. 2011a,b; Koskinen et al. 2013b), which leads to the escape of hydrogen and heavier particles into the exosphere (Lecavelier Des Etangs et al. 2010; Lecavelier des Etangs et al. 2012; Bourrier et al. 2013a; Ben-Jaffel and Ballester 2013).

For HD189733b, the low-resolution transmission spectrum is flattened by the scattering of stellar light by aerosols suspended in the troposphere of the planet (Pont et al. 2013; Sing et al. 2016); instead, the ground-based, high-resolution transmission spectrum reveals the presence of sharp absorption features in the core of the sodium doublet lines (Wyttenbach et al. 2015). These results are apparently contrasting. By modelling the two data sets simultaneously we aim to reconcile them. Furthermore, Vidal-Madjar et al. (2011a,b) and Wyttenbach et al. (2015) have measured a positive temperature gradient through the sodium doublet, indicative of thermospheric heating (the Wyttenbach et al. 2015 result was confirmed by Heng et al. 2015, via an independent analysis of the same data set). With our analysis we aim to investigate the biases and degeneracies introduced by the presence of tropospheric aerosols (neglected in previous works) in the retrieval based on high-resolution data. Using the $^{\pi}\eta$code, which we present in section 3.2, we produce high-resolution ($R \sim 10^6$) transmission spectrum models in order to simulate HST and HARPS data sets. These simulations are described in sections 3.3 and 3.4. High-resolution models with a broad spectral coverage are computationally very demanding. Instead of performing a full retrieval approach which requires the computation of up to millions of models (Madhusudhan and Seager 2009; Lavie et al. 2017), we adopt a hybrid forward modelling/retrieval approach. In section 3.5, we describe this method. In section 3.6, we discuss the models that best reproduce the data and focus on their consistency with both low- and high-resolution spectra. Furthermore, we explore how the different data sets are sensitive to different atmospheric parameters and discuss their complementarity.

3.2 The $^{\pi}\eta$ code

We introduce $^{\pi}\eta$ (a Python code for extra-solar transiting atmospheres), an improved version of the η code presented in Ehrenreich et al. (2006) and expanded in Ehrenreich et al. (2012) to compute transmission spectra of exoplanetary atmospheres. There are three main characteristics of $^{\pi}\eta$:

1. High-resolution ($\mathcal{R} \sim 10^6$). This is necessary to compare models with ground-based, high-resolution data;

2. Broad wavelength coverage (200 nm – 2 μm). This is necessary to compare models with space-borne, optical to NIR data;

3. Flexibility of the input composition and $T-p$ profile. $^{\pi}\eta$ is used to model simultaneously several orders of magnitudes in pressure where common assumptions such as equilibrium chemistry may break down.

In the following we summarize the basic concept of η (see Ehrenreich et al. 2006 and Brown 2001 for a more complete description of the basic equations of the problem). We then describe the improvements of $^{\pi}\eta$ with respect to its former version.

3.2.1 The η code

The η code is a plane parallel, line-by-line radiative transfer code used to compute the transmission spectra $\delta(\lambda)$ of exoplanetary atmospheres. More precisely, $\delta(\lambda)$ is the transit depth, i.e. the flux absorbed by the planetary atmosphere in units of stellar flux. The total opacity arising from photoabsorption by atoms and molecules and scattering by molecules and aerosols in the atmosphere determines the spectral shape of the absorption. Practically, this code computes $\tau_b(\lambda)$, the total optical depth encountered by a light ray traversing the atmosphere at an impact parameter b at wavelength λ, and integrates over all impact parameters (see Eq. 1-3 in Ehrenreich et al. 2006 and figure 3.1 in this paper). By assuming hydrostatic equilibrium and spherical symmetry, the slant optical depth for the species i along a chord at impact parameter b is

$$\begin{aligned}\tau_{b,\,i}(\lambda) = {} & X_i n_0 \cdot \\ & \cdot \int_{-\infty}^{\infty} \sigma_{b,\,i}(\lambda, x) \frac{T_0}{T(\sqrt{b^2+x^2})} \exp\left[- \int_{r_0}^{\sqrt{b^2+x^2}} \frac{dr}{H(r)} \right] dx \ , \end{aligned} \tag{3.1}$$

where n is the total particle numerical density in the atmosphere, $X_i = n_i/n$ is the volume mixing ratio of species i, T is the temperature and $\sigma_{b,\,i}$ is the cross section profile along the considered chord. Quantities subscripted with 0 are taken at a reference level r_0 well inside the opaque part of the atmosphere of a gaseous giant or at the surface of a rocky planet. All of these quantities are functions of the position in the atmosphere. The typical local spatial vertical scale is given by the scale height defined by

$$H(r) = \frac{k_{\mathrm{B}} T(r)}{\mu(r) g(r)} \ , \tag{3.2}$$

where $g(r)$ is the gravity acceleration and $\mu(r)$ is the molecular weight of the species present in the atmosphere. If the atmosphere is composed of more than one species, the total optical depth is the sum

$$\tau_b(\lambda) = \sum_i \tau_{b,\,i}(\lambda) \ . \tag{3.3}$$

Integration of Eq. (3.3) over all the layers that contribute to a measurable atmospheric absorption gives a wavelength dependent atmospheric equivalent surface of absorption $\Sigma(\lambda)$, which is the surface of a completely optically thick disk that absorbs as much light as the entire translucent atmosphere.
A synthetic transmission spectrum is produced in three steps: computing the atmospheric structure (section 3.2.2), computing the cross section and thus the optical depth of the absorbing species at each altitude layer (Sects. 3.2.3, 3.2.4), and finally summing all the contributions from the layers.

3.2.2 Atmospheric structure

Hydrodynamical models of hot Jupiters show that the motion up to the lower part of the thermosphere is subsonic, which implies that hydrostatic balance is a good assumption (e.g. Yelle 2004, Koskinen et al. 2013b). In ${}^{\pi}\eta$ the temperature profile can be assigned as an arbitrary function of the height in the atmosphere to keep generality. We introduce the possibility of assigning this quantity as a function of either r or p (pressure). Keeping p as an independent variable allows us to account parametrically for temperature inversions, whose intensity is determined by the pressure in the atmosphere and not by the absolute height. The hydrostatic equilibrium equations are then integrated with the boundary condition that the pressure is p_0 at a reference layer r_0, both chosen by the user. If p is the independent variable:

$$r\left(p\right) = \left(\frac{1}{r_0} + \int_{p_0}^{p} \frac{k_{\rm b} T\left(p\right)}{m_{\rm H}\mu\left(p\right) G M_{\rm p} p} dp\right)^{-1} \, . \tag{3.4}$$

3.2.3 Geometry

Because of the spectral resolution required for our models (millions of wavelength points in each layer), the implementation of geometry must compromise between time consumption and memory usage. With reference to Fig. (3.1), we divide the vertical axis z in layers of height h. The optical depth in each layer $z_{\rm n}$ is computed and stored. We verified with a step-doubling method that an adaptive grid with four layers per local scale height is enough to grant accuracy in our case. The axis crossing the atmosphere (x) is divided into bins of width $\Delta x_{\rm n}$ which are the projection of h along the chord. From geometric considerations:

$$\Delta x_{\rm n} = \sqrt{\left(z_{\rm l,\ n} + r_0\right)^2 - b^2} - \sqrt{\left(z_{\rm l,\ n-1} + r_0\right)^2 - b^2} \, . \tag{3.5}$$

The value of the optical depth in layer $z_{\rm n}$ can now be used as a proxy for the value of the optical depth in this bin. A typical run of the code then requires $\sim$ 3 GB of RAM and $\sim$ 10 minutes to run on an Intel® Xeon® CPU E5620 (2.40 GHz) using pre-computed opacity tables (see Sects. 3.2.4).

3.2.4 Photoabsorption cross sections at high spectral resolution

Difficulties in accurately modelling the cross section $\sigma(\lambda)$ arise from poor theoretical knowledge of broadening, position and intensity of the lines and from the computational requirements set by the high number of lines to be considered in a line-by-line code.

Atomic lines: For bound-bound processes the cross section can be written as (Seager 2010; Rybicki and Lightman 1986)

$$\sigma_{\rm at}(\nu) = \frac{\pi e^2}{m_e c} f \Phi(\nu) \, , \tag{3.6}$$

where e and m_e are the elementary charge and mass of the electron, c the speed of light, f the oscillator strength of the transition and $\Phi(\nu)$ the line profile. Many physical effects determine the atomic line shape. Here we model each line as a Voigt profile, accounting for four types of broadening: thermal Doppler broadening, turbulent broadening, intrinsic broadening, and collisional broadening. We compute the Voigt profile as the real part of the Faddeeva function, computed with standard Python libraries (`scipy.special.wofz`).

The ASD line list (Kramida et al. 2015) provides the natural broadening widths, while for the collisional broadening of the sodium and potassium doublet, by far the

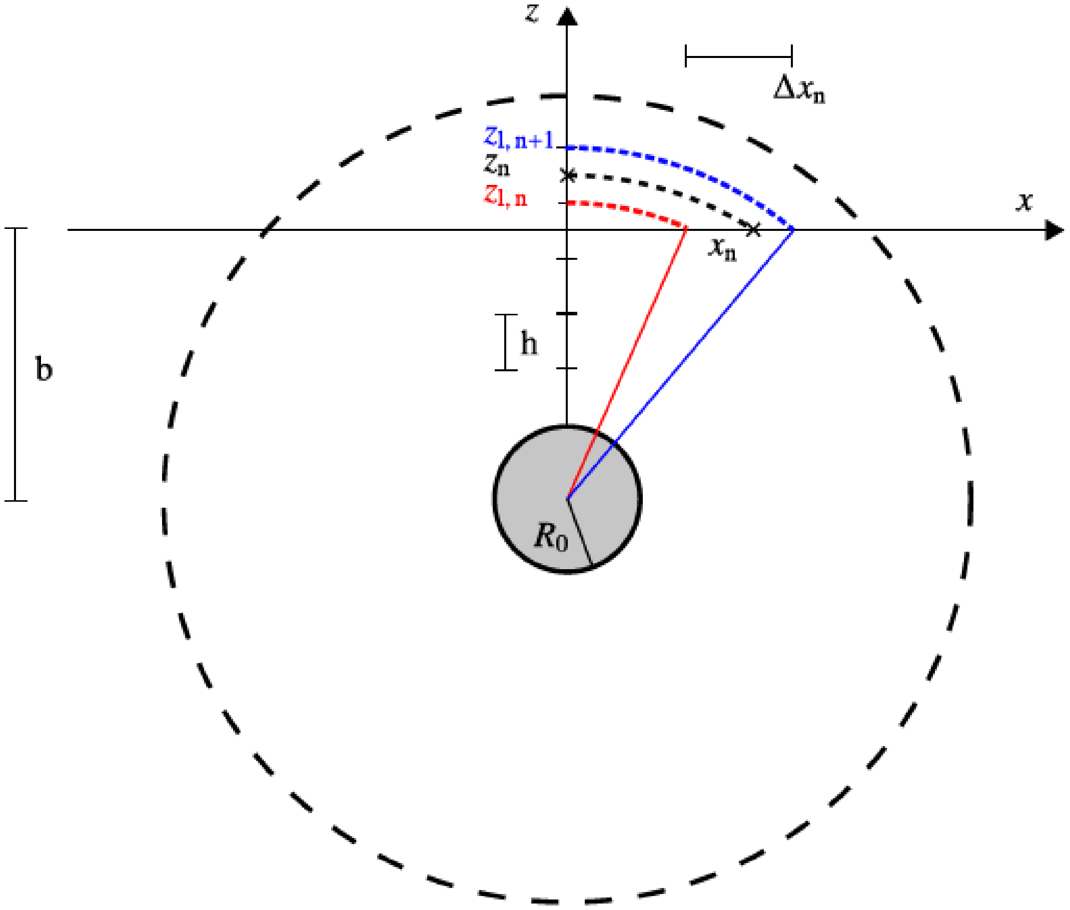

Figure 3.1: Geometry of transmission spectroscopy.

dominant atomic transitions, we follow Iro et al. (2005) and Burrows et al. (2000) and set

$$\gamma_{\mathrm{coll},\left[\substack{\mathrm{Na}\\ \mathrm{K}}\right]} = \begin{bmatrix}0.071\\ 0.14\end{bmatrix}\left(\frac{T}{2000}\right)^{-0.7} \mathrm{cm}^{-1}\mathrm{atm}^{-1}\cdot P\cdot X_{\mathrm{H}_2}\ , \tag{3.7}$$

where X_{H_2} is the volume mixing ratio of H_2, the relevant perturbing species.

Molecular transitions: We focus on water, which was detected in HD189733b using WFC3 data (McCullough et al. 2014). To model H_2O absorption, we adopt the HITEMP line list (Rothman et al. 2013)[1]. Since the temperature in the atmosphere of HJs can reach well above 1000 K, it is necessary to use the HITEMP line list instead of the HITRAN line list (Rothman et al. 2010). The HITEMP line list includes transitions that may be of negligible intensity at laboratory temperature, but due to the temperature dependence of the line intensities might play a role at high temperatures (Tinetti et al. 2007). This results in the inclusion of $2.7\cdot10^7$ H_2O transitions in the wavelength range 3 300–20 000 Å that interests us. Each line has to be modelled precisely at very high resolution ($\mathcal{R}\sim10^6$). The task requires state-of-the-art numerical techniques: we therefore rely on the HELIOS-K opacity calculator (Grimm and Heng 2015). HELIOS-K is an ultrafast, open-source line-by-line opacity calculator for radiative transfer that extensively exploits parallel computing on GPUs to compute opacity tables generated from the HITRAN or HITEMP line list. The shape of each line is modelled as a Voigt profile with a characteristic intensity, broadening and central wavelength. These are in turn determined by the thermodynamical conditions of the molecular gas:

- A change in temperature has the effect of changing the partition function of a given molecule, i.e. the number density of the molecules associated with an energy level with respect to the total number density of that molecule. This impacts the intensity of a given line.

- A change in temperature or pressure changes the half width half maximum of a given line (Mihalas 1970; Rothman et al. 1995; Grimm and Heng 2015; Hedges and Madhusudhan 2016).

- A change in pressure induces a shift of the central wavelength of the line.

All of these effects are considered in HELIOS-K, which is thus able to accurately model each line present in the HITEMP line list in the selected wavelength range.
We precomputed a grid of opacity tables covering the temperature range 500–3000 K with a sampling of 50 K and the pressure range $10^{-9}-10$ bar in 21 logarithmically spaced points. Each opacity table is calculated on a wavenumber grid with a resolution of 0.01 cm^{-1} over the entire spectral range 3 300–20 000 Å, corresponding to a wavelength resolution between 0.0033 and 0.02 Å or $\mathcal{R}\gtrsim5\cdot10^5$, which is enough to grant no opacity loss (see also Hedges and Madhusudhan 2016). We extend the calculation for each line out to 25 cm^{-1} from its centre.
Our high-resolution approach is aimed at limiting molecular opacity loss. It is not optimal, however, since it requires a large amount of disk space to store the opacity tables and long computational times to model the entire spectral range. For the purposes of this paper, computational time is not an issue: it is sufficient to compute

---

[1] In appendix 3.9 we discuss possible alternatives.

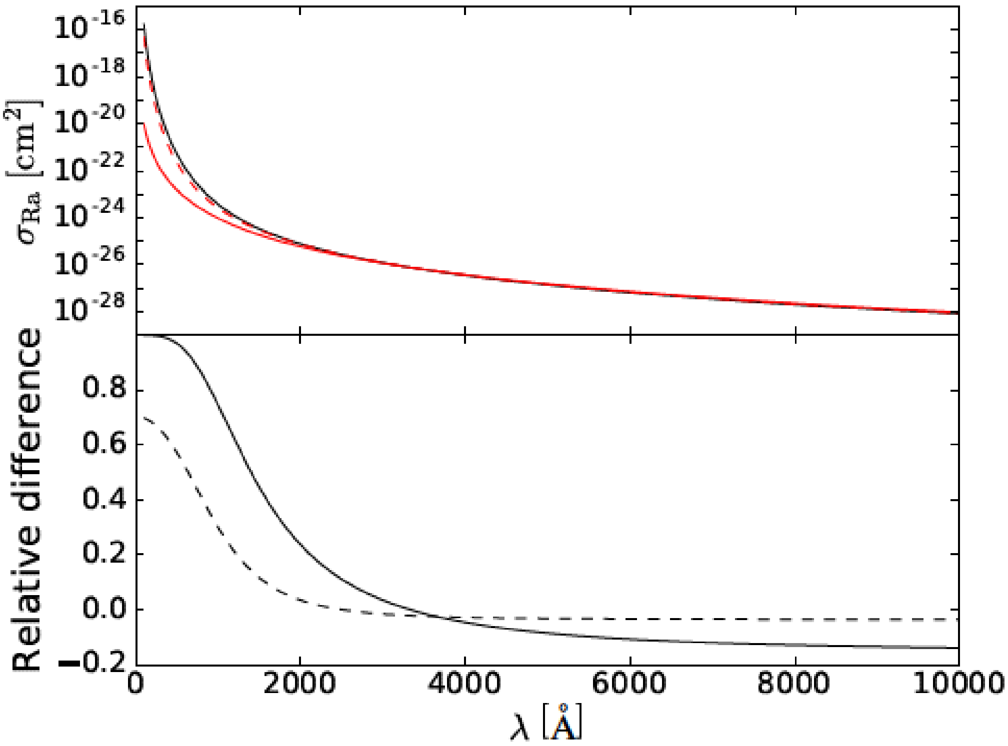

Figure 3.2: Comparison between different Rayleigh scattering prescriptions used in the literature. The black solid line is the prescription adopted in this work (Dalgarno and Williams 1962) and recommended by (Seager 2010). The red solid line is the prescription adopted in the previous version of the program, based on Karplus (1964). Finally, the red dashed line is the version adopted by Heng (2016), based on Cox (2000). The relative difference between the prescriptions by Dalgarno and Williams (1962) and Karplus (1964) (lower panel, solid line) is negligible for wavelengths longer than 3 300 Å, of interest for this work. The difference between Dalgarno and Williams (1962) and Cox (2000) is negligible even bluewards.

a limited number of models ($\sim 10^2$, see section 3.5). In future implementations we will explore several possibilities to speed up the code, such as k-distribution tables (Goody et al. 1989; Lacis and Oinas 1991; Fu and Liou 1992; Grimm and Heng 2015), the opacity sampling method (Sneden et al. 1976; Kitzmann 2016) and the recently proposed super-line approach (Rey et al. 2016; Yurchenko et al. 2017).

Continuum absorption The absorption lines emerge from a 'continuum' absorption, due to Rayleigh scattering by several species and to scattering by aerosols when present. We implement Rayleigh scattering due to H_2. In $^{\pi}\eta$ we adopt the prescription by Dalgarno and Williams (1962, 1965) commonly adopted in both solar system and exoplanets communities (Seager 2010):

$$\sigma_{\mathrm{H}_2}(\lambda) = \frac{8.14 \cdot 10^{-13}}{\lambda^4} + \frac{1.28 \cdot 10^{-6}}{\lambda^6} + \frac{1.61}{\lambda^8} \,, \tag{3.8}$$

which is accurate to $O\left(\lambda^{-10}\right)$.
Ehrenreich et al. (2006) implemented a different prescription for H_2, based on the

ab initio calculations given in Karplus (1964). A third alternative, based on Cox (2000), is adopted by other authors (Heng 2016). In Fig. (3.2), we show a comparison between the Rayleigh cross sections for molecular hydrogen computed according to the prescriptions by Dalgarno and Williams (1962), Karplus (1964), and Cox (2000). They differ by $< 10\%$ in the wavelength range 3 300–20 000 Å. We conclude that our analysis is consistent with all prescriptions. However, possible studies sensitive to Rayleigh scattering in the UV spectral range will have to consider which is the most appropriate law to follow.

We also include a simple treatment of aerosols as an opaque opacity source. Following Sing et al. (2016), we distinguish between a grey absorber, to which we call 'clouds', and a chromatic absorber that we generically call 'hazes'[2]. With this distinction, clouds mask the transmission spectrum below a pressure level p_c that coincides with the clouds top. Clouds are aerosols with particles that are larger than the wavelength of incident light. What we call hazes are, on the other hand, small particle aerosols (smaller than the wavelength of incident light) whose cross sections depend on wavelength and on the particle size. We model the global haze contribution as a scattering cross section:

$$\sigma_{\mathrm{h}} = \sigma_{\mathrm{h}}(\lambda_0)\left(\frac{\lambda}{\lambda_0}\right)^{-s} . \tag{3.9}$$

Here, $\sigma_{\mathrm{h}}(\lambda_0) = A\sigma_{\mathrm{H}_2}(\lambda_0)$, where A is the amplitude of the hazes scattering cross section in units of the H_2 Rayleigh scattering cross section. s is a slope that is determined by the composition and the sizes of the particles that scatter light (Pont et al. 2013). Observations are not able to distinguish all the different populations of scatterers (but see e.g. Ehrenreich et al. 2014); on the other hand leaving s as a parameter allows us to have full generality when dealing with aerosol scattering.

In the limit for $\lambda \to \infty$, Eq. (3.8) reduces to a pure power law with $s = 4$ (Rayleigh scattering with a wavelength independent refraction index). In this case the cross sections of hazes and Rayleigh scattering by molecular hydrogen can be combined in an "effective Rayleigh scattering" cross section:

$$\sigma_{\mathrm{Ra,\ eff}}(\lambda) = \sigma_{\mathrm{H}_2}(\lambda_0)\left(\frac{\lambda}{\lambda_0}\right)^{-4}\left[1 + \mathrm{A}\left(\frac{\lambda}{\lambda_0}\right)^{4-s}\right] . \tag{3.10}$$

From Eq. (3.10), it is clear that hazes affect the transmission spectrum only if the scale parameter A is high enough. Depending on the index s the effect may be more severe at longer wavelengths ($s < 4$) or shorter wavelengths ($s > 4$).

Despite its simplicity, several studies based on similar prescriptions for clouds and hazes showed that this treatment is sufficient to capture degeneracies between the presence of clouds and water abundance (e.g. Kreidberg et al. 2015; Sing et al. 2016).

In standard conditions, symmetric molecules such as H_2 do not possess any dipole moment, and thus are not strong emitters. However, they may acquire a transient dipole during collisions with other molecules if the density is high enough. In

---

[2] The naming convention we have adopted is commonly used by Earth scientists. The planetary science community generally distinguish clouds and hazes in terms of formation pathways rather than in terms of size. See also a blog entry by Sarah Hörst on this topic: `http://www.planetary.org/blogs/guest-blogs/2016/0324-clouds-and-haze-and-dust-oh-my.html`

extremely hydrogen-rich dense environments, such as cool low-metallicity stars (Borysow et al. 1997; Morley et al. 2014) and some solar system planets (Wordsworth 2013; Zhang et al. 2015), the absorption due to this phenomenon (collisional-induced absorption, CIA) should usually not be neglected. In our case of transmission geometry of a hot Jupiter, CIA contribution is negligible in the wavelength range considered (as molecular opacities are dominant at the pressures sounded). For consistency with the literature (e.g. Madhusudhan 2012; Moses et al. 2013; Malik et al. 2017), we nonetheless include in $^{\pi}\eta$ the CIA by H_2–H_2 and H_2–He couples from the density-normalized HITRAN coefficients presented in Richard et al. (2012).
Finally, we neglect the effects of refraction and multiple-scattering, working in approximation of pure absorption (where scattering opacity is treated as absorption opacity). Brown (2001) and Burrows et al. (2000) claimed that these effects are unimportant in hot Jupiters. More recently, Bétrémieux (2016) argued that there may be a few cases in which this simplification is inaccurate (mainly cold and small planets, which we do not investigate here). Robinson (2017) demonstrated that aerosol forward scattering can be an important consideration for planets whose host star is relatively large in angular size, as is the case for hot Jupiters. However, for the models presented here, haze/cloud forward scattering would likely reduce our predicted transit depths by less than a scale height (Robinson et al. 2017; Robinson, private communication).

3.3 Simulating observed transmission spectra

A comparison between theoretical models and observations is only possible after the following steps:

1. Convolution with the line spread function (LSF). Since the FWHM of the LSF varies by orders of magnitude between low- and high-resolution (~ 0.048 Å for HARPS, up to $\sim$ 107.7Å for HST), its impact on the transmission spectrum in these different regimes must be taken into account;

2. Binning at the data sampling;

3. Only for ground-based data: wavelength normalization. Contrary to space-based observations, ground-based, high-resolution spectra are double differential (in time and wavelength, Snellen et al. 2008; Wyttenbach et al. 2015; Heng et al. 2015). The wavelength differentiation is required to remove time-varying signals due to the Earth's atmosphere or to the instrument. However, it removes the absolute reference for the absorption, a limitation that we need to take into account when making a comparison to models.

3.3.1 Convolution with the instrumental LSF

We model the LSF of all the instruments as Gaussians with full width half maximum (FWHM) equal to their nominal resolving power. The resolving power is defined as

$$\Re = \frac{c}{\Delta v} = \frac{\lambda}{\Delta\lambda} , \tag{3.11}$$

where Δv and $\Delta\lambda$ are the FWHM of one resolution element of the instrument considered in the velocity space and in the wavelength space, respectively. In Table 3.1 we list the adopted parameters for the LSF of the instruments used for observations.

We compute the chromatic absorption due to the atmosphere of the planet, or transit depth, $\delta(\lambda)$. Then, we convolve this quantity with the LSF of the instrument,

$$\delta_{\mathrm{conv}}(\lambda) = (\delta * \mathrm{LSF})(\lambda) = \int_{-\infty}^{+\infty} \delta(\lambda)\, \mathrm{LSF}(\lambda - \lambda')\, d\lambda' \,. \tag{3.12}$$

To compute the integral on the right-hand term, it is necessary to limit its calculation in the wavelength space. We made sure that integration over 3 times the FWHM of the LSF causes no loss of flux for all simulated instruments.

3.3.2 Binning

After the stellar light is dispersed, it hits the CCD pixels. In a calibrated spectrograph, each pixel is associated with a wavelength. The net effect is that the photons are binned by wavelength, each bin corresponding to a pixel. To compare the model with the observations it is necessary to bin the model in the same bins the observations are provided with.
Binning to the instrumental sampling must conserve flux, thus by

$$\delta_{\mathrm{bin}}\,(\lambda_i) = \frac{\int_{\lambda_i - dx_i}^{\lambda_i + dx_i} \delta_{\mathrm{conv}}(\lambda)\; d\lambda}{2\, dx_i} \,, \tag{3.13}$$

where λ_i and dx_i represent the centre and the half width of a pixel in the wavelength space.

3.3.3 Wavelength normalization

To remove flux variations only due to the instrument or the atmosphere of Earth, ground-based observations require a wavelength differentiation (Snellen et al. 2008; Wyttenbach et al. 2015; Heng et al. 2015). Practically, the differential transmission spectrum $\tilde{\mathfrak{R}}(\lambda)$ presented in Wyttenbach et al. (2015, 2017) is normalized to a reference band. To compare the models to this data set, it is necessary to normalize the models in the same fashion. The relation between the transit depth and the differential transmission spectrum is

$$\tilde{\mathfrak{R}}_{\mathrm{bin}}(\lambda_i) = \frac{1 - \delta_{\mathrm{bin}}(\lambda_i)}{1 - \delta_{\mathrm{bin}}(\lambda_{\mathrm{ref}})} \,, \tag{3.14}$$

where $\delta_{\mathrm{bin}}(\lambda_{\mathrm{ref}})$ is the transit depth after convolution with the LSF and binning, averaged in a reference band where no features are expected. Equation 3.14 is demonstrated in Appendix 3.9.

3.4 Transmission spectrum and planetary absorption

The procedure we have outlined in section 3.3 is commonly adopted to compare models and observations. However, it does not account for the fact that transmission spectra are built by dividing out stellar fluxes during the transit (in-transit, F_{in}) and out-of-transit (F_{out}). This is different from what is simulated by following the

Table 3.1: Instrument setups of the observations used. For each data set, we indicate the walength range covered, the resolving power and the width of the instrumental LSF that we adopted. The HST data sets were also analyzed by Sing et al. (2016), who corrected the observations for the effect of stellar activity. We use their version of the HST transmission spectra in our work.

Instrument and setup	λ range [Å]	$\mathcal{R}$	FWHM [km/s]	FWHM [Å]	Reference
HARPS	3 800–6 900	115 000	2.6	~ 0.048	Wyttenbach et al. 2015
HST STIS G430L	2 900–5 700	530	565	~ 8	Sing et al. 2011
HST STIS G750M	5 808–6 380	5 000	60	~ 1.2	Huitson et al. 2012
HST ACS HRC G800L	5 500–10 500	140	2 140	~ 40	Pont et al. 2008
HST WFC3 G141	11 000–17 000	130	2 300	~ 108	McCullough et al. 2014

procedure outlined in the previous section, since neither convolution nor integration (or sum) are distributive with respect to division. For example, for convolution,

$$\mathrm{LSF} * (f/g) \neq (\mathrm{LSF} * f) \,/\, (\mathrm{LSF} * g) \ .$$

Thus, a more realistic simulation should compute as

$$\delta_{\mathrm{bin}}\,(\lambda_i) = \frac{F_{\mathrm{in,\,bin}}\,(\lambda_i)}{F_{\mathrm{out,\,bin}}\,(\lambda_i)} = \frac{\int_{\lambda_i - dx_i}^{\lambda_i + dx_i} F_{\mathrm{in,\ conv}}(\lambda)\ d\lambda}{\int_{\lambda_i - dx_i}^{\lambda_i + dx_i} F_{\mathrm{out,\ conv}}(\lambda)\ d\lambda}\ , \tag{3.15}$$

$$F_{\mathrm{in/out,\ conv}}(\lambda) = \int_{\sim 3 \cdot \mathrm{FWHM(LSF)}} F_{\mathrm{in/out}}(\lambda)\,\mathrm{LSF}(\lambda - \lambda')\ d\lambda' \ . \tag{3.16}$$

However, the computational cost of these more realistic simulations is doubled with respect to computing δ_{bin} and $\tilde{\mathfrak{R}}_{\mathrm{bin}}$ directly from the theoretical planetary absorption $\delta(\lambda)$ (Eq. 3.13).

If the integrand can be approximated as a constant in the domain of integration it can pass through the sign of integral. If this applies to both Eq. (3.15) and Eq. (3.16) the order of integration and division does not matter, and we can proceed following section 3.3.

We test numerically if this is the case for our spectra. To perform the test, the stellar (F_{out}) should be known. To represent it we use a PHOENIX model representative of the spectrum of HD189733 ($T = 4900$ K, $\log g = 4.5$, [Fe/H] $= 0$, $\alpha = 0$). The $^{\pi}\eta$ code computes the absorption δ due to the planet, thus it is possible to compute $F_{\mathrm{in}} = F_{\mathrm{out}}(1 - \delta)$. This is the stellar flux, planetary absorption included, before it is observed with an instrument. Then, the transmission spectra can be computed following Eq. (3.13), Eq. (3.15), and Eq. (3.16), and compared.

In Fig. (3.3) we show the difference between the transmission spectrum computed using the stellar spectrum (Eq.3.15 and Fig. 3.3, blue line), which is more accurate, and that using the absorption directly (Eq. 3.13, red line). The statistical difference between the models is non-significant (using the BIC, defined in section 3.5, ΔBIC ~ 3 for HARPS, less than 1 for WFC3); this is also confirmed by the small residuals between the two models compared to the error bar (Fig. 3.3). We note, however, that for observations at higher signal-to-noise such as ESPRESSO, the E-ELTs, or JWST might deliver or with different host stars, this effect might become significant. Indeed, Deming and Sheppard (2017) showed that neglecting this effect, which they call resolution-linked bias (RLB), yields a difference of 12% in the peak transmittance for TRAPPIST-1b in the region around 1.4 μm. The effect is severe because cold stars likes TRAPPIST-1 have spectra dominated by forests of molecular lines. HD189733b is a K dwarf, thus the effect is less important.

3.5 HD189733b case: methods

We compare models of transmission spectra of HD189733b with optical, high-resolution differential transmission spectroscopy HARPS data (Wyttenbach et al. 2015) and optical, low-resolution HST STIS G430L and ACS HRC G800 (Pont et al. 2008; Sing et al. 2011, 2016), medium-resolution HST STIS G750M (Huitson et al. 2012) and NIR, low-resolution WFC3 (McCullough et al. 2014) data. The observations used are listed in Table 3.1. All the HST data are taken in the version presented by

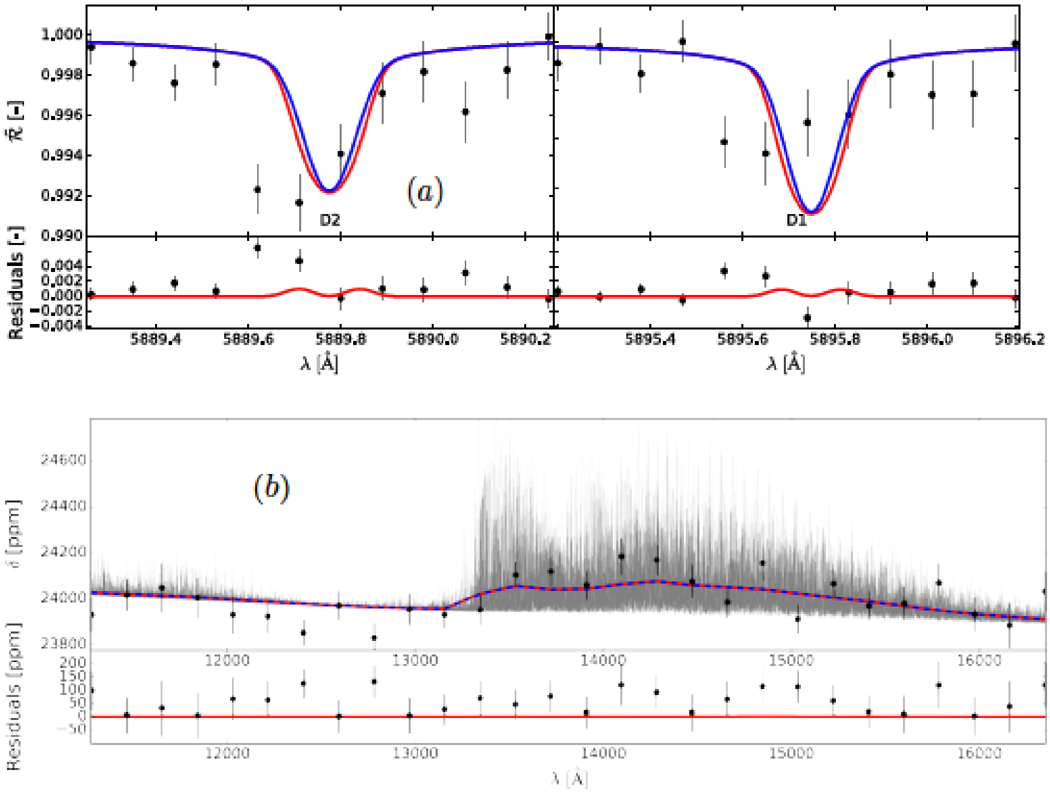

Figure 3.3: Effect on the transmission spectrum of non-distributivity of convolution and binning with respect to division. In blue are shown models that are convolved and averaged in flux before division, and thus represent more closely the observed transmission spectrum; in red are shown models obtained by downgrading directly the planetary absorption, as usually done in the literature and throughout the rest of this paper. The black dots with error bars are the observed data. We show also the comparison between the residuals between data and the more accurate, blue model and the residuals between the models. *Fig. (a)*: In the case of HARPS data (binned 9x in the picture, but full resolution was used in the comparison), the difference in shape between the two models is visible by eye. However, the difference between the two models is still lower than the residuals between data and model (see lower panel). *Fig. (b)*: in the case of WFC3 the sharp short period variations (single molecular lines) are averaged out, while the longer period variations (molecular bands) are well sampled even at low-resolution. As a result, the difference between the models is also negligible.

Sing et al. 2016, who corrects for possible systematic offsets between the data sets that are mainly due to stellar activity. For G750M, Sing et al. (2016) presents the data in wavelength bins of 60 Å. However, a single point in the core of potassium is presented at higher sampling (bin width of 10 Å). Its wavelength domain is already covered by the neighbouring lower sampling data points. We thus exclude this point from our analysis.

We calculate the χ^2 between the HST transit depths or the normalized HARPS transmission spectrum in a wavelength bin λ_i, and the model processed as described in section 3.3 in the same wavelength bin. We also compute the corresponding Bayesian information criterion (BIC, Liddle 2007). The lowest BIC corresponds to the favoured model; a model whose BIC differs by more than 5 is statistically different. Moreover, the BIC takes into account the number of model parameters, preferring simpler models.

3.5.1 HST data set

We find a model that minimizes the $\mathrm{BIC_{HST}}$ for the full HST data set (best fit HST, BF-HST). Throughout this operation we fix the following parameters:

1. Star radius: $R_\star = 0.756\ R_\odot$;
2. Planetary mass: $M_P = 1.138\ M_\mathrm{J}$;
3. Constant solar composition, i.e. we adopt the following fixed mixing ratios:
   (a) $X_{H_2} = 0.9289989$;
   (b) $X_{He} = 0.07$;
   (c) $X_{H_2O} = 10^{-3}$;
   (d) $X_{Na} = 10^{-6}$;
   (e) $X_K = 10^{-7}$.

We adopt p as an independent variable, and fix the $T-p$ profile. For the lower part of the atmosphere ($p > 1$ mbar), we adopt the profile presented in Sing et al. (2016). For the thermosphere ($p < 1$ mbar), we adopt the profile presented in Wyttenbach et al. (2015).

The remaining parameters are adjusted to minimize $\mathrm{BIC_{HST}}$. These parameters are:

- The reference radius, which we take as the radius at 10 bar: $r_{10\ \mathrm{atm}} = r(p = 10\ \mathrm{atm})$ (but see Heng and Kitzmann 2017 for a discussion on why this causes a degeneracy in inferring the values of mixing ratios at the order-of-magnitude level);
- The hazes parameters $\sigma_\mathrm{h}(\lambda_0)$ and s;
- The top pressure of the cloud deck p_c.

The HST data set is further divided into optical (both STIS gratings and ACS) and WFC3. The optical data set is mainly sensitive to the haze parameters and to the reference radius, while the WFC3 data set is mainly sensitive to p_c and to the reference radius. Instead of performing a full retrieval, we exploit this difference to design a step-by-step optimization algorithm:

Step 1: Adjust $r_{10\ \mathrm{atm}}$ using the average absorption in the WFC3 band;

Step 2: Adjust $\sigma_{\mathrm{h}}(\lambda_0)$ and s using STIS + ACS data;

Step 3: Adjust the cloud level p_c using the WFC3 data. For step 3, the full WFC3 spectral information is used.

In each step, all parameters that are not being adjusted are fixed to values from the previous steps. If the parameters were perfectly uncorrelated, the procedure would converge to a minimum of $\mathrm{BIC}_{\mathrm{HST}}$ after one iteration. This is not the case (e.g. optical and WFC3 data sets both depend on the reference radius), thus we iterate the three steps until convergence. Convergence is achieved when $\Delta\mathrm{BIC}_{\mathrm{HST}} < 5$ among the six models obtained in the last two iterations. The initialization for the first iteration assumes an aerosol-free atmosphere.
The intermediate nature between forward modelling and retrieval of our approach, which we refer to as 'retrieval by hand', allows us to limit the number of models to be computed, and thus treat the problem numerically. At the same time, it allows us to reproduce the HST data set satisfactorily (see section 3.6).

3.5.2 HARPS data set

The BF-HST is then adjusted to reproduce the HARPS data set. For the wavelength normalization, we adopt the reference band 5870 – 5882.22 Å, 5903.24 – 5916 Å (the same adopted by Wyttenbach et al. 2015, grey background in Fig. 3.4). The merit functions are computed in two bands centred in the cores of the sodium lines: 5889.22 Å – 5890.26 Å and 5895.20 Å – 5896.24 Å (Wyttenbach et al. 2015, yellow background in Fig. 3.4). For each model, we compute the difference in BIC of the fit to the combined data set $\Delta\mathrm{BIC}_{\mathrm{HR+HST}}$ with respect to the reference model BF-HST. We also compute the difference in BIC of the fit to the low- and high-resolution data sets separately ($\Delta\mathrm{BIC}_{\mathrm{HR}}$ and $\Delta\mathrm{BIC}_{\mathrm{HST}}$), to highlight which data set is driving the fit.
To adjust the HARPS data we modify a different set of parameters that mainly affects the thermosphere, leaving the troposphere mostly unchanged:

1. Thermospheric $T-p$ profile ($P < 0.1$ mbar);
2. Sodium abundance, X_{Na}.

The strongest water lines may be affected by the $T-p$ profile modification and the sodium wings are produced in the troposphere. It is thus necessary to verify a posteriori that the quality of the fit to the HST data set is comparable to the quality obtained with the BF-HST for each modification.

3.6 HD189733b case: results and discussion

3.6.1 HST data set

After six iterations we obtain a model that reproduces adequately the whole HST data set (BF-HST, see Fig. 3.5). We find a reduced chi square $\chi^2_{\mathrm{HST},\,\nu=43} = 1.1$. When considering only the optical data sets (STIS G430L and G750M, and ACS), we obtain $\chi^2_{\nu=17} = 0.8$. For the WFC3 data set we find $\chi^2_{\nu=26} = 1.3$. The bluest points of the WFC3 observations would be reproduced better by the model if the scattering slope were weaker in this region, but a reduction of the haze content would cause a decrease in the quality of the reduced chi square obtained with the optical data set. The final model parameters are

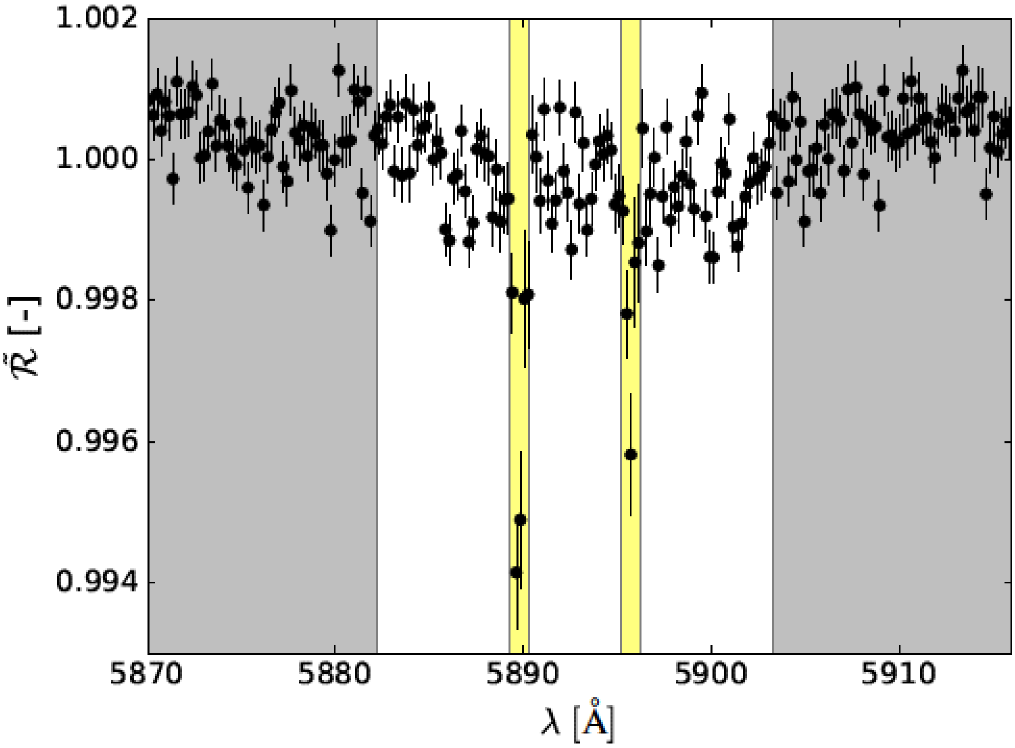

Figure 3.4: Bullet points represent the observed transmission spectrum previously published on Wyttenbach et al. (2015), binned 21x (for the fit the full resolution data are used). The sodium excess absorption is clearly visible within the yellow bands, where optimization is performed. In the grey bands no clear signal is found, and these are used to normalize the spectrum.

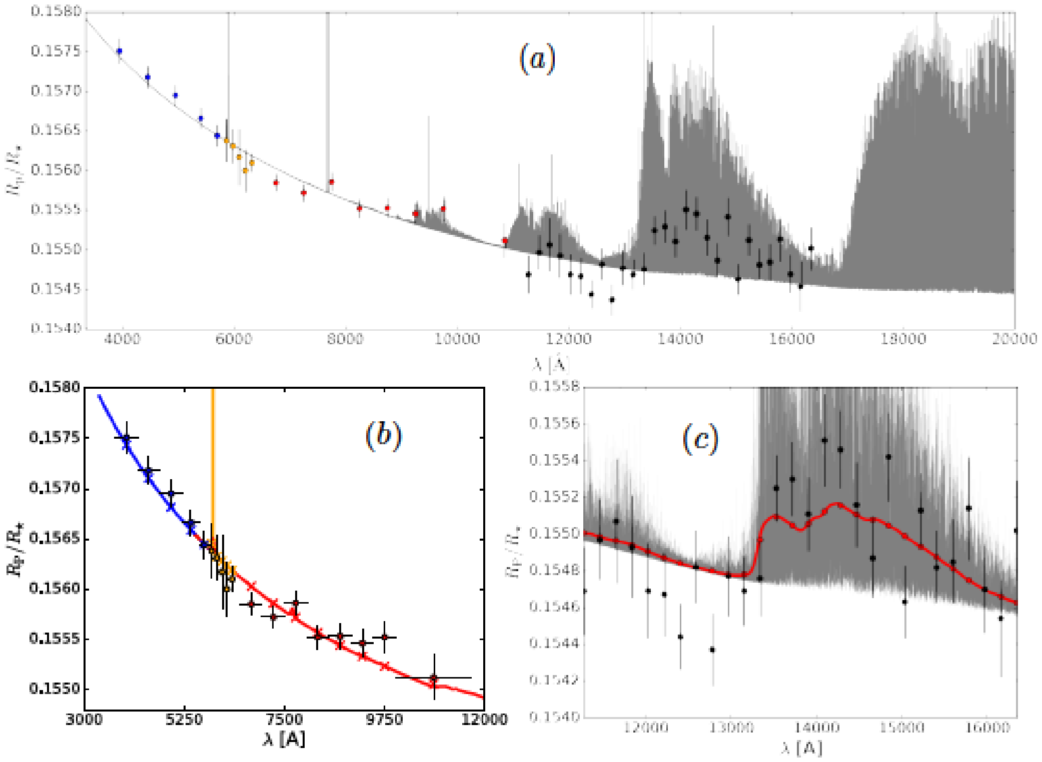

Figure 3.5: BF-HST seen at various zoom levels. In panel (a), we show the whole transmission spectrum obtained after the parameters have been adjusted to reproduce the combined low-resolution data set. In panel (b) we show a zoom on the two STIS and the ACS data sets. Different colors correspond to models convolved with the different instrumental LSF (solid lines) and binned (dots). At the resolution of STIS G750M sodium is still quite sharp, while the lower resolution of ACS smears out the potassium doublet. This region of the spectrum is particularly sensitive to the presence of haze scattering. In panel (c) we show a zoom on the WFC3 data set. The water band is clearly visible, however its intensity is reduced with comparison to an aerosol-free model.

- $\sigma_{\mathrm{h}} \sim 8000 \cdot \sigma_{\mathrm{H_2}}(589.46\ \mathrm{nm}) \left(\dfrac{\lambda}{589.46\ \mathrm{nm}} \right)^{-3.17}$,
- $p_{\mathrm{c}} \sim 0.4$ mbar ,
- $r_{10\ \mathrm{atm}} \sim 1.1082\ \mathrm{R_J}$.

Consistent with the literature, we find that the spectrum is dominated by aerosol scattering. An enhanced scattering due to a mix of different small particles (which produces an effective opacity with slope different than 4, see Pont et al. 2013; Ehrenreich et al. 2014) is required to explain the slope in the optical. The reduced intensity of the water feature probed by WFC3 is reproduced with a grey opacity cloud-deck.

3.6.2 HARPS data set

We show the results of the comparison with the HARPS data in Fig. 3.6. The absorption in both sodium lines of the BF-HST model is low compared to the data

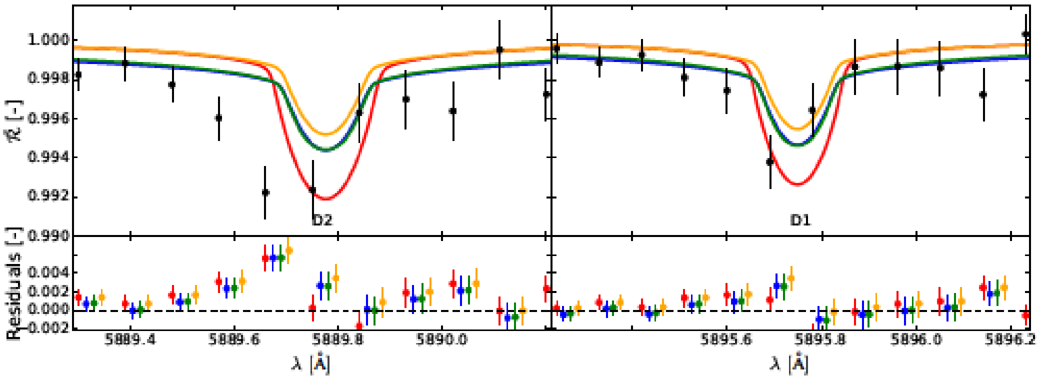

Figure 3.6: Comparison between several models and the HARPS data set. Orange line: BF-HST. The sodium line cores absorption is too low to reproduce the high-resolution data set. Blue line: aerosol-free model. This model reproduces better the high-resolution data set, but is not consistent with the low-resolution data set. Green line: 10Na. Due to our rigorous wavelength-normalization process it is indistinguishable from the aerosol-free model. It is however penalized compared to the previous for the presence of three additional parameters to describe aerosols. Red line: HTT. A higher thermospheric temperature increases the scale height of the outermost layers, and makes the sodium cores sharper.

(Fig. 3.6). Since we adopted a $T-p$ profile consistent with Wyttenbach et al. (2015), which in turn is a result of a fit to the same data set considered here, this comes as a partial surprise. The most likely reason is that Wyttenbach et al. (2015) assumed an aerosol-free atmosphere. Since the cores of the sodium lines are detected, aerosols are likely confined to the troposphere. The sodium core features probed by HARPS are generated higher up, in the lower thermosphere. However, it was already noticed from medium-resolution observations that scattering by aerosols may in some cases partially mask the sodium spectral feature (e.g. Charbonneau et al. 2002; Pont et al. 2013; Sing et al. 2016; Heng 2016). To test whether aerosols in HD189733b are at high enough altitudes to have an effect on the high-resolution transmission spectrum we run an aerosol-free model (AF) that otherwise has the same parameters as the BF-HST.

The aerosol-free model reproduces the data better, as evinced by $\Delta\mathrm{BIC}_{\mathrm{HR}} \sim 45$ and by smaller residuals. We can thus confirm that the discrepancy between our results and the results by Wyttenbach et al. (2015) is due to the presence of aerosols and their effect on wavelength normalization. Indeed, aerosols are not high enough to affect the inner cores of the lines, but they are high enough to occult the sodium wings in the reference bands (see Fig. 3.7). The difference in absorption between the core of the lines and the reference band is thus reduced in the presence of aerosols. Thanks to the correct wavelength normalization of the models, we are sensitive to this difference, and can distinguish between the BF-HST and its aerosol-free version. However, the low-resolution data set firmly excludes the aerosol-free case; $\Delta\mathrm{BIC}_{\mathrm{HST}} > 10\,000$ supports the aerosol-rich case. To reconcile the space-borne and ground-based data sets we need to keep the aerosols and increase the contrast of the sodium feature. We thus modify the thermospheric $T-p$ profile to increase the scale height of the layers where the cores of the sodium lines are generated. This is obtained by increasing the thermospheric temperature with respect to the BF-HST. The high

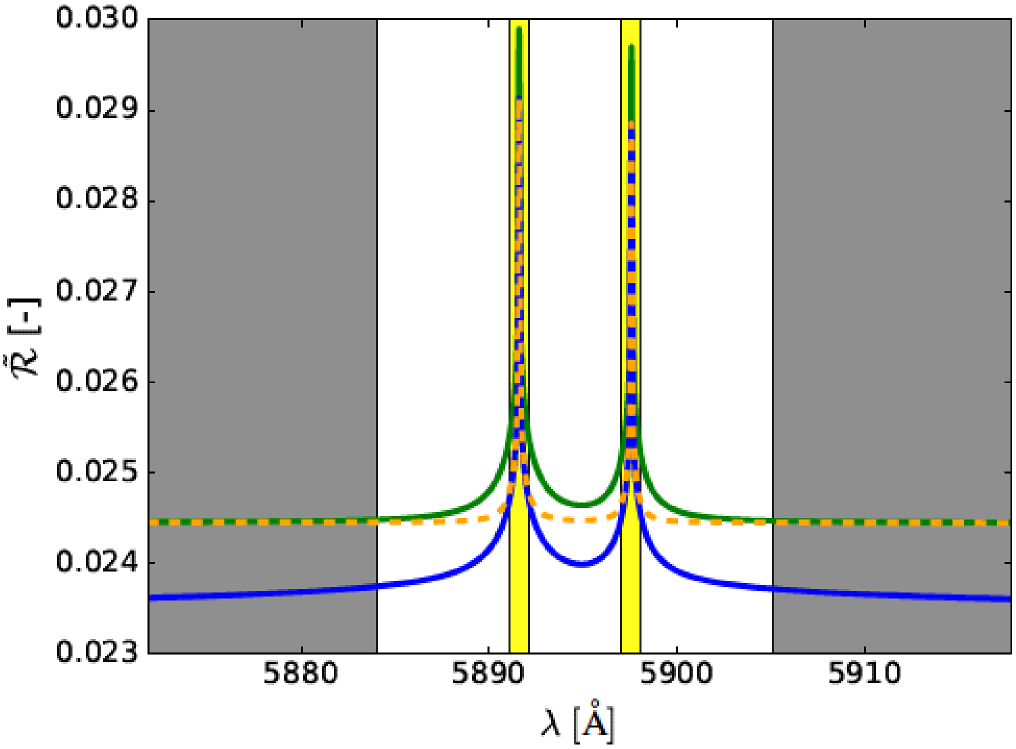

Figure 3.7: The theoretical models also shown in Fig. 3.6, with the same color code (orange: BF-HST, blue: AF, green: 10Na), but before wavelength-normalization. The HTT model is not shown for clarity. Aerosols do not affect the cores of the sodium lines of the BF-HST model, which overlaps with the aerosol-free model in the yellow band used to compute the merit functions. However, they mask the wings in the reference bands (gray background). This example shows that high-resolution data are sensitive to the presence of aerosols. The 10Na model has a higher absorption in the sodium region compared to the aerosol-free model because the global optical depth is higher. However, HARPS alone cannot distinguish the two cases (Fig. 3.6) because of the double differential technique through which transmission spectra are obtained.

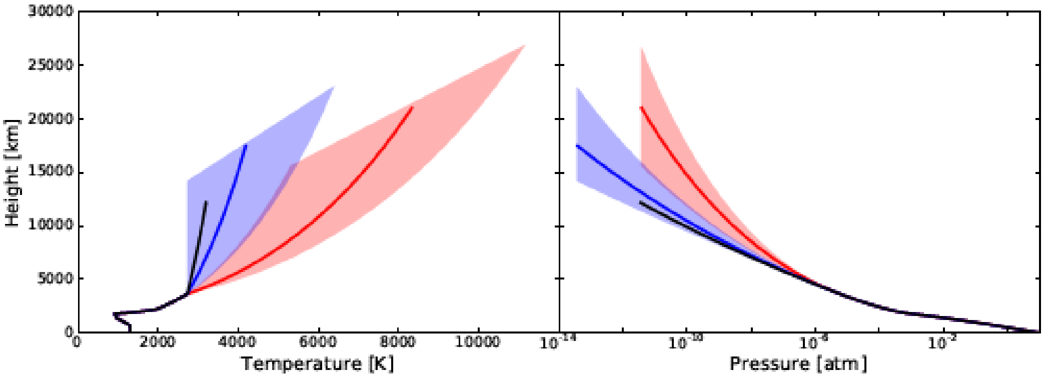

Figure 3.8: Black solid line: $T-p$ profile adopted throughout the fit to the low resolution data set. This is the combination of the temperature profile reported in Sing et al. 2016 for the troposphere and by Wyttenbach et al. 2015 for the thermosphere. Red solid line: best choice to reproduce the high-resolution data set in the case of solar sodium abundance with aerosols at the 0.1 mbar level (HTT). Red background: region where variations in the $T-p$ profile produce models of similar quality to the HTT model ($\Delta\mathrm{BIC}_{\mathrm{HR}} < 5$). The incompatibility between the HTT $T-p$ profile and the profile by Wyttenbach et al. (2015) is explained by the fact that they did not include aerosols in their analysis. Blue solid line and blue shadowed area: the same analysis for an assumed sodium abundance of 50 times the solar value. In this case the enhanced sodium abundance mimicks an aerosol-free atmosphere such as the one assumed by Wyttenbach et al. (2015), thus the $T-p$ profiles are compatible. We did not allow for a negative temperature gradient in the $P < 10^{-6}$ bar region, as poorly physically motivated.

thermospheric temperature (HTT) model transmission spectrum is shown in Fig. 3.7. For this model we find $\Delta\mathrm{BIC}_{\mathrm{HR}} \sim 13$, indicating that it reproduces the HARPS data significantly better than the BF-HST. In Fig. 3.8 we show the $T-p$ profile that best reproduces the HARPS data (red curve and shadowed area), and the comparison with Wyttenbach et al. (2015) (black curve).

Furthermore, the HTT model is also consistent with the HST data ($\Delta\mathrm{BIC}_{\mathrm{HST}} < 1$), indicating that the troposphere is indeed left unchanged by the enhanced thermospheric heating. Finally, we note that our $T-p$ profile is in qualitative agreement with observation (Vidal-Madjar et al. 2013) and models (e.g. Yelle 2004; Koskinen et al. 2013b) of the HD209458b thermosphere, with temperatures of up to 10 000 K. HD209458b is in similar irradiation and gravity conditions to those of HD189733b, and both have expanded upper thermospheres.

The presence of aerosols also introduces a degeneracy between sodium abundance and thermospheric temperature. Intuitively, the more abundant the sodium is, the higher up in the atmosphere its features originate. For an abundance that is high enough, an aerosol-free atmosphere can be mimicked when focusing on the narrow wavelength band probed by high-resolution data. In Fig. 3.6, we show in green a model with the same parameters as the BF-HST, but with 10 times its sodium abundance (10Na). The sodium lines are now generated higher up in the atmosphere, and part of their wings are generated above the aerosol scattering-deck (see Fig. 3.7, green line). As a result, when normalized, the enhanced sodium abundance model is nearly indistinguishable from the aerosol-free model in the χ^2 band (see Fig. 3.6). It also reproduces the HARPS data significantly better than the BF-HST. Models with 50 to 100 times the solar sodium abundance lead to even better matches with HARPS data. The quality of the fit to the HST data set is slightly decreased for such high sodium abundances because the wings of the doublets start to be visible. Overall, the BIC value resulting by the combined analysis of low- and high-resolution data favours the 50Na model.

The degeneracy between thermospheric heating and sodium abundance is further illustrated by constructing a second HTT model, with sodium abundance fixed at 50 times the solar value (HTT 50Na). Indeed, the difference in the global BIC between HTT 50Na and 50Na is not significant ($\Delta\mathrm{BIC}_{\mathrm{HR+HST}} \sim 1.1$). In other words, a strongly (50x) enriched atmosphere would not require an enhanced thermospheric heating to exhibit the observed sodium signature (see also Fig. 3.8). We summarize our results in Table 3.2.

We draw the following conclusions:

1. The low- to medium-resolution data set can be reconciled with the high-resolution data set;

2. The presence of aerosols at the 0.1 mbar level, with which we explain the low- to medium-resolution data set, requires an enhanced thermospheric heating or enhanced sodium abundance in order to reproduce the high-resolution data set;

3. Having assumed solar sodium abundance, Wyttenbach et al. (2015) has underestimated the role of thermospheric heating because they assumed an aerosol-free atmosphere.

Rather than the absolute abundance of sodium, it is its optical depth compared to scattering by aerosols that determines the contrast of its lines in the high-resolution transmission spectrum. This point is distinct but linked to the degeneracy between abundance and reference level first pointed out by Lecavelier Des Etangs et al. (2008a) and generalized by Heng and Kitzmann (2017). A complete analysis aimed at measuring sodium abundance or the precise value of the thermospheric temperature would thus need to fully explore this degeneracy, and is beyond the scope of this paper.

Finally, we note that the residuals between high-resolution data and models are asymmetric (see Fig. 3.6). This could be due to the uncorrected Rossiter-McLaughlin effect (Louden and Wheatley 2015). This effect has to be modelled before any quantitative conclusion can be obtained from the high-resolution data set. However, it does not affect our conclusion that high-resolution observations are sensitive to the set of parameters that complements lower resolution observations when the two techniques are combined.

3.7 Towards the atmosphere of HD189733b as a whole

The framework presented in Pino et al. (2017) – and sections from 3.1 to 3.6 – exploits the capabilities of $^{\pi}\eta$ to model observations across resolutions and across location in the exoplanetary atmosphere. Within this framework we obtained an atmospheric model whose structure is for the first time consistent across tens of scale heights, from the lower to the upper atmosphere. The results indicate that this is not only possible, but that it constitutes a *required* step towards constraining the structure of the upper part of exoplanetary atmospheres. Indeed, previous interpretations were misled by the assumption that observations of the sodium doublet are decoupled by tropospheric aerosols. Conversely, correctly accounting for their presence, we found that the sodium doublet may be probing regions as hot as 10 000 K at 20 000 km ≈ 0.25 R_p ($p < 1$ nbar), thus higher than what reported in the literature.

The temperature that we retrieved may seem very high, but it agrees with models of the thermosphere. The value of the thermospheric temperature depends on the cooling rate induced by infrared emission of different molecular species, such as H_2, CO, H_2O or CH_4 (Yelle 2004; Koskinen et al. 2013b,a, 2007). Within a "stability limit", located between 0.14 AU and 0.16 AU for a Jupiter-like planet orbiting a Sun-like star, the coolants dissociate and the energy absorbed from the star can no longer be balanced by infrared radiation. The absorbed EUV and XUV flux is then available to power escape: the upper atmosphere is expanded and temperatures within it can reach up to 10 000–20 000 K. HD189733b orbits its K2V host at ~ 0.03 AU. "The EUV flux from HD189733 has never been measured and is unknown. However, for a K-type star, it can be estimated to be in the range 1 to 100 times the solar EUV flux (Schmitt and Liefke 2004)"[3]. The irradiation conditions in which HD189733b lies thus suggest that it is well inside the stability limit. Furthermore, Lecavelier Des Etangs et al. (2010) detected an escaping atmosphere for HD189733b, as evinced by strong far ultraviolet absorption in the Ly–α line (see also Bourrier et al. 2013a).

Our analysis made a clear connection between parameters that we can define typically tropospheric (aerosol coverage and composition, sodium abundance) and others that we can define typically thermospheric (thermospheric temperature, and again sodium abundance). Thermospheric temperature, in particular, is a key parameter

---

[3] Within quotes: Lecavelier Des Etangs et al. (2010)

Table 3.2: BIC values computed for the models described in the text, for the HST and HARPS datasets, and their combination.

Model	$\sigma_{\mathrm{h}}(\lambda_0)$	s	P_{c} [mbar]	Thermospheric $T-p$ profile	X_{Na}	$\Delta\mathrm{BIC}_{\mathrm{HR}}$	$\Delta\mathrm{BIC}_{\mathrm{HST}}$	$\Delta\mathrm{BIC}_{\mathrm{HR+HST}}$
BF-HST	8000	-3.17	0.4	Wyttenbach et al. (2015)	10^{-6}	0	0	0
AF	None	None	None	Wyttenbach et al. (2015)	10^{-6}	-45.5	$> 10^4$	$> 10^4$
10Na	8000	-3.17	0.4	Wyttenbach et al. (2015)	10^{-5}	-29.1	+0.5	-28.6
50Na	8000	-3.17	0.4	Wyttenbach et al. (2015)	$5 \cdot 10^{-4}$	-37.7	+2.2	-35.5
100Na	8000	-3.17	0.4	Wyttenbach et al. (2015)	10^{-4}	-37.9	+4.0	-33.9
HTT	8000	-3.17	0.4	Enhanced (red curve, Fig. 3.8)	10^{-6}	-13.3	-0.3	-13.6
HTT 50Na	8000	-3.17	0.4	Enhanced (blue curve, Fig. 3.8)	$5 \cdot 10^{-4}$	-38.9	+2.3	-36.6

in the study of the exosphere. We can conclude that we demonstrated the existence of a *fil rouge* that runs through the whole atmosphere, connecting weather phenomena such as clouds to the particles that escape the gravity of their planet. Improvements on the physics and modelling that we used, which is relatively simple, will hopefully clarify the nature of this link.

3.8 Extending the project

3.8.1 Extension based on HARPS and HARPS-N

The results presented in Wyttenbach et al. (2015), and reinterpreted in Pino et al. (2017), showcased the capability of 4m class, stabilized spectrographs to investigate the aeronomical properties of exoplanets, such as the temperature profile of the thermosphere and its dynamics (winds). This prompted us to extend the sample of planets observed with HARPS(-N). We successfully collected observations for 23 targets with the observational programs HEARTS (Hot Exoplanetary Atmospheres Resolved with Transit Spectroscopy, based at HARPS in the southern hemisphere. PI: D. Ehrenreich) and SPADES (Sensing Planetary Atmospheres with Differential Echelle Spectroscopy, based at HARPS-N in the northern hemisphere. PI: D. Ehrenreich), complemented by HARPS-N observations of a few outstanding targets led by the University of Padova (HD209458b, three transits, PI: Nascimbeni; WASP-103b, three transits, PI: Nascimbeni; WASP-33b, two transits, PI: Nascimbeni). By exploring sodium absorption in several hot Jupiters, warm Neptunes and mini-Neptunes, the programs aim to:

1. Bridge UV observations of the exosphere and IR observations of the troposphere, by studying the thermospheric properties of the planet through the sodium doublet;

2. Infer the role of ionization and condensation by studying the temperature gradient, dynamics and chemical composition of a comprehensive sample of planets. Indeed, the wavelength range probed by HARPS(-N) (380–690 nm) includes absorption by atomic species such as H, Na, Ca, Mg, Sc, Fe, etc., and molecular species such as H_2O, TiO, VO;

3. Shed light on the role of evaporation in evolution of hot gaseous giants, for the first time in the visible (for now this kind of studies studies have been focused on UV). This question can be addressed by detecting hints of evaporation in the sodium doublet, and by measuring the thermospheric temperature;

4. Investigate the nature of the lack of intermediate mass planets (indicatively between Neptune and Saturn) with periods shorter than ~ 10 days, thus heavily irradiated. Our observations will clarify if there is a link with evaporation phenomena.

First results: WASP-49b The first results have been published in Wyttenbach et al. (2017), for the hot Saturn WASP-49b. This planet lies at the verge of the desert of intermediate mass planets. It thus makes an ideal test case to understand if evaporation phenomena actually play a role in this region. Notwithstanding the low signal-to-noise ratio (the host star is relatively dim), an absorption signature was recovered in each line of the sodium doublet (4σ and 3σ in the D_2 and D_1 lines respectively). Assuming that this signal is of planetary origin, absorption in the core of the lines must originate as high as 80 planetary scale heights above the white light radius of the planet. I contributed to this paper by modelling the absorption feature. Assuming an isothermal, aerosol-free, solar-abundance atmosphere, I obtained that the temperature required to explain this absorption must be of $\sim 3\,000$ K. This is well above the equilibrium temperature of the planet, $T_{\rm eq} \sim 1400$ K, thus firmly placing the sodium absorption in the thermosphere of the planet.

Lendl et al. (2016) found hints of the presence of condensates in the atmosphere of this planet at $p_{\rm c} \lesssim 1$ mbar. In light of the results presented in Pino et al. (2017), the assumption that these have no impact on the sodium feature is questionable. I thus performed a follow-up analysis, sticking to the isothermal assumption adopted in Wyttenbach et al. (2017) but adding the presence of aerosols. I produced a grid of isothermal models with temperatures varying between 1400 K and 4000 K, and condensates at pressures spanning 0.1 bar and 1 nbar, and computed the BIC. I present the results in Fig. 3.9. On the x-axis, the temperature of the atmosphere increases on the right; on the y-axis, the aerosol-deck top pressure decreases upwards (clouds are found higher in the atmosphere). For $p_{\rm c}$ down to ~ 1 mbar no variation is observed in the BIC, indicating that aerosols up to this level do not significantly alter the absorption. The orange dashed line shows the lower limit on $p_{\rm c}$ found by Lendl et al. (2016). Aerosols at this level do not induce a statistical deviation from the aerosol-free model, and the temperature determination is accurate also for aerosols at a higher altitude. I conclude that the assumption of an aerosol-free atmosphere adopted by Wyttenbach et al. (2017) is consistent with the findings by Lendl et al. (2016). Indeed, sodium in this planet seems to be present higher up in the atmosphere compared to HD189733b. However, the wavelength range covered by the observations by Lendl et al. (2016) (738–1026 nm) is not sensitive to a population of small scatterers inducing Rayleigh scattering at short wavelengths. As in HD189733b, these may cause dominant absorption which would possibly impact our conclusions on the thermospheric temperature.

3.8.2 Extension based on HST

The curious case of WASP-43b In spite of the challenges posed by reduction and interpretation of ground-based, high-resolution data, some clear-cut results have already emerged (Wyttenbach et al. 2015, 2017; Pino et al. 2017). However, the complexity of the data reduction technique, whose accuracy is limited by the telluric correction, casts doubts on other possible detections. The most outstanding example is certainly the case of WASP-43b, a very irradiated hot Jupiter with a 2.03 $M_{\rm J}$ mass, a 1.04 $R_{\rm J}$ radius orbiting a K7V type star (Hellier et al. 2011; Gillon et al. 2012). This planet has been observed in both the HEARTS and SPADES program during five nights. Three were good, and were used to build a transmission spectrum in the region of the Na I doublet (see Fig. 3.10).

The analysis showed a resolved sodium absorption of 1.5% at 11σ over two 2 Å wide bands centred in the single lines. This level of absorption places sodium at 200 scale heights above the surface of the planet, to compare with $\lesssim 10$ for HD189733b[4]. It is

---

[4] For WASP-43b the value is computed assuming $T = 10\,000$ K, required to explain the preliminary high-resolution transmission spectrum. For HD189733b we used the temperature at the base of the troposphere, $T \sim 1\,200$ K. Since temperature raises in the thermosphere, 10 is an upper limit to the number of scale heights spanned by the sodium feature.

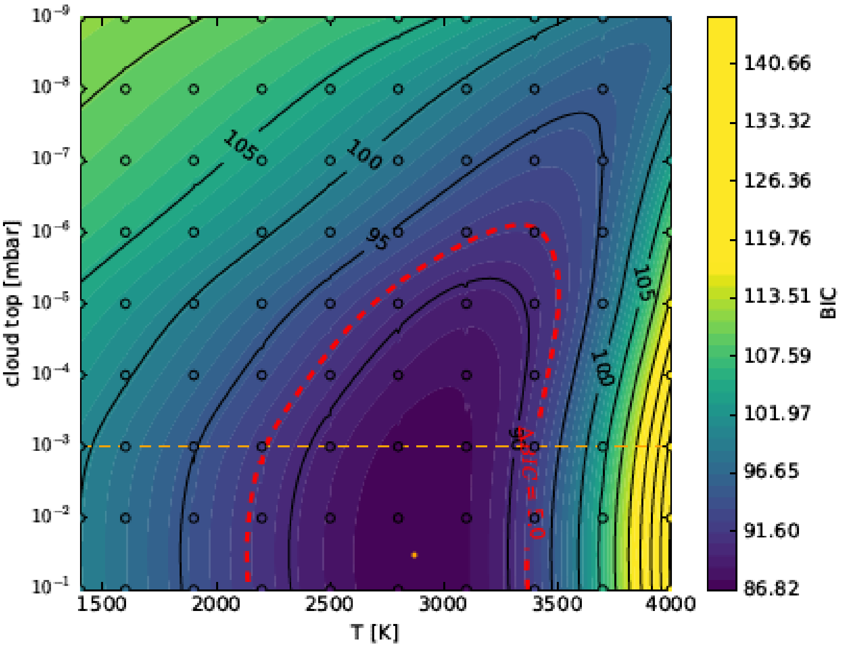

Figure 3.9: The contour plot represents the results of a fit to the data set published by Wyttenbach et al. (2017), where we varied atmospheric temperature (assumed isothermal) and aerosol coverage. A red dashed curve indicates the region of best confidence (identified as models that deviate by less then $\Delta\mathrm{BIC} < 5$ from the best fit, represented by a golden dot). The horizontal dashed orange line is the upper limit in pressure (lower limit in height) of the aerosol deck found by Lendl et al. (2016). The parameter space above their limit is broadly consistent with the high-resolution data and the thermospheric temperature range identified by Wyttenbach et al. (2017).

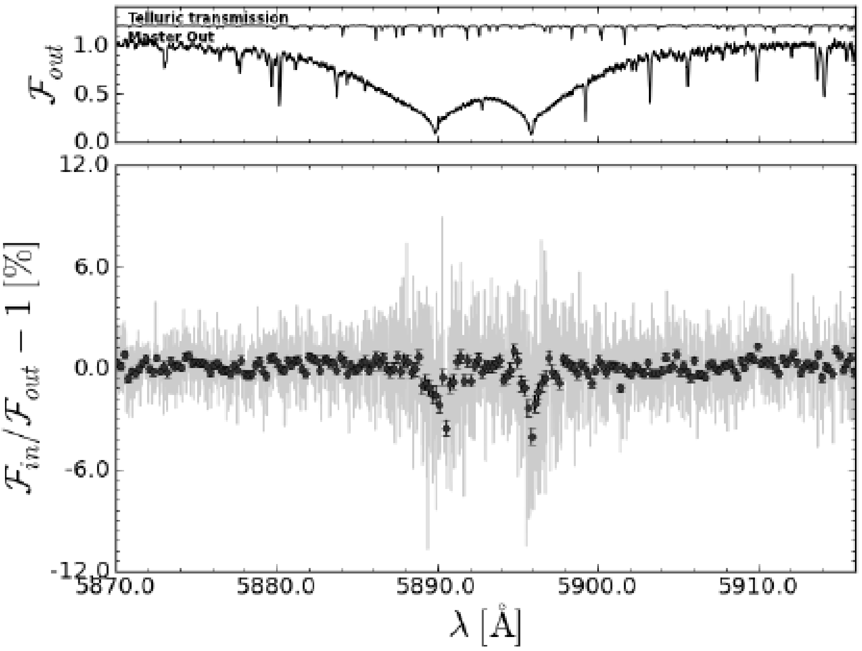

Figure 3.10: Preliminary ground-based, high-resolution transmission spectrum of WASP-43b. In gray, data at full resolution are shown. In black, a binned version is showed for clarity. Courtesy of A. Wyttenbach.

however hard to make a fair comparison in terms of scale heights, since both planets have non-isothermal atmospheres, especially when looking at their upper part. I thus compared the height up to which sodium absorbs with the Roche lobe radius (Eggleton 1983), defined by

$$r_{\mathrm{Roche}} = \frac{0.49 q^{\frac{2}{3}}}{0.6 q^{\frac{2}{3}} + \ln\left(1 + q^{\frac{1}{3}}\right)} \ . \tag{3.17}$$

Pino et al. (2017) demonstrated that, in HD189733b, absorption happens up to 22 000 km = 0.084 r_{Roche}. On the other hand, a simple isothermal model at T = 10 000 K, consistent with the ground-based data, shows that in WASP-43b sodium is optically thick up to 30 000 km $\sim$ 0.2 r_{Roche}. It is well established that sodium in HD189733b is probing the lower part of the thermosphere, where evaporation starts. This induces me to think that in WASP-43b we may be observing sodium that is escaping from the atmosphere.

Interpretation of such a strong sodium absorption is challenging. Indeed, alkali atoms this high are expected to be promptly ionized by stellar irradiation. However, if their density is large enough, a shielding effect can be expected, such that part of the atoms can be maintained in the neutral state and thus produce the observed feature. Such a density can only be sustained if neutral Na is actively being pumped in the exosphere. Lofting of heavy species can only be understood in a scenario of extreme blow-off in the atmosphere of the exoplanet. In fact, as discussed in chapter 2, several UV observations have already revealed the presence of hydrogen and heavier elements (carbon, oxygen, magnesium) in the upper parts of the atmosphere of a handful of planets, such as the Neptune-mass planet GJ436b (Ehrenreich et al. 2015) and the hot Jupiters HD189733b (Bourrier et al. 2013a; Lecavelier Des Etangs et al. 2010) and HD209458b (Vidal-Madjar et al. 2003, 2004, 2013). The last case is particularly well studied, and made possible to identify the physical mechanism responsible for the presence of heavy elements in its upper atmosphere. Hydrogen is a volatile element and, due to irradiation, it leaves the atmosphere of the planet at a high rate (as revealed by its Lyman–α signature, Vidal-Madjar et al. 2003). This hydrodynamical flow drags upwards the heavy elements, that are then revealed through their spectral signature.

Still, such a phenomenon was never observed for sodium. We thus performed a more careful analysis. Huge Signal-to-Noise Ratio (SNR) variations due to the variability of the Earth atmospheric conditions are present in the ground-based data. An accurate scrutiny showed that the signal is strongest in the nights with lowest SNR. Even if the signal is very strong, and thus possibly due to the exoplanetary atmosphere, this behaviour indicates that some residual telluric contamination might not have been removed. Indeed, for this planet, the telluric contamination is expected to be very important because of the low flux due to faintness of the host star WASP-43b (V = 12.4), and to the further drop in flux in correspondence of its sodium lines, which are particularly deep: in other words, the result is strongly hampered by telluric lines that might not have been completely removed, and present conclusions may not completely reliable yet. Additional observations with HARPS/HARPS-N would hardly settle the matter, and no current other ground-based facility would be able to deliver spectra of a comparable quality. A space-based confirmation of this signal is thus needed. For this reason, I asked and obtained 4 HST orbits to observe one transit with STIS, using the $R \sim 5\,000$ grism G750M centred in $\lambda = 6094$ Å (GO14782, PI: Pino). A confirmation of this extreme sodium absorption would open an exciting path to study exospheres without the need of a UV telescope, crucial in the post-HST era, and for much fainter targets (stellar fluxes in the UV are much lower than in the optical).

Preliminary results from WASP-43b STIS@HST spectra Observations have been carried out on 2017–04–13. The data has not been fully analyzed yet, but I performed a preliminary reduction that I present in the following. The observational strategy follows previous similar, successful proposals (GO14461, PI: D. Ehrenreich; GO12473, GO11572, PI: D. Sing among others). I adopted exposure times of $\sim$ 270 sec. With similar exposure times, Nikolov et al. (2014) demonstrated that dedicated cosmic ray correction techniques need to be developed. It is still possible to use the *sx1* 1D spectra extracted by the CALSTIS pipeline to have a preliminary look at the data. The *sx1* spectra are obtained by summing the sub-exposures within one exposure, that for me coincided with one orbit (excluded a one second exposure taken before the science exposure, aimed at minimizing systematics; Nikolov et al. 2014). Thus, there are four *sx1* spectra. The chosen observational strategy places the transit in the third orbit. As a first check, I computed the white light flux in each orbit. This was done by summing on every wavelength within each exposure. I then divided the flux in each orbit by the average of the fluxes in orbits 1, 2 and 4 (out-of-transit). I obtained the black data points in Fig. 3.11. A horizontal black dashed line represents the expected transit depth (Hoyer et al. 2016), which is compatible within 2σ.

As a further test I selected a region of 12 Å around the sodium absorption, and repeated the white light curve calculations (producing a "sodium light curve"). The results are shown in red in the same figure. The horizontal red dashed line is the expected value when focusing in this band, obtained by summing the white light absorption and the preliminary excess measured from the high-resolution data. At the STIS G750M resolving power, the excess absorption amounts to 0.5%. The second orbit of the light curve seems anomalously low compared to the first and the last orbit, while in the last orbit I registered a higher flux consistent with the first orbit. This behaviour does not correspond to what is observed in the white light curve. I thus produced a second sodium light curve by normalizing only by orbits 1 and 4, obtaining the results in the right panel of Fig. 3.11.

With this simple analysis, I found a hint of extra absorption in the sodium band consistent with the expectations from previous ground-based observations. However, the anomalous behaviour of the sodium light curve during the second orbit requires a much deeper investigation, with time resolved information and accurate correction of the systematics (such as the breathing effect).

3.8.3 The ESPRESSO and CARMENES opportunities

Thermospheric temperature is a key parameter to constrain predictions of evaporation rates. By simultaneously modeling lower and upper atmosphere, in Pino et al. (2017) we were able to constrain it. Unfortunately, we also found a degeneracy between thermospheric heating and sodium abundance. However, the degeneracy may be lifted by improving on the precision of HARPS(-N). Indeed, as shown in Fig. 3.6, the detailed effect of variations of thermospheric temperature and abundance of sodium on its transmission spectrum are different. A temperature increase in the thermosphere increases the scale height of the outermost layers, enhancing absorption preferentially in the core of the sodium lines. Conversely, a higher abundance does not increase the contrast of the feature, but rather makes it "pop out" from the cloud deck. In other words, the contrast is increased with respect to a lower abundance model in the presence of aerosols, but in their absence the two models differ only by an offset (Fig. 3.7). *A precise measurement of the core of the alkali lines, interpreted in a framework that combines lower and upper atmosphere of exoplanets, could allow to break this degeneracy and better constrain measure thermospheric temperatures.*

Furthermore, the technique presented in this chapter and Pino et al. (2017) can be extended to include the potassium doublet. The potassium doublet has a similar cross-section to the sodium doublet, and should be easily accessible when observed at high-resolution. Condensation of potassium is expected at similar temperatures as sodium (Lodders 1999; Burrows et al. 2001), and its ionization potential is lower. Thus, the potassium feature should be weaker than the sodium feature.

Nonetheless, potassium has been detected in a few cases (e.g. Sing et al. 2016; Sedaghati et al. 2016). In the hot Jupiter WASP-31b, Sing et al. (2015) found that $Na/K < 1$. This unique case is particularly puzzling, as it implies one of the two following possibilities:

1. That the temperature of the lower atmosphere of the night side of the planet is comprised between 800 K and 1 000 K, the only range where sodium is expected to condense while potassium is not;
2. That there is a primordial lack of sodium (or excess of potassium), that need to be interpreted in terms of formation or evolution of the planetary system.

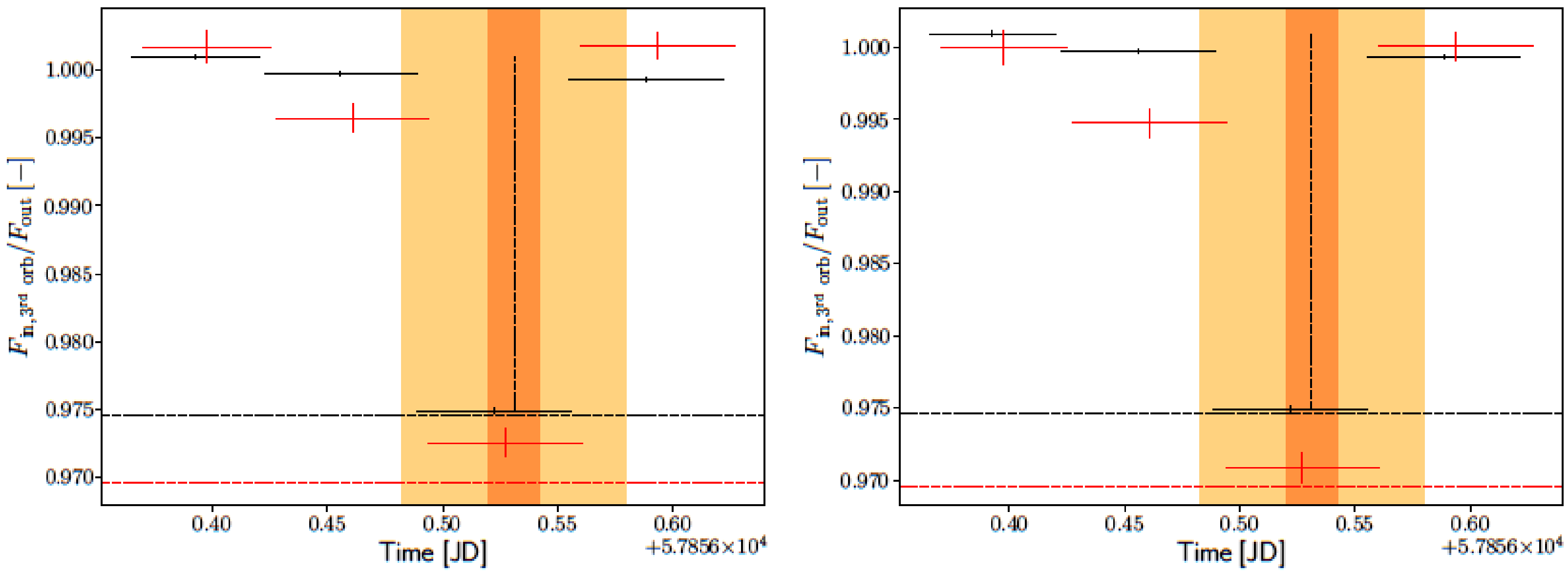

Figure 3.11: Preliminary white and “sodium” light curves. Black points correspond to flux integrated over the whole G750M band-pass, and are consistent within 2σ with previous determinations of the radius of the planet (Hoyer et al. 2016). Red points correspond to flux integrated within a 12 Å region centred in the sodium doublet. Left and right panel differ for the normalization of the sodium light curve. In the left panel, we used orbits 1,2 and 4 (same as in white light), while in the right panel orbit 2 was excluded because of its seemingly inconsistent value with orbits 1 and 4. Further analysis is required to confirm an extra absorption in this region and to shed light on the nature of the tentative extra absorption found in orbit 2.

The conclusions by Sing et al. (2015) indicate that the joint study of alkali atoms may constrain the conditions in the lower atmosphere, and/or the formation history of planetary systems. However, higher resolution observations are warranted to confirm and compare more in detail the absorption features of the two alkali atoms. The CARMENES spectrograph, and the next generation ESPRESSO spectrograph, have a similar resolving power as HARPS (CARMENES: $R \sim 94\,600$ in the VIS channel; ESPRESSO: $R \sim 134\,000$). ESPRESSO will be mounted at VLT, with a gain in flux of 6.25 times, and thus a signal-to-noise increase by 2.5. Furthermore, the wavelength coverage of both instruments includes both the sodium and the potassium doublet. By observing both doublets at high-resolution, they will provide the means to carry out a quantitative comparison of the shape of their spectral features. *CARMENES and ESPRESSO constitute ideal facilities to improve our knowledge of the thermosphere, and reveal the importance of processes such as condensation and ionization of the alkali atoms. They will provide the natural extension to the surveys of the sodium doublet which we are currently carrying out.*

3.9 Conclusions

I developed a method to simultaneously compare theoretical models with high-resolution ($R \sim 10^5$), double-differential transmission spectra and low- to medium-resolution ($R \sim 10^2 - 10^3$) transmission spectra. It relies on a dedicated 1D, line-by-line, high resolution ($R \sim 10^6$) radiative transfer code, called ${}^{\pi}\eta$. Within this framework, I:

- Built model atmospheres of the hot Jupiter HD189733b, consistent with HST STIS, ACS and WFC3, and HARPS transmission spectra. These models are consistent with observations on an unprecedented range of pressures (tens of scale heights), from the troposphere to the thermosphere of the exoplanet. They show that the apparent discrepancy between flattened spectra observed at low-resolution and peaked features observed at high-resolution can be solved. This was obtained by adjusting a model that reproduces the low-resolution data to the high-resolution data, adopting a best set of parameters (sodium abundance, thermospheric $T - p$ profile) that affects the cores of the sodium lines while leaving the troposphere mainly unaffected;

- Showed that ground-based, high-resolution observations are sensitive to the presence of aerosols. Neglecting aerosols has led to an underestimation of the thermospheric heating in this planet by Wyttenbach et al. (2015). For a solar abundance of sodium, the same assumed by Wyttenbach et al. (2015), we obtain thermospheric temperatures of up to $\sim$ 10 000 K, in qualitative agreement with models and observations of the similar hot Jupiter HD209458b;

- Identified a degeneracy between sodium abundance and thermospheric heating that affects double-differential techniques in the presence of scattering by aerosols, linked to, but distinct, from the well known degeneracy between abundance and reference level (Lecavelier Des Etangs et al. 2008a; Heng and Kitzmann 2017). Retrievals of the absolute sodium abundance must take into account the presence of this degeneracy;

- Showed that the sodium feature observed with the HARPS spectrograph in the irradiated Saturn-mass planet WASP-49b is generated at a temperature higher than the equilibrium temperature, thus in the thermosphere. Sodium is present up to 80 scale heights above the white light radius of this planet, much higher compared to the $\sim$ 10 scale heights signature found in HD189733b. Aerosols where found in the atmosphere of this planet (Lendl et al. 2016), but the cores of the sodium lines are unaffected by them at the achieved precision;
- An even more extreme case may be represented by WASP-43b. A preliminary analysis of ground-based data, complicated by the faintness of the star, revealed that sodium may be present up to 200 scale heights above the white light radius of this planet. This corresponds to 0.2 r_{Roche}. At these heights, sodium may be leaving the atmosphere of the planet. A preliminary reduction of a dedicated HST follow up strengthens the ground-based detection and presents a hint of pre-transit absorption in the sodium. Further work is necessary to confirm and interpret the results.

In synthesis, alkali atoms are effective probes of the upper atmosphere, from the thermosphere possibly to the base of the exosphere. High-resolution, ground-based observations are sensitive to thermospheric heating and to the alkali abundances when properly interpreted and combined with lower resolution observations. My analysis opens new perspectives for the optimal exploitation of future facilities such as e.g. the JWST on the one hand, CARMENES, ESPRESSO and the E-ELTs on the other hand.

Appendix 1

What is measured: The procedure followed by Wyttenbach et al. (2015, 2017) to obtain $\tilde{\mathfrak{R}}$ is the following:

1. All out-of-transit and in-transit spectra are normalized to a reference band:
$$\tilde{f}_{\mathrm{in/out}}(\lambda) = \frac{f_{\mathrm{in/out}}(\lambda)}{\left\langle f_{\mathrm{in/out}}(\lambda)\right\rangle_{\lambda_{\mathrm{ref}}}} \tag{3.18}$$
2. A master out $\tilde{F}_{\mathrm{out}}$ is built as the sum of the out-of-transit spectra and normalized.
3. The spectrum ratio is obtained as the sum of all the self-normalized in-transit spectra divided by the master out after having shifted them in the planetary rest frame:
$$\tilde{\mathfrak{R}}(\lambda) = \sum_{\mathrm{transit}} \left.\frac{\tilde{f}_{\mathrm{in}}(\lambda, t)}{\tilde{F}_{\mathrm{out}}(\lambda)}\right|_{P} . \tag{3.19}$$

What is simulated: The quantity $\delta(\lambda)$ is the transit depth, i.e. the absorption due to the planet in units of stellar flux. This is then related to $f_{\mathrm{in/out}}$ by:

$$\delta(\lambda) = \frac{f_{\mathrm{out}} - f_{\mathrm{in}}}{f_{\mathrm{out}}} = 1 - \frac{f_{\mathrm{in}}}{f_{\mathrm{out}}} , \tag{3.20}$$

and thus:

$$\frac{f_{\mathrm{in}}}{f_{\mathrm{out}}} = 1 - \delta(\lambda) \ . \tag{3.21}$$

Furthermore, our tests in section 3.4 legitimate us to write:

$$\frac{\langle f_{\mathrm{in}} \rangle_{\lambda_{\mathrm{ref}}}}{\langle f_{\mathrm{out}} \rangle_{\lambda_{\mathrm{ref}}}} \approx \left\langle \frac{f_{\mathrm{in}}}{f_{\mathrm{out}}} \right\rangle_{\lambda_{\mathrm{ref}}} = 1 - \langle \delta(\lambda) \rangle_{\lambda_{\mathrm{ref}}} \ . \tag{3.22}$$

If we assume that the only time varying signal is due to the transit of the atmosphere of the planet, when we divide 3.21 and 3.22 we obtain Eq. (3.14).

Appendix 2

The so called "Million- to Billion-line radiative transfer challenge" (Grimm and Heng 2015) is a well known one. The exact solution to the radiative transfer equation would require to model precisely each single molecular absorption line ("line-by-line" approach). For several molecules (e.g. water, methane) billions of lines contribute to the opacity at high temperatures ($> 1\,000$ K). To add complexity to the problem, multiple line lists are available. The impact of the choice of a line list over the others has never been fully quantified. We review here the state of the art knowledge for water.

The ExoMol project (Tennyson and Yurchenko 2012) is the most up-to-date effort to provide line lists suitable for hot environments. In some cases this line list clearly outperforms previous efforts (such as for methane HITRAN vs ExoMol, Lavie et al. 2017). For water, however, there is general agreement that the line lists by Barber et al. (2006) and Partridge and Schwenke (1997) are solid and complete, and indeed the BT2 line list by Barber et al. (2006) has been adopted by ExoMol (but a new line list is being developed inside the ExoMol project, Polyansky et al., in prep). The BT2 line list also constitutes the basis for the HITEMP water line list adopted in this paper. The HITEMP line list contains 25% of the lines of the BT2 line list. The lines are selected in order to reduce the size of the line list while avoiding opacity losses at high-temperatures. This line list is adopted by several groups to model exoplanetary atmospheres (e.g. Benneke and Seager 2012; Mollière et al. 2015; Birkby et al. 2017; Mollière et al. 2017; MacDonald and Madhusudhan 2017; Gandhi and Madhusudhan 2017). Furthermore, Kilpatrick et al. (2017) provides a thorough analysis of the WFC3 spectrum of WASP-63b using forward modeling and retrieval methods based on both line lists. The authors conclude that there is "general agreement amongst all the results", suggesting that in this case differences due to the choice of the line list are minor. Brogi et al. (2017) pointed out that the HITEMP and the Freedman et al. (2014) (based on BT2) line lists may differ when dealing with high-resolution data; however, the culprit is not uniquely identified in their analysis (shift in line positions, line intensity, completeness, different treatment of broadening are all possible candidates). It is thus not clear at which extent these differences would propagate to the comparison with low-resolution data. A quantitative assessment of the impact of different choices for the opacity tables is certainly warranted; in absence (to our knowledge) of such an assessment we consider the HITEMP line list as state-of-the art to simulate WFC3 data.

Chapter 4

Observing the lower atmosphere at high-resolution

Pino et al. (2017) demonstrated that a correct interpretation of thermospheric signatures requires knowledge of the conditions in the troposphere, specifically on the presence of atmospheric aerosols. Aerosols have cross sections that vary slowly with wavelength (for large particles, constant cross section). Thus, they induce features that span thousands of Angstroms on the transmission spectrum. To detect them, the best strategy is thus acquiring spectra over a broad wavelength range (Sing et al. 2016).

This can be problematic from the ground. As discussed in chapter 2, Earth atmosphere induces chromatic signals that artificially alter the measured transit depth between two regions distant in wavelength. This effect can be corrected by using a telluric reference star. However, this strategy is not applicable with current high-resolution spectrographs. These chromatic effects are important already over a few hundreds of Angstroms, and need to be corrected prior to studying atmospheric features over such a range. This is usually done by normalizing the spectra with a polynomial (Snellen et al. 2010; Allart et al. 2017). This technique preserves the high-frequency signal due e.g. to molecular absorption lines, and is sufficient to infer the presence of gaseous absorbers. However, it removes low-frequency signals such as those due to aerosols.

In this chapter I present a novel technique to infer the presence of aerosols based on high-resolution transmission spectra. This technique complements an already existing alternative based on the chromatic Rossiter–McLaughlin effect (see sec. 4.1). Combined, the techniques can be applied to a wide range of cases (with the possible limitation of signal-to-noise ratio). The importance of obtaining information on the presence of aerosols directly from high-resolution, ground-based observations is discussed in section 4.2. The technique itself is presented in section 4.3, which will be part of a paper in preparation.

Even if the study is not published yet, it is due to mention that the work presented in this chapter has greatly benefit from discussions and collaborations with a number of persons. I thus wish to thank (in alphabetical order) R. Allart, M. Brogi, D. Ehrenreich, C. Lovis, M. Malik, V. Nascimbeni, F. Pepe and G. Piotto for their valuable contributions.

4.1 Chromatic Rossiter–McLaughlin effect

Snellen (2004) first proposed a technique aimed at measuring atmospheric signatures with high-resolution observations. The technique aims at circumventing the need to compare in- and out-of-transit spectra of traditional transmission spectroscopy. Indeed, by necessity, these spectra span a wide range of airmasses, which complicates the task of removing chromatic telluric effects from the spectra.

The method relies on the Rossiter–McLaughlin (RM) effect (Holt 1893; Rossiter 1924; McLaughlin 1924). While a planet transits in front of the host star, it occults different parts of its surface. Owing to the rotation of the star, the occulted surface is first blue-shifted and then red-shifted (it would be the opposite for a planet with an anti-aligned orbit). Radial velocities thus present a "wobble", whose amplitude depends on the size of the planet compared to the host star. In the presence of an atmosphere, the size of the planet depends on wavelength, thus the amplitude of the effect is maximized in correspondence of absorption features.

This technique only relies on the shift of stellar lines, that does not depend on the level of the continuum. Thus, the normalization required to remove the effects of Earth atmosphere (see chapter 2) does not remove the possible atmospheric signal. In other words, this technique has the great advantage that it can access features of the planetary continuum. Indeed, Di Gloria et al. (2015) was able to recover at 2.5σ the Rayleigh slope due to the presence of hazes in HD189733b based on HARPS data (the same analysed by Wyttenbach et al. 2015). As shown in Fig. 4.1, the technique gives results that are consistent with the well-established space-born measurement of the same feature (Pont et al. 2008; Lecavelier Des Etangs et al. 2008a; Pont et al. 2013).

The applicability of the chromatic RM mainly depends on (1) stellar rotation (2) wavelength range. Fast rotators have larger amplitude of the RM effect. However, if rotation is too fast stellar lines are broadened at the extent that their shift cannot be measured (Dreizler et al. 2009). This is the case, for example, for WASP-33, an A5 star hosting a hot Jupiter that we observed with the HARPS-N spectrograph. Furthermore, there need to be strong stellar lines in the region we are interested to explore. For instance, this complicates (or even excludes) the analysis of some relevant molecular bands, such as water, which is usually dissociated in stars.

4.2 Stellar and planetary variability

As discussed in chapter 2, currently available observations are mainly sensitive to a single part of the atmosphere. For this reason, to study the atmosphere as whole it is necessary to combine observations taken at different times and with different configurations (Sing et al. 2016; Pino et al. 2017). However, combination of observations taken at different times relies on the assumption that the transmission spectrum is consistent over time. Unfortunately, there are at least two astrophysical effects that may invalidate this assumption: variability in the star and variability in the planet. I briefly discuss available evidence for these phenomena and current mitigation strategies.

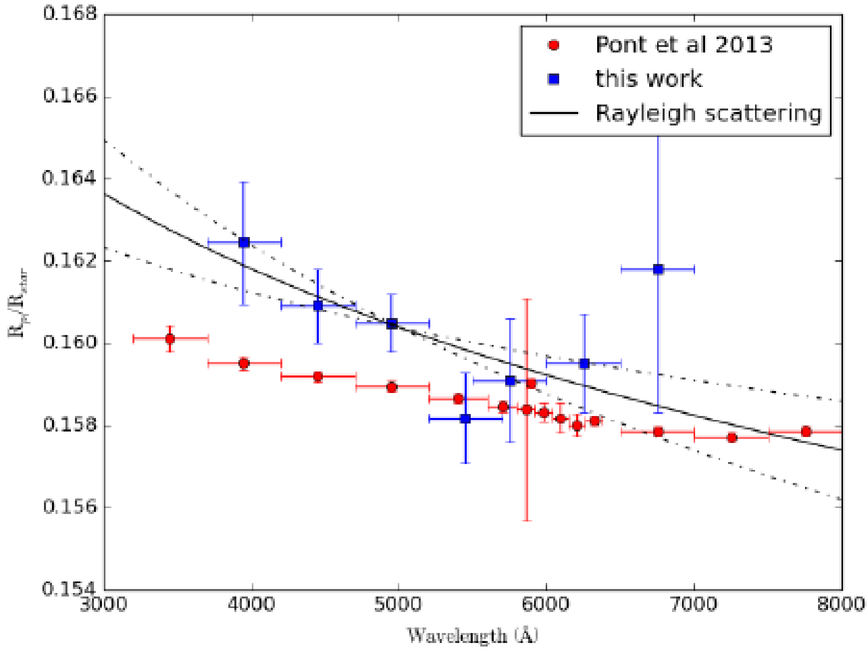

Figure 4.1: Figure from Di Gloria et al. (2015). Comparison between planet-to-star radius ratio for measurements by Di Gloria et al. (2015) and Pont et al. (2013). Error bars are at 1σ. The solid and dashed lines correspond to the best fit and 1σ confidence interval on the slope determined by a fit to the HARPS data. The temperature reconstructed from the slope is compatible with the equilibrium temperature of the planet. The HARPS and ACS reconstructed optical slopes agree within 1σ.

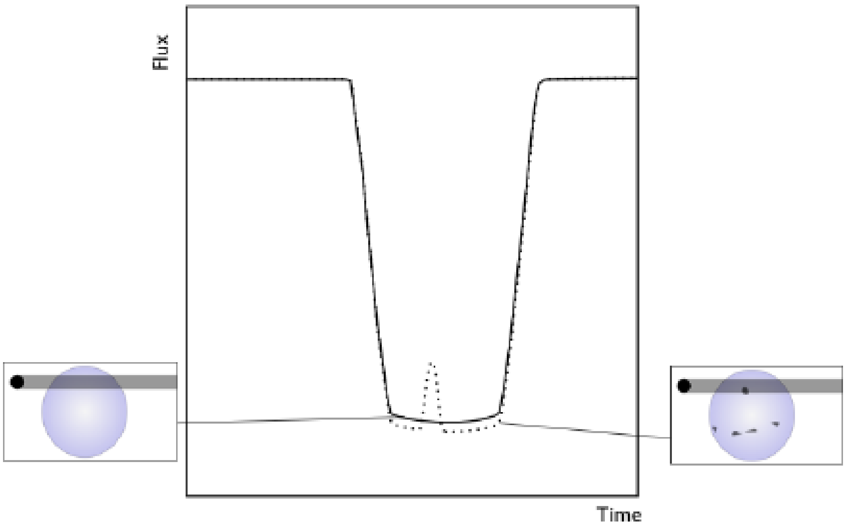

Figure 4.2: Figure from Pont et al. (2013). Occulted and unocculted stellar spots have a different effect on the light curve of the planet. Unocculted spots lower the brightness of the star, thus making the transit signal deeper. In other words, they “add up” to the planetary transit. When a star spot is occulted, on the opposite, stellar brightness is increased. The star spot crossing appears as a bump in the transit light curve. The effect is stronger in the optical because the flux contrast between stellar surface and spots is higher (not shown).

4.2.1 Stellar activity

Stellar activity manifests in different ways. However, for transmission spectroscopy, the main concern is the presence of stellar spots and plages on the surface of the star. These are regions of the stellar surface that are respectively cooler and hotter than the surface of the star. They affect the measurement of the transmission spectrum in two ways:

1. They cause luminosity variations in the star. They thus affect the transit depth, which can then be offset among observations taken at different epochs (see Fig. 4.2).
2. They can mimic the presence of a slope in the optical part of the transmission spectrum. This is the result of the chromatic dependence of their luminosity.

The importance of these effects is evident in the case of the active star HD189733 and its companion (Pont et al. 2007, 2008; Sing et al. 2011; Pont et al. 2013; Oshagh et al. 2014; McCullough et al. 2014; Sing et al. 2016). Indeed, dimming of spots in the visible is here at the 1–2% level, similar to the transit depth of the planet. Using an extensive photometric monitoring, Pont et al. (2013) was able to estimate the effect of both occulted and unocculted stellar spots on the transmission spectrum, and thus correct for their effect. The result is a low-resolution, optical to near-infrared transmission spectrum, compatible with an aerosol rich atmosphere (see chapter 3). With their analysis, Pont et al. (2013) demonstrated that stellar activity is not a showstopper for combining transmission spectra acquired at different epochs. Still, their correction would have been impossible without more than five years of nearly continuous photmetric monitoring. Furthermore, the quality of the monitoring is important as well. For example, the quality of the photometric season coinciding with STIS observations was poorer. By applying the correction obtained from photometry to the STIS data, Pont et al. (2013) observes a large discrepancy with the partially overlapped ACS transmission spectrum. In the absence of other evidence for planetary "weather" (see next paragraph) the authors chose to calibrate the STIS transmission spectrum on the ACS transmission spectrum, but this approach is not assumption free. Furthermore, McCullough et al. (2014) finds that the presence of persistent, unocculted polar spots is able to explain the optical slope with an aerosol-free model (this possibility is mentioned also by Pont et al. 2013, who regard it as less likely than the aerosols explanation). Finally, an uneven latitudinal distribution of stellar spots would undermine the treatment to correct the effect of stellar spots in the infrared, biasing the connection between the optical and the infrared part of the spectrum (Pont et al. 2013).

Note that while these effects are important and add to the uncertainty, there is still significant evidence that the slope in the optical transmission spectrum is in many cases due to the presence of aerosols. Sing et al. (2016) analysed a set of hot Jupiter hosted by stars of various kinds and different activity levels. No correlation was found between activity level and the presence of the optical slope. Furthermore, multi-epoch STIS observations of various targets showed consistency among each other. Finally, they observed that the temperature determined from the Rayleigh slope (Lecavelier Des Etangs et al. 2008a) is consistent with the equilibrium temperature of the planet, which would require fine tuning of the stellar activity to be reproduced. Still, the aforementioned analyses confirm that the connection between optical and infrared is non-trivial, while fundamental to discriminate aerosol-free and aerosol-rich atmospheres.

4.2.2 Planetary weather

Solar System objects exhibit a wide range of atmospheric phenomena on different spatial and time scales[1]. Variability has been predicted (Morley et al. 2014) and confidently detected also in extrasolar objects, such as brown dwarfs (Artigau et al. 2009; Radigan et al. 2012). There is thus no a priori reason to expect that exoplanetary atmospheres do not show the same kind of variability. Indeed, theory predicts the presence of large-scale weather in the atmosphere of hot Jupiters (Rauscher et al. 2008; Showman et al. 2009; Webber et al. 2015; Fromang et al. 2016). However, measurements of such variability are challenging because of the high precision required ($\sim 1\%$ in the infrared) and because a large temporal baseline is required. Indeed, *Spitzer* observations on HD189733b only resulted in an upper limit of 2.7% in the variation of its eclipse depth.

Still, proof of variability was already found in a few exoplanets. On the UV side of the spectrum, Lecavelier des Etangs et al. (2012) found definitive evidence of temporal variations in the Ly–α absorption of HD189733b. In a different regime, variability was detected in the eclipse depth of the super earth 55 Cnc e (Demory et al. 2016). Recently, Armstrong et al. (2016) observed periodic variations ($P \sim 100$ days) in the peak offset of the reflected light phase curve of the hot Jupiter HAT-P-7, observed by Kepler for approximately 4 years. A variable cloud coverage of the day side of

---

[1] A quick look at the beautiful NASA website dedicated to Cassini and Huygens should suffice to convince the reader: `https://saturn.jpl.nasa.gov`.

this planet would imply variations in its albedo, which would result in the observed shift of the peak of the phase curve. There is broad evidence (both from theory and observations) that hot Jupiters host superrotating equatorial jets, due to the large day–night temperature contrast in a tidally locked planet. These jets are able to advect condensates in the day side of the planet. Since the day side temperatures of HAT-P-7b are too hot to allow for the presence of condensates, the size of the covered area is determined by a trade off between the advective and the evaporation timescales. A variation in the speed of the winds (currently hard to explain, but possibly due to strong tidal forces) would then explain the observed shift.

4.2.3 Motivation of this work

Broad wavelength coverage was proved to be fundamental to remove ambiguity in the interpretation of transmission spectra, for example to discriminate between aerosol rich and metal poor atmospheres (Pont et al. 2013; Sing et al. 2016). In particular, characterization of aerosol coverage is of prime importance, as it impacts interpretation of data both at low- (Benneke and Seager 2013) and high-resolution (Pino et al. 2017). However, the combination of data sets obtained at different epochs must rely on assumptions (Sec. 4.2.1, 4.2.2).

This may not be necessary with new generation ground-based, high-resolution observatories with a broad wavelength coverage from the optical to the infrared (GIANO + HARPS-N, CARMENES, CRIRES+, ESPRESSO, HIRES and METIS, ...). With a single observation, these spectrographs are able to probe across the lower and the upper atmosphere simultaneously. However, the removal of slowly varying signals in the data reduction process hampers the diagnostic power of such observations, removing signals such as that due to aerosols. During my PhD, I developed a method that allows to overcome this difficulty, opening a new path to characterize exoplanetary atmospheres.

4.3 Diagnosing aerosols in extrasolar giant planets with water bands resolved at high-resolution

High-resolution ($\mathcal{R} \sim 10^5$), ground-based transmission spectroscopy offers a unique insight in exoplanetary atmospheres. Indeed, at such high resolution: telluric contamination, which dramatically hampers lower resolution, ground-based observations (Sing et al. 2015; Gibson et al. 2017), is better removed (Astudillo-Defru and Rojo 2013; Allart et al. 2017); the resolved cores of the alkali atoms sound up to the base of the thermosphere ($P \lesssim 10^{-9}$ bar) (Wyttenbach et al. 2015, 2017); single absorption lines are spectrally resolved and molecular fingerprints are uniquely identified (Snellen et al. 2010; de Kok et al. 2014; Brogi et al. 2016).

Single molecular bands were detected with high-resolution transmission spectroscopy in the NIR (such as H_2O and CO, e.g. Brogi et al. 2016), and solid methods have been developed to extend such techniques to the optical bands (Allart et al. 2017; Esteves et al. 2017). However, inferring chemical and physical conditions of the atmosphere from this kind of observations is challenging, and a combination with lower resolution, space-based observations has been until now necessary (Brogi et al. 2017; Pino et al. 2017).

One aspect of the problem is that high-resolution transmission spectroscopy requires a wavelength normalization, making it a "double-normalized"[2] technique. The wavelength normalization is necessary to get rid of variations in the measured flux only due to instrumental effects or the atmosphere of Earth (Snellen et al. 2008; Wyttenbach et al. 2015; Heng et al. 2015; Wyttenbach et al. 2017). During the process, the absolute level of the absorption of the planet is lost, and broadband features such as those due to aerosols are removed from the spectra. Indeed, the presence of aerosols on exoplanets was inferred with space-borne HST observations (e.g. Charbonneau et al. 2002; Ehrenreich et al. 2014; Kreidberg et al. 2014; Wakeford et al. 2017a, but see also Snellen 2004; Di Gloria et al. 2015) or lower resolution spectrophotometric observations (e.g. Bean et al. 2010; Nascimbeni et al. 2013; Lendl et al. 2016), revealing that they are very common on hot Jupiters (Sing et al. 2016; Barstow et al. 2017) and smaller Saturn- and Neptune-sized planets.

Here we demonstrate that, notwithstanding the double-normalized nature of high-resolution transmission spectroscopy, it can be used to distinguish between aerosol-free and aerosol-rich scenarios. The technique exploits the fact that the opacities of water vapour and aerosols behave differently with wavelength: the former increases with wavelength, the latter is usually constant or decreasing in the optical and NIR regions of the spectrum. The relative contrast of water bands can thus be used as a diagnostic of the presence of aerosols. At high resolution, the contrast of water bands can be measured through their cross-correlation functions (CCFs). This is obtained by cross-correlating each water band with a binary mask, and can thus be regarded as the average line within the band.

We use the $^{\pi}\eta$ code (Pino et al. 2017; see also Ehrenreich et al. 2006, 2012) to build a grid of models representative of a hot Jupiter in different temperature conditions, containing aerosols at different altitudes; build the CCFs of the grid with a set of binary masks representing water bands of interest (following the technique introduced by Allart et al. 2017); discuss how the relative contrast of different water absorption bands is an indicator of the cloudliness of an atmosphere. The technique that we describe can be applied to data obtained with current and next generation high-resolution spectrographs such as HARPS + NIRPS, GIARPS (GIANO + HARPS-N), ESPRESSO, CARMENES, SPIROU (Mayor et al. 2003; Conod et al. 2016; Oliva et al. 2006; Cosentino et al. 2012; Claudi et al. 2017; Pepe et al. 2010; Quirrenbach et al. 2014; Thibault et al. 2012).

4.4 Methods

First, we select the spectral bands to use. We consider two cases: without telluric contamination (ideal case) and with telluric contamination (realistic case). This yields two sets of bands described in table 4.1 and 4.2 respectively[3] (see also Fig. 4.3). Allart et al. (2017) demonstrated how tellurics can be efficiently corrected for in the optical. In the NIR, the contamination is more severe, and it is unlikely that correction tools can recover the planetary signal, buried in the noise. We thus select regions where the features in the telluric absorption spectrum, taken from Hinkle et al. (2003), remove less than 80% of the light, and correction is possible. These

---

[2] In wavelength and in time, the latter meaning that it needs to compare in- and out-of-transit spectra.

[3] A discussion of the theoretical water spectrum can be found at `http://www1.lsbu.ac.uk/water/water_vibrational_spectrum.html\#b` and references therein.

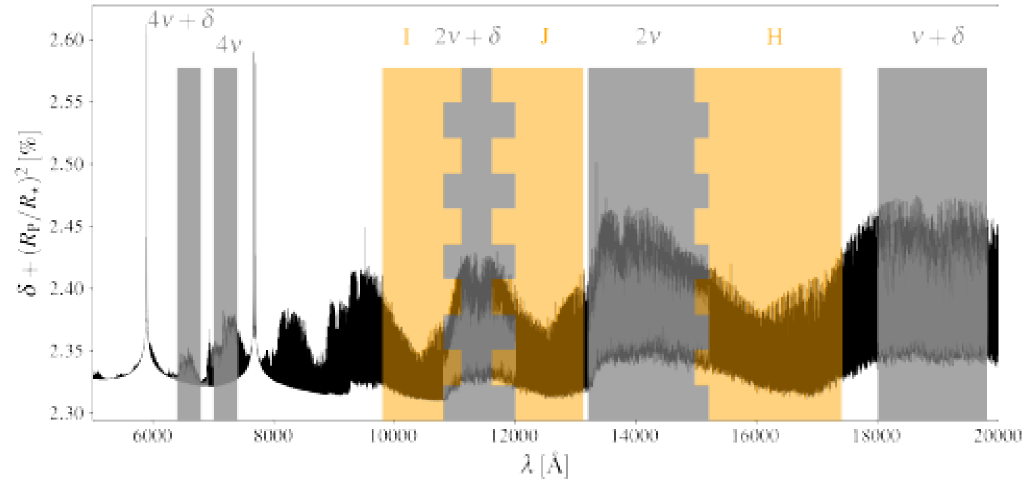

Figure 4.3: Illustration of the used water bands. Gray bands corresponds to water vibrational band. Orange bands correspond to the windows of transparency of Earth atmosphere. The bands partially overlap, as indicated by toothed areas. The solid black line represents a theoretical cloud-free isothermal model of HD189733b. Within each water vibrational band, the region of the spectrum in gray represents the spectrum seen through a seleceted instrument, thus convolved at the appropriate resolving power (see Table 4.1).

bands roughly correspond to the windows of transparency of Earth atmosphere, and we name them accordingly (see Table 4.1, and orange regions in Fig. 4.3).
We compute the expected CCF contrast in each band, following three steps:

- Simulation of a theoretical template transmission spectrum at $R \sim 10^6$;
- Simulation of observations of each water band with a relevant spectrograph (see Table 4.1), by convolving at the appropriate resolving power and binning to the instrumental resolution;
- Computing the CCF with a binary mask.

In the following, we describe the three steps (see Pino et al. (2017) for a complete description of the routines used in the first two steps).

4.4.1 High resolution template

We compute high-resolution model transmission spectra using the $^{\pi}\eta$ 1D line-by-line radiative transfer code (Pino et al. 2017). A line-by-line approach is necessary to apply the CCF technique, as the molecular lines need to be singularly resolved. The water cross-section used in the models is calculated from a high-resolution opacity table ($\Delta\overline{\nu} \sim 0.01$ cm^{-1}, $R \sim 10^6$). The table was obtained with the HELIOS-K routine applied to the HITEMP line-list (Grimm and Heng 2015), accurate up to the high-temperatures expected in hot Jupiters ($T \gtrsim 1000$K).
We assume typical parameters of a hot Jupiter ($r_{\mathrm{p=10bar}} = 1.108\ \mathrm{R_J}$, $M_{\mathrm{p}} = 1.138\ \mathrm{M_J}$, $R_\star = 0.756\ \mathrm{R_\odot}$). Besides water (Volume Mixing Ratio, VMR $= 10^{-3}$), we add opacities from sodium (VMR $= 10^{-6}$), potassium (VMR $= 10^{-7}$), and Rayleigh

Table 4.1: Definition of the water absorption bands. They are named after the vibrational mode that determines their central frequency. Rotational fine structure broadens the absorption bands around this frequency. ν indicates stretching (a combination of symmetric and asymmetric; both have similar frequencies, thus all their combinations overlap when rotational fine structure is included) and δ indicates bending. With this naming, the water band observed with WFC3 corresponds to the (2ν). We indicate some high-resolution instruments that are able to observe in the wavelength range of interest. In the last two columns, we indicate the resolving power and the resolution element of our simulated observations of each band. The simulated instruments are: HARPS for the $(4\nu+\delta)$ band; ESPRESSO for the (4ν) band; GIANO for the NIR bands.

Band name	Wavelength range [Å]	Instrumental coverage	Adopted resolving power	Resolution element
$(4\nu+\delta)$	6 400–6 800 Å	HARPS, ESPRESSO, CARMENES	115 000 $\left(2.6\ \mathrm{km\ s^{-1}}\right)$	0.01 Å
(4ν)	7 000–7 400 Å	ESPRESSO, CARMENES	134 000 $\left(2.2\ \mathrm{km\ s^{-1}}\right)$	0.01 Å
$(2\nu+\delta)$	10 800–12 000 Å	GIANO, CARMENES	50 000 $\left(6\ \mathrm{km\ s^{-1}}\right)$	$\lambda/50\,000$
(2ν)	13 200–15 200 Å	GIANO, CARMENES	50 000	$\lambda/50\,000$
$(\nu+\delta)$	18 000–19 810 Å	GIANO	50 000	$\lambda/50\,000$

Table 4.2: When we consider telluric contamination, the NIR bands are not observable. We thus replace those by the Earth transparency windows. We indicate some instruments that are able to observe in the wavelength range of interest. In the last two columns, we indicate the resolving power and the resolution element of our simulated observations of each band. The simulated instruments are: HARPS for the $(4\nu + \delta)$ band; ESPRESSO for the (4ν) band; GIANO for the NIR bands.

Band name	Wavelength range [Å]	Instrumental coverage	Adopted resolving power	Resolution element
$(4\nu + \delta)$	6 400–6 800 Å	HARPS, ESPRESSO, CARMENES	115 000 $\left(2.6\ \mathrm{km\ s^{-1}}\right)$	0.01 Å
(4ν)	7 000–7 400 Å	ESPRESSO, CARMENES	134 000 $\left(2.2\ \mathrm{km\ s^{-1}}\right)$	0.01 Å
I band	9 780–11 105 Å	GIANO, CARMENES	50 000 $\left(6\ \mathrm{km\ s^{-1}}\right)$	$\lambda/50\,000$
J band	11 605–13 135 Å	GIANO, CARMENES	50 000	$\lambda/50\,000$
H band	14 965–17 410 Å	GIANO	50 000	$\lambda/50\,000$

scattering and Collision Induced Absortpion (CIA) by H_2. Different parameters are varied to produce the templates:

1. Aerosol altitude. For illustrating the technique, a simple parametrization of the aerosol deck is sufficient. We set the atmosphere to be opaque for pressures higher than a threshold p_c, to simulate particles of size $\gtrsim 2$ ßμm. We vary p_c between 10 bar–10^{-7} bar) in logarithmic steps;

2. Temperature of the atmosphere. We assume isothermal temperature-pressure (T − p) profiles, at first order adequate to describe water absorption in transmission spectra (Heng and Kitzmann 2017). Temperature is varied between 1 200 K and 2 100 K in steps of $\sim$ 200 K.

We assume that water abundance and the pressure layers where aerosols are present are completely independent parameters. This assumption is motivated by the fact that aerosols in hot ($T_{\rm eff} \gtrsim 450$ K) exoplanets, our main focus, are not formed by water (Morley et al. 2013, 2014; Lavvas and Koskinen 2017), and their formation pathways are presumably mainly independent from water abundance.

4.4.2 Convolution with the LSF and binning

When observed with a spectrograph, spectral lines are convolved with the instrumental line spread function (LSF). Even for instruments such as HARPS or ESPRESSO, planetary molecular lines are narrower than the instrumental LSF ($\sim$ 2–3 km s^{-1} wide). Indeed, the Doppler-width for water lines at typical temperatures of a planetary atmosphere (500–3 000 K) ranges between 0.7 km s^{-1} and 1.5 km s^{-1}. This effect is severe for resolving powers $< 100\,000$, and needs to be taken into account when estimating the contrast of the CCF (see Fig. 4.4). We convolve each water band with a gaussian LSF representative of an instrument covering that wavelength range (HARPS(-N), ESPRESSO, GIANO; see Table 4.1).

Transmission spectra are built by dividing out stellar spectra taken during the transit and out-of-transit. Pino et al. (2017) discussed how, mathematically, the order of division and LSF convolution cannot be interchanged (see also Deming and Sheppard 2017). In this paper, we assume that the stellar host star has no water lines, a reasonable assumption for many cases (Brogi et al. 2016). Thus, the stellar spectrum on the background of planetary water absorption is on average flat, and we can directly convolve the planetary absorption and the instrumental LSF.

As discussed in Pino et al. (2017), a key ingredient of realistic simulations is binning the model to the correct resolution, i.e. the step with which the spectrum is sampled. For the various bands we adopt the resolution elements reported in Table 4.1. For ESPRESSO, we assume that the resolution element is the same as for HARPS(-N).

4.4.3 Cross-correlation

Individual molecular lines are weak and usually buried in the noise. However, we can enhance our detection capabilities by averaging the signal coming from hundreds or thousands of lines. This is achieved by building a Cross-Correlation Function (CCF; Baranne et al. 1996, 1979). To compute the CCF, we follow the method developed

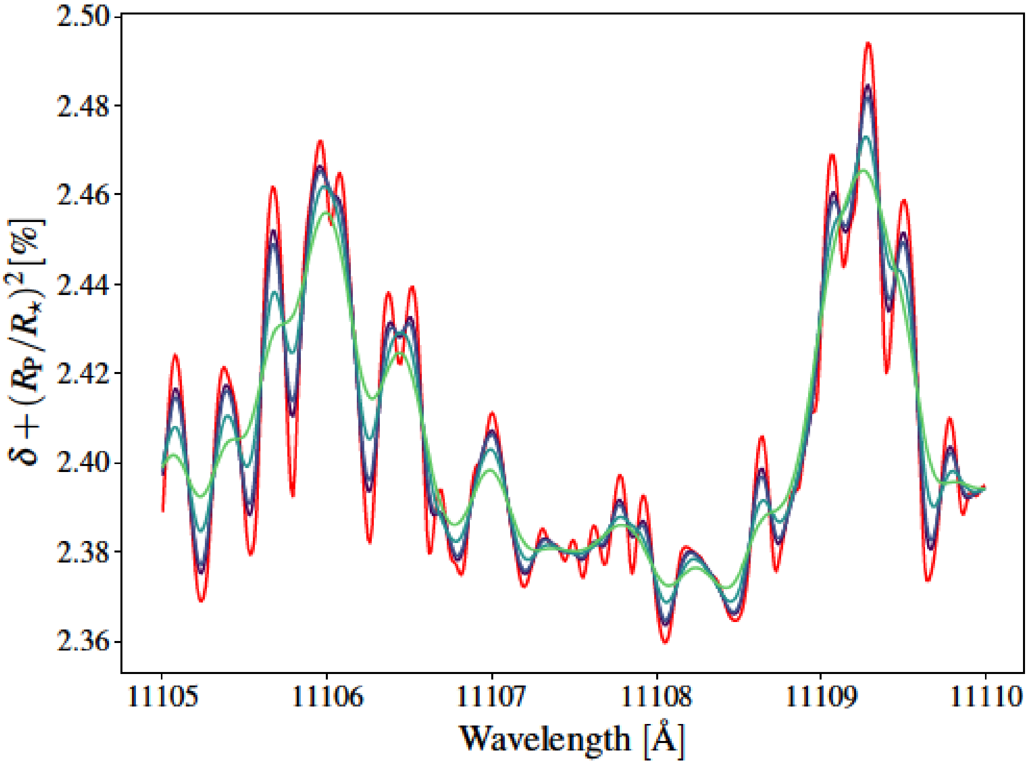

Figure 4.4: Illustration of the effect of finite resolving power on water lines. The red model corresponds to a line-by-line model (with a resolution of $R \sim 10^6$). From the light green curve to the dark blue curve we show the same spectrum convolved with gaussian LSF corresponding to the following resolving powers: at $R = 50\,000$ (GIANO), at $R = 75\,000$ (similar to CARMENES), at $R = 115\,000$ (HARPS/-N) and at $R = 134\,000$ (ESPRESSO). At the lowest resolution the molecular lines are not entirely resolved.

by Allart et al. (2017) to search water in the HARPS optical spectra of HD189733b. The cross-correlation function is defined as:

$$CCF_{N,T_u}(v) = \frac{1}{N}\sum_{i=1}^{N} S(\lambda_i) \cdot M\left[\lambda_i\left(1+\frac{v}{c}\right)\right] \ . \tag{4.1}$$

A binary mask M (with an aperture of one pixel, 0.82 km s^{-1} in HARPS and ESPRESSO and 6.38 km s^{-1} in GIANO) is projected on the spectrum S. The binary mask corresponds to the theoretical wavelengths λ_i of the lines of the molecule we are looking for. Doppler shifting the mask in the radial velocity (v) domain with steps of one pixel, allows one to reconstruct the shape of the average molecular line. Following Allart et al. (2017) we inspect the -80 km s^{-1}/ $+80$ km s^{-1} range. Since no shift is introduced in the model, we expect a peak at 0 km s^{-1}.

With reference to Eq. (4.1), S is one of the water bands defined in Table 4.1 or Table 4.2, convolved with the appropriate LSF and binned at the instrumental resolution. We build a dedicated mask for each water band starting from the HITEMP line list[4]. Within the wavelength range of each water absorption band we select the 800 lines with strongest spectral line intensity at a temperature of 1 200 K[5], typical of the terminator region of hot Jupiters. We note that the choice of the mask is not unique. However, the specific choice we made does not impact the conclusions of the study[6].

The CCF of a water absorption band is rich in information, as it encodes the average line profile within the band. In this work, we are only interested in the line contrast. We thus fit to our computed CCF a Gaussian of the form

$$C + B\cdot\lambda + \frac{A}{\sqrt{2\pi\sigma}}\exp\left(-\frac{(\lambda-\lambda_0)^2}{2\sigma^2}\right) \ , \tag{4.2}$$

leaving C, B, A, σ and λ_0 as free parameters. $\mathrm{CCF}(\lambda_0) - B\cdot\lambda_0 + C$ is then the contrast of the CCF (i.e. of the average line in the absorption band).

4.5 Results and discussion

4.5.1 Ideal case

We first discuss the case of solar water abundance with an opaque, gray absorber found at a pressure p_c, representing a population of particles of size $\gtrsim 2$ μm (see section 4.4.1) in the ideal case (telluric absorption neglected). In Fig. 4.5, we showcase the contrast of the CCF for models at various temperatures as a function of p_c for two example bands ((4ν) and ($\nu+\delta$)). The following conclusions drawn from this example hold also for the other bands:

- The CCF of the redder bands have a stronger contrast than CCF of the bluer bands;

---

[4] While the ExoMol line list by (Tennyson and Yurchenko 2012) is more accurate for several molecular species, HITEMP is accurate enough for water (see Appendix 2 in Pino et al. 2017)

[5] To rescale the lines intensity we used the partition function provided by HITRAN: `http://hitran.iao.ru/partfun`. Note also that the spectral line intensity parameter of HITEMP represents the area below the spectral line. If a very strong line is also very broadened it may be less optimal for the CCF analysis than a weaker but very narrow line. We consider this effect negligible when selecting 800 lines.

[6] This was verified by repeating the whole analysis with a mask at a temperature of 2 100 K

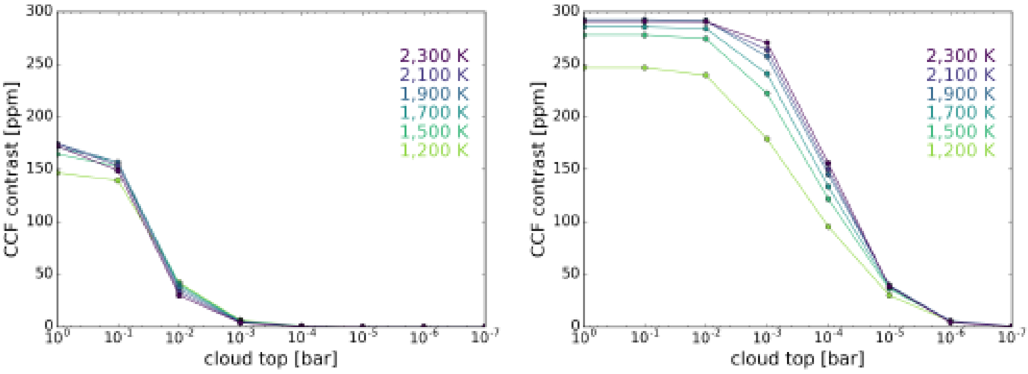

Figure 4.5: Contrast of the CCF as a function of altitude of aerosols (expressed as pressure of the cloud top). Lighter colors indicate colder models, darker colors indicate hotter models (between 1 200 and 2 100 K), as indicated by the colour-matched labels. *Left panel:* (4ν) band, observable with ESPRESSO. A sharp decrease in the contrast of the CCF happens for aerosols higher than 10^{-1} bar *Right panel:* ($\nu + \delta$) band, observable with GIANO. A sharp decrease in the contrast of the CCF is caused by aerosols higher than 10^{-3} bar, thus this water band is less muted by aerosols compared to the (4ν) band.

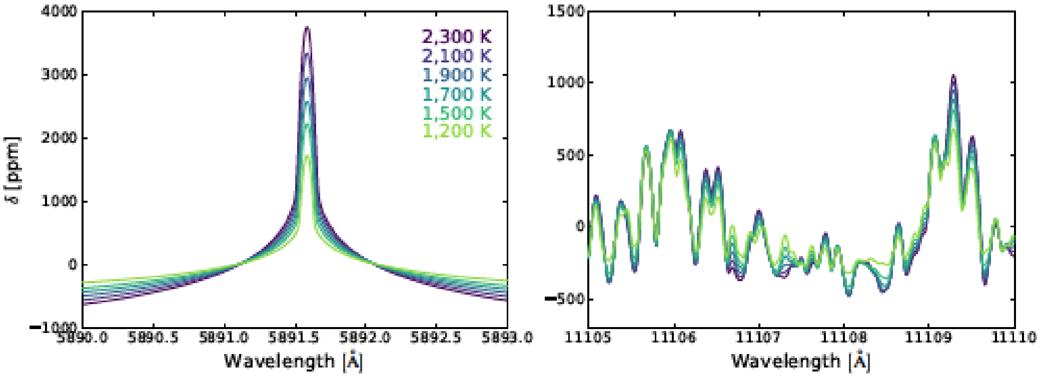

Figure 4.6: Temperature dependence of the high-resolution transmission spectrum of a hot Jupiter. The temperature varies between 1 200 K and 2 100 K in steps of ∼ 200 K (from light to dark). *Left panel:* Zoom on one line of the sodium doublet. The contrast of the sodium feature in the hottest atmosphere (dark blue) is approximately twice its contrast in the coldest atmosphere (light green). This behaviour is explained through the linear dependence of atmospheric signal on temperature through the scale height. *Right panel:* Zoom on a region of the ($2\nu + \delta$) water band. Even if in general the hottest transmission spectrum has a higher contrast compared to the coldest one, the dependence on temperature is non-linear. Some specific lines are actually stronger in a colder atmosphere (e.g. close to 11 107.5 Å).

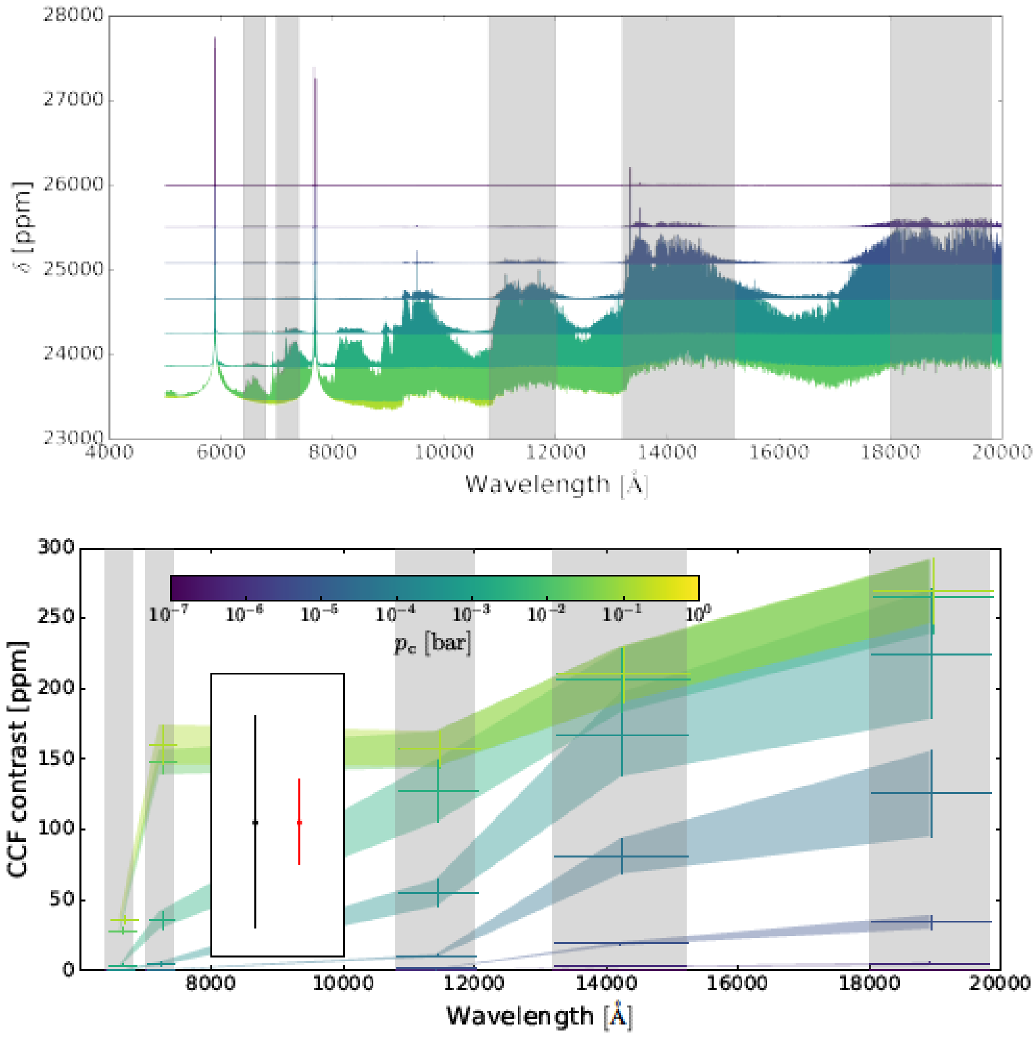

Figure 4.7: CCF contrast as a function of wavelength in the ideal case, in the presence of a gray opacity source simulating large condensates at various pressure levels, between 10^{-7} bar and 1 bar. *Upper panel:* High resolution models of a hot Jupiter with $T = 1\,700$ K and different values of p_c. Each color corresponds to a different value of p_c, and the lightest colors correspond to condensates deeper in the atmosphere. *Lower panel:* CCF contrast as a function of wavelength. The colors are in correspondence with the models shown in the upper panel. For each value of p_c, the temperature range 1 200–2 100 K is explored. We indicate with a vertical error bar the induced variation in the contrast of the CCF. *Inset:* 3σ precision of HARPS (black) and ESPRESSO (red) with three cumulated transits for HD189733 (see Appendix 4.7). Vertical axis is on scale.

- The higher the aerosols are found, the more damped is the signal. A sharp drop in the signal is observed for aerosols higher than a critical pressure;
- The precise value of this critical pressure depends on which band is considered;
- The temperature dependence, represented by curves of different colors in Fig. 4.5, is modest.

Within our grid, temperature varies by a factor of ~ 2, but the CCF contrast in each band varies by less than 10% between the coldest (1 200 K) and the hottest (2 100 K) model. At first glance, it is surprising that the CCF contrast is not linearly increasing with temperature, since, at first order, the contrast of every atmospheric signature is proportional to temperature through the scale height. Indeed, the contrast of the sodium and potassium doublets nearly doubles between the hottest and the coldest temperatures considered (Fig. 4.6, left panel). However, in high-resolution transmission spectroscopy of molecules, the strongly non-linear relation between temperature and population of energetic levels plays an important role, by impacting the relative strength of single molecular lines (see right panel of Fig. 4.6). For a binary mask built for a fixed temperature, the match with the model transmission spectrum is not perfect, and the gain due to the larger scale height is damped. We emphasize that optimization of detection techniques of molecular signatures through cross-correlation needs to properly account for this factor (Allart et al. 2017; 4.6).
Fig. 4.7 shows the contrast of the CCF of all considered water bands in the ideal case. Here, each color corresponds to a cloud deck at a given pressure, as shown in the upper panel. In the lower panel, the vertical error bar in each band represents the CCF contrast values spun when temperature is varied between 1 200 K and 2 100 K. The fact that curves corresponding to different values of p_c do not overlap indicates that indeed it is possible to discriminate among the different cases. The models are best distinguished with a broad wavelength coverage. We indicate as vertical error bars the 3σ precision of HARPS and ESPRESSO, obtained from Allart et al. (2017) and valid for HD189733b (see Appendix 4.7).

4.5.2 A metric to diagnose aerosols

The fact that the critical pressure above which the CCF is damped differs from band to band is crucial to discriminate aerosol-free and aerosol-rich atmospheres. This is quantified by the difference between the CCF contrast of pairs of bands (ΔC). In Fig. 4.8, we showcase this difference for the bands $(\nu + \delta)$ and (4ν). This difference is significantly higher when aerosols are found around 1–10 mbar, high enough to conceil the (4ν) water band but not the $(\nu + \delta)$ water band. The contrast difference ΔC between different pairs of bands peaks for different pressures of the aerosols, depending on the value of the critical pressure of both bands. Furthermore, the maximum value of ΔC indicates how much the pair of bands discriminates among models. We perform this analysis for every pair of bands, and show the results in Fig. 4.9. Overall, combinations of bands covering the optical to the near infrared can discriminate at the 200 ppm level aerosol decks at 1 bar $< p_c <$ 0.1 mbar. This value of ΔC is readily detectable to current or upcoming stabilized spectrographs. Indeed, by rescaling the precision obtained by Allart et al. (2017) to our case yields a precision of 36 ppm on the CCF contrast with HARPS, and of 14 ppm

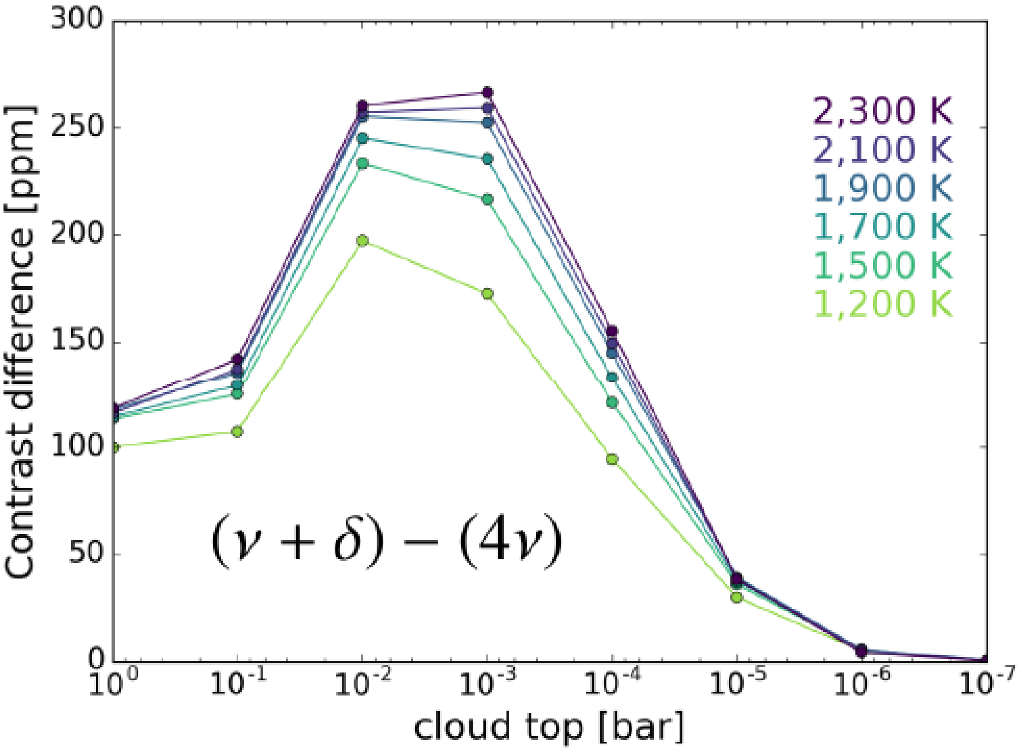

Figure 4.8: The difference in contrast between the CCF of the $(\nu + \delta)$ and the (4ν) bands (both shown in Fig. 4.5). The difference is highest when aerosols are at the 10^{-2}–10^{-3} bar. Thus, the measurment of the contrast of both CCFs constrains the presence of aerosols at that height. Note that this pair of water bands is partially sensitive to aerosols lower in the atmosphere as well.

with ESPRESSO. We summarize in table 4.3 the maximum value of ΔC and the pressure range where it is achieved for different pairs of water bands .

4.5.3 Telluric contamination

We repeated the analysis focusing on the infrared transparency windows of Earth. These coincide with the transparency windows in the exoplanet. In transmission geometry, the loss in absorption in not so abrupt because the stellar light-rays cross transversely the atmosphere. The net result is that the analysis is still sensitive to the presence of aerosols, but at the reduced level of $\sim$ 100 ppm (see Table 4.4 and Fig. 4.11). While this may already be enough to place some constraints on the presence of aerosols, at least two strategies to increase the signal are possible:

1. We did not fully explore the wavelength range. CARMENES is sensitive to two other water bands not considered in this work, that are less intense but much less contaminated by telluric lines; GIANO is sensitive also to the K band, not considered here.
2. We considered a resolving power of $\sim$ 50 000 in the NIR, however instruments at higher resolving power are available (CARMENES) and several others will

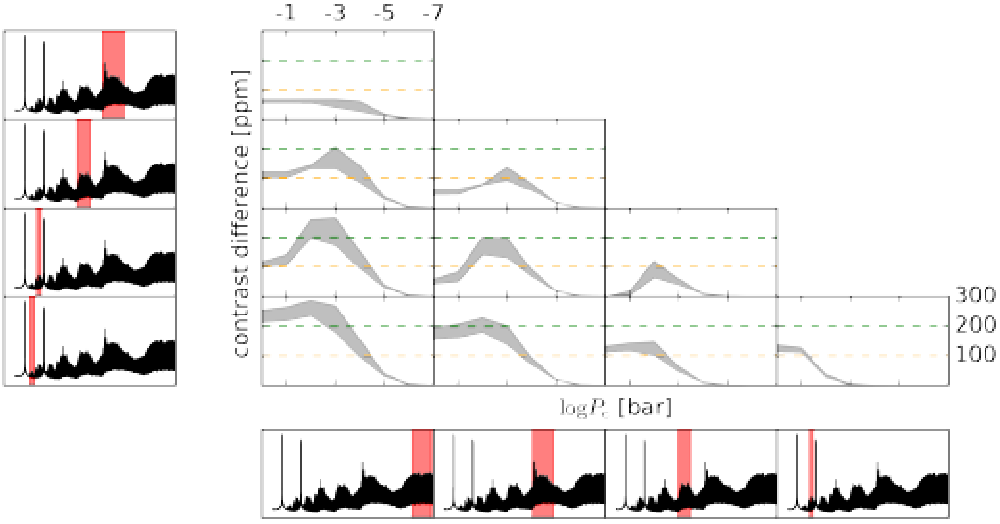

Figure 4.9: Sensitivity of different combinations of water bands to the presence of aerosols. Each panel shows the difference between the band highlighted in the bottom row and the band highlighted in the left column. The x- and y-axes are the same as for Fig. 4.8, running between 1 bar and 10^{-7} bar and between 0 ppm and 300 ppm respectively. Orange and green horizontal dashed lines are put in correspondence of the 100 ppm and the 200 ppm level. Note that these values are arbitrary.

Table 4.3: Typical CCF contrast difference (ΔC) between pairs of water bands and pressure range where this maximum difference is reached. See also Fig. 4.9

Water bands	Cloud pressure [bar]	ΔC [ppm]
$(\nu+\delta)$-(2ν)	1–10^{-4}	50
$(\nu+\delta)$-$(2\nu+\delta)$	10^{-2}–10^{-4}	150–200
$(\nu+\delta)$-(4ν)	10^{-2}–10^{-3}	200
$(\nu+\delta)$-$(4\nu+\delta)$	1–10^{-3}	250
(2ν)-$(2\nu+\delta)$	10^{-3}	100
(2ν)-(4ν)	10^{-2}–10^{-3}	150–200
(2ν)-$(4\nu+\delta)$	1–10^{-3}	150–200
$(2\nu+\delta)$-$(4\nu+\delta)$	1–10^{-2}	120
$(2\nu+\delta)$-(4ν)	10^{-2}	100
(4ν)-$(4\nu+\delta)$	1–10^{-1}	100

Table 4.4: Typical CCF contrast difference (ΔC) between pairs of water bands and pressure range where this maximum difference is reached when considering regions where telluric correction is possible. See also Fig. 4.11.

Water bands	Cloud pressure [bar]	ΔC [ppm]
H band-J band	10^{-3}	50
H band-I band	10^{-2}–10^{-3}	50
H band-(4ν)	10^{-2}–10^{-3}	50–100
H band-($4\nu + \delta$)	1–10^{-2}	100
J band-I band	1–10^{-2}	25
J band-(4ν)	10^{-2}–10^{-3}	50–25
J band-($4\nu + \delta$)	1–10^{-2}	100
I band-($4\nu + \delta$)	1–10^{-2}	50
I band-(4ν)	10^{-2}	< 50
(4ν)-($4\nu + \delta$)	1–10^{-1}	100

be in the near future (NIRPS, SPIRou, ...). A higher resolving power has the advantage that the CCF contrast is higher, because of the narrower LSF and because less molecular lines are blended in the spectrum (see Fig. 4.4).

Finally, we stress that our assumption of aerosols of grain size > 2 μm is a conservative one. Indeed, when particle size approaches the wavelength range considered, scattering becomes chromatic (Rayleigh scattering). Several hot Jupiters host aerosols of this kind (Sing et al. 2016; Barstow et al. 2017). In this scenario, scattering is able to completely mask the optical water bands, but affects much less the NIR water bands. We tested this case by simulating an atmosphere compatible with HD189733b, which hosts a marked optical slope attributed to a severe coverage with this kind of particles (Pont et al. 2013; Pino et al. 2017). Even in this conservative case, ΔC reaches up to 100 ppm.

4.6 A search for water in the HARPS spectrum of HD189733b

In Pino et al., in prep. we applied a cross-correlation technique with a binary mask (Baranne et al. 1996; Pepe et al. 2002). This was applied for the first time in the field of exoplanet atmospheres by Allart et al. (2017), in the search for water in the HARPS spectrum of HD189733b. I contributed to this paper by building an optimal line list to match with water lines in the spectrum of the planet, and by modelling the expected signal.

The problem of computing an optimal line list is different than the problem discussed in Pino et al. in prep. Indeed, in that analysis we kept fixed the number of lines in the binary mask and varied the underlying model. This was required to have a consistent analysis across the models. However, to find the optimal mask to extract the water signal in HD189733b the opposite approach must be adopted: we assumed a reasonable model for the planet and varied the number of lines within the binary mask to maximize the expected signal-to-noise ratio.

The signal-to-noise ratio is computed as follows:

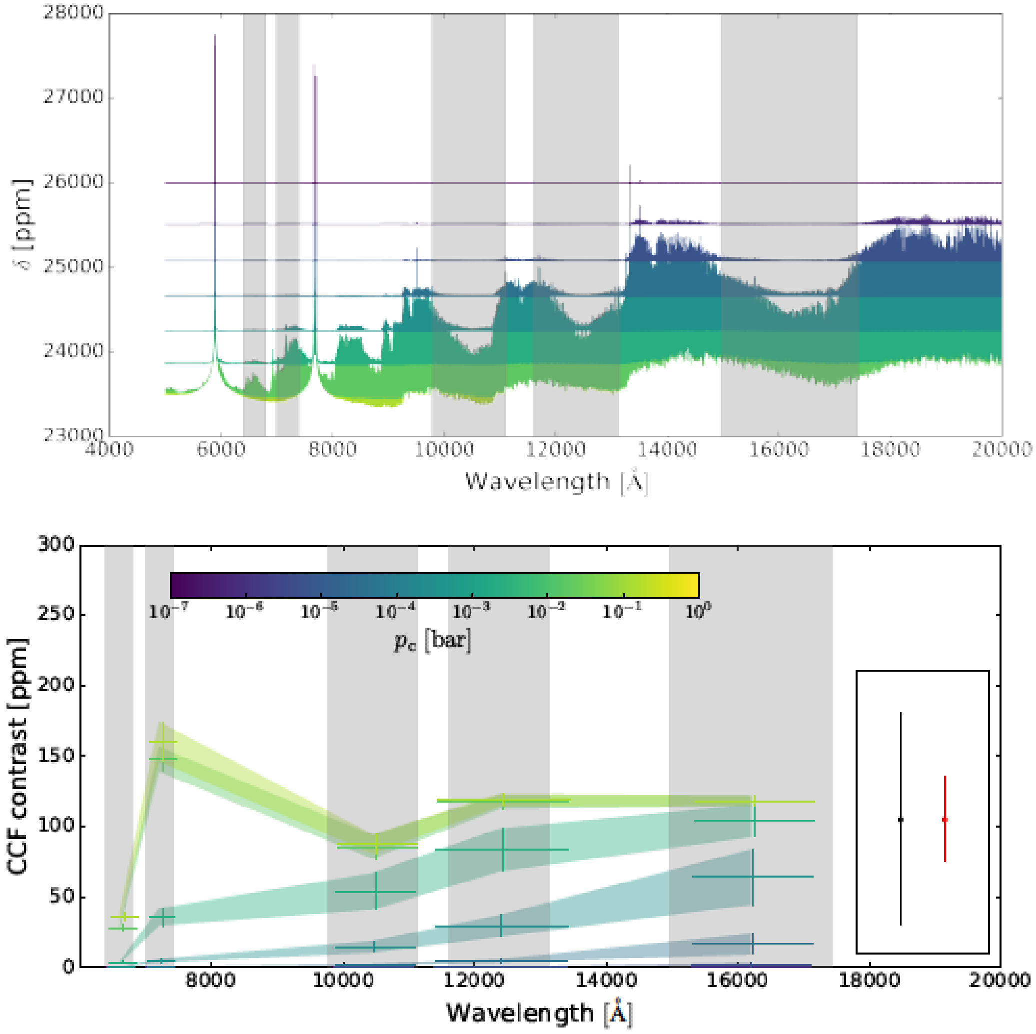

Figure 4.10: CCF contrast as a function of wavelength in the case where telluric contamination is considered, in the presence of a gray opacity source simulating large condensates at various pressure levels, between 10^{-7} bar and 1 bar. *Upper panel:* High resolution models of a hot Jupiter. Each color corresponds to a different value of p_c, and the lightest colors correspond to condensates deeper in the atmosphere. Only the case $T = 1\,700$ K is shown. *Lower panel:* CCF contrast as a function of wavelength. The colors are in correspondence with the models shown in the upper panel. For each value of p_c, the temperature range 1 200–2 100 K is explored. We indicate with a vertical error bar the induced variation in the contrast of the CCF. *Inset:* 3σ precision of HARPS (black) and ESPRESSO (red) with three cumulated transits for HD189733 (see Appendix 4.7). Vertical axis is on scale.

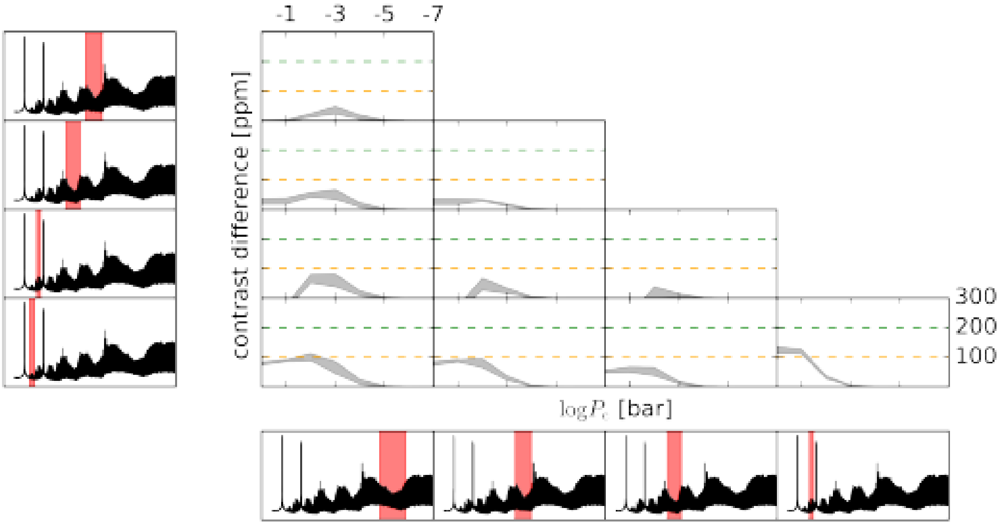

Figure 4.11: Sensitivity to the presence of aerosols of different combinations of bands that are accessible from the ground even in the presence of tellurics. Each panel shows the difference between the band highlighted in the bottom row and the band highlighted in the left column. The x- and y-axes are the same as for Fig. 4.8, running between 1 bar and 10^{-7} bar and between 0 ppn and 300 ppm respectively. Orange and green horizontal dashed lines are put in correspondence of the 100 ppm and the 200 ppm level. Note that these values are arbitrary. Scatterers up to the 0.1 mbar level produce values of ΔC up to 100 ppm.

1. We compute an aerosol-free, isothermal model for the atmosphere of the planet at a temperature T;

2. We build a set of binary masks $M_{\mathrm{T,N}}$ at the same temperature T of the model, by keeping the N strongest lines within the band of HARPS. N is varied between a few hundred up to a few thousands[7];

3. We cross-correlate the set of binary masks with the model, obtaining a set of CCFs. For each CCF, we compute the contrast fitting a Gaussian of the form Eq. (4.2). This is the "signal";

4. In the photon limited case, which Allart et al. (2017) reached with their analysis, noise scales with $\sigma_1/\sqrt{N}$. σ_1 is unknown, but constant (see Appendix);

5. We compute the ratio between signal and noise as a function of N. The position of the maximum depends on N, but not on σ_1. Thus, we are able to find the optimal line list by maximizing this function.

It may be counter-intuitive that the maximum information is not extracted by including all the water lines. This is due to the fact that we are not yet able to build a set of weights for the lines. This task requires accurate knowledge of the planetary atmosphere (e.g. aerosol content) which we do not currently possess. The result of the CCF with the binary mask in the unweighted case is simply the average line. The more lines are included, the more the average is smeared out (as we are including weaker lines). On the other hand, white noise is abated. Our analysis is therefore able to identify the trade-off between these two competing effects.

4.7 Conclusions and future prospects

High-resolution, ground-based transmission spectra are obtained by using double-normalized data reduction techniques. These techniques remove broad band features such as those due to aerosols. Here, we demonstrated that this does not prevent their use as probes of the presence of aerosols. The technique we presented is based on the relative depth of water absorption in different bands. We simulated the Cross-Correlation Function of a fixed binary mask with a grid of models spanning a range of temperatures and aerosols at different altitudes in the atmosphere. We showed that the dependence of the CCF contrast on temperature is not very strong as a result of the non-linear dependence on temperature of the partition function of water. Aerosols at different altitudes in the atmosphere attenuate water absorption differently according to the band considered. The contrast difference of the CCF of different bands (ΔC) is thus a diagnostic of aerosol altitude. The typical signals that it is necessary to measure are of $\sim$ 100–200 ppm, while typical precisions with available techniques amount to 15–30 ppm. A key factor for the success of this technique is having a broad wavelength coverage, which is provided by current instrumentation. Of particular interest is the HIRES optical to NIR spectrograph for the E-ELT, now under phase A study (Zerbi et al. 2014; Marconi et al. 2016).
We limited our analysis to the contrast of the CCF, and thus did not consider the full information encoded in the CCF. For example, the broadening of the CCF is a function of temperature, and rotation and atmospheric dynamics. We thus plan

---

[7] Practically, we perform several cuts in the "line intensity" parameter of HITEMP, after rescaling the line list to the correct temperature.

to extend our technique to consider the full CCF as a probe of the conditions in the atmosphere. Furthermore, the technique can be extended to other molecular species. Methane is a good candidate as indicator of aerosol-rich atmospheres, as it possess a wealth of absorption bands (that in general do not coincide with telluric absorption bands) that span a broad wavelength range evenly. It can be expected in planets colder than the one simulated here, thus extending the range of cases where our technique can be applied. The new ExoMol line list (Tennyson et al. 2016), that contains billions of lines, is challenging to model but possesses the required accuracy for this kind of studies (Lavie et al. 2017). Finally, an extension to the infrared of our technique is possible and warranted in view of future instruments such as CRIRES+ (Follert et al. 2014) and METIS (Brandl et al. 2014).

Appendix: 1σ precision of HARPS(-N) and ESPRESSO

Given the mask $M_{N,T_{ll}}$, we want to estimate the noise on $CCF_{N,T_{ll}}$. We assume a photon limited regime. We can then write:

$$\sigma_N = \frac{\sigma_1}{\sqrt{N}} \, , \tag{4.3}$$

where σ_1 is the error on the CCF computed on a single line (i.e. on the transmission spectrum) and we use the fact that the noise does not depend on the temperature chosen for the mask. To be as realistic as possible we obtain σ_1 from observations. Allart et al. (2017) computed the optical water CCF for three cumulated transits of HD189733b, by applying to an observed transmission spectrum binary masks at 1700 K and 2100 K containing 873 and 606 lines respectively. The following dispersion values were obtained in the continuum of the optical water CCF on a single HARPS pixel:

1. $\sigma_{873} = 34$ ppm with $T_{ll} = 1700$. Then $\sigma_1 = \sqrt{873} \cdot \sigma_{873} = 1004$ ppm;
2. $\sigma_{606} = 43$ ppm with $T_{ll} = 2100$. Then $\sigma_1 = \sqrt{606} \cdot \sigma_{606} = 1058$ ppm.

The two values are similar, indicating that indeed Allart et al. (2017) reached the photon-noise limit. Then, we assume:

1. For HARPS(-N), $\sigma_{1,\,\mathrm{HARPS}} = 1031$ ppm, the average of the values obtained by Allart et al. (2017) with the two masks;
2. For ESPRESSO, $\sigma_{1,\,\mathrm{HARPS}} = 412$ ppm. This value accounts for the 6.25 times increased flux due to better throughput and mirror size ESPRESSO.

In our analysis we considered 800 lines, thus the precision on the CCF contrast presented in our analysis amounts to 36 ppm and 14 ppm for HARPS(-N) and ESPRESSO respectively.

Chapter 5

On the accuracy of $^{\pi}\eta$ (and more)

Modelling frameworks can be broadly (and somewhat arbitrarily, in my opinion) divided in "forward models" (or "parametric models") and "retrieval" (e.g. Madhusudhan et al. 2014b). Forward models make physical assumptions (such as equilibrium/disequilibrium chemistry, thermochemical equilibrium, ...) in order to produce simulations as realistic as possible. Retrieval schemes, on the other hand, leave quantities such as temperature-pressure profile and chemical abundances as free parameters. These parameters are constrained by comparing the models to data within a statistical framework (grid-based optimization, e.g. Madhusudhan and Seager 2009; Bayesian Markov Chain Monte Carlo methods, e.g. Madhusudhan et al. 2011; Benneke and Seager 2012; Line et al. 2013, ...).

During this PhD, I was asked multiple times if $^{\pi}\eta$ (Pino et al. 2017) is a forward modeling scheme or a retrieval framework. The only possible answer is that $^{\pi}\eta$ does not fully fall within neither category. In Pino et al. (2017) and chapter 3, it was used in "an hybrid forward modelling/retrieval scheme". Indeed, I used a statistical framework to compare models to data, however the exploration of the parameter space was admittedly not complete (a required condition for retrieval schemes). In chapter 4, I used $^{\pi}\eta$ as forward model, i.e. to simulate observations of transmission spectra at high-resolution from the optical to near-infrared, focusing on the impact of aerosols. However, the limited physics and chemistry included in $^{\pi}\eta$ clearly distinguish it from pure forward models.

The limitations of $^{\pi}\eta$ are compensated and explained by the employment of state of the art opacities[1] in a line-by-line framework (Pino et al. 2017). This feature makes $^{\pi}\eta$ a state of the art tool to model high-resolution ($R \sim 10^6$) transmission spectra over a broad wavelength range (0.3–2 μm), from the lower to the upper atmosphere (10 bar $\gtrsim p \gtrsim 10^{-12}$ bar). With these requirements, each atmospheric layer consists of $\sim 2.5 \cdot 10^6$ wavelength points. The vertical spatial sampling has at least four points per scale height, resulting in more than 100 atmospheric layers. Typical runs thus require $\sim$ 10 min per model on a regular processor (Pino et al. 2017).

The trade-off between simplification and computational efficiency is not a problem specific to $^{\pi}\eta$, and was widely studied by many groups. My choices were based

---

[1] This is the main difference with its precursor ETA (Ehrenreich et al. 2006, 2012), which included some extra-features such as Mie scattering but was focused on cooler planets. ETA adopted the HITRAN line list, that features up to a factor of 1 000 less lines than HITEMP included in $^{\pi}\eta$ and is inaccurate at high temperatures. See also appendix in chapter 3 and Pino et al. (2017).

on their work and on supplementary tests that I made myself. In the following, I will summarize and justify my main assumptions. I will also discuss their possible impact on interpretation of data from current and future observational facilities.

5.1 Hydrostatic equilibrium

For a given input temperature pressure profile, ${}^{\pi}\eta$ computes the heights corresponding to the pressure layers in the atmosphere (Eq. 3.4). The assumption behind Eq. 3.4 is hydrostatic equilibrium. While this is a reasonable assumption in the lower atmosphere (e.g. Seager 2010), one may question if it holds in the upper atmosphere. In fact, e.g. Yelle (2004) demonstrated that the upward velocity of the atmosphere plays a key role in hot Jupiters. The high temperatures in the upper atmosphere of these planets imply a large scale height, and thus a relatively large density and pressure even far from the planet. This leads to an unbalance with the low pressure of interplanetary space. This discrepancy can be reconciled by accounting for an outward, solar wind-like flow. Indeed, in the absence of viscosity, the numerical density of an atmosphere at a distance $\xi = r/r_0$ reads (Parker 1965)

$$n(\xi)c^2(\xi) = n_0 c_0^2 \exp\left(-\int_1^{\xi} \frac{\mathrm{d}u}{u^2}\left(\frac{GM_{\mathrm{P}}}{r_0}\right)^2 \frac{1}{c^2}\right) \exp\left(-\int_1^{\xi} \frac{\mathrm{d}u}{c^2} v \frac{\mathrm{d}v}{\mathrm{d}u}\right) \quad . \tag{5.1}$$

In Eq. 5.1, n is the numerical density, c is the speed of sound and v is the vertical flow. The first term on the right hand side is the barometric term, while the second is the advective term. If the velocity v is directed outwards ($v > 0$) the advective term tends to reduce the density. At large distances from the planet, i.e. at large ξ, the outward flow is fast enough to balance the low interplanetary space pressure (e.g. Yelle 2004).

However, the advective term is close to 1 up to the sonic point ($v = c$). Out to that point, the denisty profile can thus be approximated with a hydrostatic profile. As an example, Yelle (2004) and Koskinen et al. (2010, 2013b) located the sonic point of the hot Jupiter HD209458b at $\sim 3\ R_{\mathrm{p}}$. Indeed, Fig. 5.1 shows that for this planet the gravity is balanced by the pressure gradient up to that point.

Salz et al. (2015) individuated the sonic point of HD189733b to be at 4 R_{p}. The models by Pino et al. (2017) extend up to 1.3 R_{P} in this planet. Hydrostatic equilibrium is thus likely a good assumption. *However, the hypothesis of hydrostatic equilibrium may not be suitable to interpret the possibly exospheric absorption feature in WASP-43b.*

5.2 Equilibrium and disequilibrium chemistry

Retrieval frameworks usually leave chemical abundances and temperature-pressure profiles as free parameters. The reasoning behind this choice is that enforcing a particular chemical (e.g. equilibrium chemistry) or physical (e.g. Local Thermodynamic Equilibrium, LTE) condition may mislead interpretation of data[2]An example of this topic are the works by Madhusudhan et al. (2011) and Kreidberg et al. (2015) on the hot Jupiter WASP-12b. Both works aimed to constrain the C/O ratio of the planet

---

[2] There are exceptions, e.g. the SCARLET retrieval code (Benneke and Seager 2012, 2013; Benneke 2015).

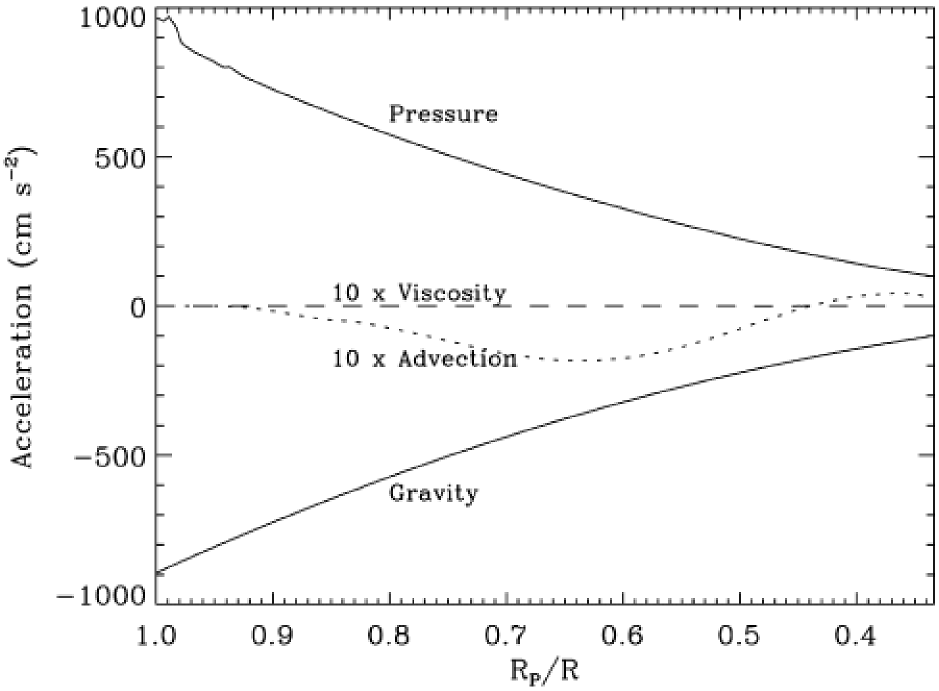

Figure 5.1: Figure from Yelle (2004). The figure shows that gravitational acceleration in HD209458b is primarily balanced by the pressure gradient between 1 R_p and ~ 3 R_p. Advection of momentum is minor, with a contribution of less than 5% at all levels. Viscous forces are negligible. Note that a hydrostatic balance corresponds to the case where the acceleration is entirely compensated by pressure.

with a retrieval analysis. Madhusudhan et al. (2011) claimed that C/O > 1 based on multi wavelength photometric data, higher than the solar value (C/O $= 0.54$, Asplund et al. 2005). Kreidberg et al. (2015) applied an independent retrieval scheme to a more accurate spectroscopic combined HST WFC3 G141 and WFC3 G102 data set covering between 0.8 Å and 1.7 Å. They performed two kinds of retrieval: in the first case, they left abundances and (isothermal) temperature as free parameters. The retrieval indicated that the data favours C/O < 1, but is consistent with C/O > 1 at 2σ. As a further test, they repeated the analysis by enforcing chemical equilibrium along a retrieved T–p profile. In this second case, a carbon-dominated chemistry was excluded at 3σ. The more stringent constraints derived from the fact that, by enforcing chemical equilibrium, a much stronger (not necessarily justified) prior is set. Oreshenko et al. (2017) confirmed that the current precision of the HST + Spitzer data adopted by previous works results in prior dominated constraints on retrieved quantities.

This example calls for a discussion of my assumption of solar abundance of water ($\chi_{\mathrm{H_2O}} \sim 10^{-3}$), adopted both in chapter 3 and 4. This was broadly supported by equilibrium chemistry calculations over a broad range of temperatures (see Fig. 5.2) and by current observational evidence (see Fig. 5.3). However, it is well known that water abundance and altitude of aerosols of size $\gtrsim 2\ \mu$m (from now on "large particle aerosols") are correlated. Indeed, the water spectral feature can be either masked by Mie scattering by aerosols, or intrinsically weak because of a low water abundance (that leads to the dominance of other continuum opacity sources such as CIA). The correlation is exemplified in in Fig. 5.4, that shows the results of a SCARLET retrieval based on HST WFC3 transmission spectra of HD209458b (Benneke 2015). A decrease in water abundance is compensated by shifting aerosols at higher pressures (deeper in the atmosphere). See also Line and Parmentier (2016) for an analytical derivation of this correlation.

The effect of this assumption on the work presented in chapter 3 and in Pino et al. (2017) is presumably small. Indeed, aerosol opacity in the sodium region of HD189733b is mainly due to sub-micron particles, whose altitude is mainly constrained through the optical transmission spectrum (where they cause Rayleigh scattering).

On the other hand, the correlation between the height of the large particle aerosol deck and the abundance of water has direct consequences for the work I presented in chapter 4. In Fig. 5.5, I show the contrast of the CCF of the $(\nu + \delta)$ band as a function of altitude (the same considered in the right panel of Fig. 4.5, here with temperature dependence captured by the shadowed area). The two curves correspond to water fixed at solar abundance (blue, same as in Fig. 4.5) and 0.1 times solar abundance (red). A key parameter of the analysis presented in chapter 4 is the critical pressure below which aerosols sharply reduce the contrast of the CCF. This pressure is ~ 10 times higher in the subsolar case, demonstrating that the correlation between aerosol height and water abundance similarly holds for low and high resolution transmission spectra[3].

I repeated the analysis of chapter 4 fixing the water abundance to 0.1 times solar. The conclusion that high-resolution transmission spectroscopy of water over a broad wavelength range can be used to constrain the altitude of aerosols still holds (see

---

[3] As discussed in chapter 4, my analysis considers only the contrast of the CCF. A scheme that considers the full shape of the CCF may allow to decorrelate the effects of aerosols and water abundance. I will explore this possibility in future work.

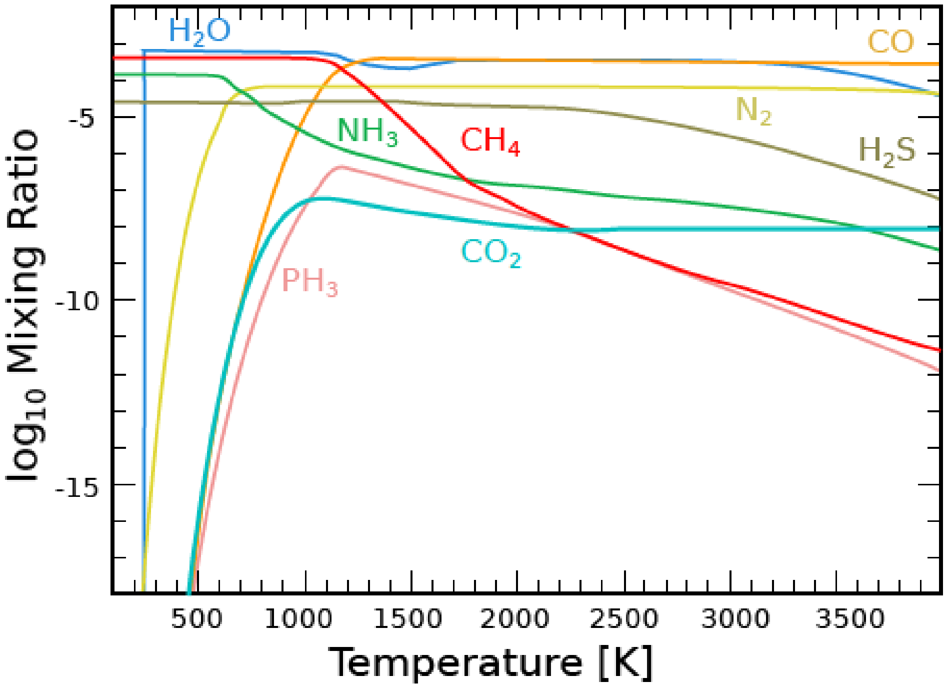

Figure 5.2: Figure from Crossfield (2015), in turn adapted from Sharp and Burrows (2007); Miguel and Kaltenegger (2014). Molecular equilibrium abundances for a solar-metallicity atmosphere at 1 bar.

results in Fig. 5.6). *However, a detailed characterization of aerosols through transmission spectroscopy must account for the uncertainty introduced by the unknown water abundance.*

I finally note that $^{\pi}\eta$ was developed in order to be able to use an arbitrary input T–p profile and chemical profile (and abundances can be a function of height). $^{\pi}\eta$ can thus be coupled with atmospheric models considering thermochemical and non-LTE effects. Upon availability of such models, $^{\pi}\eta$ could be easily used as a forward model to simulate high-resolution transmission spectra under more realistic assumptions.

5.3 Aerosols

Models of transmission spectra need to account for scattering by aerosols. Due to the slant geometry, even trace species can impact considerably the spectrum by muting atomic and molecular features (Fortney 2005). In $^{\pi}\eta$, I parametrized the effect of particles of different sizes on the transmission spectrum. One parameter allows to set a completely opaque gray opacity source located below a threshold altitude in the atmosphere (p_c). Two other parameters regulate magnitude and slope of an extra absorption in the optical, decreasing towards infrared and observed in several planets (see chapters 2 and 3).

These prescriptions capture two limiting cases of the Mie theory, an analytical solution to Maxwell's equations that describes how to calculate phase functions and scattering cross sections of solid or liquid particles (e.g. Wakeford and Sing 2015). These limits are:

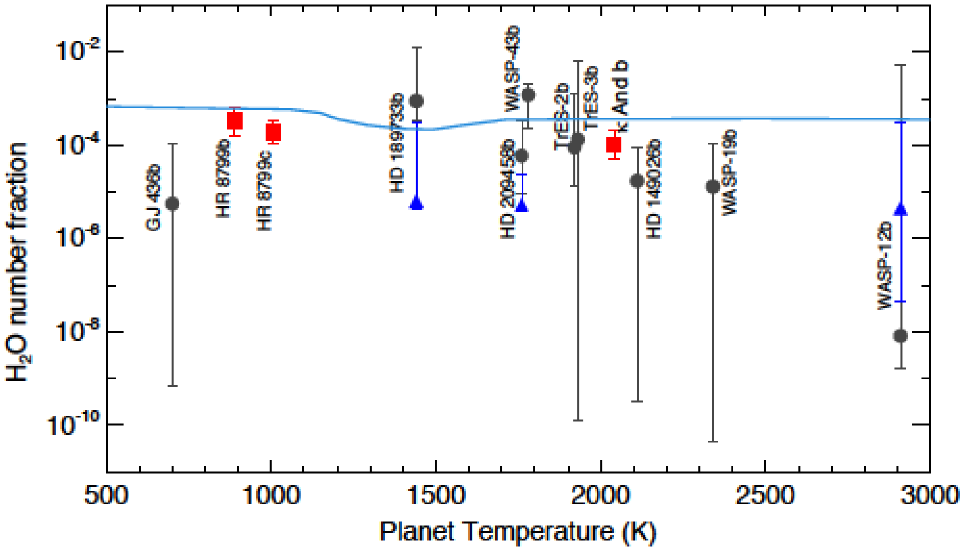

Figure 5.3: Figure from Crossfield (2015), in turn adapted from Todorov et al. (2016) with addition data from Diamond-Lowe et al. (2014); Barman et al. (2015). H_2O abundances reported in extrasolar planets. Red squares indicate directly imaged planets, while the grey circles and blue triangles indicate transiting planet emission and transmission spectra, respectively. No clear trends with temperature (or planet mass) are apparent in the present data.

1. The geometric optics limit, obtained when the size of the particle greatly exceeds the considered wavelength. In this case, cross-section is independent from wavelength;
2. The Rayleigh scattering limit, obtained in the opposite case of particle size greatly smaller than the considered wavelength. In this case, the cross section has the shape of a power law $\sigma = \sigma_0 \lambda^\alpha$ with $\alpha = 4$. σ_0 determines the magnitude of the cross section and depends on the distribution of particles size. The distribution of the particle size can change the slope measured in the transmission spectrum (Pont et al. 2013), which I thus left as free parameter.

These assumptions were motivated by a comparison with more complex models of Mie scattering. Fig. 5.7 shows the total extinction cross section (absorption + scattering) of various condensates, modelled as spheres of various sizes, from 10^{-2} μm to 1 μm. Up to $\lambda \sim 3$ μm, the cross section of most condensates is either flat (optical limit) or decreasing with wavelength (Rayleigh limit) and is thus captured by my prescription. At wavelengths longer than 3 μm, absorption features of the condensates arise, and my simple treatment is no longer adequate (Wakeford and Sing 2015; Pinhas and Madhusudhan 2017). Note that JWST will access these absorption features, providing key insight in aerosol composition on exoplanets (Wakeford and Sing 2015; Mollière et al. 2017; Pinhas and Madhusudhan 2017). The MIRI instrument, in particular, will provide spectral coverage up to 30 μm (see Fig. 5.8). *Mie scattering by aerosols should be included in transmission spectroscopy models for wavelengths longer than ~ 3 μm. This aspect is key in the JWST era, which will allow us to characterize composition and size distribution of aerosols.*

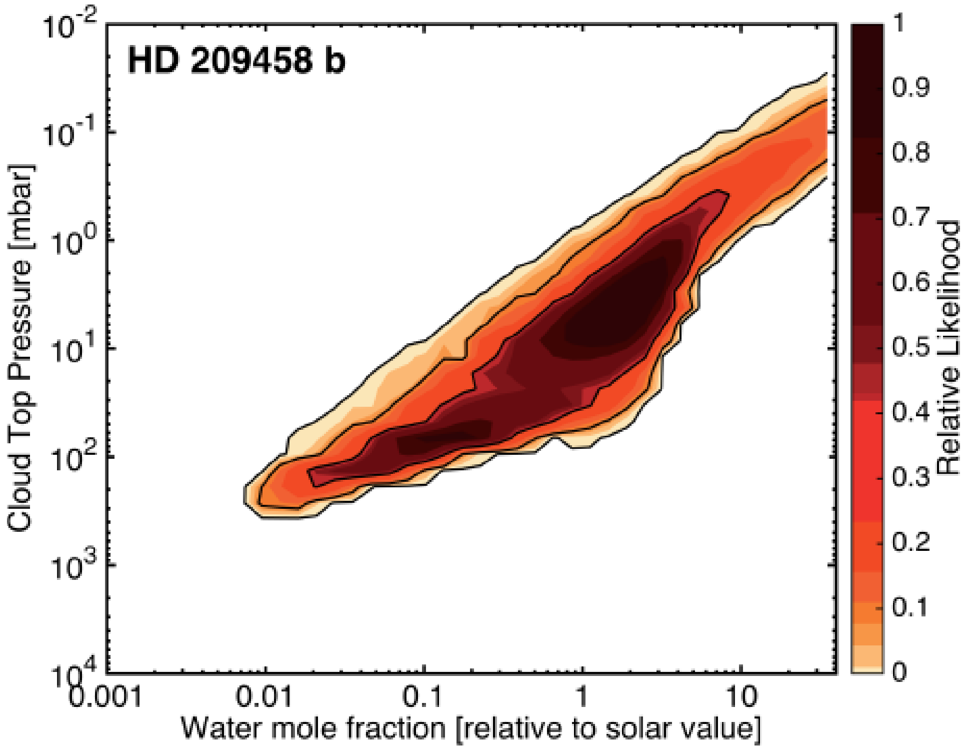

Figure 5.4: Figure from Benneke (2015). Joint constraints on the water abundance and cloud top pressure for HD 209458b, retrieved from WFC3 transmission spectra. The colored shading indicates the relative likelihood of atmospheric models as a function of water mole fraction and cloud top pressure. A log-uniform prior on the water mole fraction ia assumed. Scenarios with largely cloud-free atmosphere are near the bottom of each panel; scenarios with high altitude clouds are at the top. Water abundance and cloud top pressure are highly correlated, preventing precise constraints on water abundance and cloud top pressure individually.

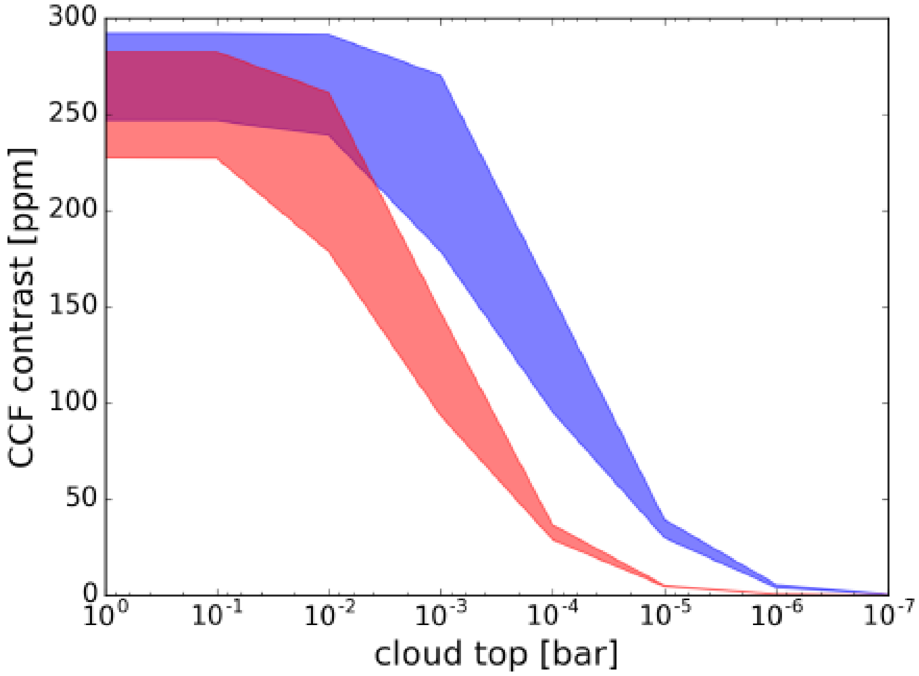

Figure 5.5: Contrast of the CCF of the $(\nu + \delta)$ band (observable with GIANO) as a function of altitude of aerosols, expressed as pressure of the cloud top. The shadowed area is spanned by the models when temperature is varied between 1 200 and 2 100 K. A sharp decrease in the contrast of the CCF is caused by aerosols higher than a threshold. For solar water abundance, this threshold is located at $\sim 10^{-3}$ bar. For 0.1 times solar abundance, this threshold is located at $\sim 10^{-2}$ bar. This test shows that a correlation between aerosol deck and water abundance holds at high resolution as well.

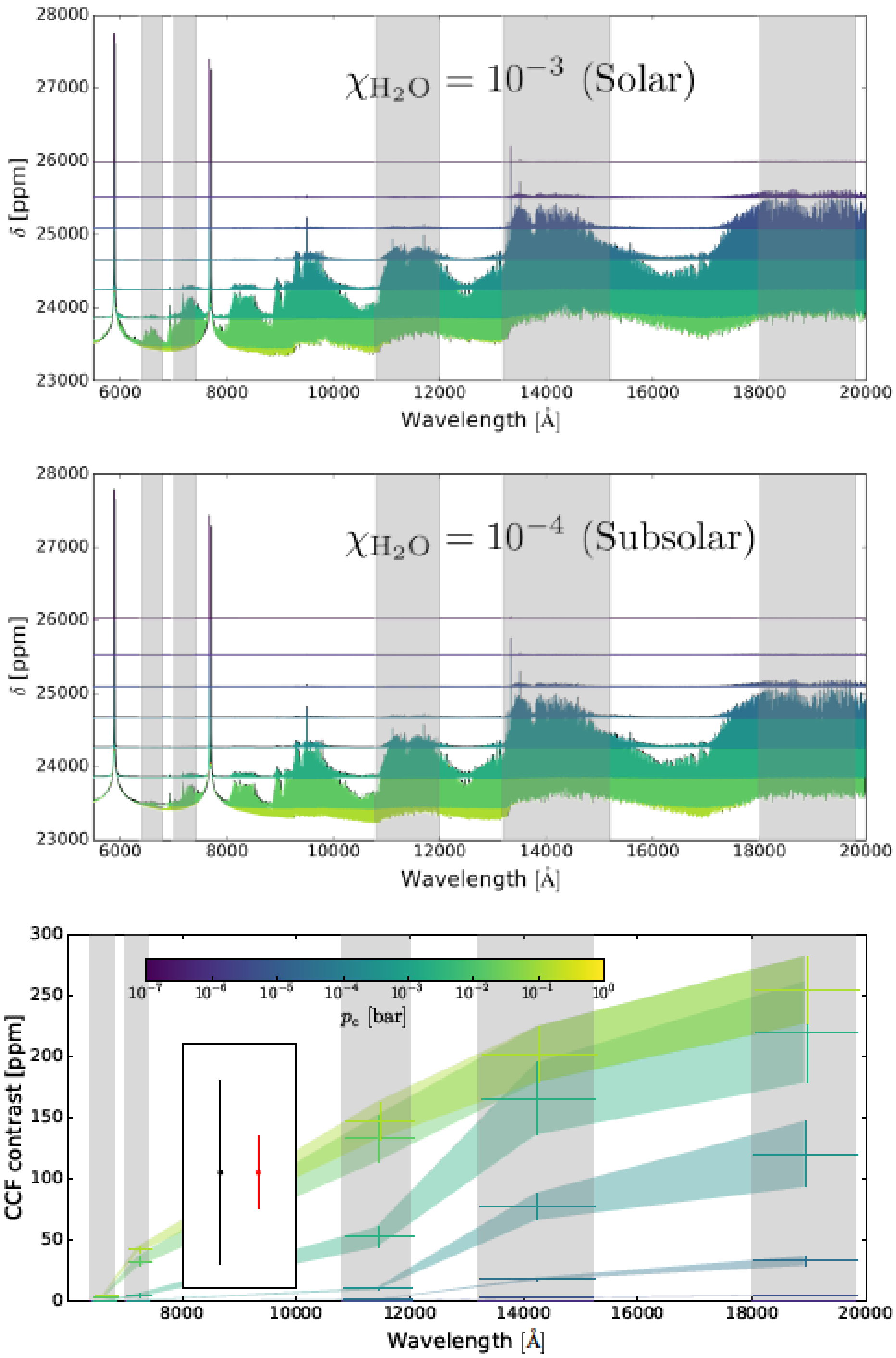

Figure 5.6: CCF contrast as a function of wavelength for 0.1 times solar abundance, in the presence of aerosols between 10^{-7} bar and 1 bar. *Upper and middle panel:* models of a hot Jupiter with $T = 1\,700$ K and different values of p_c. The upper panel represents the solar abundance case (see 4), the middle panel is the case under study. Each color corresponds to a different value of p_c, and the lightest colors correspond to condensates deeper in the atmosphere. *Lower panel:* CCF contrast as a function of wavelength. For each value of p_c, the temperature range 1 200–2 100 K is explored. We indicate with a vertical error bar the induced variation in the contrast of the CCF. *Inset:* 3σ precision of HARPS (black) and ESPRESSO (red) with three cumulated transits for HD189733. Vertical axis is on scale.

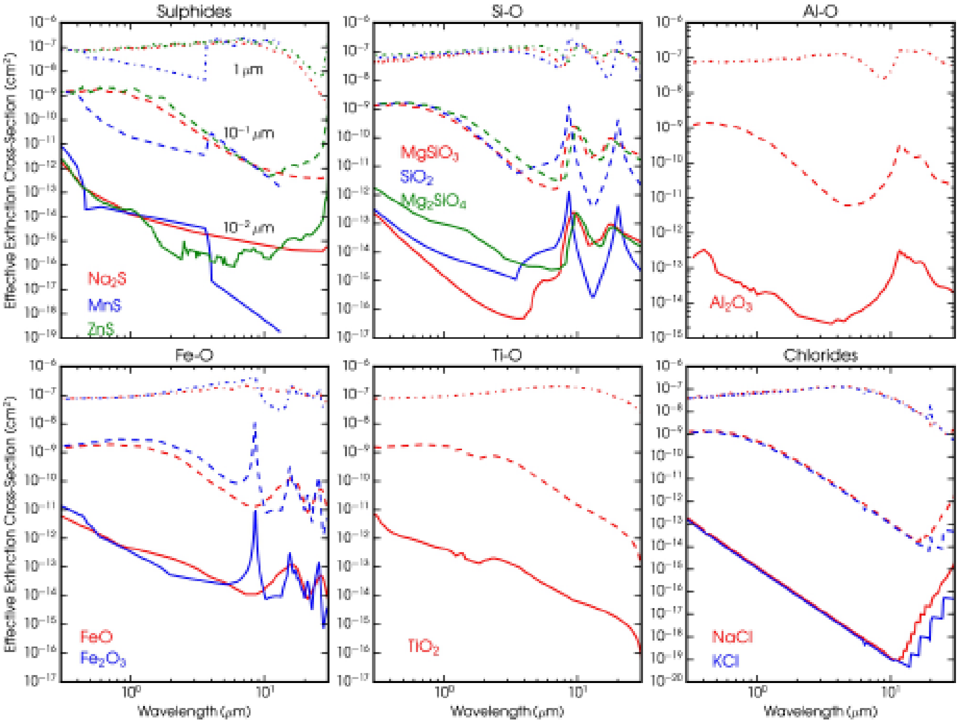

Figure 5.7: Figure from Pinhas and Madhusudhan (2017). Effective cross-sections of condensates calculated using our Mie theory code. Shown are the cross-sections for modal particle sizes of 10^{-2} μm (solid), 1 μm (dashed) and 1 μm (dot–dashed). The cross section of most condensates can be approximated with a gray absotpion or a uniform slope up to ~ 3 μm. Redwards, condensates absorb in specific spectral features thta may allow to distinguish among them.

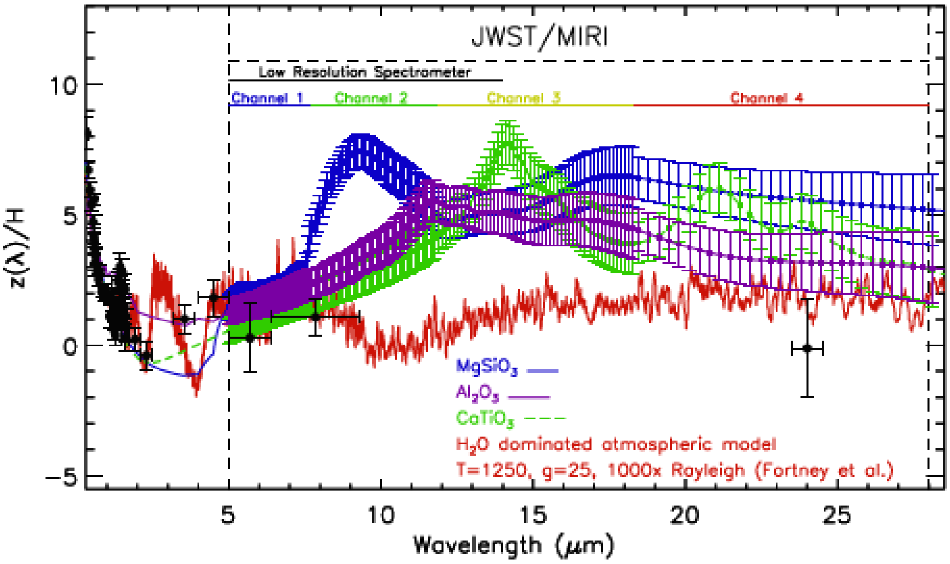

Figure 5.8: Figure from Wakeford and Sing (2015). Transmission spectrum of HD 189733b over-plotted on aerosol model spectra set to $R \sim 50$ for JWST/MIRI Medium resolution spectrograph channels 1–3 and $R \sim 30$ for channel 4 with the wavelength coverage highlighted above the different regions of the spectra they cover. Measuring the absorption features of condensates with JWST/MIRI will enabel a detailed characterization of aerosols, including their chemistry and size.

5.4 Temperature profile

Transmission spectra are relatively insensitive to the detailed temperature profile (Barstow et al. 2013, 2014; Kreidberg et al. 2015)[4]. Still, the strength of molecular features in transmission increases linearly with temperature due to the increase in scale height (see left panel of Fig. 4.6). Heng and Kitzmann (2017) showed that, at WFC3 precision, the use of isothermal temperature profiles is sufficient to capture this effect (but maybe not at JWST precision, e.g. Barstow et al. 2015; Rocchetto et al. 2016; Baudino et al. 2017).

Does the same assumption hold at high resolution? This question is not easy to answer, and I limited myself to study the impact of a thermal inversion on high-resolution transmission spectra (see Fig. 5.9). For emission spectroscopy the effect can be quite dramatic, as thermal inversions cause spectral lines to be in emission (albeit this effect was never detected; see de Kok et al. 2014; Schwarz et al. 2015).

I built two models with the same decreasing temperature profile up to 10^{-1} bar (from 1 750 K to 1 350 K). Higher up the two models converge to two separate isothermal profiles. Their temperature is set to 500 K in the case where no thermal inversion is present, and to 1 500 K to simulate a stratosphere (see Fig. 5.9). These temperature profiles are the same tested by (Brogi et al. 2016), that could not distinguish between them with one CRIRES transit of HD189733b[5].

---

[4] If the considered models implement self-consistent thermochemistry, the effect of the detailed temperature profile may not be negligible as it changes the composition of the atmosphere, but I do not discuss this here (e.g. Moses 2014; Drummond et al. 2016; Mollière et al. 2017).

[5] M. Brogi has kindly shared the models he produced, using a pipeline originally written by R. de Kok. I used these models to further validate $^{\pi}\eta$, see appendix 5.5. I thank P. Giacobbo for useful discussions and for facilitating the comparison process.

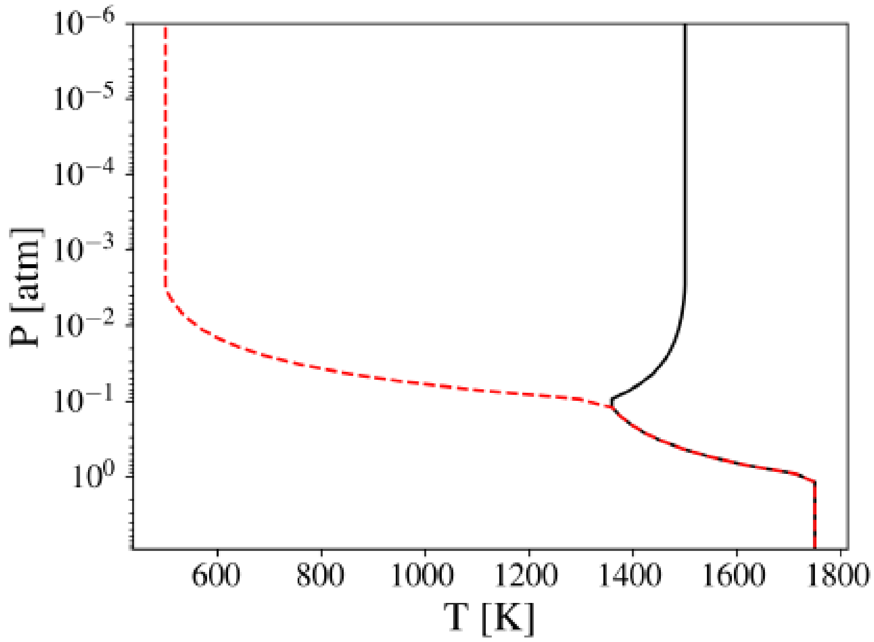

Figure 5.9: Temperature profiles adopted for models with a temperature inversion (black), and no temperature inversion (red); following Brogi et al. (2016).

In the presence of a temperature inversion, the upper part of the atmosphere is hotter, leading to an increased scale height. The absorption in the core of the molecular lines, generated higher up in the atmosphere, is thus expected to be stronger in the presence of an inversion; on the other hand, the wings of the lines should be similar, as they are generated at the same temperature. I computed the CCF of the two models using a binary mask at 1 200 K including 800 lines (the same used in chapter 4). Results are shown in figure 5.10. The reddest water bands have stronger lines, and indeed the contrast of their CCFs is larger. However, the effect is enhanced in the model with a temperature inversion, and leads to differences in contrast of up to ~ 50 ppm. Inspection of the two model transmission spectra confirms that the difference in absorption between the core and the wings of the lines of the model with the temperature inversion is indeed stronger than in the case with no inversion, and relative to their respective wings (see Fig. 5.11).
Although far from definitive, this test demonstrates that high resolution transmission spectra over a large wavelength range may be sensitive to the presence of a (strong) temperature inversion in hot Jupiters at the level of 50 ppm. Likely, Brogi et al. (2016) couldn't distinguish between the models for two main reasons: (1) the CRIRES observations that they employed have a limited wavelength coverage covered; (2) their cross correlation technique rescales the models, and is thus not sensitive to a difference in contrast but only in shape (see Appendix).

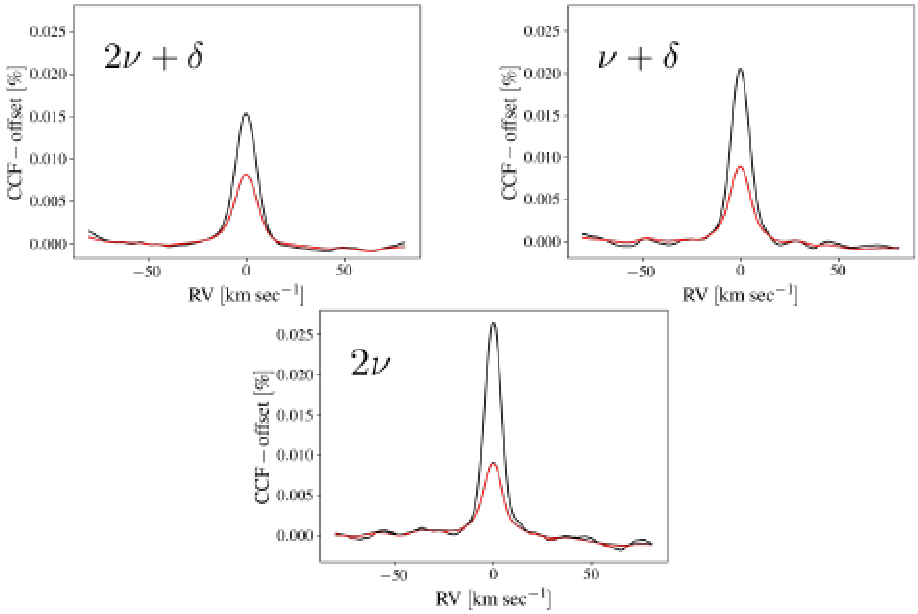

Figure 5.10: CCFs of $^{\pi}\eta$ models including a temperature inversion (black) and with no temperature inversion (red). An offset, measured in the wings of each CCF, was subtracted to each CCF. The three bands considered are ordered from shorter wavelengths to longer wavelengths as follows: upper left, upper right, bottom. The different behaviour between the models can be interpreted in terms of the presence of a temperature inversion (see text).

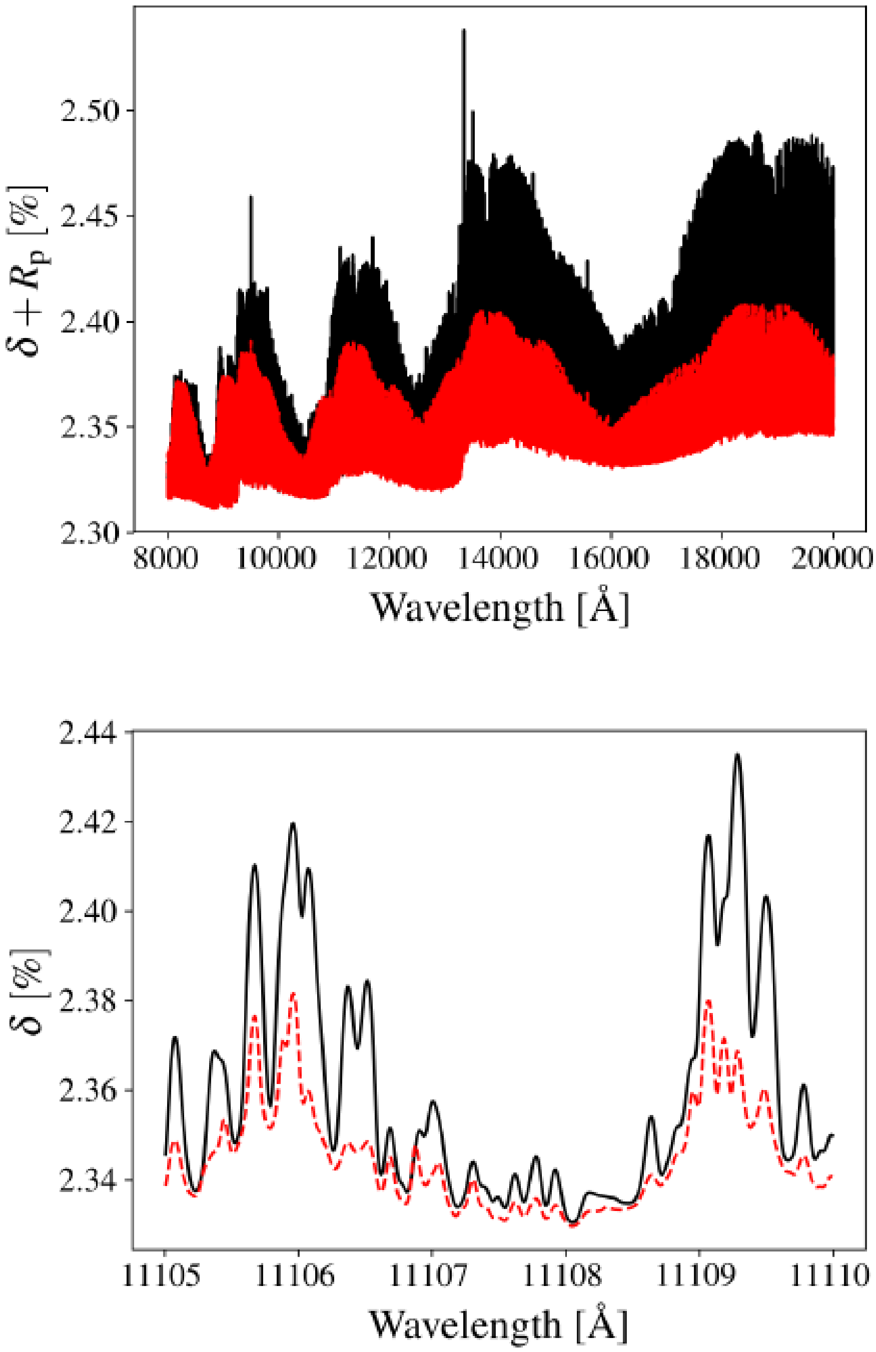

Figure 5.11: Red line: no temperature inversion. Black line: temperature inversion. *Upper panel:* in the presence of a temperature inversion, the molecular bands at longer wavelengths are generated higher up because of a larger scale height. *Lower panel:* a zoom on a narrow 5 Å region reveals that the wings of the lines of the two models is generated approximately at the same level, but not their cores. Also, the relative intensities of the lines change slightly. This is a result of the change in partition function, but is of secondary importance (see chapter 4).

5.5 Efficiently producing low- to medium-resolution spectra

The requirement of fully exploring a huge parameter space forces exoatmospheric scientists to include hypothesis and simplifications in their codes. As discussed in this chapter, this approach is safe when done with a grain of salt, but could sometimes lead to wrong conclusions. The precision and the accuracy of available data are among the factors that determine the degree of accuracy required in the models. The quality of data is continuously improving, and will make a leap forward with JWST and the E-ELTs. Computational efficiency is thus a key factor, as it allows to use more sophisticated models to interpret data. In this section, I describe a few methods that I will explore to optimize the simulation of low- to medium-resolution transmission spectra with ${}^{\pi}\eta$. This will allow me to include more physics, necessary for a comparison with data from the next generation observatories.
The bottleneck of ${}^{\pi}\eta$ is that it currently models the whole spectral range at a resolution of $\mathcal{R} \sim 10^6$. This approach qualifies ${}^{\pi}\eta$ as line-by-line code, and grants no (or slight) opacity loss, thus accuracy[6]. However, several alternatives to reduce the number of wavelength bins to be considered exist.
The "k-distribution tables" (Goody et al. 1989; Lacis and Oinas 1991; Fu and Liou 1992; Grimm and Heng 2015) are among the most commonly used techniques (e.g. Irwin et al. 2008; Amundsen et al. 2014; Mollière et al. 2015; Malik et al. 2017). This method is only exact for homogeneous atmospheres (constant pressure, temperature and mixing ratios). If one wants to apply it to inhomogeneous atmospheres, the "correlated-k" approximation needs to be invoked (Grimm and Heng 2015).
In a different approach, the "opacity sampling" method (Sneden et al. 1976; Kitzmann 2016), one solves the radiative-transfer equation on a limited number of wavelength (or wavenumber) bins. These bins are chosen so that the solution of the radiative-transfer equation is close to the true line-by-line case. Provided that the wavelength grid is chosen properly, no extra-assumption is required in this approach. Note that, de facto, ${}^{\pi}\eta$ uses an opacity sampling method, but the grid is so fine that it is practically equivalent to a line-by-line code. Several authors adopt this approach with coarser grids that allow them to perform retrieval (e.g. Madhusudhan and Seager 2009; Benneke and Seager 2013; Line et al. 2013; Waldmann et al. 2015; Lavie et al. 2017). Min (2017) recently presented an accurate combined opacity sampling – k-distribution method, and demonstrated a precision of 1% when simulating spectra at $R = 300$ with the ExoMol CH_4 line list ($\sim 10^{10}$ lines). The method is also very efficient (~ 1.5 hr to simulate the full line list at a given pressure and temperature).
In some cases, the number of lines to be treated is so large that even the application of opacity sampling methods may be inefficient, if a relatively high resolution ($R \gtrsim 10^2$) is required in the final spectrum. Recently, Yurchenko et al. (2017) applied a hybrid-approach to an extension of the ExoMol methane line-list up to 2 000 K. In this approach ("super-line", Rey et al. 2016), the strongest lines are fully modeled and weaker lines are treated as a continuum (a similar idea was followed in Hargreaves et al. 2015, but based on experimental data). Compared to a pure line-by-line calculation, a super-line approach demonstrates an accuracy of 1% on opacity grids of similar resolution as the one adopted by ${}^{\pi}\eta$, while fully modeling only $\sim 10^7$ molecular lines compared to the original 10^{10}. Cubillos (2017) presented

---

[6] Plus, the ability to simulate high-resolution transmission spectra, which was a primary aim for my work.

an open source implementation of a similar technique, accurate at the 1% on wavelength bins of 1 cm^{-1}. These are promising results, but a full exploration of the error induced on atmospheric spectra is still missing and warranted, especially at high-resolution.

Appendix: comparison with models by M. Brogi and R. De Kok

M. Brogi kindly provided a model that he produced with the code originally developed by R. de Kok (de Kok et al. 2013, 2014; Brogi et al. 2016). The model parameters follow closely the case with no thermal inversion discussed in Brogi et al. (2016), with water volume mixing ratio at 10^{-4}. I was thus able to use it as a validation test for $^{\pi}\eta$.

$^{\pi}\eta$ and the model suite by Brogi et al. (2016) share the input line list (HITEMP) and use a similar wavelength resolution (independently chosen by the two teams to simulate high resolution transmission spectra). They differ in the CIA implementation ($^{\pi}\eta$ adopts a more recent implementation by Richard et al. 2012, while Brogi et al. 2016 follow the prescription by Borysow et al. 2001; Borysow 2002), and $^{\pi}\eta$ allows for the inclusion of aerosols (not included for the comparison model since they were not considered in Brogi et al. 2016). I am not aware of other major differences; however, the two model suites were developed independently, thus the comparison is difficult (key aspects to check are, e.g., computation of the cross-sections and line broadening, treatment of Rayleigh scattering).

The comparison is shown in Fig. 5.12 in the common wavelength range, and in a zoomed part of the spectrum (lower panel). The overall agreement is remarkable: the shape of the bands is well reproduced and the single lines qualitatively match in position, relative intensity and broadening. The residual differences in the contrast are likely due to slight differences in the implemented temperature profile or in gravity.

As a further test, I computed the cross correlation function of both models with a binary mask at $T = 1\,200$ K containing 800 lines. To compare the two CCFs I removed the offset between the models to get rid of the dependence on the reference radius. I show the comparison for the band (2ν) in Fig. 5.13. Both models cross correlate well with the binary mask. The difference in contrast, already observed in Fig. 5.12, is preserved by my cross correlation technique. On the other hand, Brogi and collaborators make use of the C_CORRELATE IDL routine, which automatically normalizes the function to be cross correlated[7]. I thus rescaled the CCF obtained with $^{\pi}\eta$ to the CCF obtained from the model by M. Brogi/R. de Kok. The new comparison is shown in the right panel of Fig. 5.13. There are some residual differences, such as a small asymmetry in the CCF of $^{\pi}\eta$ (possibly due to Rayleigh scattering), and a hint of difference in the width of the CCFs. I emphasize that, while the agreement between the models is already remarkable, the comparison is to be considered only qualitative.

---

[7] M. Brogi and P. Giacobbe, private communication. Note that the (non-)sensitivity to the contrast of the models of the two techniques appears to be a major difference, and will be further explored in future work.

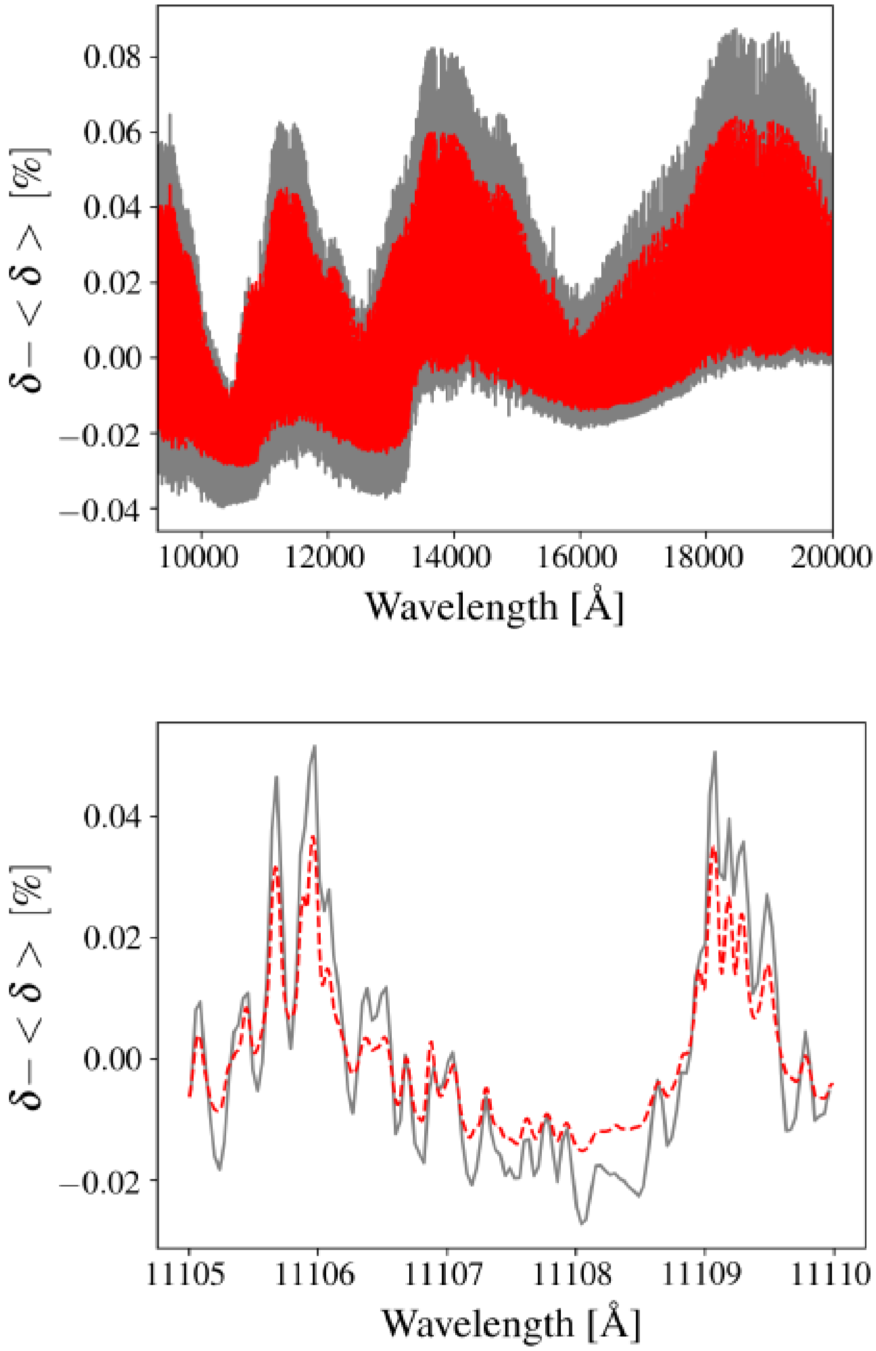

Figure 5.12: Red line: $^{\pi}\eta$. Gray line: model kindly provided by M. Brogi. The respective average was subtracted to each model to remove the dependence on the reference level. *Upper panel:* the shape of the molecular bands is in good agreement. *Lower panel:* a zoom on a narrow 5 Å region reveals that the positions and relative intensity of the lines are in very good agreement. The difference in contrast could be due to (1) a small difference in the input T–p profile or (2) a different gravity in the models.

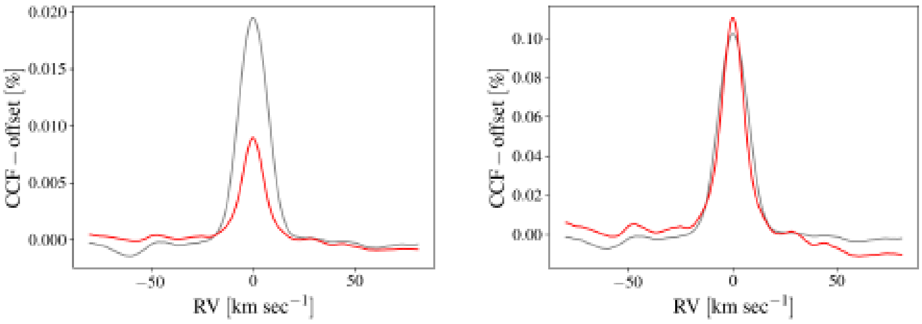

Figure 5.13: Comparison between the CCFs obtained with $^{\pi}\eta$ (red) and with the model by M. Brogi (gray). The offset, measured in the wings of each CCF, was subtracted to each CCF to remove the dependence on the reference level. *Left panel:* output of my cross correlation routine applied to the models. *Right panel:* I rescaled the CCF obtained from $^{\pi}\eta$ to compare the shape of the CCFs. The asymmetry visible in the $^{\pi}\eta$ CCF could be due to Rayleigh scattering. I consider the resemblance between the two CCFs a successful test for $^{\pi}\eta$.

A final remark

In this chapter, I hope I conveyed one of the most important lessons that I learned during this PhD, and tried to apply to my work. It's worth remarking it explicitly: it is the awareness of the assumptions done to obtain a scientific result that determines its solidity, and not how sophisticated is the tool employed to obtain it.

Chapter 6

Conclusions

During this thesis I studied exoplanetary atmospheres, with a focus on transmission spectroscopy of hot Jupiters. I extended the ETA code (Ehrenreich et al. 2006, 2012) to model high-resolution transmission spectra over a broad spectral range, including the lower and the upper atmosphere of hot Jupiters (${}^{\pi}\eta$; Pino et al. 2017). I tested ${}^{\pi}\eta$ extensively by comparing its predictions with observations and other models.

I used the code to assess the observational capabilities of forthcoming instruments that will provide transmission spectra at $R \sim 100\,000$ from the optical to the near infrared (GIANO+HARPS-N, ESPRESSO, ...). I found that, already with current precision, it will be possible to characterize aerosols in the atmospheres of hot Jupiters while simultaneously resolving the single lines of molecules.

I compared my models to data from different instruments, ranging from space-borne, low- to medium-resolution HST STIS + WFC3 (Pino et al. 2017), to ground-based, high-resolution HARPS transmission spectra (Wyttenbach et al. 2017; Allart et al. 2017; Pino et al. 2017). In Wyttenbach et al. (2017), we detected sodium at high-resolution in WASP-49b. This is the fourth planet in total to have such a detection, and the lowest one in mass. With my models, I confirmed the thermospheric origin of the feature. In Allart et al. (2017), we demonstrated the exquisite precision of cross-correlation techniques applied to current stabilized high-resolution, optical spectrographs, by benchmarking the technique in the search for water in the hot Jupiter HD189733b with HARPS. The wavelength coverage and the size of the telescope did not allow for a detection. Still, using my models, we were able to predict that ESPRESSO will be able to identify water in an HD189733b-like, aerosol-free atmosphere.

In Pino et al. (2017), I simultaneously reproduced observations of the lower and the upper atmosphere of HD189733b. This work confirmed the importance of broad wavelength coverage to constrain the altitude of aerosols, the use of the sodium feature as a probe of the thermosphere, and showed that the combination of different observational techniques is possible and brings deeper understanding of the chemical and physical conditions in the atmosphere.

This is why I asked (and obtained) HST medium-resolution observations (GO14782, PI: Pino. Data reduction ongoing) of WASP-43b, which shows a possible hint of exospheric sodium in previous high-resolution, ground-based HARPS+HARPS-N data. By combining the low- and high-resolution data sets it will be possible to reconstruct the thermal and dynamical conditions of the upper atmosphere of this planet, by inspecting both the wings and the core of the lines, as well as a (preliminary) hint of pre-transit absorption.

Future perspectives: observations I am involved in several observational projects that will inspect the atmosphere of exoplanets in a range of irradiation conditions and masses at high-resolution. As of today: 23 targets have successfully been observed in the context of HEARTS and SPADES (PI: D. Ehrenreich; including 1 DDT, PI: A. Wyttenbach; including three proposals with PI: V. Nascimbeni. See chapter 3), based at HARPS/-N; one target has successfully been observed with CARMENES (HAT-P-11b, PI: R. Allart); two targets has successfully been observed with PEPSI (WASP-76b, PI: M. Mallonn; HD189733b, PI: Turner); 7 targets will be observed in the forthcoming GAPS (Global Architecture of Planetary Systems)[1] program (PI: Sozzetti; observations not obtained yet), based on GIANO+HARPS-N. Using these data, I and collaborators will be able to constrain the thermal structure, the chemical composition and the presence of aerosols in the upper atmosphere and the lower atmosphere of tens of planets. With such detailed information for planets in a broad range of conditions, we will seek traces that their formation and evolution history left in their atmosphere.

These first steps are small, but give the direction for the leap forward that we will take in the next decades. First, a number of survey missions will enormously expand the number of planets transiting bright stars, thus suitable for atmospheric characterization (ground based: NGTS, Chazelas et al. 2012; SPECULOOS, Gillon et al. 2013; ExTrA, Bonfils et al. 2015; MASCARA, Snellen et al. 2012; ...; spaceborne: TESS, Ricker et al. 2014; and PLATO 2.0, Rauer et al. 2014). Second, a set of new instruments will combine increased spectral range and resolving power, and reveal details that are nowadays impossible to see (HARPS+NIRPS, Mayor et al. 2003, Conod et al. 2016; Bouchy et al. 2017; HARPS-N+GIANO, Oliva et al. 2006, Cosentino et al. 2012, Claudi et al. 2017; ESPRESSO, Pepe et al. 2010; CRIRES+, Follert et al. 2014; PEPSI, Strassmeier et al. 2008; IRD, Tamura et al. 2012, CARMENES, Quirrenbach et al. 2014; SPIRou, Thibault et al. 2012...).

The real game changers will be the 20–40 m class ELTs, (E-ELT, GMT, TMT) and JWST. The high-resolution spectrographs mounted on the ELTs (e.g. HIRES, Zerbi et al. 2014, Marconi et al. 2016; METIS, Brandl et al. 2014) and the infrared coverage of JWST will finally allow us to pierce through clouds and understand, among other aspects, the global circulation mechanisms and the chemistry of smaller and smaller planets.

Preparing to exploit the next generation observatories The increased precision of the observations requires models to evolve as well. I am thus planning to update ${}^{\pi}\eta$. The first step will be to make the code more efficient. The bottleneck of ${}^{\pi}\eta$ is currently the requirement to model a broad wavelength range (0.3 μm–2 μm) at high-resolution ($R \sim 10^6$). Two are the reasons that led to this choice: (1) a line-by-line approach grants no opacity loss, thus accuracy; (2) the simulation of high-resolution transmission spectra requires molecular lines to be singularly resolved.

As discussed in section 5.5, I will explore a number of schemes that are promising in terms of accuracy. On the one hand, JWST will cover a broad wavelength range, from 0.6 μm to 28.3 μm with a maximum resolving power of $\sim 3\,000$. Thus,

---

[1] `http://www.oact.inaf.it/exoit/EXO-IT/Projects/Entries/2011/12/27_GAPS.html`

molecular lines will not be resolved, and k-correlated methods, opacity sampling and super-line approaches are all valid alternatives to optimize the opacity treatment in $^{\pi}\eta$. On the other hand, high-resolution spectrographs resolve molecular lines, and many of these methods may result in inaccurate simulations. The super-line approach seems a promising alternative also in this case. Indeed, as shown by Allart et al. (2017), and discussed in chapter 4, hundreds, at most thousands of resolved lines are sufficient to apply the cross-correlation techniques. By decomposing opacity contributions in a table of $\sim 10^3$ resolved lines and a continuum, a super-line approach may allow to efficiently simulate accurate cross-correlation functions for high-resolution spectrographs. With an increased efficiency, including more molecular species or Mie scattering in $^{\pi}\eta$ should not be an issue.

With the refined version of $^{\pi}\eta$, I will aim to combine JWST and high-resolution, ground-based transmission spectra. JWST will constrain the abundance of the major carbon and oxygen bearing molecules, as well as the size distribution (and possibly composition) of aerosol scatterers. Ground-based, $R \sim 10^5$ observatories partially overlap with the wavelength range of JWST, and extend it to the optical. In this wavelength range, they will detect strong optical absorbers such as TiO, H_2O, possibly CH_4 and the alkali doublets, which all play a fundamental role in heat redistribution in the atmosphere. Combination of observations of the alkali doublets at low-resolution (HST STIS, JWST NIRSpec, JWST NIRISS, ground-based spectrophotometry, ...) and high-resolution (HARPS/-N, CARMENES, ESPRESSO, PEPSI, the ELTs, ...) will probe from the lower atmosphere, through their wings, to the upper atmosphere, through their narrow cores.

Summarizing, by optimizing $^{\pi}\eta$ I will combine low- to high-resolution transmission spectra provided by next generation observatories, with the aim to provide a global picture of exoplanetary atmospheres from their lower part to their upper part. This effort will contribute to shed light on formation and evolution of planets, and lead us closer to characterize the atmosphere of small, rocky planets.

Bibliography

V. Z. Adibekyan, E. Delgado Mena, S. G. Sousa, N. C. Santos, G. Israelian, J. I. González Hernández, M. Mayor, and A. A. Hakobyan. Exploring the α-enhancement of metal-poor planet-hosting stars. The Kepler and HARPS samples. *Astronomy & Astrophysics*, 547:A36, November 2012. doi: 10.1051/0004-6361/201220167.

R. Allart, C. Lovis, L. Pino, A. Wyttenbach, D. Ehrenreich, and F. Pepe. Search for water vapor in the high-resolution transmission spectrum of HD 189733b in the visible. *Astronomy & Astrophysics*, 606:A144, October 2017. doi: 10.1051/0004-6361/201730814.

D. S. Amundsen, I. Baraffe, P. Tremblin, J. Manners, W. Hayek, N. J. Mayne, and D. M. Acreman. Accuracy tests of radiation schemes used in hot Jupiter global circulation models. *Astronomy & Astrophysics*, 564:A59, April 2014. doi: 10.1051/0004-6361/201323169.

D. Angerhausen, G. Mandushev, A. Mandell, E. Dunham, E. Becklin, P. Collins, R. Hamilton, S. E. Logsdon, M. McElwain, I. McLean, E. Pfüller, M. Savage, S. Shenoy, W. Vacca, J. van Cleve, and J. Wolf. First exoplanet transit observation with the Stratospheric Observatory for Infrared Astronomy: confirmation of Rayleigh scattering in HD 189733 b with the High-Speed Imaging Photometer for Occultations. *Journal of Astronomical Telescopes, Instruments, and Systems*, 1(3):034002, July 2015. doi: 10.1117/1.JATIS.1.3.034002.

D. J. Armstrong, E. de Mooij, J. Barstow, H. P. Osborn, J. Blake, and N. F. Saniee. Variability in the atmosphere of the hot giant planet HAT-P-7 b. *Nature Astronomy*, 1:0004, December 2016. doi: 10.1038/s41550-016-0004.

É. Artigau, S. Bouchard, R. Doyon, and D. Lafrenière. Photometric Variability of the T2.5 Brown Dwarf SIMP J013656.5+093347: Evidence for Evolving Weather Patterns. *Astrophysical Journal*, 701:1534–1539, August 2009. doi: 10.1088/0004-637X/701/2/1534.

M. Asplund, N. Grevesse, and A. J. Sauval. The Solar Chemical Composition. In T. G. Barnes, III and F. N. Bash, editors, *Cosmic Abundances as Records of Stellar Evolution and Nucleosynthesis*, volume 336 of *Astronomical Society of the Pacific Conference Series*, page 25, September 2005.

N. Astudillo-Defru and P. Rojo. Ground-based detection of calcium and possibly scandium and hydrogen in the atmosphere of HD 209458b. *Astronomy & Astrophysics*, 557:A56, September 2013. doi: 10.1051/0004-6361/201219018.

A. Baranne, M. Mayor, and J. L. Poncet. CORAVEL - A new tool for radial velocity measurements. *Vistas in Astronomy*, 23:279–316, 1979. doi: 10.1016/0083-6656(79)90016-3.

A. Baranne, D. Queloz, M. Mayor, G. Adrianzyk, G. Knispel, D. Kohler, D. Lacroix, J.-P. Meunier, G. Rimbaud, and A. Vin. ELODIE: A spectrograph for accurate radial velocity measurements. *Astronomy and Astrophysics, Supplement*, 119: 373–390, October 1996.

R. J. Barber, J. Tennyson, G. J. Harris, and R. N. Tolchenov. A high-accuracy computed water line list. *Monthly Notices of the RAS*, 368:1087–1094, May 2006. doi: 10.1111/j.1365-2966.2006.10184.x.

T. Barman. Identification of Absorption Features in an Extrasolar Planet Atmosphere. *Astrophysical Journal, Letters*, 661:L191–L194, June 2007. doi: 10.1086/518736.

T. S. Barman, Q. M. Konopacky, B. Macintosh, and C. Marois. Simultaneous Detection of Water, Methane, and Carbon Monoxide in the Atmosphere of Exoplanet HR8799b. *Astrophysical Journal*, 804:61, May 2015. doi: 10.1088/0004-637X/804/1/61.

J. R. Barnes, C. A. Haswell, D. Staab, and G. Anglada-Escudé. The origin of the excess transit absorption in the HD 189733 system: planet or star? *Monthly Notices of the RAS*, 462:1012–1028, October 2016. doi: 10.1093/mnras/stw1713.

J. K. Barstow, S. Aigrain, P. G. J. Irwin, N. Bowles, L. N. Fletcher, and J.-M. Lee. On the potential of the EChO mission to characterize gas giant atmospheres. *Monthly Notices of the RAS*, 430:1188–1207, April 2013. doi: 10.1093/mnras/sts686.

J. K. Barstow, S. Aigrain, P. G. J. Irwin, T. Hackler, L. N. Fletcher, J. M. Lee, and N. P. Gibson. Clouds on the Hot Jupiter HD189733b: Constraints from the Reflection Spectrum. *Astrophysical Journal*, 786:154, May 2014. doi: 10.1088/0004-637X/786/2/154.

J. K. Barstow, S. Aigrain, P. G. J. Irwin, S. Kendrew, and L. N. Fletcher. Transit spectroscopy with James Webb Space Telescope: systematics, starspots and stitching. *Monthly Notices of the RAS*, 448:2546–2561, April 2015. doi: 10.1093/mnras/stv186.

J. K. Barstow, S. Aigrain, P. G. J. Irwin, and D. K. Sing. A Consistent Retrieval Analysis of 10 Hot Jupiters Observed in Transmission. *Astrophysical Journal*, 834: 50, January 2017. doi: 10.3847/1538-4357/834/1/50.

J.-L. Baudino, P. Molliere, O. Venot, P. Tremblin, B. Bezard, and P.-O. Lagage. Toward the analysis of JWST exoplanet spectra: Identifying troublesome model parameters. *ArXiv e-prints*, October 2017.

J. L. Bean, E. Miller-Ricci Kempton, and D. Homeier. A ground-based transmission spectrum of the super-Earth exoplanet GJ 1214b. *Nature*, 468:669–672, December 2010. doi: 10.1038/nature09596.

J. L. Bean, J.-M. Désert, P. Kabath, B. Stalder, S. Seager, E. Miller-Ricci Kempton, Z. K. Berta, D. Homeier, S. Walsh, and A. Seifahrt. The Optical and Near-infrared Transmission Spectrum of the Super-Earth GJ 1214b: Further Evidence for a Metal-rich Atmosphere. *Astrophysical Journal*, 743:92, December 2011. doi: 10.1088/0004-637X/743/1/92.

J. P. Beaulieu, S. Carey, I. Ribas, and G. Tinetti. Primary Transit of the Planet HD 189733b at 3.6 and 5.8 μm. *Astrophysical Journal*, 677:1343-1347, April 2008. doi: 10.1086/527045.

L. Ben-Jaffel. Exoplanet HD 209458b: Inflated Hydrogen Atmosphere but No Sign of Evaporation. *Astrophysical Journal, Letters*, 671:L61–L64, December 2007. doi: 10.1086/524706.

L. Ben-Jaffel. Spectral, Spatial, and Time Properties of the Hydrogen Nebula around Exoplanet HD 209458b. *Astrophysical Journal*, 688:1352-1360, December 2008. doi: 10.1086/592101.

L. Ben-Jaffel and G. E. Ballester. Hubble Space Telescope detection of oxygen in the atmosphere of exoplanet HD 189733b. *Astronomy & Astrophysics*, 553:A52, May 2013. doi: 10.1051/0004-6361/201221014.

L. Ben-Jaffel and S. Sona Hosseini. On the Existence of Energetic Atoms in the Upper Atmosphere of Exoplanet HD209458b. *Astrophysical Journal*, 709:1284–1296, February 2010. doi: 10.1088/0004-637X/709/2/1284.

B. Benneke. Strict Upper Limits on the Carbon-to-Oxygen Ratios of Eight Hot Jupiters from Self-Consistent Atmospheric Retrieval. *ArXiv e-prints*, April 2015.

B. Benneke and S. Seager. Atmospheric Retrieval for Super-Earths: Uniquely Constraining the Atmospheric Composition with Transmission Spectroscopy. *Astrophysical Journal*, 753:100, July 2012. doi: 10.1088/0004-637X/753/2/100.

B. Benneke and S. Seager. How to Distinguish between Cloudy Mini-Neptunes and Water/Volatile-dominated Super-Earths. *Astrophysical Journal*, 778:153, December 2013. doi: 10.1088/0004-637X/778/2/153.

Y. Bétrémieux. Effects of refraction on transmission spectra of gas giants: decrease of the Rayleigh scattering slope and breaking of retrieval degeneracies. *Monthly Notices of the RAS*, 456:4051–4060, March 2016. doi: 10.1093/mnras/stv2955.

J. L. Birkby, R. J. de Kok, M. Brogi, H. Schwarz, and I. A. G. Snellen. Discovery of Water at High Spectral Resolution in the Atmosphere of 51 Peg b. *Astronomical Journal*, 153:138, March 2017. doi: 10.3847/1538-3881/aa5c87.

S. Bolton and Juno Science Team. The Juno New Frontiers Jupiter polar orbiter mission. In *European Planetary Science Congress 2006*, page 535, 2006.

X. Bonfils, J. M. Almenara, L. Jocou, A. Wunsche, P. Kern, A. Delboulbé, X. Delfosse, P. Feautrier, T. Forveille, L. Gluck, S. Lafrasse, Y. Magnard, D. Maurel, T. Moulin, F. Murgas, P. Rabou, S. Rochat, A. Roux, and E. Stadler. ExTrA: Exoplanets in transit and their atmospheres. In *Techniques and Instrumentation for Detection of Exoplanets VII*, volume 9605 of *Proceedings of the SPIE*, page 96051L, September 2015. doi: 10.1117/12.2186999.

A. Borysow. Collision-induced absorption coefficients of H_2 pairs at temperatures from 60 K to 1000 K. *Astronomy & Astrophysics*, 390:779–782, August 2002. doi: 10.1051/0004-6361:20020555.

A. Borysow, U. G. Jorgensen, and C. Zheng. Model atmospheres of cool, low-metallicity stars: the importance of collision-induced absorption. *Astronomy & Astrophysics*, 324:185–195, August 1997.

A. Borysow, U. G. Jorgensen, and Y. Fu. High-temperature (1000-7000 K) collision-induced absorption of H"2 pairs computed from the first principles, with application to cool and dense stellar atmospheres. *Journal of Quantitative Spectroscopy and Radiative Transfer*, 68:235–255, February 2001. doi: 10.1016/S0022-4073(00)00023-6.

F. Bouchy, S. Udry, M. Mayor, C. Moutou, F. Pont, N. Iribarne, R. da Silva, S. Ilovaisky, D. Queloz, N. C. Santos, D. Ségransan, and S. Zucker. ELODIE metallicity-biased search for transiting Hot Jupiters. II. A very hot Jupiter transiting the bright K star HD 189733. *Astronomy & Astrophysics*, 444:L15–L19, December 2005. doi: 10.1051/0004-6361:200500201.

F. Bouchy, R. Doyon, É. Artigau, C. Melo, O. Hernandez, F. Wildi, X. Delfosse, C. Lovis, P. Figueira, B. L. . Canto Martins, J. I. . González Hernández, S. Thibault, V. Reshetov, F. Pepe, N. C. Santos, J. R. . de Medeiros, R. Rebolo, M. Abreu, V. Z. Adibekyan, T. Bandy, W. Benz, N. Blind, D. Bohlender, I. Boisse, S. Bovay, C. Broeg, D. Brousseau, A. Cabral, B. Chazelas, R. Cloutier, J. Coelho, U. Conod, A. Cumming, B. Delabre, L. Genolet, J. Hagelberg, R. Jayawardhana, H.-U. Käufl, D. Lafrenière, I. . de Castro Leão, L. Malo, A. . de Medeiros Martins, J. M. Matthews, S. Metchev, M. Oshagh, M. Ouellet, V. C. Parro, J. L. . Rasilla Piñeiro, P. Santos, M. Sarajlic, A. Segovia, M. Sordet, S. Udry, D. Valencia, P. Vallée, K. Venn, G. A. Wade, and L. Saddlemyer. Near-InfraRed Planet Searcher to Join HARPS on the ESO 3.6-metre Telescope. *The Messenger*, 169: 21–27, September 2017. doi: 10.18727/0722-6691/5034.

V. Bourrier, A. Lecavelier des Etangs, H. Dupuy, D. Ehrenreich, A. Vidal-Madjar, G. Hébrard, G. E. Ballester, J.-M. Désert, R. Ferlet, D. K. Sing, and P. J. Wheatley. Atmospheric escape from HD 189733b observed in H I Lyman-α: detailed analysis of HST/STIS September 2011 observations. *Astronomy & Astrophysics*, 551:A63, March 2013a. doi: 10.1051/0004-6361/201220533.

V. Bourrier, A. Lecavelier des Etangs, H. Dupuy, D. Ehrenreich, A. Vidal-Madjar, G. Hébrard, G. E. Ballester, J.-M. Désert, R. Ferlet, D. K. Sing, and P. J. Wheatley. Atmospheric escape from HD 189733b observed in H I Lyman-α: detailed analysis of HST/STIS September 2011 observations. *Astronomy & Astrophysics*, 551:A63, March 2013b. doi: 10.1051/0004-6361/201220533.

V. Bourrier, H. M. Cegla, C. Lovis, and A. Wyttenbach. Refined architecture of the WASP-8 system: A cautionary tale for traditional Rossiter-McLaughlin analysis. *Astronomy & Astrophysics*, 599:A33, March 2017. doi: 10.1051/0004-6361/201629973.

B. R. Brandl, M. Feldt, A. Glasse, M. Guedel, S. Heikamp, M. Kenworthy, R. Lenzen, M. R. Meyer, F. Molster, S. Paalvast, E. J. Pantin, S. P. Quanz, E. Schmalzl,

R. Stuik, L. Venema, and C. Waelkens. METIS: the mid-infrared E-ELT imager and spectrograph. In *Ground-based and Airborne Instrumentation for Astronomy V*, volume 9147 of *Proceedings of the SPIE*, page 914721, August 2014. doi: 10.1117/12.2056468.

M. Brogi, R. J. de Kok, S. Albrecht, I. A. G. Snellen, J. L. Birkby, and H. Schwarz. Rotation and Winds of Exoplanet HD 189733 b Measured with High-dispersion Transmission Spectroscopy. *Astrophysical Journal*, 817:106, February 2016. doi: 10.3847/0004-637X/817/2/106.

M. Brogi, M. Line, J. Bean, J.-M. Désert, and H. Schwarz. A Framework to Combine Low- and High-resolution Spectroscopy for the Atmospheres of Transiting Exoplanets. *Astrophysical Journal, Letters*, 839:L2, April 2017. doi: 10.3847/2041-8213/aa6933.

T. M. Brown. Transmission Spectra as Diagnostics of Extrasolar Giant Planet Atmospheres. *Astrophysical Journal*, 553:1006–1026, June 2001. doi: 10.1086/320950.

A. Burrows, M. S. Marley, and C. M. Sharp. The Near-Infrared and Optical Spectra of Methane Dwarfs and Brown Dwarfs. *Astrophysical Journal*, 531:438–446, March 2000. doi: 10.1086/308462.

A. Burrows, W. B. Hubbard, J. I. Lunine, and J. Liebert. The theory of brown dwarfs and extrasolar giant planets. *Reviews of Modern Physics*, 73:719–765, July 2001. doi: 10.1103/RevModPhys.73.719.

P. W. Cauley, S. Redfield, A. G. Jensen, and T. Barman. Variation in the Pre-transit Balmer Line Signal Around the Hot Jupiter HD 189733b. *Astronomical Journal*, 152:20, July 2016. doi: 10.3847/0004-6256/152/1/20.

H. M. Cegla, C. Lovis, V. Bourrier, B. Beeck, C. A. Watson, and F. Pepe. The Rossiter-McLaughlin effect reloaded: Probing the 3D spin-orbit geometry, differential stellar rotation, and the spatially-resolved stellar spectrum of star-planet systems. *Astronomy & Astrophysics*, 588:A127, April 2016. doi: 10.1051/0004-6361/201527794.

J. W. Chamberlain and D. M. Hunten. *Theory of planetary atmospheres. An introduction to their physics andchemistry.* 1987.

D. Charbonneau, T. M. Brown, R. W. Noyes, and R. L. Gilliland. Detection of an Extrasolar Planet Atmosphere. *Astrophysical Journal*, 568:377–384, March 2002. doi: 10.1086/338770.

B. Chazelas, D. Pollacco, D. Queloz, H. Rauer, P. J. Wheatley, R. West, J. Da Silva Bento, M. Burleigh, J. McCormac, P. Eigmüller, A. Erikson, L. Genolet, M. Goad, A. Jordán, M. Neveu, and S. Walker. NGTS: a robotic transit survey to detect Neptune and super-Earth mass planets. In *Ground-based and Airborne Telescopes IV*, volume 8444 of *Proceedings of the SPIE*, page 84440E, September 2012. doi: 10.1117/12.925755.

G. Chen, E. W. Guenther, E. Pallé, L. Nortmann, G. Nowak, S. Kunz, H. Parviainen, and F. Murgas. The GTC exoplanet transit spectroscopy survey. V. A spectrally-resolved Rayleigh scattering slope in GJ 3470b. *Astronomy & Astrophysics*, 600: A138, April 2017. doi: 10.1051/0004-6361/201630228.

R. Claudi, S. Benatti, I. Carleo, A. Ghedina, J. Guerra, G. Micela, E. Molinari, E. Oliva, M. Rainer, A. Tozzi, C. Baffa, A. Baruffolo, N. Buchschacher, M. Cecconi, R. Cosentino, D. Fantinel, L. Fini, F. Ghinassi, E. Giani, E. Gonzalez, M. Gonzalez, R. Gratton, A. Harutyunyan, N. Hernandez, M. Lodi, L. Malavolta, J. Maldonado, L. Origlia, N. Sanna, J. Sanjuan, S. Scuderi, U. Seemann, A. Sozzetti, H. Perez Ventura, M. Hernandez Diaz, A. Galli, C. Gonzalez, L. Riverol, and C. Riverol. GIARPS@TNG: GIANO-B and HARPS-N together for a wider wavelength range spectroscopy. *European Physical Journal Plus*, 132: 364, August 2017. doi: 10.1140/epjp/i2017-11647-9.

U. Conod, N. Blind, F. Wildi, and F. Pepe. Adaptive optics for high resolution spectroscopy: a direct application with the future NIRPS spectrograph. In *Adaptive Optics Systems V*, volume 9909 of *Proceedings of the SPIE*, page 990941, July 2016. doi: 10.1117/12.2233651.

R. Cosentino, C. Lovis, F. Pepe, A. Collier Cameron, D. W. Latham, E. Molinari, S. Udry, N. Bezawada, M. Black, A. Born, N. Buchschacher, D. Charbonneau, P. Figueira, M. Fleury, A. Galli, A. Gallie, X. Gao, A. Ghedina, C. Gonzalez, M. Gonzalez, J. Guerra, D. Henry, K. Horne, I. Hughes, D. Kelly, M. Lodi, D. Lunney, C. Maire, M. Mayor, G. Micela, M. P. Ordway, J. Peacock, D. Phillips, G. Piotto, D. Pollacco, D. Queloz, K. Rice, C. Riverol, L. Riverol, J. San Juan, D. Sasselov, D. Segransan, A. Sozzetti, D. Sosnowska, B. Stobie, A. Szentgyorgyi, A. Vick, and L. Weber. Harps-N: the new planet hunter at TNG. In *Ground-based and Airborne Instrumentation for Astronomy IV*, volume 8446 of *Proceedings of the SPIE*, page 84461V, September 2012. doi: 10.1117/12.925738.

A. N. Cox. *Allen's astrophysical quantities.* 2000.

I. J. M. Crossfield. Observations of Exoplanet Atmospheres. *Publications of the ASP*, 127:941, October 2015. doi: 10.1086/683115.

P. Cubillos. An Algorithm to Compress Line-transition Data for Radiative-transfer Calculations. *ArXiv e-prints*, October 2017.

S. Czesla, T. Klocová, S. Khalafinejad, U. Wolter, and J. H. M. M. Schmitt. The center-to-limb variation across the Fraunhofer lines of HD 189733. Sampling the stellar spectrum using a transiting planet. *Astronomy & Astrophysics*, 582:A51, October 2015. doi: 10.1051/0004-6361/201526386.

A. Dalgarno and D. A. Williams. Rayleigh Scattering by Molecular Hydrogen. *Astrophysical Journal*, 136:690–692, September 1962. doi: 10.1086/147428.

A. Dalgarno and D. A. Williams. Properties of the hydrogen molecule. *Proceedings of the Physical Society*, 85:685–689, April 1965. doi: 10.1088/0370-1328/85/4/308.

R. J. de Kok, M. Brogi, I. A. G. Snellen, J. Birkby, S. Albrecht, and E. J. W. de Mooij. Detection of carbon monoxide in the high-resolution day-side spectrum of the exoplanet HD 189733b. *Astronomy & Astrophysics*, 554:A82, June 2013. doi: 10.1051/0004-6361/201321381.

R. J. de Kok, J. Birkby, M. Brogi, H. Schwarz, S. Albrecht, E. J. W. de Mooij, and I. A. G. Snellen. Identifying new opportunities for exoplanet characterisation at high spectral resolution. *Astronomy & Astrophysics*, 561:A150, January 2014. doi: 10.1051/0004-6361/201322947.

D. Deming and K. Sheppard. Spectral Resolution-linked Bias in Transit Spectroscopy of Extrasolar Planets. *Astrophysical Journal, Letters*, 841:L3, May 2017. doi: 10.3847/2041-8213/aa706c.

D. Deming, A. Wilkins, P. McCullough, A. Burrows, J. J. Fortney, E. Agol, I. Dobbs-Dixon, N. Madhusudhan, N. Crouzet, J.-M. Desert, R. L. Gilliland, K. Haynes, H. A. Knutson, M. Line, Z. Magic, A. M. Mandell, S. Ranjan, D. Charbonneau, M. Clampin, S. Seager, and A. P. Showman. Infrared Transmission Spectroscopy of the Exoplanets HD 209458b and XO-1b Using the Wide Field Camera-3 on the Hubble Space Telescope. *Astrophysical Journal*, 774:95, September 2013. doi: 10.1088/0004-637X/774/2/95.

B.-O. Demory, M. Gillon, N. Madhusudhan, and D. Queloz. Variability in the super-Earth 55 Cnc e. *Monthly Notices of the RAS*, 455:2018–2027, January 2016. doi: 10.1093/mnras/stv2239.

J.-M. Désert, A. Vidal-Madjar, A. Lecavelier Des Etangs, D. Sing, D. Ehrenreich, G. Hébrard, and R. Ferlet. TiO and VO broad band absorption features in the optical spectrum of the atmosphere of the hot-Jupiter ¡ASTROBJ¿HD 209458b¡/ASTROBJ¿. *Astronomy & Astrophysics*, 492:585–592, December 2008. doi: 10.1051/0004-6361:200810355.

J.-M. Désert, A. Lecavelier des Etangs, G. Hébrard, D. K. Sing, D. Ehrenreich, R. Ferlet, and A. Vidal-Madjar. Search for Carbon Monoxide in the Atmosphere of the Transiting Exoplanet HD 189733b. *Astrophysical Journal*, 699:478–485, July 2009. doi: 10.1088/0004-637X/699/1/478.

E. Di Gloria, I. A. G. Snellen, and S. Albrecht. Using the chromatic Rossiter-McLaughlin effect to probe the broadband signature in the optical transmission spectrum of HD 189733b. *Astronomy & Astrophysics*, 580:A84, August 2015. doi: 10.1051/0004-6361/201526218.

H. Diamond-Lowe, K. B. Stevenson, J. L. Bean, M. R. Line, and J. J. Fortney. New Analysis Indicates No Thermal Inversion in the Atmosphere of HD 209458b. *Astrophysical Journal*, 796:66, November 2014. doi: 10.1088/0004-637X/796/1/66.

D. Dragomir, B. Benneke, K. A. Pearson, I. J. M. Crossfield, J. Eastman, T. Barman, and L. I. Biddle. Rayleigh Scattering in the Atmosphere of the Warm Exo-Neptune GJ 3470b. *Astrophysical Journal*, 814:102, December 2015. doi: 10.1088/0004-637X/814/2/102.

S. Dreizler, A. Reiners, D. Homeier, and M. Noll. On the possibility of detecting extrasolar planets' atmospheres with the Rossiter-McLaughlin effect. *Astronomy & Astrophysics*, 499:615–621, May 2009. doi: 10.1051/0004-6361/200810656.

C. D. Dressing, D. Charbonneau, X. Dumusque, S. Gettel, F. Pepe, A. Collier Cameron, D. W. Latham, E. Molinari, S. Udry, L. Affer, A. S. Bonomo, L. A. Buchhave, R. Cosentino, P. Figueira, A. F. M. Fiorenzano, A. Harutyunyan, R. D. Haywood, J. A. Johnson, M. Lopez-Morales, C. Lovis, L. Malavolta, M. Mayor, G. Micela, F. Motalebi, V. Nascimbeni, D. F. Phillips, G. Piotto, D. Pollacco, D. Queloz, K. Rice, D. Sasselov, D. Ségransan, A. Sozzetti, A. Szentgyorgyi, and C. Watson. The Mass of Kepler-93b and The Composition of Terrestrial Planets.

Astrophysical Journal, 800:135, February 2015. doi: 10.1088/0004-637X/800/2/135.

B. Drummond, P. Tremblin, I. Baraffe, D. S. Amundsen, N. J. Mayne, O. Venot, and J. Goyal. The effects of consistent chemical kinetics calculations on the pressure-temperature profiles and emission spectra of hot Jupiters. *Astronomy & Astrophysics*, 594:A69, October 2016. doi: 10.1051/0004-6361/201628799.

P. P. Eggleton. Approximations to the radii of Roche lobes. *Astrophysical Journal*, 268:368, May 1983. doi: 10.1086/160960.

D. Ehrenreich, G. Tinetti, A. Lecavelier Des Etangs, A. Vidal-Madjar, and F. Selsis. The transmission spectrum of Earth-size transiting planets. *Astronomy & Astrophysics*, 448:379–393, March 2006. doi: 10.1051/0004-6361:20053861.

D. Ehrenreich, G. Hébrard, A. Lecavelier des Etangs, D. K. Sing, J.-M. Désert, F. Bouchy, R. Ferlet, and A. Vidal-Madjar. A Spitzer Search for Water in the Transiting Exoplanet HD 189733b. *Astrophysical Journal, Letters*, 668:L179–L182, October 2007. doi: 10.1086/522792.

D. Ehrenreich, A. Lecavelier Des Etangs, G. Hébrard, J.-M. Désert, A. Vidal-Madjar, J. C. McConnell, C. D. Parkinson, G. E. Ballester, and R. Ferlet. New observations of the extended hydrogen exosphere of the extrasolar planet HD 209458b. *Astronomy & Astrophysics*, 483:933–937, June 2008. doi: 10.1051/0004-6361:200809460.

D. Ehrenreich, A. Vidal-Madjar, T. Widemann, G. Gronoff, P. Tanga, M. Barthélemy, J. Lilensten, A. Lecavelier Des Etangs, and L. Arnold. Transmission spectrum of Venus as a transiting exoplanet. *Astronomy & Astrophysics*, 537:L2, January 2012. doi: 10.1051/0004-6361/201118400.

D. Ehrenreich, X. Bonfils, C. Lovis, X. Delfosse, T. Forveille, M. Mayor, V. Neves, N. C. Santos, S. Udry, and D. Ségransan. Near-infrared transmission spectrum of the warm-Uranus GJ 3470b with the Wide Field Camera-3 on the Hubble Space Telescope. *Astronomy & Astrophysics*, 570:A89, October 2014. doi: 10.1051/0004-6361/201423809.

D. Ehrenreich, V. Bourrier, P. J. Wheatley, A. Lecavelier des Etangs, G. Hébrard, S. Udry, X. Bonfils, X. Delfosse, J.-M. Désert, D. K. Sing, and A. Vidal-Madjar. A giant comet-like cloud of hydrogen escaping the warm Neptune-mass exoplanet GJ 436b. *Nature*, 522:459–461, June 2015. doi: 10.1038/nature14501.

L. J. Esteves, E. J. W. de Mooij, R. Jayawardhana, C. Watson, and R. de Kok. A Search for Water in a Super-Earth Atmosphere: High-resolution Optical Spectroscopy of 55Cancri e. *Astronomical Journal*, 153:268, June 2017. doi: 10.3847/1538-3881/aa7133.

T. M. Evans, D. K. Sing, T. Kataria, J. Goyal, N. Nikolov, H. R. Wakeford, D. Deming, M. S. Marley, D. S. Amundsen, G. E. Ballester, J. K. Barstow, L. Ben-Jaffel, V. Bourrier, L. A. Buchhave, O. Cohen, D. Ehrenreich, A. García Muñoz, G. W. Henry, H. Knutson, P. Lavvas, A. L. D. Etangs, N. K. Lewis, M. López-Morales, A. M. Mandell, J. Sanz-Forcada, P. Tremblin, and R. Lupu. An ultrahot gas-giant exoplanet with a stratosphere. *Nature*, 548:58–61, August 2017. doi: 10.1038/nature23266.

P. D. Fischer, H. A. Knutson, D. K. Sing, G. W. Henry, M. W. Williamson, J. J. Fortney, A. S. Burrows, T. Kataria, N. Nikolov, A. P. Showman, G. E. Ballester, J.-M. Désert, S. Aigrain, D. Deming, A. Lecavelier des Etangs, and A. Vidal-Madjar. HST Hot-Jupiter Transmission Spectral Survey: Clear Skies for Cool Saturn WASP-39b. *Astrophysical Journal*, 827:19, August 2016. doi: 10.3847/0004-637X/827/1/19.

R. Follert, R. J. Dorn, E. Oliva, J. L. Lizon, A. Hatzes, N. Piskunov, A. Reiners, U. Seemann, E. Stempels, U. Heiter, T. Marquart, M. Lockhart, G. Anglada-Escude, T. Löwinger, D. Baade, J. Grunhut, P. Bristow, B. Klein, Y. Jung, D. J. Ives, F. Kerber, E. Pozna, J. Paufique, H. U. Kaeufl, L. Origlia, E. Valenti, D. Gojak, M. Hilker, L. Pasquini, A. Smette, and J. Smoker. CRIRES+: a cross-dispersed high-resolution infrared spectrograph for the ESO VLT. In *Ground-based and Airborne Instrumentation for Astronomy V*, volume 9147 of *Proceedings of the SPIE*, page 914719, July 2014. doi: 10.1117/12.2054197.

J. J. Fortney. The effect of condensates on the characterization of transiting planet atmospheres with transmission spectroscopy. *Monthly Notices of the RAS*, 364: 649–653, December 2005. doi: 10.1111/j.1365-2966.2005.09587.x.

J. J. Fortney, M. S. Marley, and J. W. Barnes. Planetary Radii across Five Orders of Magnitude in Mass and Stellar Insolation: Application to Transits. *Astrophysical Journal*, 659:1661–1672, April 2007. doi: 10.1086/512120.

J. J. Fortney, K. Lodders, M. S. Marley, and R. S. Freedman. A Unified Theory for the Atmospheres of the Hot and Very Hot Jupiters: Two Classes of Irradiated Atmospheres. *Astrophysical Journal*, 678:1419-1435, May 2008. doi: 10.1086/528370.

L. Fossati, C. A. Haswell, C. S. Froning, L. Hebb, S. Holmes, U. Kolb, C. Helling, A. Carter, P. Wheatley, A. Collier Cameron, B. Loeillet, D. Pollacco, R. Street, H. C. Stempels, E. Simpson, S. Udry, Y. C. Joshi, R. G. West, I. Skillen, and D. Wilson. Metals in the Exosphere of the Highly Irradiated Planet WASP-12b. *Astrophysical Journal, Letters*, 714:L222–L227, May 2010. doi: 10.1088/2041-8205/714/2/L222.

J. Fraine, D. Deming, B. Benneke, H. Knutson, A. Jordán, N. Espinoza, N. Madhusudhan, A. Wilkins, and K. Todorov. Water vapour absorption in the clear atmosphere of a Neptune-sized exoplanet. *Nature*, 513:526–529, September 2014. doi: 10.1038/nature13785.

R. S. Freedman, M. S. Marley, and K. Lodders. Line and Mean Opacities for Ultracool Dwarfs and Extrasolar Planets. *Astrophysical Journal, supplement*, 174: 504–513, February 2008. doi: 10.1086/521793.

R. S. Freedman, J. Lustig-Yaeger, J. J. Fortney, R. E. Lupu, M. S. Marley, and K. Lodders. Gaseous Mean Opacities for Giant Planet and Ultracool Dwarf Atmospheres over a Range of Metallicities and Temperatures. *Astrophysical Journal, supplement*, 214:25, October 2014. doi: 10.1088/0067-0049/214/2/25.

S. Fromang, J. Leconte, and K. Heng. Shear-driven instabilities and shocks in the atmospheres of hot Jupiters. *Astronomy & Astrophysics*, 591:A144, July 2016. doi: 10.1051/0004-6361/201527600.

Q. Fu and K. N. Liou. On the correlated k-distribution method for radiative transfer in nonhomogeneous atmospheres. *Journal of Atmospheric Sciences*, 49:2139–2156, November 1992. doi: 10.1175/1520-0469(1992)049⟨2139:OTCDMF⟩2.0.CO;2.

S. Gandhi and N. Madhusudhan. genesis: new self-consistent models of exoplanetary spectra. *Monthly Notices of the RAS*, 472:2334–2355, December 2017. doi: 10.1093/mnras/stx1601.

N. P. Gibson, N. Nikolov, D. K. Sing, J. K. Barstow, T. M. Evans, T. Kataria, and P. A. Wilson. VLT/FORS2 comparative transmission spectroscopy II: Confirmation of a cloud deck and Rayleigh scattering in WASP-31b, but no potassium? *Monthly Notices of the RAS*, 467:4591–4605, June 2017. doi: 10.1093/mnras/stx353.

R. L. Gilliland, W. J. Chaplin, E. W. Dunham, V. S. Argabright, W. J. Borucki, G. Basri, S. T. Bryson, D. L. Buzasi, D. A. Caldwell, Y. P. Elsworth, J. M. Jenkins, D. G. Koch, J. Kolodziejczak, A. Miglio, J. van Cleve, L. M. Walkowicz, and W. F. Welsh. Kepler Mission Stellar and Instrument Noise Properties. *Astrophysical Journal, supplement*, 197:6, November 2011. doi: 10.1088/0067-0049/197/1/6.

M. Gillon, A. H. M. J. Triaud, J. J. Fortney, B.-O. Demory, E. Jehin, M. Lendl, P. Magain, P. Kabath, D. Queloz, R. Alonso, D. R. Anderson, A. Collier Cameron, A. Fumel, L. Hebb, C. Hellier, A. Lanotte, P. F. L. Maxted, N. Mowlavi, and B. Smalley. The TRAPPIST survey of southern transiting planets. I. Thirty eclipses of the ultra-short period planet WASP-43 b. *Astronomy & Astrophysics*, 542:A4, June 2012. doi: 10.1051/0004-6361/201218817.

M. Gillon, E. Jehin, L. Delrez, P. Magain, C. Opitom, and S. Sohy. SPECULOOS: Search for habitable Planets EClipsing ULtra-cOOl Stars. In *Protostars and Planets VI Posters*, July 2013.

R. Goody, R. West, L. Chen, and D. Crisp. The correlated-k method for radiation calculations in nonhomogeneous atmospheres. *Journal of Quantitative Spectroscopy and Radiative Transfer*, 42:539–550, December 1989. doi: 10.1016/0022-4073(89)90044-7.

C. A. Griffith. Disentangling degenerate solutions from primary transit and secondary eclipse spectroscopy of exoplanets. *Philosophical Transactions of the Royal Society of London Series A*, 372:20130086–20130086, March 2014. doi: 10.1098/rsta.2013.0086.

S. L. Grimm and K. Heng. HELIOS-K: An Ultrafast, Open-source Opacity Calculator for Radiative Transfer. *Astrophysical Journal*, 808:182, August 2015. doi: 10.1088/0004-637X/808/2/182.

T. Guillot. Interior of Giant Planets Inside and Outside the Solar System. *Science*, 286, October 1999. doi: 10.1126/science.286.5437.72.

R. J. Hargreaves, P. F. Bernath, J. Bailey, and M. Dulick. Empirical Line Lists and Absorption Cross Sections for Methane at High Temperatures. *Astrophysical Journal*, 813:12, November 2015. doi: 10.1088/0004-637X/813/1/12.

C. Hedges and N. Madhusudhan. Effect of pressure broadening on molecular absorption cross sections in exoplanetary atmospheres. *Monthly Notices of the RAS*, 458:1427–1449, May 2016. doi: 10.1093/mnras/stw278.

W. D. Heintz. Reexamination of suspected unresolved binaries. *Astrophysical Journal*, 220:931–934, March 1978. doi: 10.1086/155982.

W. D. Heintz. The binary star 70 Ophiuchi revisited. *Journal of the RAS Canada*, 82:140–145, June 1988.

R. Helled and J. Lunine. Measuring Jupiter's water abundance by Juno: the link between interior and formation models. *Monthly Notices of the RAS*, 441:2273–2279, July 2014. doi: 10.1093/mnras/stu516.

C. Hellier, D. R. Anderson, A. Collier Cameron, M. Gillon, E. Jehin, M. Lendl, P. F. L. Maxted, F. Pepe, D. Pollacco, D. Queloz, D. Ségransan, B. Smalley, A. M. S. Smith, J. Southworth, A. H. M. J. Triaud, S. Udry, and R. G. West. WASP-43b: the closest-orbiting hot Jupiter. *Astronomy & Astrophysics*, 535:L7, November 2011. doi: 10.1051/0004-6361/201117081.

K. Heng. A Cloudiness Index for Transiting Exoplanets Based on the Sodium and Potassium Lines: Tentative Evidence for Hotter Atmospheres Being Less Cloudy at Visible Wavelengths. *Astrophysical Journal, Letters*, 826:L16, July 2016. doi: 10.3847/2041-8205/826/1/L16.

K. Heng and D. Kitzmann. The theory of transmission spectra revisited: a semi-analytical method for interpreting WFC3 data and an unresolved challenge. *Monthly Notices of the RAS*, 470:2972–2981, September 2017. doi: 10.1093/mnras/stx1453.

K. Heng and M. Marley. Radiative Transfer for Exoplanet Atmospheres. *ArXiv e-prints*, June 2017.

K. Heng, A. Wyttenbach, B. Lavie, D. K. Sing, D. Ehrenreich, and C. Lovis. A Non-isothermal Theory for Interpreting Sodium Lines in Transmission Spectra of Exoplanets. *Astrophysical Journal, Letters*, 803:L9, April 2015. doi: 10.1088/2041-8205/803/1/L9.

K. H. Hinkle, L. Wallace, and W. Livingston. Atmospheric Transmission Above Kitt Peak, 0.5 to 5.5 microns. In *American Astronomical Society Meeting Abstracts*, volume 35 of *Bulletin of the American Astronomical Society*, page 1260, December 2003.

H. J. Hoeijmakers, R. J. de Kok, I. A. G. Snellen, M. Brogi, J. L. Birkby, and H. Schwarz. A search for TiO in the optical high-resolution transmission spectrum of HD 209458b: Hindrance due to inaccuracies in the line database. *Astronomy & Astrophysics*, 575:A20, March 2015. doi: 10.1051/0004-6361/201424794.

J. R. Holt. Spectroscopic Determination of Stellar Rotation. *Astronomy and Astro-Physics (formerly The Sidereal Messenger)*, 12:646, 1893.

A. R. Howe and A. S. Burrows. Theoretical Transit Spectra for GJ 1214b and Other "Super-Earths". *Astrophysical Journal*, 756:176, September 2012. doi: 10.1088/0004-637X/756/2/176.

S. Hoyer, E. Pallé, D. Dragomir, and F. Murgas. Ruling out the Orbital Decay of the WASP-43b Exoplanet. *Astronomical Journal*, 151:137, June 2016. doi: 10.3847/0004-6256/151/6/137.

I. Hubeny, A. Burrows, and D. Sudarsky. A Possible Bifurcation in Atmospheres of Strongly Irradiated Stars and Planets. *Astrophysical Journal*, 594:1011–1018, September 2003. doi: 10.1086/377080.

C. M. Huitson, D. K. Sing, A. Vidal-Madjar, G. E. Ballester, A. Lecavelier des Etangs, J.-M. Désert, and F. Pont. Temperature-pressure profile of the hot Jupiter HD 189733b from HST sodium observations: detection of upper atmospheric heating. *Monthly Notices of the RAS*, 422:2477–2488, May 2012. doi: 10.1111/j.1365-2966.2012.20805.x.

N. Iro, B. Bézard, and T. Guillot. A time-dependent radiative model of HD 209458b. *Astronomy & Astrophysics*, 436:719–727, June 2005. doi: 10.1051/0004-6361:20048344.

P. G. J. Irwin. *Giant planets of our solar system : atmospheres compositions, and structure*. 2003.

P. G. J. Irwin, N. A. Teanby, R. de Kok, L. N. Fletcher, C. J. A. Howett, C. C. C. Tsang, C. F. Wilson, S. B. Calcutt, C. A. Nixon, and P. D. Parrish. The NEMESIS planetary atmosphere radiative transfer and retrieval tool. *Journal of Quantitative Spectroscopy and Radiative Transfer*, 109:1136–1150, April 2008. doi: 10.1016/j.jqsrt.2007.11.006.

A. G. Jensen, S. Redfield, M. Endl, W. D. Cochran, L. Koesterke, and T. S. Barman. A Survey of Alkali Line Absorption in Exoplanetary Atmospheres. *Astrophysical Journal*, 743:203, December 2011. doi: 10.1088/0004-637X/743/2/203.

M. Karplus. Refractive Index of the Hydrogen Molecule. *Journal of Chemical Physics*, 41:880–883, August 1964. doi: 10.1063/1.1725976.

W. Kausch, S. Noll, A. Smette, S. Kimeswenger, M. Barden, C. Szyszka, A. M. Jones, H. Sana, H. Horst, and F. Kerber. Molecfit: A general tool for telluric absorption correction. II. Quantitative evaluation on ESO-VLT/X-Shooterspectra. *Astronomy & Astrophysics*, 576:A78, April 2015. doi: 10.1051/0004-6361/201423909.

S. Khalafinejad, C. von Essen, H. J. Hoeijmakers, G. Zhou, T. Klocová, J. H. M. M. Schmitt, S. Dreizler, M. Lopez-Morales, T.-O. Husser, T. O. B. Schmidt, and R. Collet. Exoplanetary atmospheric sodium revealed by orbital motion. Narrowband transmission spectroscopy of HD 189733b with UVES. *Astronomy & Astrophysics*, 598:A131, February 2017. doi: 10.1051/0004-6361/201629473.

B. M. Kilpatrick, P. E. Cubillos, K. B. Stevenson, N. K. Lewis, H. Wakeford, R. J. Macdonald, N. Madhusudhan, J. Blecic, G. Bruno, A. Burrows, D. Deming, K. Heng, M. R. Line, C. V. Morley, V. Parmentier, G. S. Tucker, J. A. Valenti, I. P. Waldmann, J. L. Bean, C. Beichman, J. Fraine, J. E. Krick, J. D. Lothringer, and A. M. Mandell. Community targets for JWST's early release science program: evaluation of WASP-63b. *ArXiv e-prints*, April 2017.

J. Kirk, P. J. Wheatley, T. Louden, S. P. Littlefair, C. M. Copperwheat, D. J. Armstrong, T. R. Marsh, and V. S. Dhillon. Transmission spectroscopy of the inflated exoplanet WASP-52b, and evidence for a bright region on the stellar surface. *Monthly Notices of the RAS*, 463:2922–2931, December 2016. doi: 10.1093/mnras/stw2205.

D. Kitzmann. Revisiting the Scattering Greenhouse Effect of CO_2 Ice Clouds. *Astrophysical Journal, Letters*, 817:L18, February 2016. doi: 10.3847/2041-8205/817/2/L18.

H. A. Knutson, D. Dragomir, L. Kreidberg, E. M.-R. Kempton, P. R. McCullough, J. J. Fortney, J. L. Bean, M. Gillon, D. Homeier, and A. W. Howard. Hubble Space Telescope Near-IR Transmission Spectroscopy of the Super-Earth HD 97658b. *Astrophysical Journal*, 794:155, October 2014. doi: 10.1088/0004-637X/794/2/155.

T. T. Koskinen, A. D. Aylward, and S. Miller. A stability limit for the atmospheres of giant extrasolar planets. *Nature*, 450:845–848, December 2007. doi: 10.1038/nature06378.

T. T. Koskinen, R. V. Yelle, P. Lavvas, and N. K. Lewis. Characterizing the Thermosphere of HD209458b with UV Transit Observations. *Astrophysical Journal*, 723:116–128, November 2010. doi: 10.1088/0004-637X/723/1/116.

T. T. Koskinen, M. J. Harris, R. V. Yelle, and P. Lavvas. The escape of heavy atoms from the ionosphere of HD209458b. I. A photochemical-dynamical model of the thermosphere. *Icarus*, 226:1678–1694, November 2013a. doi: 10.1016/j.icarus.2012.09.027.

T. T. Koskinen, R. V. Yelle, M. J. Harris, and P. Lavvas. The escape of heavy atoms from the ionosphere of HD209458b. II. Interpretation of the observations. *Icarus*, 226:1695–1708, November 2013b. doi: 10.1016/j.icarus.2012.09.026.

A. E. Kramida, Yu Ralchenko, J. Reader, and Nist A. S. D. Team. NIST Atomic Spectra Database (version 3.1.5), 2015. URL `http://www.google.co.uk/search?hl=en\&\#38;client=firefox-a\&\#38;rls=org.mozilla:en-US:official\&\#38;hs=lmg\&\#38;q=NIST+Atomic+Spectra+Database+citation\&\#38;start=10\&\#38;sa=N`.

L. Kreidberg. Exoplanet Atmosphere Measurements from Transmission Spectroscopy and other Planet-Star Combined Light Observations. *ArXiv e-prints*, September 2017.

L. Kreidberg, J. L. Bean, J.-M. Désert, B. Benneke, D. Deming, K. B. Stevenson, S. Seager, Z. Berta-Thompson, A. Seifahrt, and D. Homeier. Clouds in the atmosphere of the super-Earth exoplanet GJ1214b. *Nature*, 505:69–72, January 2014. doi: 10.1038/nature12888.

L. Kreidberg, M. R. Line, J. L. Bean, K. B. Stevenson, J.-M. Désert, N. Madhusudhan, J. J. Fortney, J. K. Barstow, G. W. Henry, M. H. Williamson, and A. P. Showman. A Detection of Water in the Transmission Spectrum of the Hot Jupiter WASP-12b and Implications for Its Atmospheric Composition. *Astrophysical Journal*, 814:66, November 2015. doi: 10.1088/0004-637X/814/1/66.

A. A. Lacis and V. Oinas. A description of the correlated-k distribution method for modelling nongray gaseous absorption, thermal emission, and multiple scattering in vertically inhomogeneous atmospheres. *Journal of Geophysics Research*, 96: 9027–9064, May 1991. doi: 10.1029/90JD01945.

H. Lammer, F. Selsis, I. Ribas, E. F. Guinan, S. J. Bauer, and W. W. Weiss. Atmospheric Loss of Exoplanets Resulting from Stellar X-Ray and Extreme-Ultraviolet Heating. *Astrophysical Journal, Letters*, 598:L121–L124, December 2003. doi: 10.1086/380815.

L. E. Langland-Shula, S. S. Vogt, D. Charbonneau, P. Butler, and G. Marcy. A HIRES/Keck Spectroscopic Investigation of the Measurement of Sodium in the Atmosphere of HD 209458b. *Astrophysical Journal*, 696:1355–1366, May 2009. doi: 10.1088/0004-637X/696/2/1355.

D. W. Latham, R. P. Stefanik, T. Mazeh, M. Mayor, and G. Burki. The unseen companion of HD114762 - A probable brown dwarf. *Nature*, 339:38–40, May 1989. doi: 10.1038/339038a0.

B. Lavie, J. M. Mendonça, C. Mordasini, M. Malik, M. Bonnefoy, B.-O. Demory, M. Oreshenko, S. L. Grimm, D. Ehrenreich, and K. Heng. HELIOS-RETRIEVAL: An Open-source, Nested Sampling Atmospheric Retrieval Code; Application to the HR 8799 Exoplanets and Inferred Constraints for Planet Formation. *Astronomical Journal*, 154:91, September 2017. doi: 10.3847/1538-3881/aa7ed8.

P. Lavvas and T. Koskinen. Aerosol properties in the atmospheres of extrasolar giant planets. *ArXiv e-prints*, August 2017.

A. Lecavelier Des Etangs, F. Pont, A. Vidal-Madjar, and D. Sing. Rayleigh scattering in the transit spectrum of HD 189733b. *Astronomy & Astrophysics*, 481:L83–L86, April 2008a. doi: 10.1051/0004-6361:200809388.

A. Lecavelier Des Etangs, A. Vidal-Madjar, J.-M. Désert, and D. Sing. Rayleigh scattering by H_2 in the extrasolar planet HD 209458b. *Astronomy & Astrophysics*, 485:865–869, July 2008b. doi: 10.1051/0004-6361:200809704.

A. Lecavelier Des Etangs, D. Ehrenreich, A. Vidal-Madjar, G. E. Ballester, J.-M. Désert, R. Ferlet, G. Hébrard, D. K. Sing, K.-O. Tchakoumegni, and S. Udry. Evaporation of the planet HD 189733b observed in H I Lyman-α. *Astronomy & Astrophysics*, 514:A72, May 2010. doi: 10.1051/0004-6361/200913347.

A. Lecavelier des Etangs, V. Bourrier, P. J. Wheatley, H. Dupuy, D. Ehrenreich, A. Vidal-Madjar, G. Hébrard, G. E. Ballester, J.-M. Désert, R. Ferlet, and D. K. Sing. Temporal variations in the evaporating atmosphere of the exoplanet HD 189733b. *Astronomy & Astrophysics*, 543:L4, July 2012. doi: 10.1051/0004-6361/201219363.

J. Leconte and G. Chabrier. A new vision of giant planet interiors: Impact of double diffusive convection. *Astronomy & Astrophysics*, 540:A20, April 2012. doi: 10.1051/0004-6361/201117595.

M. Lendl, L. Delrez, M. Gillon, N. Madhusudhan, E. Jehin, D. Queloz, D. R. Anderson, B.-O. Demory, and C. Hellier. FORS2 observes a multi-epoch transmission spectrum of the hot Saturn-mass exoplanet WASP-49b. *Astronomy & Astrophysics*, 587:A67, March 2016. doi: 10.1051/0004-6361/201527594.

M. Lendl, P. E. Cubillos, J. Hagelberg, A. Müller, I. Juvan, and L. Fossati. Signs of strong Na and K absorption in the transmission spectrum of WASP-103b. *Astronomy & Astrophysics*, 606:A18, September 2017. doi: 10.1051/0004-6361/201731242.

A. R. Liddle. Information criteria for astrophysical model selection. *Monthly Notices of the RAS*, 377:L74–L78, May 2007. doi: 10.1111/j.1745-3933.2007.00306.x.

M. R. Line and V. Parmentier. The Influence of Nonuniform Cloud Cover on Transit Transmission Spectra. *Astrophysical Journal*, 820:78, March 2016. doi: 10.3847/0004-637X/820/1/78.

M. R. Line, H. Knutson, D. Deming, A. Wilkins, and J.-M. Desert. A Near-infrared Transmission Spectrum for the Warm Saturn HAT-P-12b. *Astrophysical Journal*, 778:183, December 2013. doi: 10.1088/0004-637X/778/2/183.

M. R. Line, K. B. Stevenson, J. Bean, J.-M. Desert, J. J. Fortney, L. Kreidberg, N. Madhusudhan, A. P. Showman, and H. Diamond-Lowe. No Thermal Inversion and a Solar Water Abundance for the Hot Jupiter HD 209458b from HST/WFC3 Spectroscopy. *Astronomical Journal*, 152:203, December 2016. doi: 10.3847/0004-6256/152/6/203.

J. L. Linsky, H. Yang, K. France, C. S. Froning, J. C. Green, J. T. Stocke, and S. N. Osterman. Observations of Mass Loss from the Transiting Exoplanet HD 209458b. *Astrophysical Journal*, 717:1291–1299, July 2010. doi: 10.1088/0004-637X/717/2/1291.

K. Lodders. Alkali Element Chemistry in Cool Dwarf Atmospheres. *Astrophysical Journal*, 519:793–801, July 1999. doi: 10.1086/307387.

K. Lodders. Jupiter Formed with More Tar than Ice. *Astrophysical Journal*, 611:587–597, August 2004. doi: 10.1086/421970.

T. Louden and P. J. Wheatley. Spatially Resolved Eastward Winds and Rotation of HD 189733b. *Astrophysical Journal, Letters*, 814:L24, December 2015. doi: 10.1088/2041-8205/814/2/L24.

R. J. MacDonald and N. Madhusudhan. HD 209458b in new light: evidence of nitrogen chemistry, patchy clouds and sub-solar water. *Monthly Notices of the RAS*, 469:1979–1996, August 2017. doi: 10.1093/mnras/stx804.

N. Madhusudhan. C/O Ratio as a Dimension for Characterizing Exoplanetary Atmospheres. *Astrophysical Journal*, 758:36, October 2012. doi: 10.1088/0004-637X/758/1/36.

N. Madhusudhan and S. Seager. A Temperature and Abundance Retrieval Method for Exoplanet Atmospheres. *Astrophysical Journal*, 707:24–39, December 2009. doi: 10.1088/0004-637X/707/1/24.

N. Madhusudhan, J. Harrington, K. B. Stevenson, S. Nymeyer, C. J. Campo, P. J. Wheatley, D. Deming, J. Blecic, R. A. Hardy, N. B. Lust, D. R. Anderson,

A. Collier-Cameron, C. B. T. Britt, W. C. Bowman, L. Hebb, C. Hellier, P. F. L. Maxted, D. Pollacco, and R. G. West. A high C/O ratio and weak thermal inversion in the atmosphere of exoplanet WASP-12b. *Nature*, 469:64–67, January 2011. doi: 10.1038/nature09602.

N. Madhusudhan, N. Crouzet, P. R. McCullough, D. Deming, and C. Hedges. H_2O Abundances in the Atmospheres of Three Hot Jupiters. *Astrophysical Journal, Letters*, 791:L9, August 2014a. doi: 10.1088/2041-8205/791/1/L9.

N. Madhusudhan, H. Knutson, J. J. Fortney, and T. Barman. Exoplanetary Atmospheres. *Protostars and Planets VI*, pages 739–762, 2014b. doi: 10.2458/azu_uapress_9780816531240-ch032.

N. Madhusudhan, B. Bitsch, A. Johansen, and L. Eriksson. Atmospheric signatures of giant exoplanet formation by pebble accretion. *Monthly Notices of the RAS*, 469:4102–4115, August 2017. doi: 10.1093/mnras/stx1139.

Nikku Madhusudhan, Marcelino Agúndez, Julianne I. Moses, and Yongyun Hu. Exoplanetary atmospheres—chemistry, formation conditions, and habitability. *Space Science Reviews*, 205(1):285–348, Dec 2016. ISSN 1572-9672. doi: 10.1007/s11214-016-0254-3. URL `https://doi.org/10.1007/s11214-016-0254-3`.

M. Malik, L. Grosheintz, J. M. Mendonça, S. L. Grimm, B. Lavie, D. Kitzmann, S.-M. Tsai, A. Burrows, L. Kreidberg, M. Bedell, J. L. Bean, K. B. Stevenson, and K. Heng. HELIOS: An Open-source, GPU-accelerated Radiative Transfer Code for Self-consistent Exoplanetary Atmospheres. *Astronomical Journal*, 153:56, February 2017. doi: 10.3847/1538-3881/153/2/56.

M. Mallonn and K. G. Strassmeier. Transmission spectroscopy of HAT-P-32b with the LBT: confirmation of clouds/hazes in the planetary atmosphere. *Astronomy & Astrophysics*, 590:A100, May 2016. doi: 10.1051/0004-6361/201527898.

M. Mallonn and H. R. Wakeford. Near-UV transit photometry of HAT-P-32 b with the LBT: Silicate aerosols in the planetary atmosphere. *ArXiv e-prints*, July 2017.

M. Mallonn, I. Bernt, E. Herrero, S. Hoyer, J. Kirk, P. J. Wheatley, M. Seeliger, F. Mackebrandt, C. von Essen, K. G. Strassmeier, T. Granzer, A. Künstler, V. S. Dhillon, T. R. Marsh, and J. Gaitan. Broad-band spectrophotometry of HAT-P-32 b: search for a scattering signature in the planetary spectrum. *Monthly Notices of the RAS*, 463:604–614, November 2016. doi: 10.1093/mnras/stw1999.

A. Marconi, P. Di Marcantonio, V. D'Odorico, S. Cristiani, R. Maiolino, E. Oliva, L. Origlia, M. Riva, L. Valenziano, F. M. Zerbi, M. Abreu, V. Adibekyan, C. Allende Prieto, P. J. Amado, W. Benz, I. Boisse, X. Bonfils, F. Bouchy, L. Buchhave, D. Buscher, A. Cabral, B. L. Canto Martins, A. Chiavassa, J. Coelho, L. B. Christensen, E. Delgado-Mena, J. R. de Medeiros, I. Di Varano, P. Figueira, M. Fisher, J. P. U. Fynbo, A. C. H. Glasse, M. Haehnelt, C. Haniff, C. J. Hansen, A. Hatzes, P. Huke, A. J. Korn, I. C. Leão, J. Liske, C. Lovis, P. Maslowski, I. Matute, R. A. McCracken, C. J. A. P. Martins, M. J. P. F. G. Monteiro, S. Morris, T. Morris, H. Nicklas, A. Niedzielski, N. J. Nunes, E. Palle, P. M. Parr-Burman, V. Parro, I. Parry, F. Pepe, N. Piskunov, D. Queloz, A. Quirrenbach, R. Rebolo Lopez, A. Reiners, D. T. Reid, N. Santos, W. Seifert, S. Sousa, H. C. Stempels, K. Strassmeier, X. Sun, S. Udry, L. Vanzi, M. Vestergaard, M. Weber, and E. Zackrisson.

EELT-HIRES the high-resolution spectrograph for the E-ELT. In *Ground-based and Airborne Instrumentation for Astronomy VI*, volume 9908 of *Proceedings of the SPIE*, page 990823, August 2016. doi: 10.1117/12.2231653.

M. S. Marley and T. D. Robinson. On the Cool Side: Modeling the Atmospheres of Brown Dwarfs and Giant Planets. *Annual Review of Astronomy and Astrophysics*, 53:279–323, August 2015. doi: 10.1146/annurev-astro-082214-122522.

S. Matousek. The Juno New Frontiers mission. *Acta Astronautica*, 61:932–939, November 2007. doi: 10.1016/j.actaastro.2006.12.013.

M. Mayor and D. Queloz. A Jupiter-mass companion to a solar-type star. *Nature*, 378:355–359, November 1995. doi: 10.1038/378355a0.

M. Mayor, F. Pepe, D. Queloz, F. Bouchy, G. Rupprecht, G. Lo Curto, G. Avila, W. Benz, J.-L. Bertaux, X. Bonfils, T. Dall, H. Dekker, B. Delabre, W. Eckert, M. Fleury, A. Gilliotte, D. Gojak, J. C. Guzman, D. Kohler, J.-L. Lizon, A. Longinotti, C. Lovis, D. Megevand, L. Pasquini, J. Reyes, J.-P. Sivan, D. Sosnowska, R. Soto, S. Udry, A. van Kesteren, L. Weber, and U. Weilenmann. Setting New Standards with HARPS. *The Messenger*, 114:20–24, December 2003.

P. R. McCullough, N. Crouzet, D. Deming, and N. Madhusudhan. Water Vapor in the Spectrum of the Extrasolar Planet HD 189733b. I. The Transit. *Astrophysical Journal*, 791:55, August 2014. doi: 10.1088/0004-637X/791/1/55.

D. B. McLaughlin. Some results of a spectrographic study of the Algol system. *Astrophysical Journal*, 60, July 1924. doi: 10.1086/142826.

Y. Miguel and L. Kaltenegger. Exploring Atmospheres of Hot Mini-Neptunes and Extrasolar Giant Planets Orbiting Different Stars with Application to HD 97658b, WASP-12b, CoRoT-2b, XO-1b, and HD 189733b. *Astrophysical Journal*, 780:166, January 2014. doi: 10.1088/0004-637X/780/2/166.

D. Mihalas. *Stellar atmospheres*. 1970.

M. Min. Random sampling technique for ultra-fast computations of molecular opacities for exoplanet atmospheres. *ArXiv e-prints*, October 2017.

P. Mollière, R. van Boekel, C. Dullemond, T. Henning, and C. Mordasini. Model Atmospheres of Irradiated Exoplanets: The Influence of Stellar Parameters, Metallicity, and the C/O Ratio. *Astrophysical Journal*, 813:47, November 2015. doi: 10.1088/0004-637X/813/1/47.

P. Mollière, R. van Boekel, J. Bouwman, T. Henning, P.-O. Lagage, and M. Min. Observing transiting planets with JWST. Prime targets and their synthetic spectral observations. *Astronomy & Astrophysics*, 600:A10, April 2017. doi: 10.1051/0004-6361/201629800.

C. V. Morley, J. J. Fortney, E. M.-R. Kempton, M. S. Marley, C. Visscher, and K. Zahnle. Quantitatively Assessing the Role of Clouds in the Transmission Spectrum of GJ 1214b. *Astrophysical Journal*, 775:33, September 2013. doi: 10.1088/0004-637X/775/1/33.

C. V. Morley, M. S. Marley, J. J. Fortney, R. Lupu, D. Saumon, T. Greene, and K. Lodders. Water Clouds in Y Dwarfs and Exoplanets. *Astrophysical Journal*, 787:78, May 2014. doi: 10.1088/0004-637X/787/1/78.

T. D. Morton, S. T. Bryson, J. L. Coughlin, J. F. Rowe, G. Ravichandran, E. A. Petigura, M. R. Haas, and N. M. Batalha. False Positive Probabilities for all Kepler Objects of Interest: 1284 Newly Validated Planets and 428 Likely False Positives. *Astrophysical Journal*, 822:86, May 2016. doi: 10.3847/0004-637X/822/2/86.

J. I. Moses. Chemical kinetics on extrasolar planets. *Philosophical Transactions of the Royal Society of London Series A*, 372:20130073–20130073, March 2014. doi: 10.1098/rsta.2013.0073.

J. I. Moses, N. Madhusudhan, C. Visscher, and R. S. Freedman. Chemical Consequences of the C/O Ratio on Hot Jupiters: Examples from WASP-12b, CoRoT-2b, XO-1b, and HD 189733b. *Astrophysical Journal*, 763:25, January 2013. doi: 10.1088/0004-637X/763/1/25.

F. Motalebi, S. Udry, M. Gillon, C. Lovis, D. Ségransan, L. A. Buchhave, B. O. Demory, L. Malavolta, C. D. Dressing, D. Sasselov, K. Rice, D. Charbonneau, A. Collier Cameron, D. Latham, E. Molinari, F. Pepe, L. Affer, A. S. Bonomo, R. Cosentino, X. Dumusque, P. Figueira, A. F. M. Fiorenzano, S. Gettel, A. Harutyunyan, R. D. Haywood, J. Johnson, E. Lopez, M. Lopez-Morales, M. Mayor, G. Micela, A. Mortier, V. Nascimbeni, D. Philips, G. Piotto, D. Pollacco, D. Queloz, A. Sozzetti, A. Vanderburg, and C. A. Watson. The HARPS-N Rocky Planet Search. I. HD 219134 b: A transiting rocky planet in a multi-planet system at 6.5 pc from the Sun. *Astronomy & Astrophysics*, 584:A72, December 2015. doi: 10.1051/0004-6361/201526822.

V. Nascimbeni, G. Piotto, I. Pagano, G. Scandariato, E. Sani, and M. Fumana. The blue sky of GJ3470b: the atmosphere of a low-mass planet unveiled by ground-based photometry. *Astronomy & Astrophysics*, 559:A32, November 2013. doi: 10.1051/0004-6361/201321971.

V. Nascimbeni, M. Mallonn, G. Scandariato, I. Pagano, G. Piotto, G. Micela, S. Messina, G. Leto, K. G. Strassmeier, S. Bisogni, and R. Speziali. Large Binocular Telescope view of the atmosphere of GJ1214b. *Astronomy & Astrophysics*, 579:A113, July 2015. doi: 10.1051/0004-6361/201425350.

N. Nikolov, D. K. Sing, F. Pont, A. S. Burrows, J. J. Fortney, G. E. Ballester, T. M. Evans, C. M. Huitson, H. R. Wakeford, P. A. Wilson, S. Aigrain, D. Deming, N. P. Gibson, G. W. Henry, H. Knutson, A. Lecavelier des Etangs, A. P. Showman, A. Vidal-Madjar, and K. Zahnle. Hubble Space Telescope hot Jupiter transmission spectral survey: a detection of Na and strong optical absorption in HAT-P-1b. *Monthly Notices of the RAS*, 437:46–66, January 2014. doi: 10.1093/mnras/stt1859.

E. Oliva, L. Origlia, C. Baffa, C. Biliotti, P. Bruno, F. D'Amato, C. Del Vecchio, G. Falcini, S. Gennari, F. Ghinassi, E. Giani, M. Gonzalez, F. Leone, M. Lolli, M. Lodi, R. Maiolino, F. Mannucci, G. Marcucci, I. Mochi, P. Montegriffo, E. Rossetti, S. Scuderi, and M. Sozzi. The GIANO-TNG spectrometer. In *Society of*

Photo-Optical Instrumentation Engineers (SPIE) Conference Series, volume 6269 of *Proceedings of the SPIE*, page 626919, June 2006. doi: 10.1117/12.670006.

M. Oreshenko, B. Lavie, S. L. Grimm, S.-M. Tsai, M. Malik, B.-O. Demory, C. Mordasini, Y. Alibert, W. Benz, S. P. Quanz, R. Trotta, and K. Heng. Retrieval Analysis of the Emission Spectrum of WASP-12b: Sensitivity of Outcomes to Prior Assumptions and Implications for Formation History. *Astrophysical Journal, Letters*, 847:L3, September 2017. doi: 10.3847/2041-8213/aa8acf.

G. S. Orton. Atmospheric structure of the outer planets from thermal emission data. In C. G. Wynn-Williams and D. P. Cruikshank, editors, *Infrared Astronomy*, volume 96 of *IAU Symposium*, pages 35–55, 1981.

M. Oshagh, N. C. Santos, D. Ehrenreich, N. Haghighipour, P. Figueira, A. Santerne, and M. Montalto. Impact of occultations of stellar active regions on transmission spectra. Can occultation of a plage mimic the signature of a blue sky? *Astronomy & Astrophysics*, 568:A99, August 2014. doi: 10.1051/0004-6361/201424059.

E. N. Parker. Dynamical Properties of Stellar Coronas and Stellar Winds, IV. The Separate Existence of Subsonic and Supersonic Solutions. *Astrophysical Journal*, 141:1463, May 1965. doi: 10.1086/148235.

V. Parmentier. *Thermal structure, composition, atmospheric dynamics and long-term evolution of irradiated exoplanets*. PhD thesis, LAGRANGE - Joseph Louis LAGRANGE - Université Nice Sophia Antipolis (UNS); Observatoire de la Côte d'Azur CNRS : UMR7293 ¡EMAIL¿vivien.parmentier@oca.eu¡/EMAIL¿, 2014.

H. Partridge and D. W. Schwenke. The determination of an accurate isotope dependent potential energy surface for water from extensive ab initio calculations and experimental data. *Journal of Chemical Physics*, 106:4618–4639, March 1997. doi: 10.1063/1.473987.

H. Parviainen, E. Pallé, L. Nortmann, G. Nowak, N. Iro, F. Murgas, and S. Aigrain. The GTC exoplanet transit spectroscopy survey. II. An overly large Rayleigh-like feature for exoplanet TrES-3b. *Astronomy & Astrophysics*, 585:A114, January 2016. doi: 10.1051/0004-6361/201526313.

F. Pepe, M. Mayor, F. Galland, D. Naef, D. Queloz, N. C. Santos, S. Udry, and M. Burnet. The CORALIE survey for southern extra-solar planets VII. Two short-period Saturnian companions to ¡ASTROBJ¿HD 108147¡/ASTROBJ¿ and ¡ASTROBJ¿HD 168746¡/ASTROBJ¿. *Astronomy & Astrophysics*, 388:632–638, June 2002. doi: 10.1051/0004-6361:20020433.

F. A. Pepe, S. Cristiani, R. Rebolo Lopez, N. C. Santos, A. Amorim, G. Avila, W. Benz, P. Bonifacio, A. Cabral, P. Carvas, R. Cirami, J. Coelho, M. Comari, I. Coretti, V. De Caprio, H. Dekker, B. Delabre, P. Di Marcantonio, V. D'Odorico, M. Fleury, R. García, J. M. Herreros Linares, I. Hughes, O. Iwert, J. Lima, J.-L. Lizon, G. Lo Curto, C. Lovis, A. Manescau, C. Martins, D. Mégevand, A. Moitinho, P. Molaro, M. Monteiro, M. Monteiro, L. Pasquini, C. Mordasini, D. Queloz, J. L. Rasilla, J. M. Rebordão, S. Santana Tschudi, P. Santin, D. Sosnowska, P. Spanò, F. Tenegi, S. Udry, E. Vanzella, M. Viel, M. R. Zapatero Osorio, and F. Zerbi. ESPRESSO: the Echelle spectrograph for rocky exoplanets and stable spectroscopic observations. In *Ground-based and Airborne Instrumentation for*

Astronomy III, volume 7735 of *Proceedings of the SPIE*, page 77350F, July 2010. doi: 10.1117/12.857122.

A. Pinhas and N. Madhusudhan. On signatures of clouds in exoplanetary transit spectra. *Monthly Notices of the RAS*, 471:4355–4373, November 2017. doi: 10.1093/mnras/stx1849.

L. Pino, D. Ehrenreich, A. Wyttenbach, V. Bourrier, V. Nascimbeni, K. Heng, S. Grimm, C. Lovis, M. Malik, F. Pepe, and G. Piotto. Combining low- to high-resolution transit spectroscopy of HD189733b. *ArXiv e-prints*, September 2017.

F. Pont, R. L. Gilliland, C. Moutou, D. Charbonneau, F. Bouchy, T. M. Brown, M. Mayor, D. Queloz, N. Santos, and S. Udry. Hubble Space Telescope time-series photometry of the planetary transit of HD 189733: no moon, no rings, starspots. *Astronomy & Astrophysics*, 476:1347–1355, December 2007. doi: 10.1051/0004-6361:20078269.

F. Pont, H. Knutson, R. L. Gilliland, C. Moutou, and D. Charbonneau. Detection of atmospheric haze on an extrasolar planet: the 0.55-1.05 μm transmission spectrum of HD 189733b with the HubbleSpaceTelescope. *Monthly Notices of the RAS*, 385: 109–118, March 2008. doi: 10.1111/j.1365-2966.2008.12852.x.

F. Pont, D. K. Sing, N. P. Gibson, S. Aigrain, G. Henry, and N. Husnoo. The prevalence of dust on the exoplanet HD 189733b from Hubble and Spitzer observations. *Monthly Notices of the RAS*, 432:2917–2944, July 2013. doi: 10.1093/mnras/stt651.

A. Quirrenbach, P. J. Amado, J. A. Caballero, R. Mundt, A. Reiners, I. Ribas, W. Seifert, M. Abril, J. Aceituno, F. J. Alonso-Floriano, M. Ammler-von Eiff, R. Antona Jiménez, H. Anwand-Heerwart, M. Azzaro, F. Bauer, D. Barrado, S. Becerril, V. J. S. Béjar, D. Benítez, Z. M. Berdiñas, M. C. Cárdenas, E. Casal, A. Claret, J. Colomé, M. Cortés-Contreras, S. Czesla, M. Doellinger, S. Dreizler, C. Feiz, M. Fernández, D. Galadí, M. C. Gálvez-Ortiz, A. García-Piquer, M. L. García-Vargas, R. Garrido, L. Gesa, V. Gómez Galera, E. González Álvarez, J. I. González Hernández, U. Grözinger, J. Guàrdia, E. W. Guenther, E. de Guindos, J. Gutiérrez-Soto, H.-J. Hagen, A. P. Hatzes, P. H. Hauschildt, J. Helmling, T. Henning, D. Hermann, L. Hernández Castaño, E. Herrero, D. Hidalgo, G. Holgado, A. Huber, K. F. Huber, S. Jeffers, V. Joergens, E. de Juan, M. Kehr, R. Klein, M. Kürster, A. Lamert, S. Lalitha, W. Laun, U. Lemke, R. Lenzen, M. López del Fresno, B. López Martí, J. López-Santiago, U. Mall, H. Mandel, E. L. Martín, S. Martín-Ruiz, H. Martínez-Rodríguez, C. J. Marvin, R. J. Mathar, E. Mirabet, D. Montes, R. Morales Muñoz, A. Moya, V. Naranjo, A. Ofir, R. Oreiro, E. Pallé, J. Panduro, V.-M. Passegger, A. Pérez-Calpena, D. Pérez Medialdea, M. Perger, M. Pluto, A. Ramón, R. Rebolo, P. Redondo, S. Reffert, S. Reinhardt, P. Rhode, H.-W. Rix, F. Rodler, E. Rodríguez, C. Rodríguez-López, E. Rodríguez-Pérez, R.-R. Rohloff, A. Rosich, E. Sánchez-Blanco, M. A. Sánchez Carrasco, J. Sanz-Forcada, L. F. Sarmiento, S. Schäfer, J. Schiller, C. Schmidt, J. H. M. M. Schmitt, E. Solano, O. Stahl, C. Storz, J. Stürmer, J. C. Suárez, R. G. Ulbrich, G. Veredas, K. Wagner, J. Winkler, M. R. Zapatero Osorio, M. Zechmeister, F. J. Abellán de Paco, G. Anglada-Escudé, C. del Burgo, A. Klutsch, J. L. Lizon, M. López-Morales, J. C. Morales, M. A. C. Perryman, S. M. Tulloch, and

W. Xu. CARMENES instrument overview. In *Ground-based and Airborne Instrumentation for Astronomy V*, volume 9147 of *Proceedings of the SPIE*, page 91471F, July 2014. doi: 10.1117/12.2056453.

J. Radigan, R. Jayawardhana, D. Lafrenière, É. Artigau, M. Marley, and D. Saumon. Large-amplitude Variations of an L/T Transition Brown Dwarf: Multi-wavelength Observations of Patchy, High-contrast Cloud Features. *Astrophysical Journal*, 750: 105, May 2012. doi: 10.1088/0004-637X/750/2/105.

H. Rauer, C. Catala, C. Aerts, T. Appourchaux, W. Benz, A. Brandeker, J. Christensen-Dalsgaard, M. Deleuil, L. Gizon, M.-J. Goupil, M. Güdel, E. Janot-Pacheco, M. Mas-Hesse, I. Pagano, G. Piotto, D. Pollacco, Ċ. Santos, A. Smith, J.-C. Suárez, R. Szabó, S. Udry, V. Adibekyan, Y. Alibert, J.-M. Almenara, P. Amaro-Seoane, M. A.-v. Eiff, M. Asplund, E. Antonello, S. Barnes, F. Baudin, K. Belkacem, M. Bergemann, G. Bihain, A. C. Birch, X. Bonfils, I. Boisse, A. S. Bonomo, F. Borsa, I. M. Brandão, E. Brocato, S. Brun, M. Burleigh, R. Burston, J. Cabrera, S. Cassisi, W. Chaplin, S. Charpinet, C. Chiappini, R. P. Church, S. Csizmadia, M. Cunha, M. Damasso, M. B. Davies, H. J. Deeg, R. F. Díaz, S. Dreizler, C. Dreyer, P. Eggenberger, D. Ehrenreich, P. Eigmüller, A. Erikson, R. Farmer, S. Feltzing, F. de Oliveira Fialho, P. Figueira, T. Forveille, M. Fridlund, R. A. García, P. Giommi, G. Giuffrida, M. Godolt, J. Gomes da Silva, T. Granzer, J. L. Grenfell, A. Grotsch-Noels, E. Günther, C. A. Haswell, A. P. Hatzes, G. Hébrard, S. Hekker, R. Helled, K. Heng, J. M. Jenkins, A. Johansen, M. L. Khodachenko, K. G. Kislyakova, W. Kley, U. Kolb, N. Krivova, F. Kupka, H. Lammer, A. F. Lanza, Y. Lebreton, D. Magrin, P. Marcos-Arenal, P. M. Marrese, J. P. Marques, J. Martins, S. Mathis, S. Mathur, S. Messina, A. Miglio, J. Montalban, M. Montalto, M. J. P. F. G. Monteiro, H. Moradi, E. Moravveji, C. Mordasini, T. Morel, A. Mortier, V. Nascimbeni, R. P. Nelson, M. B. Nielsen, L. Noack, A. J. Norton, A. Ofir, M. Oshagh, R.-M. Ouazzani, P. Pápics, V. C. Parro, P. Petit, B. Plez, E. Poretti, A. Quirrenbach, R. Ragazzoni, G. Raimondo, M. Rainer, D. R. Reese, R. Redmer, S. Reffert, B. Rojas-Ayala, I. W. Roxburgh, S. Salmon, A. Santerne, J. Schneider, J. Schou, S. Schuh, H. Schunker, A. Silva-Valio, R. Silvotti, I. Skillen, I. Snellen, F. Sohl, S. G. Sousa, A. Sozzetti, D. Stello, K. G. Strassmeier, M. Švanda, G. M. Szabó, A. Tkachenko, D. Valencia, V. Van Grootel, S. D. Vauclair, P. Ventura, F. W. Wagner, N. A. Walton, J. Weingrill, S. C. Werner, P. J. Wheatley, and K. Zwintz. The PLATO 2.0 mission. *Experimental Astronomy*, 38:249–330, November 2014. doi: 10.1007/s10686-014-9383-4.

E. Rauscher, K. Menou, J. Y-K. Cho, S. Seager, and B. M. S. Hansen. On Signatures of Atmospheric Features in Thermal Phase Curves of Hot Jupiters. *Astrophysical Journal*, 681:1646-1652, July 2008. doi: 10.1086/589499.

S. Redfield, M. Endl, W. D. Cochran, and L. Koesterke. Sodium Absorption from the Exoplanetary Atmosphere of HD 189733b Detected in the Optical Transmission Spectrum. *Astrophysical Journal, Letters*, 673:L87, January 2008. doi: 10.1086/527475.

D. Reuyl and E. Holmberg. On the Existence of a Third Component in the System 70 Ophiuchi. *Astrophysical Journal*, 97:41, January 1943. doi: 10.1086/144489.

M. Rey, A. V. Nikitin, Y. L. Babikov, and V. G. Tyuterev. TheoReTS - An information system for theoretical spectra based on variational predictions from molecular potential energy and dipole moment surfaces. *Journal of Molecular Spectroscopy*, 327:138–158, September 2016. doi: 10.1016/j.jms.2016.04.006.

C. Richard, I. E. Gordon, L. S. Rothman, M. Abel, L. Frommhold, M. Gustafsson, J.-M. Hartmann, C. Hermans, W. J. Lafferty, G. S. Orton, K. M. Smith, and H. Tran. New section of the HITRAN database: Collision-induced absorption (CIA). *Journal of Quantitative Spectroscopy and Radiative Transfer*, 113:1276–1285, July 2012. doi: 10.1016/j.jqsrt.2011.11.004.

G. R. Ricker, J. N. Winn, R. Vanderspek, D. W. Latham, G. Á. Bakos, J. L. Bean, Z. K. Berta-Thompson, T. M. Brown, L. Buchhave, N. R. Butler, R. P. Butler, W. J. Chaplin, D. Charbonneau, J. Christensen-Dalsgaard, M. Clampin, D. Deming, J. Doty, N. De Lee, C. Dressing, E. W. Dunham, M. Endl, F. Fressin, J. Ge, T. Henning, M. J. Holman, A. W. Howard, S. Ida, J. Jenkins, G. Jernigan, J. A. Johnson, L. Kaltenegger, N. Kawai, H. Kjeldsen, G. Laughlin, A. M. Levine, D. Lin, J. J. Lissauer, P. MacQueen, G. Marcy, P. R. McCullough, T. D. Morton, N. Narita, M. Paegert, E. Palle, F. Pepe, J. Pepper, A. Quirrenbach, S. A. Rinehart, D. Sasselov, B. Sato, S. Seager, A. Sozzetti, K. G. Stassun, P. Sullivan, A. Szentgyorgyi, G. Torres, S. Udry, and J. Villasenor. Transiting Exoplanet Survey Satellite (TESS). In *Space Telescopes and Instrumentation 2014: Optical, Infrared, and Millimeter Wave*, volume 9143 of *Proceedings of the SPIE*, page 914320, August 2014. doi: 10.1117/12.2063489.

G. R. Ricker, J. N. Winn, R. Vanderspek, D. W. Latham, G. Á. Bakos, J. L. Bean, Z. K. Berta-Thompson, T. M. Brown, L. Buchhave, N. R. Butler, R. P. Butler, W. J. Chaplin, D. Charbonneau, J. Christensen-Dalsgaard, M. Clampin, D. Deming, J. Doty, N. De Lee, C. Dressing, E. W. Dunham, M. Endl, F. Fressin, J. Ge, T. Henning, M. J. Holman, A. W. Howard, S. Ida, J. M. Jenkins, G. Jernigan, J. A. Johnson, L. Kaltenegger, N. Kawai, H. Kjeldsen, G. Laughlin, A. M. Levine, D. Lin, J. J. Lissauer, P. MacQueen, G. Marcy, P. R. McCullough, T. D. Morton, N. Narita, M. Paegert, E. Palle, F. Pepe, J. Pepper, A. Quirrenbach, S. A. Rinehart, D. Sasselov, B. Sato, S. Seager, A. Sozzetti, K. G. Stassun, P. Sullivan, A. Szentgyorgyi, G. Torres, S. Udry, and J. Villasenor. Transiting Exoplanet Survey Satellite (TESS). *Journal of Astronomical Telescopes, Instruments, and Systems*, 1(1):014003, January 2015. doi: 10.1117/1.JATIS.1.1.014003.

T. D. Robinson. A Theory of Exoplanet Transits with Light Scattering. *Astrophysical Journal*, 836:236, February 2017. doi: 10.3847/1538-4357/aa5ea8.

T. D. Robinson and D. C. Catling. Common 0.1bar tropopause in thick atmospheres set by pressure-dependent infrared transparency. *Nature Geoscience*, 7:12–15, January 2014. doi: 10.1038/ngeo2020.

T. D. Robinson, J. J. Fortney, and W. B. Hubbard. Analytic Scattering and Refraction Models for Exoplanet Transit Spectra. *ArXiv e-prints*, November 2017.

M. Rocchetto, I. P. Waldmann, O. Venot, P.-O. Lagage, and G. Tinetti. Exploring Biases of Atmospheric Retrievals in Simulated JWST Transmission Spectra of Hot Jupiters. *Astrophysical Journal*, 833:120, December 2016. doi: 10.3847/1538-4357/833/1/120.

R. A. Rossiter. On the detection of an effect of rotation during eclipse in the velocity of the brigher component of beta Lyrae, and on the constancy of velocity of this system. *Astrophysical Journal*, 60, July 1924. doi: 10.1086/142825.

L. S. Rothman, R. B. Wattson, R. Gamache, J. W. Schroeder, and A. McCann. HITRAN HAWKS and HITEMP: high-temperature molecular database. In J. C. Dainty, editor, *Atmospheric Propagation and Remote Sensing IV*, volume 2471 of *Proceedings of the SPIE*, pages 105–111, June 1995. doi: 10.1117/12.211919.

L. S. Rothman, I. E. Gordon, R. J. Barber, H. Dothe, R. R. Gamache, A. Goldman, V. I. Perevalov, S. A. Tashkun, and J. Tennyson. HITEMP, the high-temperature molecular spectroscopic database. *Journal of Quantitative Spectroscopy and Radiative Transfer*, 111:2139–2150, October 2010. doi: 10.1016/j.jqsrt.2010.05.001.

L. S. Rothman, I. E. Gordon, Y. Babikov, A. Barbe, D. Chris Benner, P. F. Bernath, M. Birk, L. Bizzocchi, V. Boudon, L. R. Brown, A. Campargue, K. Chance, E. A. Cohen, L. H. Coudert, V. M. Devi, B. J. Drouin, A. Fayt, J.-M. Flaud, R. R. Gamache, J. J. Harrison, J.-M. Hartmann, C. Hill, J. T. Hodges, D. Jacquemart, A. Jolly, J. Lamouroux, R. J. Le Roy, G. Li, D. A. Long, O. M. Lyulin, C. J. Mackie, S. T. Massie, S. Mikhailenko, H. S. P. Müller, O. V. Naumenko, A. V. Nikitin, J. Orphal, V. Perevalov, A. Perrin, E. R. Polovtseva, C. Richard, M. A. H. Smith, E. Starikova, K. Sung, S. Tashkun, J. Tennyson, G. C. Toon, V. G. Tyuterev, and G. Wagner. The HITRAN2012 molecular spectroscopic database. *Journal of Quantitative Spectroscopy and Radiative Transfer*, 130:4–50, November 2013. doi: 10.1016/j.jqsrt.2013.07.002.

G. B. Rybicki and A. P. Lightman. *Radiative Processes in Astrophysics*. June 1986.

M. Salz, P. C. Schneider, S. Czesla, and J. H. M. M. Schmitt. High-energy irradiation and mass loss rates of hot Jupiters in the solar neighborhood. *Astronomy & Astrophysics*, 576:A42, April 2015. doi: 10.1051/0004-6361/201425243.

J. H. M. M. Schmitt and C. Liefke. NEXXUS: A comprehensive ROSAT survey of coronal X-ray emission among nearby solar-like stars. *Astronomy & Astrophysics*, 417:651–665, April 2004. doi: 10.1051/0004-6361:20030495.

H. Schwarz, M. Brogi, R. de Kok, J. Birkby, and I. Snellen. Evidence against a strong thermal inversion in HD 209458b from high-dispersion spectroscopy. *Astronomy & Astrophysics*, 576:A111, April 2015. doi: 10.1051/0004-6361/201425170.

D. W. Schwenke. Opacity of TiO from a coupled electronic state calculation parametrized by AB initio and experimental data. *Faraday Discussions*, 109: 321, 1998. doi: 10.1039/a800070k.

S. Seager. *Exoplanet Atmospheres: Physical Processes*. 2010.

S. Seager and D. D. Sasselov. Theoretical Transmission Spectra during Extrasolar Giant Planet Transits. *Astrophysical Journal*, 537:916–921, July 2000. doi: 10.1086/309088.

S. Seager, L. J. Richardson, B. M. S. Hansen, K. Menou, J. Y.-K. Cho, and D. Deming. On the Dayside Thermal Emission of Hot Jupiters. *Astrophysical Journal*, 632:1122–1131, October 2005. doi: 10.1086/444411.

S. Seager, M. Kuchner, C. A. Hier-Majumder, and B. Militzer. Mass-Radius Relationships for Solid Exoplanets. *Astrophysical Journal*, 669:1279–1297, November 2007. doi: 10.1086/521346.

E. Sedaghati, H. M. J. Boffin, S. Csizmadia, N. Gibson, P. Kabath, M. Mallonn, and M. E. Van den Ancker. Regaining the FORS: optical ground-based transmission spectroscopy of the exoplanet WASP-19b with VLT+FORS2. *Astronomy & Astrophysics*, 576:L11, April 2015. doi: 10.1051/0004-6361/201525822.

E. Sedaghati, H. M. J. Boffin, T. Jeřabková, A. García Muñoz, J. L. Grenfell, A. Smette, V. D. Ivanov, S. Csizmadia, J. Cabrera, P. Kabath, M. Rocchetto, and H. Rauer. Potassium detection in the clear atmosphere of a hot-Jupiter. FORS2 transmission spectroscopy of WASP-17b. *Astronomy & Astrophysics*, 596:A47, November 2016. doi: 10.1051/0004-6361/201629090.

E. Sedaghati, H. M. J. Boffin, R. J. MacDonald, S. Gandhi, N. Madhusudhan, N. P. Gibson, M. Oshagh, A. Claret, and H. Rauer. Detection of titanium oxide in the atmosphere of a hot Jupiter. *Nature*, 549:238–241, September 2017. doi: 10.1038/nature23651.

C. M. Sharp and A. Burrows. Atomic and Molecular Opacities for Brown Dwarf and Giant Planet Atmospheres. *Astrophysical Journal, supplement*, 168:140–166, January 2007. doi: 10.1086/508708.

A. P. Showman, J. J. Fortney, Y. Lian, M. S. Marley, R. S. Freedman, H. A. Knutson, and D. Charbonneau. Atmospheric Circulation of Hot Jupiters: Coupled Radiative-Dynamical General Circulation Model Simulations of HD 189733b and HD 209458b. *Astrophysical Journal*, 699:564–584, July 2009. doi: 10.1088/0004-637X/699/1/564.

A. P. Showman, J. J. Fortney, N. K. Lewis, and M. Shabram. Doppler Signatures of the Atmospheric Circulation on Hot Jupiters. *Astrophysical Journal*, 762:24, January 2013. doi: 10.1088/0004-637X/762/1/24.

D. K. Sing, A. Vidal-Madjar, A. Lecavelier des Etangs, J.-M. Désert, G. Ballester, and D. Ehrenreich. Determining Atmospheric Conditions at the Terminator of the Hot Jupiter HD 209458b. *Astrophysical Journal*, 686:667-673, October 2008. doi: 10.1086/590076.

D. K. Sing, F. Pont, S. Aigrain, D. Charbonneau, J.-M. Désert, N. Gibson, R. Gilliland, W. Hayek, G. Henry, H. Knutson, A. Lecavelier Des Etangs, T. Mazeh, and A. Shporer. Hubble Space Telescope transmission spectroscopy of the exoplanet HD 189733b: high-altitude atmospheric haze in the optical and near-ultraviolet with STIS. *Monthly Notices of the RAS*, 416:1443–1455, September 2011. doi: 10.1111/j.1365-2966.2011.19142.x.

D. K. Sing, H. R. Wakeford, A. P. Showman, N. Nikolov, J. J. Fortney, A. S. Burrows, G. E. Ballester, D. Deming, S. Aigrain, J.-M. Désert, N. P. Gibson, G. W. Henry, H. Knutson, A. Lecavelier des Etangs, F. Pont, A. Vidal-Madjar, M. W. Williamson, and P. A. Wilson. HST hot-Jupiter transmission spectral survey: detection of potassium in WASP-31b along with a cloud deck and Rayleigh scattering. *Monthly Notices of the RAS*, 446:2428–2443, January 2015. doi: 10.1093/mnras/stu2279.

D. K. Sing, J. J. Fortney, N. Nikolov, H. R. Wakeford, T. Kataria, T. M. Evans, S. Aigrain, G. E. Ballester, A. S. Burrows, D. Deming, J.-M. Désert, N. P. Gibson, G. W. Henry, C. M. Huitson, H. A. Knutson, A. L. D. Etangs, F. Pont, A. P. Showman, A. Vidal-Madjar, M. H. Williamson, and P. A. Wilson. A continuum from clear to cloudy hot-Jupiter exoplanets without primordial water depletion. *Nature*, 529:59–62, January 2016. doi: 10.1038/nature16068.

A. Smette, H. Sana, S. Noll, H. Horst, W. Kausch, S. Kimeswenger, M. Barden, C. Szyszka, A. M. Jones, A. Gallenne, J. Vinther, P. Ballester, and J. Taylor. Molecfit: A general tool for telluric absorption correction. I. Method and application to ESO instruments. *Astronomy & Astrophysics*, 576:A77, April 2015. doi: 10.1051/0004-6361/201423932.

C. Sneden, H. R. Johnson, and B. M. Krupp. A statistical method for treating molecular line opacities. *Astrophysical Journal*, 204:281–289, February 1976. doi: 10.1086/154169.

I. Snellen, S. Albrecht, E. de Mooij, and R. L. Poole. Lessons Learned from Ground-based Transmission Spectroscopy of Extrasolar Planets. In J. P. Beaulieu, S. Dieters, and G. Tinetti, editors, *Molecules in the Atmospheres of Extrasolar Planets*, volume 450 of *Astronomical Society of the Pacific Conference Series*, page 39, December 2011.

I. A. G. Snellen. A new method for probing the atmospheres of transiting exoplanets. *Monthly Notices of the RAS*, 353:L1–L6, September 2004. doi: 10.1111/j.1365-2966.2004.08169.x.

I. A. G. Snellen, S. Albrecht, E. J. W. de Mooij, and R. S. Le Poole. Ground-based detection of sodium in the transmission spectrum of exoplanet HD 209458b. *Astronomy & Astrophysics*, 487:357–362, August 2008. doi: 10.1051/0004-6361:200809762.

I. A. G. Snellen, R. J. de Kok, E. J. W. de Mooij, and S. Albrecht. The orbital motion, absolute mass and high-altitude winds of exoplanet HD209458b. *Nature*, 465:1049–1051, June 2010. doi: 10.1038/nature09111.

I. A. G. Snellen, R. Stuik, R. Navarro, F. Bettonvil, M. Kenworthy, E. de Mooij, G. Otten, R. ter Horst, and R. le Poole. Ground-based search for the brightest transiting planets with the Multi-site All-Sky CAmeRA: MASCARA. In *Ground-based and Airborne Telescopes IV*, volume 8444 of *Proceedings of the SPIE*, page 84440I, September 2012. doi: 10.1117/12.925178.

J. Southworth and D. F. Evans. Contamination from a nearby star cannot explain the anomalous transmission spectrum of the ultrashort period giant planet WASP-103 b. *Monthly Notices of the RAS*, 463:37–44, November 2016. doi: 10.1093/mnras/stw1943.

J. Southworth, L. Mancini, S. Ciceri, J. Budaj, M. Dominik, R. Figuera Jaimes, T. Haugbølle, U. G. Jørgensen, A. Popovas, M. Rabus, S. Rahvar, C. von Essen, R. W. Schmidt, O. Wertz, K. A. Alsubai, V. Bozza, D. M. Bramich, S. Calchi Novati, G. D'Ago, T. C. Hinse, T. Henning, M. Hundertmark, D. Juncher, H. Korhonen, J. Skottfelt, C. Snodgrass, D. Starkey, and J. Surdej. High-precision photometry by telescope defocusing - VII. The ultrashort period planet

WASP-103. *Monthly Notices of the RAS*, 447:711–721, February 2015. doi: 10.1093/mnras/stu2394.

D. S. Spiegel, K. Silverio, and A. Burrows. Can TiO Explain Thermal Inversions in the Upper Atmospheres of Irradiated Giant Planets? *Astrophysical Journal*, 699: 1487–1500, July 2009. doi: 10.1088/0004-637X/699/2/1487.

K. B. Stevenson. Quantifying and Predicting the Presence of Clouds in Exoplanet Atmospheres. *Astrophysical Journal, Letters*, 817:L16, February 2016. doi: 10.3847/2041-8205/817/2/L16.

K. B. Stevenson, J. L. Bean, A. Seifahrt, J.-M. Désert, N. Madhusudhan, M. Bergmann, L. Kreidberg, and D. Homeier. Transmission Spectroscopy of the Hot Jupiter WASP-12b from 0.7 to 5 μm. *Astronomical Journal*, 147:161, June 2014. doi: 10.1088/0004-6256/147/6/161.

K. A. Strand. 61 Cygni as a Triple System. *Publications of the ASP*, 55:29–32, February 1943. doi: 10.1086/125484.

K. G. Strassmeier, M. Woche, I. Ilyin, E. Popow, S.-M. Bauer, F. Dionies, T. Fechner, M. Weber, A. Hofmann, J. Storm, R. Materne, W. Bittner, J. Bartus, T. Granzer, C. Denker, T. Carroll, M. Kopf, I. DiVarano, E. Beckert, and M. Lesser. PEPSI: the Potsdam Echelle Polarimetric and Spectroscopic Instrument for the LBT. In *Ground-based and Airborne Instrumentation for Astronomy II*, volume 7014 of *Proceedings of the SPIE*, page 70140N, July 2008. doi: 10.1117/12.787376.

M. Tamura, H. Suto, J. Nishikawa, T. Kotani, B. Sato, W. Aoki, T. Usuda, T. Kurokawa, K. Kashiwagi, S. Nishiyama, Y. Ikeda, D. Hall, K. Hodapp, J. Hashimoto, J. Morino, S. Inoue, Y. Mizuno, Y. Washizaki, Y. Tanaka, S. Suzuki, J. Kwon, T. Suenaga, D. Oh, N. Narita, E. Kokubo, Y. Hayano, H. Izumiura, E. Kambe, T. Kudo, N. Kusakabe, M. Ikoma, Y. Hori, M. Omiya, H. Genda, A. Fukui, Y. Fujii, O. Guyon, H. Harakawa, M. Hayashi, M. Hidai, T. Hirano, M. Kuzuhara, M. Machida, T. Matsuo, T. Nagata, H. Ohnuki, M. Ogihara, S. Oshino, R. Suzuki, H. Takami, N. Takato, Y. Takahashi, C. Tachinami, and H. Terada. Infrared Doppler instrument for the Subaru Telescope (IRD). In *Ground-based and Airborne Instrumentation for Astronomy IV*, volume 8446 of *Proceedings of the SPIE*, page 84461T, September 2012. doi: 10.1117/12.925885.

J. Tennyson and S. N. Yurchenko. ExoMol: molecular line lists for exoplanet and other atmospheres. *Monthly Notices of the RAS*, 425:21–33, September 2012. doi: 10.1111/j.1365-2966.2012.21440.x.

J. Tennyson, S. N. Yurchenko, A. F. Al-Refaie, E. J. Barton, K. L. Chubb, P. A. Coles, S. Diamantopoulou, M. N. Gorman, C. Hill, A. Z. Lam, L. Lodi, L. K. McKemmish, Y. Na, A. Owens, O. L. Polyansky, T. Rivlin, C. Sousa-Silva, D. S. Underwood, A. Yachmenev, and E. Zak. The ExoMol database: Molecular line lists for exoplanet and other hot atmospheres. *Journal of Molecular Spectroscopy*, 327:73–94, September 2016. doi: 10.1016/j.jms.2016.05.002.

S. Thibault, P. Rabou, J.-F. Donati, P. Desaulniers, X. Dallaire, E. Artigau, F. Pepe, Y. Micheau, P. Vallée, F. Pepe, G. Barrick, V. Reshetov, O. Hernandez, L. Saddlemyer, J. Pazder, L. P. Parès, R. Doyon, X. Delfosse, D. Kouach, and D. Loop.

SPIRou @ CFHT: spectrograph optical design. In *Ground-based and Airborne Instrumentation for Astronomy IV*, volume 8446 of *Proceedings of the SPIE*, page 844630, September 2012. doi: 10.1117/12.926697.

G. Tinetti, M.-C. Liang, A. Vidal-Madjar, D. Ehrenreich, A. Lecavelier des Etangs, and Y. L. Yung. Infrared Transmission Spectra for Extrasolar Giant Planets. *Astrophysical Journal, Letters*, 654:L99–L102, January 2007. doi: 10.1086/510716.

K. O. Todorov, M. R. Line, J. E. Pineda, M. R. Meyer, S. P. Quanz, S. Hinkley, and J. J. Fortney. The Water Abundance of the Directly Imaged Substellar Companion κ And b Retrieved from a Near Infrared Spectrum. *Astrophysical Journal*, 823: 14, May 2016. doi: 10.3847/0004-637X/823/1/14.

A. Tsiaras, I. P. Waldmann, T. Zingales, M. Rocchetto, G. Morello, M. Damiano, K. Karpouzas, G. Tinetti, L. K. McKemmish, J. Tennyson, and S. N. Yurchenko. A population study of hot Jupiter atmospheres. *ArXiv e-prints*, April 2017.

A. Vidal-Madjar, A. Lecavelier des Etangs, J.-M. Désert, G. E. Ballester, R. Ferlet, G. Hébrard, and M. Mayor. An extended upper atmosphere around the extrasolar planet HD209458b. *Nature*, 422:143–146, March 2003. doi: 10.1038/nature01448.

A. Vidal-Madjar, J.-M. Désert, A. Lecavelier des Etangs, G. Hébrard, G. E. Ballester, D. Ehrenreich, R. Ferlet, J. C. McConnell, M. Mayor, and C. D. Parkinson. Detection of Oxygen and Carbon in the Hydrodynamically Escaping Atmosphere of the Extrasolar Planet HD 209458b. *Astrophysical Journal, Letters*, 604: L69–L72, March 2004. doi: 10.1086/383347.

A. Vidal-Madjar, D. K. Sing, A. Lecavelier Des Etangs, R. Ferlet, J.-M. Désert, G. Hébrard, I. Boisse, D. Ehrenreich, and C. Moutou. The upper atmosphere of the exoplanet HD 209458 b revealed by the sodium D lines. Temperature-pressure profile, ionization layer, and thermosphere. *Astronomy & Astrophysics*, 527:A110, March 2011a. doi: 10.1051/0004-6361/201015698.

A. Vidal-Madjar, D. K. Sing, A. Lecavelier Des Etangs, R. Ferlet, J.-M. Désert, G. Hébrard, I. Boisse, D. Ehrenreich, and C. Moutou. The upper atmosphere of the exoplanet HD 209458 b revealed by the sodium D lines. Temperature-pressure profile, ionization layer, and thermosphere. *Astronomy & Astrophysics*, 527:A110, March 2011b. doi: 10.1051/0004-6361/201015698.

A. Vidal-Madjar, C. M. Huitson, V. Bourrier, J.-M. Désert, G. Ballester, A. Lecavelier des Etangs, D. K. Sing, D. Ehrenreich, R. Ferlet, G. Hébrard, and J. C. McConnell. Magnesium in the atmosphere of the planet HD 209458 b: observations of the thermosphere-exosphere transition region. *Astronomy & Astrophysics*, 560:A54, December 2013. doi: 10.1051/0004-6361/201322234.

S. M. Wahl, W. B. Hubbard, B. Militzer, T. Guillot, Y. Miguel, N. Movshovitz, Y. Kaspi, R. Helled, D. Reese, E. Galanti, S. Levin, J. E. Connerney, and S. J. Bolton. Comparing Jupiter interior structure models to Juno gravity measurements and the role of a dilute core. *Geophysics Research Letters*, 44:4649–4659, May 2017. doi: 10.1002/2017GL073160.

H. R. Wakeford and D. K. Sing. Transmission spectral properties of clouds for hot Jupiter exoplanets. *Astronomy & Astrophysics*, 573:A122, January 2015. doi: 10.1051/0004-6361/201424207.

H. R. Wakeford, K. B. Stevenson, N. K. Lewis, D. K. Sing, M. López-Morales, M. Marley, T. Kataria, A. Mandell, G. E. Ballester, J. Barstow, L. Ben-Jaffel, V. Bourrier, L. A. Buchhave, D. Ehrenreich, T. Evans, A. García Muñoz, G. Henry, H. Knutson, P. Lavvas, A. Lecavelier des Etangs, N. Nikolov, and J. Sanz-Forcada. HST PanCET program: A Cloudy Atmosphere for the Promising JWST Target WASP-101b. *Astrophysical Journal, Letters*, 835:L12, January 2017a. doi: 10.3847/2041-8213/835/1/L12.

H. R. Wakeford, C. Visscher, N. K. Lewis, T. Kataria, M. S. Marley, J. J. Fortney, and A. M. Mandell. High-temperature condensate clouds in super-hot Jupiter atmospheres. *Monthly Notices of the RAS*, 464:4247–4254, February 2017b. doi: 10.1093/mnras/stw2639.

I. P. Waldmann, G. Tinetti, M. Rocchetto, E. J. Barton, S. N. Yurchenko, and J. Tennyson. Tau-REx I: A Next Generation Retrieval Code for Exoplanetary Atmospheres. *Astrophysical Journal*, 802:107, April 2015. doi: 10.1088/0004-637X/802/2/107.

J. Wang and D. A. Fischer. Revealing a Universal Planet-Metallicity Correlation for Planets of Different Sizes Around Solar-type Stars. *Astronomical Journal*, 149:14, January 2015. doi: 10.1088/0004-6256/149/1/14.

M. W. Webber, N. K. Lewis, M. Marley, C. Morley, J. J. Fortney, and K. Cahoy. Effect of Longitude-dependent Cloud Coverage on Exoplanet Visible Wavelength Reflected-light Phase Curves. *Astrophysical Journal*, 804:94, May 2015. doi: 10.1088/0004-637X/804/2/94.

A. Wolszczan and D. A. Frail. A planetary system around the millisecond pulsar PSR1257 + 12. *Nature*, 355:145–147, January 1992. doi: 10.1038/355145a0.

P. L. Wood, P. F. L. Maxted, B. Smalley, and N. Iro. Transmission spectroscopy of the sodium 'D' doublet in WASP-17b with the VLT. *Monthly Notices of the RAS*, 412:2376–2382, April 2011. doi: 10.1111/j.1365-2966.2010.18061.x.

R. Wordsworth. Hydrogen and climate in primitive terrestrial and super-Earth atmospheres (Invited). *AGU Fall Meeting Abstracts*, December 2013.

A. Wyttenbach, D. Ehrenreich, C. Lovis, S. Udry, and F. Pepe. Spectrally resolved detection of sodium in the atmosphere of HD 189733b with the HARPS spectrograph. *Astronomy & Astrophysics*, 577:A62, May 2015. doi: 10.1051/0004-6361/201525729.

A. Wyttenbach, C. Lovis, D. Ehrenreich, V. Bourrier, L. Pino, R. Allart, N. Astudillo-Defru, H. M. Cegla, K. Heng, B. Lavie, C. Melo, F. Murgas, A. Santerne, D. Ségransan, S. Udry, and F. Pepe. Hot Exoplanet Atmospheres Resolved with Transit Spectroscopy (HEARTS). I. Detection of hot neutral sodium at high altitudes on WASP-49b. *Astronomy & Astrophysics*, 602:A36, June 2017. doi: 10.1051/0004-6361/201630063.

F. Yan, E. Pallé, R. A. E. Fosbury, M. G. Petr-Gotzens, and T. Henning. Effect of the stellar absorption line centre-to-limb variation on exoplanet transmission spectrum observations. *Astronomy & Astrophysics*, 603:A73, July 2017. doi: 10.1051/0004-6361/201630144.

R. V. Yelle. Aeronomy of extra-solar giant planets at small orbital distances. *Icarus*, 170:167–179, July 2004. doi: 10.1016/j.icarus.2004.02.008.

S. N. Yurchenko, D. S. Amundsen, J. Tennyson, and I. P. Waldmann. A hybrid line list for CH_4 and hot methane continuum. *Astronomy & Astrophysics*, 605:A95, September 2017. doi: 10.1051/0004-6361/201731026.

L. Zeng, D. D. Sasselov, and S. B. Jacobsen. Mass-Radius Relation for Rocky Planets Based on PREM. *Astrophysical Journal*, 819:127, March 2016. doi: 10.3847/0004-637X/819/2/127.

F. M. Zerbi, F. Bouchy, J. Fynbo, R. Maiolino, N. Piskunov, R. Rebolo Lopez, N. Santos, K. Strassmeier, S. Udry, L. Vanzi, M. Riva, A. Basden, I. Boisse, X. Bonfils, D. Buscher, A. Cabral, P. Dimarcantonio, I. Di Varano, D. Henry, M. Monteiro, T. Morris, G. Murray, E. Oliva, I. Parry, F. Pepe, A. Quirrenbach, J. L. Rasilla, P. Rees, E. Stempels, L. Valenziano, M. Wells, F. Wildi, L. Origlia, C. Allende Prieto, A. Chiavassa, S. Cristiani, P. Figueira, B. Gustafsson, A. Hatzes, M. Haehnelt, K. Heng, G. Israelian, O. Kochukhov, C. Lovis, A. Marconi, C. J. A. P. Martins, P. Noterdaeme, P. Petitjean, T. Puzia, D. Queloz, A. Reiners, and M. Zoccali. HIRES: the high resolution spectrograph for the E-ELT. In *Ground-based and Airborne Instrumentation for Astronomy V*, volume 9147 of *Proceedings of the SPIE*, page 914723, August 2014. doi: 10.1117/12.2055329.

X. Zhang, R. A. West, P. G. J. Irwin, C. A. Nixon, and Y. L. Yung. Aerosol influence on energy balance of the middle atmosphere of Jupiter. *Nature Communications*, 6:10231, December 2015. doi: 10.1038/ncomms10231.

G. Zhou and D. D. R. Bayliss. Detection of sodium absorption in WASP-17b with Magellan. *Monthly Notices of the RAS*, 426:2483–2488, November 2012. doi: 10.1111/j.1365-2966.2012.21817.x.

W. Zhu, J. Wang, and C. Huang. Dependence of Small Planet Frequency on Stellar Metallicity Hidden by Their Prevalence. *Astrophysical Journal*, 832:196, December 2016. doi: 10.3847/0004-637X/832/2/196.